8-2021

Photophysics of substituted [1,4]Benzodioxino[3,2-b]Oxanthrene (BDO) Chromophores and their macromolecules: a spectroscopy and density functional theory study.

Abdelqader M. Jamhawi
University of Louisville

PHOTOPHYSICS OF SUBSTITUTED
[1,4]BENZODIOXINO[3,2-B]OXANTHRENE (BDO) CHROMOPHORES AND
THEIR MACROMOLECULES: A SPECTROSCOPY AND DENSITY
FUNCTIONAL THEORY STUDY

by

Abdelqader M. Jamhawi
B.Sc. Yarmouk University, Jordan 2006
M.Sc. Yarmouk University, Jordan 2010
M.Sc. University of Louisville, 2017

A dissertation Submitted to the Faculty of
College of Arts and Sciences of the University of Louisville
in Partial Fulfillment of the Requirements
for the Degree of

Doctor of Philosophy in Chemistry

Department of Chemistry
University of Louisville
Louisville, Kentucky

August 2021

PHOTOPHYSICS OF SUBSTITUTED
[1,4]BENZODIOXINO[3,2-B]OXANTHRENE (BDO) CHROMOPHORES AND
THEIR MACROMOLECULES: A SPECTROSCOPY AND DENSITY
FUNCTIONAL THEORY STUDY

by

Abdelqader M. Jamhawi
B.Sc. Yarmouk University, Jordan 2006
M.Sc. Yarmouk University, Jordan 2010
M.Sc. University of Louisville, 2017

Dissertation Approved on

June 11, 2021

By the following Dissertation committee:

—————————————————
Dissertation Director
Dr. Jinjun Liu

—————————————————
Prof. Richard J. Wittebort

—————————————————
Prof. Richard P. Baldwin

—————————————————
Prof. Gamini Sumanasekera

—————————————————
Prof. Mahendra K. Sunkara

DEDICATION

To my family, home and abroad.

ACKNOWLEDGMENTS

ABSTRACT

PHOTOPHYSICS OF SUBSTITUTED
[1,4]BENZODIOXINO[3,2-B]OXANTHRENE (BDO) CHROMOPHORES AND
THEIR MACROMOLECULES: A SPECTROSCOPY AND DENSITY
FUNCTIONAL THEORY STUDY

Abdelqader M. Jamhawi

August 10, 2021

Chromophores and macromolecules containing [1,4]benzodioxino[3,2-b]oxanthrene (BDO) has attracted attention since the beginning of this century. Previous studies demonstrated their potential in wide range of applications including gas permeability, hydrogen and energy storage, sensing, and catalysis. Better understanding of the geometrical and electronic structure characteristics of BDO–based chromophores is vital to advance their employment in these applications. This work utilizes spectroscopy techniques coupled with density functional theory methods to provide this required understanding.

Substituted BDOs exhibit red–shift of $>1\,\mathrm{eV}$ in their electronic transitions compared to unsubstituted BDOs. This shift is explained by a molecular orbital reorganization induced by the substituents. Sulfonated BDOs exhibit folding in their backbone compared to the planar dicarbonitrile BDO (BDODC). The folding originates from an $O\cdots C$ interaction between the sulfonyl substitute and the backbone of the chromophore. Photoexcitated BDODC relaxes to its first singlet excited state (S_1) in $\sim 3.8\,\mathrm{ps}$. Fast inter–system crossing (ISC) deactivates S_1 to the first triplet excited state (T_1) in $\sim 63\,\mathrm{ps}$. S_1 also deactivates to the ground state (S_0) through a

photoluminescence (PL) process in $\sim$13 ns.

Substituted BDOs retain their geometrical and electronic properties within the framework of the macromolecules. However, evidence suggests the presence of charge–transfer states (CTSs); rationalized by the Frenkel–Davydov exciton model. Theoretical methods indicate geometrical reorganization and charge redistribution associated with the lowest CTS. Spectroscopy methods reveal a relaxation to the S_1 of the macromolecules in $<$2 ps. S_1 deactivates through an ISC process in $<$65 ps and a PL process in $<$11.5 ns. Additionally, S_1 undergoes a fast charge–transfer to the CTS in $<$500 ps.

Folding of sulfonated BDOs rationalizes the higher gas separation efficiency reported for their membranes. Additionally, the geometrical reorganizations of their excited states provide a new tool to fine–tune their membranes' pore size for gas separation applications. The red–shift coupled with the fast ISC and charge–transfer processes rationalize the reported photocatalytic activity of BDO–based macromolecules. Co–polymer's size and composition control are recommended to improve their efficiency in photocatalysis applications.

TABLE OF CONTENTS

LIST OF TABLES

LIST OF FIGURES

LIST OF SCRIPTS

CHAPTER 1

INTRODUCTION

This chapter offers a literature review of the chromophores and macromolecules with [1,4]benzodioxino[3,2-b]oxanthrene (BDO) backbone in Section 1.1. The section covers synthetic methods, photophysical and geometrical properties, and applications. Section 1.2 details the underlying theory of Frenkel–Davydov exciton model used in interpreting the experimental and theoretical results. Finally, Section 1.3 summarizes the goals of this work and their effect on the applications of BDO–based chromophores and macromolecules, especially gas permeability and photocatalysis.

1.1   CHROMOPHORES AND MACROMOLECULES OF [1,4]BENZODIOXINO[3,2-B]OXANTHRENES (BDOS): HISTORY, PROPERTIES, AND APPLICATION

The backbone of BDO chromophores can be described as a heterocyclic compound with five linearly–fused, six–membered rings, Figure 1.1. Both the second and the fourth rings, within this backbone, contained two oxygen atoms in the *para* position with respect to each other. Throughout the literature, this backbone structure has also been described as both 5,7,12,14-tetraoxapentacene and Benzo[1,2-b:4,5-b']bis[1,4]benzodioxin.

The first appearance of BDO in the literature was in a patent in the early 1970s by Darsow and Schnell [1]. They synthesized the 6,13–dichloro variety of BDO and noted that it can be used as a flame resisting agent. Later, in 1978, Oliver and Lusby synthesized the unsubstituted form using a condensation reaction between
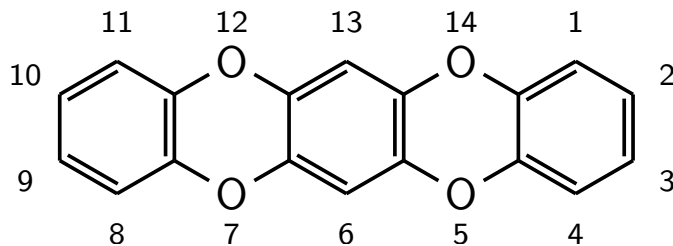
Figure 1.1: Structure of [1,4]benzodioxino[3,2-b]oxanthrene (BDO). This structure has been referred to as 5,7,12,14-Tetraoxapentacene and Benzo[1,2-b:4,5-b']bis[1,4]benzodioxin. The outermost two benzene rings were referred to as "terminal" rings, while the innermost ring as "central" ring. Numbers identify the potential substitute sites according to the IUPAC nomenclature.

catechol and 1,5–dichloro–2,4–dinitrobenzene [2]. They also synthesized the 2,3,9,10–tetrachloro variety using the same method. Oliver and Lusby reported melting points of $>350\,°C$ for both BDOs. They noted that the tetrachloro variety was homologous to 2,3,7,8–tetrachlorodibenzo–p–dioxin (TCDD), one of the most toxic compounds known [2]. They also noted that the overall structure and halogenation positions of these chlorinated heterocycles played a major rule in their toxicity [2]. However, to our knowledge there were no further toxicity studies reported on any variants of BDO.

Dembek and Fagan reported the synthesis of a Ru–complex of the unsubstituted BDO [3]. They noted that the π–complexation site was located on the central ring. This site was consistent with initial complexation with the 1,2,4,5–tetrachlorobenzene precursor. Their efforts to decomplex the BDO moiety were unsuccessful.

Photophysical properties of the unsubstituted BDO were sparse in the literature. Hellberg and Roeraade and their co–workers studied a group of non–polar oligomers of benzodioxin, one of which resembled BDO [4–6]. They reported the ultraviolet–visible absorption (UV–VIS) spectra of dioxane capped versions of both oxanthrene and BDO [6]. The central transition energies of both molecules from this report were estimated at $\sim3.95\,eV$ and $3.92\,eV$ in tetrahydrofuran, respectively. Comparatively, the uncapped oxanthrene had an estimated transition energy of $\sim4.3\,eV$ in both methanol and water/acetonitrile mixture [7, 8]. This indicated that the BDO may

exhibit an electronic transition energy from $4.5\,\mathrm{eV}$ to $3.9\,\mathrm{eV}$ depending on the solvent used.

Various central and terminal substituted versions of BDO appeared in the literature. The most commonly reported version was [1,4]benzodioxino[3,2–b]oxanthrene–6,13–dicarbonitrile (BDODC) [9–18]. Synthesis and various spectroscopic studies of BDODC were published in these reports. The UV–VIS spectrum of BDODC was reported on four separate occasions [10, 11, 13, 16]. In these reports, the central transition energy was estimated from $2.94\,\mathrm{eV}$ to $2.76\,\mathrm{eV}$.

The photoluminescence (PL) spectrum of BDODC was first reported by Fritsch and co–workers [10] and later by Maly and co–workers [16]. Both reports showed central transition energy estimates from $2.76\,\mathrm{eV}$ to $2.41\,\mathrm{eV}$. Fritsch also demonstrated that the central transition location in both UV–VIS and PL was highly dependent on the polarity of the solvent used [10]. In thin film, Maly and co–workers reported narrower bands in both UV–VIS and PL of BDODC. Their central transition energies were estimated at $2.82\,\mathrm{eV}$ and $2.56\,\mathrm{eV}$, respectively [16]. Lifetime of the first singlet excited state (S_1) of BDODC was estimated at $\sim 11.8\,\mathrm{ns}$ by Fritsch and co–workers using the Time–Correlated Single–Photon Counting (TCSPC) technique [10]. Finally, Maly and co–workers reported the emission quantum yield (Φ) of BDODC at 78% in $CHCl_3$ solution and 26% in thin film [16].

Geometrical and conformational studies of the structure of BDODC and various other substituted BDOs were also reported. The theoretical and quantum chemical calculation studies were rather lacking. Only Maly and co–workers included a brief depiction of the frontier molecular orbitals (MOs) of BDODC in their 2019 report [16]. They estimated the gap between the highest occupied molecular orbital (HOMO) and the lowest unoccupied molecular orbital (LUMO) for BDODC to be $\sim 3.39\,\mathrm{eV}$. On the other hand, crystallography studies for these variants were more abundant. The crystal structure of BDODC was first reported by Yaghi and co–workers in 2018

[13] and again by Maly and co–workers in 2019 [16]. Both reports indicated that the backbone of BDODC was nearly planar within the crystal lattice. In these lattices the dioxin rings within the backbone showed minor deformations and folding with angles <4°. These deformations were likely due to the internal electronic and steric constrains within the crystal lattice [13, 16].

Crystal structures of other substituted BDOs were also reported. The vast majority of these reports showed a near–perfect planar backbone within the BDO moiety [13, 16, 19–22]. Dawe and co–workers explored the intermolecular interactions between 6,13–diaminotriazine–substituted BDOs [20]. In these studies Dawe showed the possibility of assembling two-dimensional hydrogen–bonded sheets using this variant. These sheets packed less closely together allowing for more accessible volume to guest ions and molecules.

Maly and co–workers investigated a host of heterocycles analog to pentacene [16]. They noted that the "oxa" variety, i.e. BDOs, had a higher ability to stack due to its planarity compared to its nitrogen–based and the sulfur–based analogs. Zheng and co–workers reported on a terminally substituted BDO chromophore; 1,4,8,11–tetracyano–2,3,9,10–tetrafluoro[1,4]benzodioxino[3,2–b]oxanthrene.[21] The crystal structure reported by Zheng was also planar. In this report, Zheng showed a remarkable aggregate–induced emission with quantum yields approaching 30%. Regarding the crystal structures of these variants, as with the previous reports, mild distortions may be found in the dioxin rings within the backbone. However, none of these distortions exceeded a dioxin folding angles of 5°.

One folded geometry of an isolated and substituted BDO was reported by Yampolskii and co–workers [15]. The substituent, a phenyl–substituted quinazoline moiety, appeared to induce such folding. Three other folded geometries of a substituted BDO moiety within a macromolecule were reported by McKenown and co–workers [19, 23, 24]. These reports demonstrated the folding patterns exhibited by highly

constrained BDO dimers. These dimers were joint through the terminal rings [23] and central rings [19, 24]. Another dimer, linked through the central rings was reported by Pericás and co–workers [18]. Despite the bulkiness of the linking bridge, Pericás found the backbone of the BDO to be planar. The majority of these studies focused on the geometrical aspects of the backbone, with very few reporting on their optical properties.

Budd and McKeown and their co–workers pioneered the interest in BDO–based chromophores and polymers. They introduced in 2004 a polymer based on BDODC moiety linked through a 3,3,3′,3′-tetramethyl-1,1′-spirobiindan (SPIRO) center and dubbed it as polymer of intrinsic microporosity "1" (PIM–1) [25, 26]. In these early reports, they demonstrated the potential of this polymer to perform effectively and selectively in gas separation applications. Throughout the next two decades, they put forth nearly a hundred publication expanding on this concept [9, 17, 19, 23, 24, 27–52].

Other research groups around the world contributed to the effort to study the properties of PIM–1 [10, 11, 15, 47, 49, 53–72]. Some of these efforts introduced the concept of mixed–chromophore PIM–1–type co–polymers [11, 15, 54, 60, 62]. These co–polymers were found to exhibit improved permeability properties compared to PIM–1. Guiver and co–workers reported on temperature–dependent conformational changes exhibited by PIM–1–type co–polymer [54]. So far, over five hundred and thirty publication and patents appeared in the literature discussing the properties of BDO–based chromophores and polymers *.

The aforementioned studies also focused on various other properties and application of these BDO–based molecules and macromolecules. Dawe and Maly and their co–workers demonstrated the value of substituted BDO chromophores in liquid crystals applications [20, 22, 73, 74]. Covalent organic frameworks based on substituted

---

*These numbers were extracted from the SciFinder database as of April 29, 2021

BDOs were synthesized by Yaghi and co–workers [13] and Qui and co–workers [14]. Several research groups explored avenues to improve the permeability of PIM–1 in a mixed–matrix membranes with metal–organic frameworks [75–80]. Ye and co–workers employed a thiol–functionalized PIM–1 in mercury(II) sensing [81]. Lu and co–workers showed the potential of BDO–based heterocycle in high density memory devices [82]. Ferraris and co–workers utilized PIM–1 polymer to synthesize high density carbon nanofibers for energy storage applications [83]. Musyoka and co–workers devised a method to enhance the hydrogen storage capabilities of PIM–1 through process-ing with Zeolite templated carbon and metal organic framework [84]. Dalton and co–workers demonstrated strong electronic interaction between PIM–1 polymers and graphene oxide nanosheets in a nanohybrid framework [49]. Finally, Pericás and co–workers [18] and Handa and co–workers [85] utilized BDO–based polymers in catalytic applications.

1.2   FRENKEL–DAVYDOV EXCITON MODEL

Frenkel–Davydov exciton theory was utilized to rationalize the presence of inter–chromophore electronic transitions in the investigated BDO–based macromolecules. In a dimer of identical or similar chromophores (A–B), the electronic states resulting from the inter–chromophore interactions may be described by the Frenkel–Davydov exciton model [86–90]. This model approximated the wavefunction of the ground state of the dimer (Ψ_{GG}) as the dot product of the ground state wavefunctions of the two constituting chromophores ($|A\rangle$ and $|B\rangle$). Equation 1.1, where "GG" denoted that both chromophores were in their ground state. Additionally, it predicted four excited states resulting from the inter–chromophore interactions of these two chromophores. The first two, designated as visible states (VSs), were associated with localized transition from the HOMO to the LUMO of each chromophore. The wavefunctions of the diabats of these two excited states would be the products of the wavefunctions of one excited and

one ground chromophores. Equation 1.2 denoted the first and Equation 1.3 denoted the second VSs. $|A^*\rangle$ and $|B^*\rangle$ denoted the excited wavefunction of the first and second chromophores, respectively. "eg" and "ge" represented the state of each constituting chromophore, i.e. "excited–ground" and "ground–excited", respectively. The energy separation between these two excited states can be determined by the coupling strength of their diabats and their initial, unperturbed energies. Therefore, utilizing the second–order perturbation theory at the limit of degeneracy, the wavefunctions of these two states can be approximated as the linear combination of their diabats. Equation 1.4 depicted this relationship, where $\pm$ denoted the symmetry of the overall wavefunction.

$$\Psi_{\text{GG}} = |A\rangle \cdot |B\rangle \tag{1.1}$$

$$\Psi_{\text{eg}} = |A^*\rangle \cdot |B\rangle \tag{1.2}$$

$$\Psi_{\text{ge}} = |A\rangle \cdot |B^*\rangle \tag{1.3}$$

$$\Psi_{\text{VS}}^{\pm} = \frac{\Psi_{\text{eg}} \pm \Psi_{\text{ge}}}{\sqrt{2}} \tag{1.4}$$

The second two states, designated as charge–transfer states (CTSs), can also be described using this model. The mathematical expression of the wavefunctions of the diabats of these states can be written as Equation 1.5 and Equation 1.6. Where the "+" and the "−" signs denoted the donor and acceptor chromophores, respectively, and "c" and "a" denoted the cationic and anionic states, respectively. These diabats can be mixed, in the same fashion as the VSs, to produce their adiabatic states. The mixing mechanisms may include spin–orbit coupling and vibronic interactions. Equation 1.6 showed the linear combination expression that produced these two CTSs. Again, $\pm$ denoted the symmetry of the overall wavefunction.

$$\Psi_{\text{ca}} = |A^+\rangle \cdot |B^-\rangle \tag{1.5}$$

$$\Psi_{\text{ac}} = |A^-\rangle \cdot |B^+\rangle \tag{1.6}$$

$$\Psi^{\pm}_{\text{CTS}} = \frac{\Psi_{\text{ac}} \pm \Psi_{\text{ca}}}{\sqrt{2}} \tag{1.7}$$

According to the theory, transitions from "GG" to either of the VSs was predicted to be bright. These transitions were characterized as a localized promotion between HOMO and LUMO of the same chromophore moiety. On the other hand, transition from "GG" to CTSs were expected to be dark or near–dark. These transitions involved promotions from the HOMO of one chromophore to the LUMO of the other. Therefore, the strength of these transitions heavily depended on the overlap between the MOs of the constituting chromophores.

1.3 AIM OF THE STUDY

This study aims to provide a deeper understanding of few photophysical properties of BDO–based chromophores and macromolecules. The first are the geometrical and conformational characteristics of selected BDOs from a theoretical standpoint. These characteristics play a significant role in the gas permeability applications of BDO–based macromolecules. As shown in Section 1.1, several studies explored these properties using theoretical and experimental tools. However, the theoretical studies largely addressed the homo–polymer PIM–1 and were exclusive to the ground–state geometries of this polymer. This work draws from the results of these studies and expands on the geometrical properties of the ground and excited states of a PIM–1–like mixed co–polymer. The results of this work offer insights into the dynamical nature of the conformational characteristics of this co–polymer. These insights introduce a new set of tools that may be used to manipulate the pore size of similar co–polymers in a noninvasive manner.

The second group of characteristics is related to the electronic structure of BDO–

based chromophores and macromolecules. Improvements in applications utilizing these materials such as organic photocatalysis, photovoltaics, and memory devices depend on a thorough understanding of their electronic structure. As demonstrated in Section 1.1, the literature offered a limited understanding of the electronic structure of BDO–based chromophores and macromolecules. Our recent paper [85] tackled this problem within the framework of organic photocatalysis applications. This work draws from the results published in the aforementioned paper with significant expansions to address the isolated chromophores and the origin of their electronic transitions. Additionally, this work revises the theoretical and experimental results and analysis to improve upon their accuracy. Also, this work addresses a conflict with the underlying assumptions used in the published work arose from data collected for the isolated chromophore, BDODC. These assumptions affect the spectral band designations and their associated lifetimes. However, the overall conclusions of this work are in agreement with the published work.

CHAPTER 2

METHODS AND INSTRUMENTATION

This chapter highlighted the experimental and theoretical methods utilized in this work. To start, Section 2.1 provided a brief procedural explanation of the chromophore's and macromolecules' synthesis and solution preparations. Section 2.2 described the inner workings of the ultraviolet–visible absorption (UV–VIS) spectrophotometer. It also detailed the measurement conditions and data acquisition procedures in addition to post–processing techniques and data corrections. Additionally, it elaborated on the theory and techniques utilized in the spectral decomposition analysis.

Section 2.3 gave a schematic outline of the spectrofluorometer used in the photoluminescence (PL) measurements. It described the experimental conditions and data acquisition procedures employed. Also, it discussed procedures employed for the reconstruction of the excitation–emission matrix (EEM) spectra and post–processing, artifact corrections, and spectral decomposition analysis. This section also detailed the acquisition method and data processing in the delayed photoluminescence (dPL) experiments. Section 2.4 described the home–built time–resolved photoluminescence (TRPL) apparatus, the signal detection scheme, and data acquisition procedure. Furthermore, it detailed the ideas employed for jitter correction, and lifetime extraction via single–exponential decay fits.

Section 2.5 discussed the schematics and inner workings of the various components in the femtosecond laser system. Section 2.6 elaborated on the procedural details of

10

performing the femtosecond transient absorption pump–probe (fsTAPP) experiments. It detailed these procedures in the spirit of providing information for reliable and consistent data acquisition. Among those details were the laser beams spectral and temporal characteristics. Additionally, elaboration of the post–processing techniques, artifact handling, data analysis and fitting were presented in this section.

2.1   SAMPLES SYNTHESIS AND HANDLING

The backbone of [1,4]benzodioxino[3,2-b]oxanthrene (BDO) in the three macro-molecules as well as the isolated chromophore [1,4]benzodioxino[3,2–b]oxanthrene–6,13–dicarbonitrile (BDODC) was synthesized in a one–pot reaction. This cyclization reaction utilized a nucleophilic aromatic substitution. Scheme 2.1 depicted the synthesis of BDODC. Scheme 2.2 depicted the generalized reaction scheme employed to synthesize the three macromolecules heterotrimer sub–model (HTRMR), short–chain oligomer (OLGMR), and long–chain polymer (PLYMR). The synthesis of the HTRMR was rather elaborate in order to gain better control of the chromophoric order and composition of this macromolecule. All samples were synthesized and purified by Dr. Justin Smith from Dr. Sachin Handa's lab at the University of Louisville. Synthesis and purification procedures, reaction conditions, and characterization were detailed in reference [85]. Sample solutions were prepared by dissolving the provided bright yellow powder in a suitable volume of analytical grade Chloroform (Sigma-Aldrich), and ultrasonicated for a minimum of five minutes to ensure homogeneity.

Well–controlled sample concentrations were required for reliable spectroscopic measurements and rigorous sample comparisons. Therefore, an elaborate solution preparation procedure was devised and carried out. Using an analytical balance (Adventurer, Ohaus), four empty vials were weighed five times to the nearest 0.1 mg. Samples were transferred to the pre–weighed empty vials and reweighed five times to the nearest 0.1 mg. Sample masses were calculated by subtracting the average mass
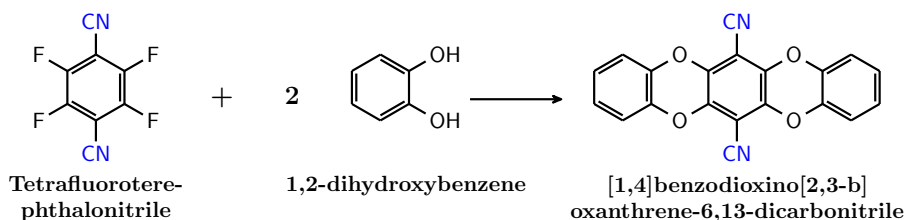
Scheme 2.1: Synthetic scheme of [1,4]benzodioxino[3,2–b]oxanthrene–6,13–dicarboni-trile (BDODC).

of the empty vials from the average mass of the vials containing the samples. Errors associated with the samples masses were estimated using the standard deviation from each step projected into the appropriate error propagation formula.

The molar masses of BDODC and the HTRMR were calculated using their atomic composition. Molar masses and chromophoric composition of the OLGMR and the PLYMR were estimated using gel permeation chromatography (GPC) [85]. An estimate of the chromophore unit concentration in each solution was calculated using the aforementioned molar masses and chromophoric compositions. The error associated with each concentration was estimated using error proper error propagation formula. Finally, a dilution step was carried out to prepare a sample solution at a chromophore concentration of about $50\,\mathrm{\mu mol\,L^{-1}}$. This $50\,\mathrm{\mu mol\,L^{-1}}$ concentration was used for the majority of the spectroscopic measurements. All values and their associated error were listed in Table 2.1.

For Beer's optical linearity test of BDODC shown in Figure 4.1b, a similar procedure was carried out to prepare a $1\,\mathrm{mmol\,L^{-1}}$ stock solution. From the stock, a dilution series was prepared using standard addition method. The final concentrations of this series were $0.005\,\mathrm{mmol\,L^{-1}}$, $0.038\,\mathrm{mmol\,L^{-1}}$, $0.074\,\mathrm{mmol\,L^{-1}}$, $0.107\,\mathrm{mmol\,L^{-1}}$, $0.138\,\mathrm{mmol\,L^{-1}}$, $0.167\,\mathrm{mmol\,L^{-1}}$, $0.286\,\mathrm{mmol\,L^{-1}}$, $0.375\,\mathrm{mmol\,L^{-1}}$ and $1.000\,\mathrm{mmol\,L^{-1}}$. fsTAPP measurements were carried out on a $0.5\,\mathrm{mmol\,L^{-1}}$ solutions. These solutions were either the original stock prepared previously, or an additional dilution step from
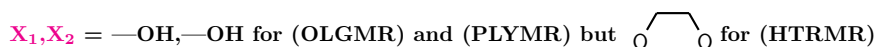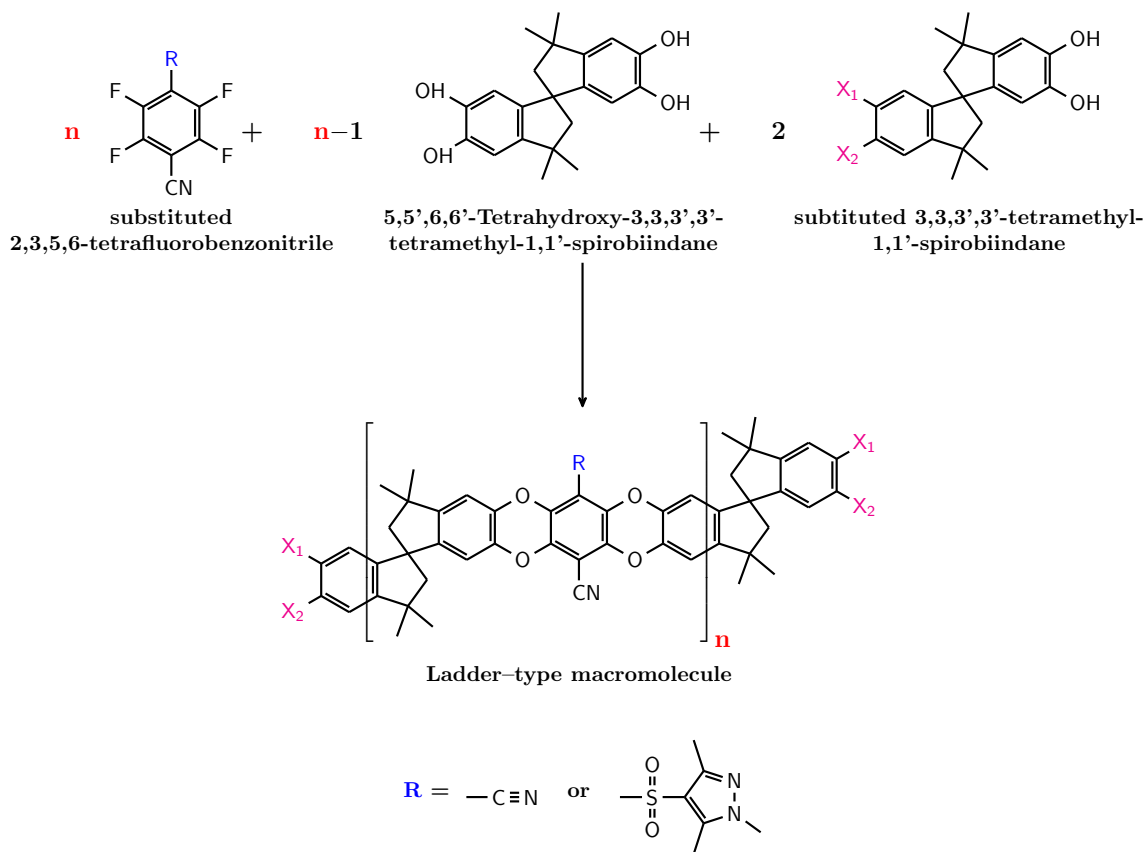
Scheme 2.2: Generalized synthetic scheme of the investigated macromolecules: the heterotrimer sub–model (HTRMR), the short–chain oligomer (OLGMR), and the long–chain polymer (PLYMR).

the stock. However, HTRMR's $0.5\,\mathrm{mmol\,L^{-1}}$ was prepared through solvent evaporation of the $0.1\,\mathrm{mmol\,L^{-1}}$ stock. The concentrations for these solutions were estimated by measuring their UV–VIS and applying the estimated molar extinction coefficient, Figure 4.1b and c. Finally, samples solutions used to measure the dPL signal were degassed by purging with N_2 gas for over $20\,\mathrm{min}$. The N_2 gas was directed through a needle reaching into the solution, with a secondary needle reaching into the sealed container without being submerged to provide a pressure release. The purged solution

Table 2.1: Summary of the concentrations of the prepared solutions and their associated calculations. "Nº of chr" is the estimated number of chromophore units in each macromolecule. "[Chr unit]$_{stock}$" is the chromophore unit concentration of the stock solution. "[Chr unit]$_{diluted}$" is the chromophore unit concentration of the final diluted solution.

Quantity	Unit	BDODC	HTRMR	OLGMR	PLYMR
mass	mg	1.4±0.2	0.3±0.2	5.9±0.2	1.8±0.2
molar mass	g mol^{-1}	340.29	1921.12	2978±468	59650±27585
Nº of chr	unit	1	3	6±2	121±54
[Chr unit]$_{stock}$	mmol L^{-1}	0.5±0.06	0.1±0.07	1.7±0.1	0.5±0.3
[Chr unit]$_{diluted}$	µmol L^{-1}	50.3±6.3	50.0±33.8	66.7±24.8	51.8±33.9

concentration was reconstituted by replenishing the evaporated solvent with similarly purged CHCl$_3$. Purged solution concentrations were confirmed through measuring their UV–VIS spectra, and deducing a correction factor if needed.

2.2 ULTRAVIOLET–VISIBLE ABSORPTION SPECTROSCOPY

2.2.1 INSTRUMENTATION

Cary–50 spectrophotometer (Varian, Agilent Technologies) was utilized to acquire all UV–VIS spectra presented in this work. A simplified optical scheme was shown in Figure 2.1a depicting the internal components of this spectrophotometer. Figure 2.1b displayed a reproduced rendition of the spectrometer from its manual [91]. Briefly, radiation from a pulsed Xenon lamp was collected and directed into Czerny-Turner monochromator through an entrance slit. In the monochromator, the movable holographic grating directed the desired wavelength through an exit slit. The exiting beam was met with a beam splitter to direct a fraction of it to a reference Si–diode detector. The passing beam was steered into the sample compartment, passing through the sample and onto the main Si–diode detector. This spectrophotometer was capable of scanning from 190 nm to 1100 nm (6.53 eV to 1.13 eV). The scan resolution was fixed at ≤1.5 nm (0.05 eV) and accuracy of <0.25 nm (0.004 eV) was expected

[91].
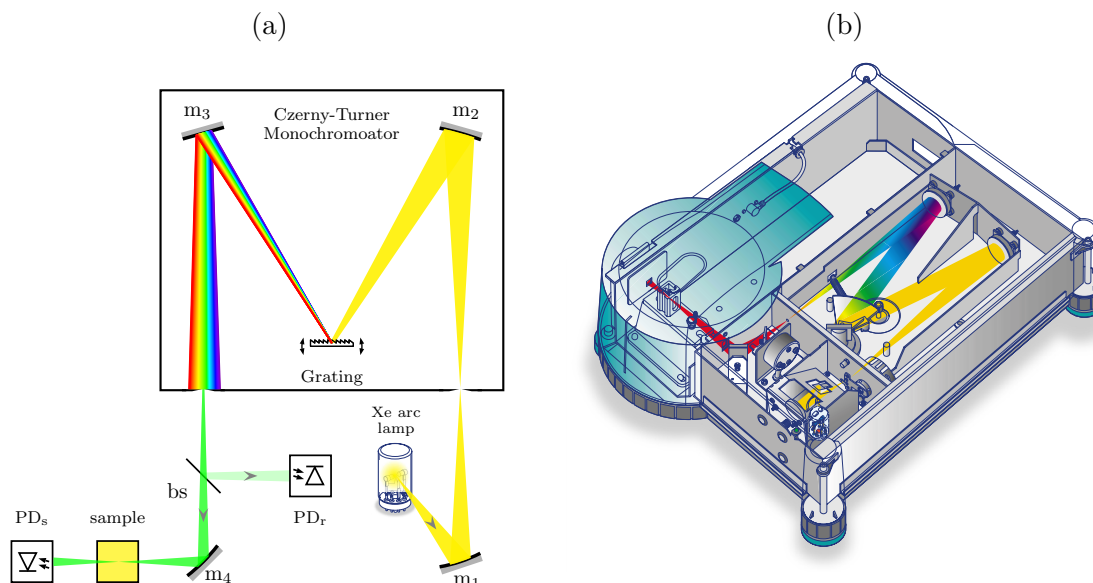
Figure 2.1: General outline of Cary–50 spectrophotometer. (a) Schematics of the optical components and beam path in the spectrometer. m: mirror, bs: beam–splitter, PD_r: reference detector, PD_s: sample detector. (b) Three dimensional rendition of the spectrometer, reproduced from [91].

2.2.2   DATA ACQUISITION

Data acquisition was carried out at room temperature, under ambient conditions using Cary's companion software, WinUV version 3.00(182). A 10 mm path–length, rectangular, quartz, fluorometer cuvette with a stopper (Starna, Spectrosil 23–Q–10) was used to acquire the UV–VIS spectra. Absorbance data was collected from 250 nm to 600 nm (4.96 eV to 2.07 eV) with 0.5 nm (<0.01 eV) increments. The higher energy side of the scan range was limited by the $CHCl_3$ solvent cut off wavelength at 245 ± 5 nm (5.06 ± 0.21 eV) [92, p. 482]. All data points acquired in the spectra were averaged for 50 ms. Initially, a cuvette filled with pure $CHCl_3$ was used to calibrate the beam transmission intensity between 0% and 100%. Then each sample solution at $50 \, \mu mol \, L^{-1}$, see Section 2.1 for details, was scanned five times, to ensure reproducibility and statistical validity. To maintain consistency, the same cuvette in

the same orientation was used for the baseline and all samples acquisitions. Finally, data was exported in comma separated values (CSV) format for further analysis and visualization.

A similar procedure was carried out to acquire Beer's optical linearity test of BDODC shown in Figure 4.1b. The scan range was from $225\,nm$ to $600\,nm$ ($2.07\,eV$ to $5.51\,eV$). Scan step was $0.2\,nm$ ($<0.005\,eV$) and the acquisition average time was $25\,ms$. Sample concentration at $1\,mmol\,L^{-1}$ had a high absorptivity. Therefore, a separate baseline and data acquisition sequence was carried out at that concentration using $1\,mm$ path–length cuvette (Starna, Spectrosil 21–Q–1).

2.2.3 DATA PROCESSING, FITTING, AND VISUALIZATION

UV–VIS raw data processing was carried out using in–house python 3.x script, Script B.2. The script utilized functions from numpy [93], scipy [94], and h5py [95] libraries. Briefly, the five spectra of each sample were imported and averaged. The spectral axis was converted to an energy axis (from nm to eV). The intensity background was subtracted from the averaged spectra. This background was estimated using the average intensity of the last 20 points on the low energy side of the energy axis. The spectral intensity was linearly interpolated on a uniform energy axis between $2.3\,eV$ to $4.8\,eV$ with a step size of $0.001\,eV$. Finally, the processed spectra were exported to a centralized HDF5 file for storage.

Spectral decomposition analysis was performed on the lowest energy band observed around $2.9\,eV$. These analyses utilized an in–house python 3.x script, Script B.3. The fitting procedure employed the nonlinear least-square minimization method as implemented in lmfit package [96]. The mathematical model was a linear combination of a simplified version of the logarithmic–normal distribution (Logn)

function, Equation 2.1.

$$I(E; I_0, E_0, H, \rho) = \begin{cases} I_0 \ exp \left\{ -\dfrac{\ln 2}{(\ln \rho)^2} \left[\ln \dfrac{E-a}{E_0-a} \right]^2 \right\} & \text{for} \quad E > a \\ \\ 0 & \text{for} \quad E \leq a \end{cases} \tag{2.1}$$

where:

$$a = E_0 - H \left[\frac{\rho}{\rho^2 - 1} \right] \qquad H = E_h - E_l \qquad \rho = \frac{E_h - E_0}{E_0 - E_l}$$

Where I_0 was the band maximum intensity, E_0 was the central transition energy, H was the band's total width at half maximum, and ρ was the band's asymmetry parameter. In here, ρ took values larger than 1, and the function would be reduced to a more symmetric Gaussian form as ρ approached 1.

The original form of this Logn function was first used for this purpose by Metzler and Siano in 1969 [97]. They argued that this mathematical model was of a physical value when considering the Franck–Condon principle. The asymmetry of the Logn provides a physically meaningful simulation for the vibronic progression often observed in electronic transition bands. The simplified version was modeled after the fluorescence Logn function introduced by Burstein and co–workers in 1996 [98]. The original form of Metzler's function and the derivation to the simplified version can be found on page 212 in Section D.1. Finally, visualization of the data and these analyses were constructed using python 3.x. They employed functions from the Matplotlib [99] library.

2.3 PHOTOLUMINESCENCE SPECTROSCOPY

2.3.1 INSTRUMENTATION

All steady–state PL and dPL measurements were carried out using LS55 spectrofluorometer (PerkinElmer). A simplified scheme of the optical layout of the instrument was depicted in Figure 2.2. Briefly, the output radiation of a Xenon flashlamp was collected and steered through a slit onto the grating of the excitation monochromator. The dispersed beam was steered onto a secondary slit, through which the desired wavelength was passed, depending on the grating angle. The exiting excitation beam was passed through a selection of bandpass filters on the filter wheel if desired. Then the beam was steered through a beamsplitter to steer as small portion of its intensity onto a reference photodiode detector. The majority of the excitation beam passed through the beamsplitter then steered into the sample holder.

The emission radiation originating from the sample was collected by a large toroidal mirror, m_5 in Figure 2.2. The collected emission was then focused through the entrance slit to the emission monochromator. If desired, the emission beam may be filtered through a selection of longpass filters placed on the filter wheel. A secondary wheel that carried a selection of polarizers was also present if needed. The dispersion grating in the emission monochromator separated the different wavelengths contained in the emission beam. Through angle changes, the grating steered the dispersed narrowband from the emission beam through an exit slit into the main photomultiplier tube detector. This spectrometer was capable of scanning a range from $200\,\text{nm}$ to $800\,\text{nm}$ ($1.55\,\text{eV}$ to $6.2\,\text{eV}$) on the excitation arm. On the emission arm it can scan a range of $200\,\text{nm}$ to $900\,\text{nm}$ ($1.38\,\text{eV}$ to $6.2\,\text{eV}$). The spectral resolution can be varied from $2.5\,\text{nm}$ to $15\,\text{nm}$ ($0.08\,\text{eV}$ to $0.44\,\text{eV}$).

PL spectra were collected by running the instrument in its "fluorescence mode". In this mode, two signal integration events were carried out on each of the two
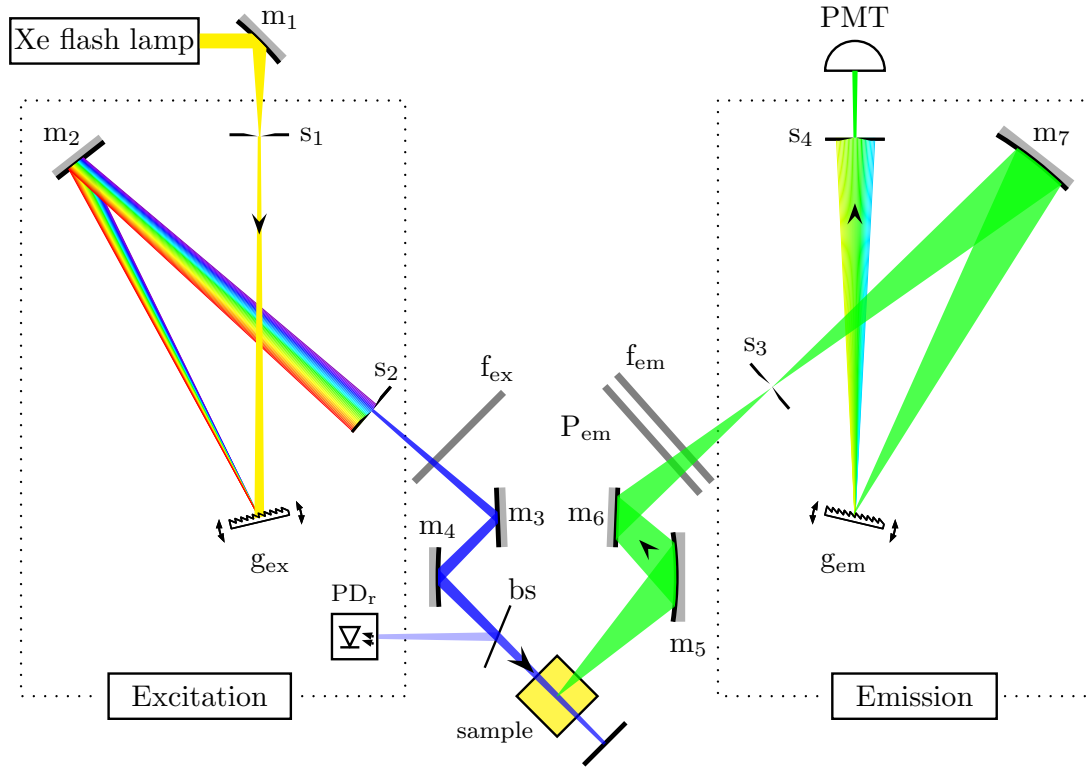
Figure 2.2: Schematics of PerkinElmer LS55 spectrofluorometer. m: mirror, bs: beamsplitter, f: filter wheel, P: polarizer, s: slit, g: grating, PD_r: reference photodiode, PMT: photomultiplier tube. "ex" and "em" subscripts refer to excitation and emission optics, respectively.

detectors during every data collection cycle. The first was the main excitation and emission signals at a fixed delay time from the last light source flash event. The second was carried out right before the next light source flash to collect the dark current background. All four integration events lasted for $80\,\mu s$, referred to as "gate". This data collection cycle produced a corrected signal with respect to the dark current and the excitation intensity fluctuation.

dPL spectra were collected by running the instrument in its "phosphorescence mode". In this mode, the delay time between the light source flash event and its integration as well as the temporal length of the integration window were controllable. The instrument was capable of varying the delay from $0\,ms$ to $9000\,ms$. The integration window, i.e. gate, can be varied from $0.01\,ms$ to $500\,ms$ with $0.01\,ms$ increments. The

source flash was approximated to have a width at half maximum of $<10\,\mu s$.

2.3.2 DATA ACQUISITION

All PL and dPL spectra were acquired using the LS55 fluorometer companion software, FL WinLab version 4.00.03. PL measurements employed two types of data acquisition routines for the four sample solutions investigated. The first, EEM, acquired the emission intensities while both excitation and emission wavelengths were being varied. This dataset served the qualitative purpose of revealing any possible correlations between the excitation transitions and the subsequent emission transitions. The second was a spectral line scan, where emission intensity was collected while the excitation or the emission wavelength was being scanned while the other was parked. This routine allowed for a denser, higher resolution dataset with better signal–to–noise ratio which was used in the subsequent decomposition analysis. Data acquisition for the dPL measurements only employed the spectral line scan routine.

PL and dPL data presented in this work were acquired from the $\sim 50\,\mu mol\,L^{-1}$ sample solutions in $CHCl_3$ described in Section 2.1. Measurements were carried out in a 10 mm path–length, rectangular, quartz, fluorometer cuvette with a stopper (Starna, Spectrosil 23–Q–10). The fluorometer monochromators' default step size of 0.5 nm was adopted for all measurements. The excitation slit was fixed at 6.0 nm, and the emission slit was set to 3.5 nm. The applied voltage on photomultiplier tube was maintained at 760 V.

The line scans were carried out to probe the main observable features in the samples' excitation and emission spectra. All line spectra were collected five times to ensure reproducibility and statistical validity. Excitation spectra were collected from 250 nm to 550 nm (2.255 eV to 4.96 eV) at a fixed emission wavelength of 480 nm (2.58 eV). Emission spectra were collected from 400 nm to 800 nm (1.55 eV to 3.1 eV) at excitation wavelengths of 295 nm and 435 nm (4.2 eV and 2.85 eV). The monochro-

mator scan rate was set to $600\,\mathrm{nm}\,\mathrm{min}^{-1}$ for all of these line scans.

The EEM data were acquired using the synchronous scan type of the instrument's 3–D scanning mode. In this configuration the excitation monochromator was scanned from $340\,\mathrm{nm}$ to $550\,\mathrm{nm}$ ($2.455\,\mathrm{eV}$ to $3.647\,\mathrm{eV}$). Simultaneously, the emission monochromator was scanned within the same range plus a variable wavelength value, called "$\Delta\lambda$". $\Delta\lambda$ value was varied from $0\,\mathrm{nm}$ to $300\,\mathrm{nm}$ with $5\,\mathrm{nm}$ increments, to produce a total of 60 individual synchronous line scans. From these parameters, the first emission scan was $340\,\mathrm{nm}$ to $550\,\mathrm{nm}$ ($2.455\,\mathrm{eV}$ to $3.647\,\mathrm{eV}$) and the last was $640\,\mathrm{nm}$ to $850\,\mathrm{nm}$ ($1.938\,\mathrm{eV}$ to $3.647\,\mathrm{eV}$). The monochromator scan rate was set to $1500\,\mathrm{nm}\,\mathrm{min}^{-1}$ for these EEM scans. Each of these scans was done only once due to the fact that these datasets will be used for qualitative analysis only. Finally, all line and EEM data files were converted and exported to a "tab delimited" text format for processing and further analysis and visualization.

2.3.3   DATA PROCESSING, FITTING, AND VISUALIZATION

Python 3.x scripts were employed to process, correct, and refine the PL, dPL, and EEM data. Script listings Script B.4, Script B.5, and Script B.6, respectively. Much like the scripts used to process the UV–VIS data, these scripts employed functions from numpy [93], scipy [94], and h5py [95] libraries.

Briefly, Script B.4 imported the five data files of each line scan then calculated their average and standard deviation. It then performed wavelength corrections using a previously determined correction factors. These correction factors were $-10\,\mathrm{nm}$ for the excitation and $+5\,\mathrm{nm}$ for the emission. Then the wavelength axis was converted from nm to eV. The next step was linearly interpolation of the intensity data to a uniform energy axis. The uniform energy axis was set from $1.55\,\mathrm{eV}$ to $4.96\,\mathrm{eV}$ with step size of $0.005\,\mathrm{eV}$. For dPL data, Script B.5 followed the same general steps. However, and additional intensity correction to the intensity data was necessary. This

correction employed the difference in absorption intensity between the degassed the ambient solutions. Additionally, the linear interpolation of the dPL intensity data was performed on a different energy axis. This axis extended from $1.4\,\text{eV}$ to $2.9\,\text{eV}$ with a step size of $0.005\,\text{eV}$.

For EEM data, Script B.6 imported the 60 data files that constitute the 3–D spectrum. It calculated the emission wavelength range using the excitation range and the $\Delta\lambda$ value of each file it imported. It then performed the wavelength correction using the previously mentioned correction factors. Once each file was properly processed, the intensity was concatenated to an XYZ coordinate array in which each entry represents one spectral data point in the EEM 3–D dataset. Finally, a 3–D linear interpolation was performed on the XYZ array over uniformly spaced excitation and emission axes. Excitation range was set from $2.55\,\text{eV}$ to $3.65\,\text{eV}$. Emission ranged from $1.55\,\text{eV}$ to $2.95\,\text{eV}$. Both ranges had a step size of $0.005\,\text{eV}$. Finally, all processed data of PL, dPL, and EEM experiments were stored in a centralized HDF5 file.

Spectral decomposition analysis was performed on both excitation and emission spectra, using an in–house python 3.x script, Script B.7. The fitting employed the nonlinear least-square minimization method as implemented in lmfit [96] package. The decomposed excitation line was the one acquired at E_{em} of $2.58\,\text{eV}$. The decomposed emission line was the one acquired at E_{ex} of $2.85\,\text{eV}$. Excitation decomposition utilized the simplified form of Metzler's Logn function, Equation 2.1, Emission decomposition employed the mirror–symmetric form of Metzler's Logn function proposed by Burstein and co–workers [98], Equation 2.2.

$$
I(E; I_0, E_0, H, \rho) =
\begin{cases}
I_0 \, exp\left\{ -\dfrac{\ln 2}{(\ln \rho)^2} \left[\ln \dfrac{a-E}{a-E_0} \right]^2 \right\} & \text{for} \quad E < a \\[2em]
0 & \text{for} \quad E \geq a
\end{cases}
\tag{2.2}
$$

where:

$$a = E_0 + H \left[\frac{\rho}{\rho^2 - 1} \right] \qquad H = E_h - E_l \qquad \rho = \frac{E_0 - E_l}{E_h - E_0}$$

I_0 was band maximum intensity, E_0 was the central transition energy, H was the band's total width at half maximum, and ρ was the band's asymmetry parameter. E_l and E_h were the energies at band's half maximum on the lower and higher energy sides, respectively. ρ had values larger than 1, and the function would approach the symmetric Gaussian form when ρ approaches 1. Finally, all data and analysis plots were all constructed in python 3.x using Matplotlib library [99].

2.4 TIME–RESOLVED PHOTOLUMINESCENCE SPECTROSCOPY

2.4.1 INSTRUMENTATION AND DATA ACQUISITION

TRPL measurements were carried out using a home–built apparatus. This apparatus utilized a femtosecond laser source for excitation, Figure 2.5, and a Si–photodiode coupled with an oscilloscope for detection. Figure 2.3 outlined the main components of this TRPL apparatus. Briefly, a fundamental beam from the femtosecond regenerative amplifier was passed through a frequency doubling β–Barium borate (BBO) crystal. The fundamental wavelength at $775\,\text{nm}$ ($1.6\,\text{eV}$) was separated from the second harmonic at $387.5\,\text{nm}$ ($3.2\,\text{eV}$) using a right–angle prism discarded. The second harmonic beam, used for excitation, was steered into the sample solution through an iris at a diameter of $\sim 4\,\text{mm}$. Emission from the sample solution was collected and refocused onto a Si–photodiode (DET10A, Thorlabs) through a set of convex lenses. These lenses were two bi–convex lenses, l_1 and l_3, Figure 2.3, with focal lengths of 1.5 and $4\,\text{cm}$, respectively. The third lens was a plano–convex, l_2, with a focal length of $12.5\,\text{cm}$. Emission was filtered from the excitation beam scattering residuals using a $500\,\text{nm}$ longpass filter (FEL0500, Thorlabs). The photodiode signal trace was monitored on

an oscilloscope (DPO4034, Tektronix; $350\,\text{MHz}$, $2.5\,\text{GS}\,\text{s}^{-1}$). The detected signal was self–triggered, i.e. the trigger channel was set to the photodiode output signal.
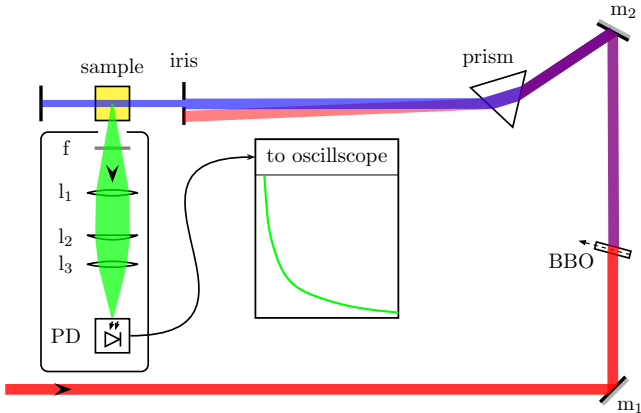
Figure 2.3: Schematics of the home–build TRPL apparatus. m: mirror, f: longpass filter, l: lens, PD: photodiode detector, BBO: β–Barium borate frequency doubling crystal.

TRPL data was acquired from the $50\,\mu\text{mol}\,\text{L}^{-1}$ sample solutions in CHCl$_3$ described in Section 2.1. Measurements were carried out in a $10\,\text{mm}$ path–length, rectangular, quartz, fluorometer cuvette with a stopper (Starna, Spectrosil 23–Q–10). The pump average power was found to be $\sim 38\,\text{mW}$, resulting in a pump fluence of $\sim 300\,\mu\text{J}$. The oscilloscope sampling frequency provided a time–axis data separation of $0.4\,\text{ns}$. TRPL traces were saved directly from the oscilloscope into a USB flash drive in a CSV file format for further processing and analysis. Ten individual traces were acquired for each sample to ensure reproducibility and statistical validity. Similarly, ten traces of the instrument response function (IRF) were acquired by placing a cuvette filled with pure CHCl$_3$ in the sample holder.

2.4.2 DATA PROCESSING, FITTING, AND VISUALIZATION

The data was processed using Python 3.x scripts, utilizing functions from numpy [93], scipy [94], and h5py [95] libraries, Script B.8. Briefly, the datasets were imported from their respective CSV files and stored in a numpy array. Empirical time–axis

and a baseline corrections were performed during the importing process. A jitter–like artifact was evident among the individual traces of the same sample. This artifact likely occurred due to the self–triggering scheme used in the acquisition sequence. The jitter artifact was corrected by locating the steepest point on the rising curve then shifting the time–axis for all traces to match. A comparative visualization of the TRPL traces before and after jitter correction can be found in Figure 2.4. Once corrected, the intensity data was linearly interpolated on a new time–axis with 0.1 ns step size for a more reliable curve fitting. Finally, the traces for each sample were averaged and stored in a central HDF5 file for future analysis and visualization.
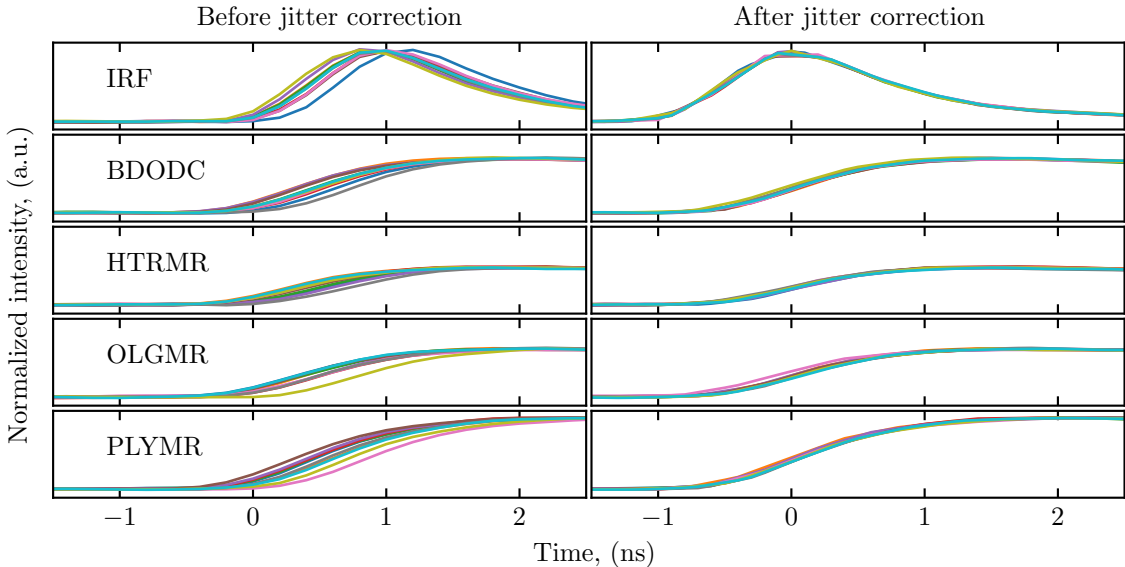
Figure 2.4: Visualization of the jitter correction effect.

To extract the excited–state lifetimes, TRPL traces were fitted with a exponentially modified gaussian (ExpGaus) function. This ExpGaus function was the analytical solution of convolution between an exponential decay function a Gaussian function. The ExpGaus function took the form:

$$I(t; I_0, t_0, \sigma, \lambda) = \frac{I_0}{2} \, exp\left[-\lambda\left(t - t_0 - \frac{\sigma^2\lambda}{2}\right)\right]\left[1 + erf\left(\frac{t - t_0 - \sigma^2\lambda}{\sqrt{2}\sigma}\right)\right]$$

where, I_0 was the trace maximum intensity, t_0 was its time zero, σ was the IRF width,

λ was the rate constant defined as $\lambda = 1/\tau$ were τ is the time constant, and erf was the "error function" defined as:

$$erf(x) = \frac{2}{\sqrt{\pi}} \int_0^x e^{-z^2} dz$$

Function details and derivation were presented in Section D.2. The fitting routine was carried out using a Python 3.x script, Script B.9. This routine employed the nonlinear least-square minimization method as implemented in lmfit [96] package. Initially, the IRF trace was fitted with a Gaussian function to extract its width (σ). This width was applied to the ExpGaus functions used to fit the TRPL traces and fixed during the fitting routine. Data and fitting visualization were all constructed using Matplotlib library [99] in Python 3.x.

2.5 FEMTOSECOND TRANSIENT ABSORPTION PUMP–PROBE (FSTAPP) INSTRUMENTATION

An integrated commercial laser system (ShapeShifter, Clark–MXR) was used to carry out the fsTAPP spectroscopy experiments It was also utilized to pump the TRPL experiment. This system consisted of a femtosecond chirped pulse regenerative amplifier (CPA), two non–collinear optical parametric amplifiers (NOPAs), a second harmonic generation (SHG), and a fsTAPP experimental apparatus. Figure 2.5 on page 28 depicted the optical path schematics of the various laser sources in this system. Figure 2.6 on page 35 outlined the fsTAPP apparatus. Only the CPA, the SHG, and the fsTAPP components were used in the work. However, and for the sake of completion, a full rundown of the components was presented in this section.

2.5.1 THE FEMTOSECOND CHIRPED PULSE REGENERATIVE AMPLIFIER (CPA)

Chirped–pulse amplification of ultrashort laser pulses was introduced by Strickland and Mourou in 1985 [100] and won them the Nobel Prize in 2018. This technique provided an innovative solution to the "gain–media damage" problem that was hindering the development of high–power laser sources. In its most basic form, this technique involved three main steps. To begin, the low power ultrashort pulse produced by a fiber oscillator was stretched few orders of magnitude longer than its original duration. For example a 100 fs would be stretched to a 100 ps pulse. During the stretching processing the gain media was pumped using a second power laser source. The stretched (or chirped) pulse was then passed through the pre–pumped gain media to be amplified. The stretched, amplified pulse was then recompressed back to near its original duration. Grating–based stretchers and compressors are the most efficient and reliable for this technique.

Chirped–pulse amplification using the regenerative amplifier configuration was the typical setup For femtosecond pulses. A regenerative amplifier was an optical configuration in which the gain media is placed in an optical resonator (cavity–like configuration) [101, 102]. Entering and exiting this resonator was typically achieved through a combination of electro–optic modulator and a polarizer acting as a quarter wave–plate. The modulator (Pockel cell) allows the number of amplifying round–trips (cycles) within the resonator to be controlled. In any given system, a delicate balance existed between repetition rate, number of cycles, and pump and seed characteristics to achieve the best amplification power and pulse quality. Nowadays, a few cycles (3–5) CPAs with low repetition rate from 1 kHz to 2 kHz can achieve produce femtosecond pulses with energies in millijoules.

Clark–MXR's CPA–2010 was a bi–level, integrated, few–cycle, $Ti:Al_2O_3$, regenerative, chirped–pulse amplifier. The seed laser used in this system, housed in the
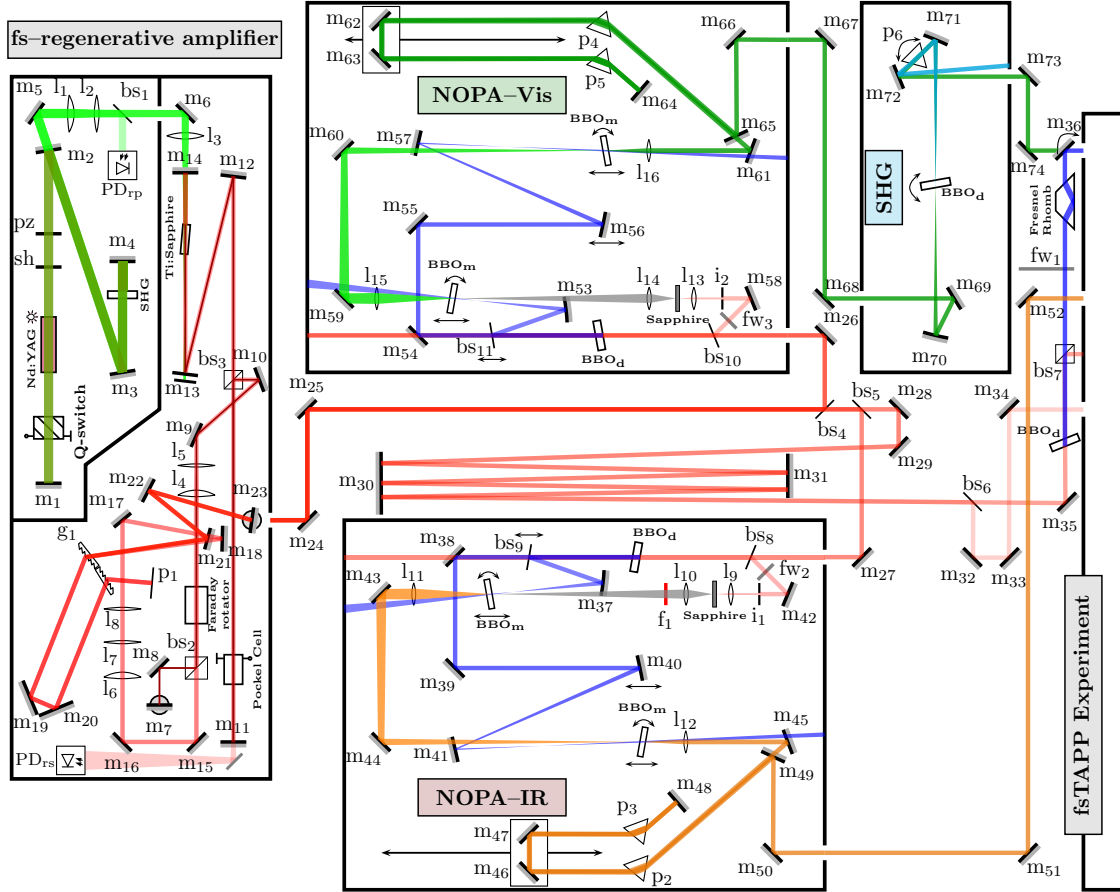
Figure 2.5: Schematics of the various laser sources in Clark–MXR's Shapeshifter. m: mirror, l: lens, g: grating, i: iris, p: prism, fw: filter wheel, PD: photodiode detector, f: filter, BBO: β–Barium borate, bs: beamsplitter

lower level, was a diode–pumped, passive mode–locked, frequency–doubled SErF fiber oscillator. This oscillator was based on Ippen and Haus's fiber ring laser design [103]. The fiber oscillator output centered at 1050 nm was passed through a temperature–stabilized periodically poled lithium niobate (PPLN) crystal for frequency doubling. At 775 nm (1.6 eV), the oscillator generally produces ∼0.5 nJ of a near 150 fs laser pulses. The repetition rate of these seed pulses was 38.4 MHz. The frequency–doubled pulse was then stretched and sent to the upper level for the amplification stage. The temperature–stabilized lower level housing the seed laser and the pulse stretcher was not user–accessible. Therefore, little was known about it aside from the technical

information aforementioned and the ones listed in the user manual [104].

The pump laser was a Q–switched Nd:YAG laser, dubbed as "ORC–1000", depicted in the upper left side of the regenerative amplifier box in Figure 2.5. The lasing media, an Nd:YAG rod ($\sim 50 \times 5\,\text{mm}$), was pumped with a Xenon arc lamp, within a Z-shaped cavity, between m_1 and m_4, Figure 2.5. Both the arc lamp and the Nd:YAG rod were housed in a temperature–stabilized assembly. The assembly cooling was done with a deionized water circulator. Frequency doubling (SHG) of the Nd:YAG to $532\,\text{nm}$ was done in an intracavity configuration. Within the cavity was a polarizer (pz) for intracavity polarization optimization, and a mechanical shutter (sh) for pump output control. The Q–switch operated at a $1\,\text{kHz}$ frequency to trigger the exit of a $10\,\text{ns}$ green pulse from the lasing cavity through the output coupler, m_2. Once outside the cavity, the pulse was steered by m_5 through l_1 and l_2 for recollimation into bs_1. A small portion of the intensity was sent onto the feedback photodetector, PD_{rp}. The rest of the intensity exited the compartment to be steered by m_6, refocused by l_3 into the Ti:Al$_2$O$_3$ crystal, i.e. gain media. The pulse passed through both mirrors m_{14} m_{13} and was terminated on a beam blocker behind m_{13}. The pump focusing point was placed few millimeters before the amplification crystal to avoid thermal damage. The Ti:Al$_2$O$_3$ crystal was water cooled for amplification stabilization. Within the normal operation of the CPA, the pump laser output average power was set near $6.2\,\text{W}$. In this system, m_6 was the primary mirror used to fine–tune the pump beam alignment into the Ti:Al$_2$O$_3$ crystal.

At the other end of the CPA housing, the seed laser pulse exited the lower level from a small window underneath m_7 onto m_7. It is then steered by m_8 onto polarization bs_2, from which it was reflected through a Faraday rotator. For efficient pump–seed spacial overlap, the beam size was shrunk through a Keplerian telescope composed of l_4 and l_5. The pulse was then steered using mirrors m_9 and m_{10} onto the second polarization bs_3 and reflected into the Pockel cell. This Pockel cell constituted

the seed's entrance point into the few–cycles amplification resonator. Within the appropriate timing, set by the controller, the Pockel cell was activated by $\sim3.5\,\mathrm{kV}$ to start the amplification cycles. The pulse was reflected off of the back mirror, m_{11} through bs_3, then m_{12} and m_{13} into the pre–pumped $Ti:Al_2O_3$ crystal. Once amplified through the first pass, the pulse was reflected off of m_{14} backward through the same path it came from. This constituted one amplification cycle. In this system, the desired amplification is achieved through 3–4 cycles. Within every cycle, a small leak from m_{14} was diffused onto the pulse train photodetector, PD_{rs} for monitoring. Once the amplification process was saturated, the Pockel cell was activated again by applying $\sim3.2\,\mathrm{kV}$ to trigger the exit process. The pulse traveling back from m_{11} was reflected from bs_3 onto m_{10} then m_9 through lenses 5 and 4 and the rotator. The pulse finally exited the amplification stage by passing through bs_2 then entered the compression stage. The maximum amplification was achieved by a temporal alignment of the Q–switch trigger and both of the Pockel cell trigger events. The timing of these events was done through the delay values in the controller. Similar to the pump side, m_7 served as the primary mirror used to fine–tune the seed beam alignment into the amplifier crystal.

Reflected off of mirrors m_{15} and m_{16}, the beam was resized and recollimated through lenses l_{6-8}. The beam was then steered using m_{17} and m_{18} into the compressor assembly. This assembly was a single–grating, dual–pass compressor with movable back mirrors, m_{19} and m_{20}, to provide compression flexibility for the user. The beam was simply steered through the grating, g_1, onto the back mirrors, from which it was reflected back through the other end of the grating into prism p_1. The prism, mounted vertically, increased the beam height and reflected it back through g_1 onto m_{19} and m_{20} to be collected by m_{21}. It was then steered by m_{21} and m_{22} onto m_{23} which sent the beam to the lower level to be reflected through the laser assembly exit. The final output was characterized as $\sim800\,\mu J$, $\leq150\,\mathrm{fs}$, linearly and horizontally polarized

pulse, centered at 775 nm, with a repetition rate of 1 kHz.

Through a series of mirrors and beamsplitters, the CPA output beam is distributed into four parts to operate the various components of the laser system. Mirrors m_{24} and m_{25} steer the beam onto bs_4, which sent 60% ($\sim$480 µJ) of the beam energy into NOPA–Vis. Using bs_5, 40% of the remaining $\sim$320 µJ ($\sim$128 µJ) were directed into NOPA–IR. The rest, $\sim$192 µJ was bounced between mirrors m_{30} and m_{31} to compensate for the delay corresponding to the beam passage through both NOPAs. After the delay correction, the beam was sent through yet another beamsplitter bs_6, where 8% of the remaining energy ($\sim$15 µJ) is reflected and steered through a series of mirrors (m_{32-34}) into the fsTAPP apparatus to be used in the probe's supercontinuum generation. The last portion passing through the beam splitter ($\sim$177 µJ) was steered through m_{35} into the SHG crystal BBO, to generate the 387.5 nm (3.2 eV) pulse used as pump in the experiments presented in this work. The SHG pulse was separated from the leftover fundamental pulse through a polarization beamsplitter bs_7, then attenuated by a neutral density filter wheel fw_1. The final step was passing the SHG beam through a half–wave Fresnel Rhomb retarder set at the magic angle ($\sim$54.7°) with respect to the polarization of the fundamental. The purpose of the last step was to minimize any anisotropy artifacts that may be present in the measured spectra. Typically, the full output of this SHG assembly was >12 µJ of pure 387.5 nm (3.2 eV). All of it was rarely steered by m_{36} into the fsTAPP apparatus to be used as a pump. Laser system operational procedures were detailed in Section E.1 on page 230.

2.5.2   THE NON–COLLINEAR OPTICAL PARAMETRIC AMPLIFIER (NOPA)

Clark–MXR's ShapeShifter incorporated two NOPAs into its assembly. Both were capable of producing $\geq$30 fs in a wide range of wavelengths. Figure 2.5 on page 28 contained both NOPAs assemblies within the framework of the ShapeShifter. The first, NOPA–Vis, was set up to cover the visible (VIS) region of the spectrum, typically

450 nm to 700 nm (2.76 eV to 1.77 eV). NOPA–Vis primary usage was for pump purposes. Therefore, the largest portion ($\sim$480 µJ) of the fundamental beam power was steered into it. The second, NOPA–IR, was set up to cover the near infrared (NIR) region of the spectrum, typically 800 nm to 1600 nm (1.55 eV to 0.775 eV). Being used primarily for the lower energy demands of the single–wavelength probe, NOPA–IR received a minimal pump power, $\sim$128 µJ. Both NOPAs design and operation were nearly identical. Therefore, NOPA–Vis will be discussed here in details. Details regarding design criteria of optical parametric amplifiers can be found in reference [105].

The NOPA incorporated in the ShapeShifter was designed in a dual–stage configuration. The first stage was used for initial wavelength selection. The second stage was used for final power amplification. Directly after entering the NOPA assembly, the fundamental beam is met with a beamsplitter bs_{10}. Through this beamsplitter most of the beam power was transmitted to a SHG crystal, BBO_d. The frequency doubled beam (775+387.5 nm) traveled onto bs_{11}, where about 30% of the 387.5 nm was reflected to m_{53}. m_{53} focused the beam few millimeters in front of the first wave–mixing crystal, BBO_m. The remaining SHG was reflected by a dichroic mirror, m_{54}, while the fundamental was transmitted through and terminated on the NOPA's box wall. The beam reflected from m_{54} was steered through mirrors m_{55-57}. The latter focused the beam few centimeters before the second wave–mixing crystal, BBO_m.

The small fraction of the fundamental reflected off of bs_{10} was steered onto m_{58}, passing through a variable neutral density filter, fw_3. From m_{58}, the beam diameter was shrunk by iris i_2 and focused by lens l_{13} onto the Al_2O_3 supercontinuum generation plate. The supercontinuum beam was collected and refocused by l_{14} onto the first wave–mixing crystal, BBO_m. When the pump, 387.5 nm, and the supercontinuum seed were specially and temporally overlapped, and the phase–matching conditions

were met, narrow–band amplification would occur in the first BBO_m. The amplified wavelength was dependent on several parameters, one of which was the pump–seed crossing angle. Typical angles of various target wavelengths were listed in Table 2.2. The first BBO_m output signal was collected and refocused by l_{15} into the second BBO_m. Similar to the first stage, when the proper conditions were met, the seed (first stage output) would be amplified. Following the second stage amplification, the beam was collected and collimated by l_{16}. After collimation, it was steered by m_{61} into the compressor assembly. The compressor was a prism–based with a dual–pass configuration. The beam traveled through prism p_4, onto m_{62} then m_{63} then p_5 where it was reflected back through the same path off of the back mirror, m_{64}. However, the output beam was at a lower height from the input. This allowed the compressed beam to be collected and steered by m_{65} to m_{66} through the NOPA exit.

Table 2.2: List of NOPA's pump–seed crossing angle for various output wavelengths. Reproduced from the manual [106].

Wavelength (nm)	Photon energy (eV)	Crossing angle (degree)	separation at 100 mm (mm)
500	2.48	5.88	10.25
550	2.25	6.60	11.50
600	2.07	6.66	11.60
650	1.91	6.32	11.00
700	1.77	5.16	09.00
>775	<1.60	<2.50	<03.15

For applications that required pump in the ultraviolet (UV) region of electromagnetic spectrum, the NOPA–Vis output may be frequency doubled in the SHG assembly. The exiting beam was steered by mirrors m_{67-69} onto the concave mirror, m_{70}, which focused it onto the SHG crystal, BBO_d. The UV+VIS beam was collected and recollimated by another concave mirror, m_{71}, and steered into a prism p_6. P_6 dispersed the beam components onto m_{72} which steered the desired UV output onto m_{73} then m_{74} to the pump entrance of the fsTAPP apparatus. The beam selection can

be made by flipping the mount of p_6. Procedural operations and wavelength tuning of NOPA–Vis and its SHG were detailed in Section E.2, on page 233.

2.5.3   THE FEMTOSECOND TRANSIENT ABSORPTION PUMP–PROBE (FSTAPP) APPARATUS

The final component of the ShapeShifter was the fsTAPP experimental apparatus. The optical schematics of the fsTAPP apparatus were depicted in Figure 2.6a. This apparatus utilized the various pump sources the Shapeshifter had to offer. Namely, the fundamental 775 nm (1.6 eV) and its SHG 387.5 nm (3.2 eV) and the NOPA–Vis output 480 nm to 700 nm (1.77 eV to 2.58 eV) and its SHG 240 nm to 350 nm (3.54 eV to 5.17 eV). Additionally, this apparatus was set up for dual probe modes; single wavelength, and broadband. In this apparatus the sample was mounted on a three–dimensional stage that permitted the fine–tuning of the sample positioning with respect to the incoming beams.

The pump wavelength was selected outside the apparatus and directed through an entrance hole in the upper right corner then through iris i_1. It was then met with a beamsplitter bs_1, which directs a small portion, $\sim$10%, onto a monitoring photodiode PD_{pm}. The rest was passed through iris i_2 into a corner hollow reflector mirror m_1. Both i_2 and m_1 were mounted on a motorized linear actuator that provided accurate temporal delay between the pump and the probe. The reflected beam was steered by m_{2-3} through a mechanical chopper that was operating at half the CPA's frequency, i.e. 500 Hz. The mechanical chopper provided the pump–on/pump–off configuration required for the fsTAPP experiment. The pump beam was then focused by m_4 and steered into the sample container by m_5. After passing through the sample, the pump was terminated on a half–closed iris, i_5. Mirror m_4 was mounted on a manual stage to allow for proper focal point positioning of the pump beam with respect to the sample.

The single wavelength probe mode utilized the NIR beam produced by NOPA–IR.
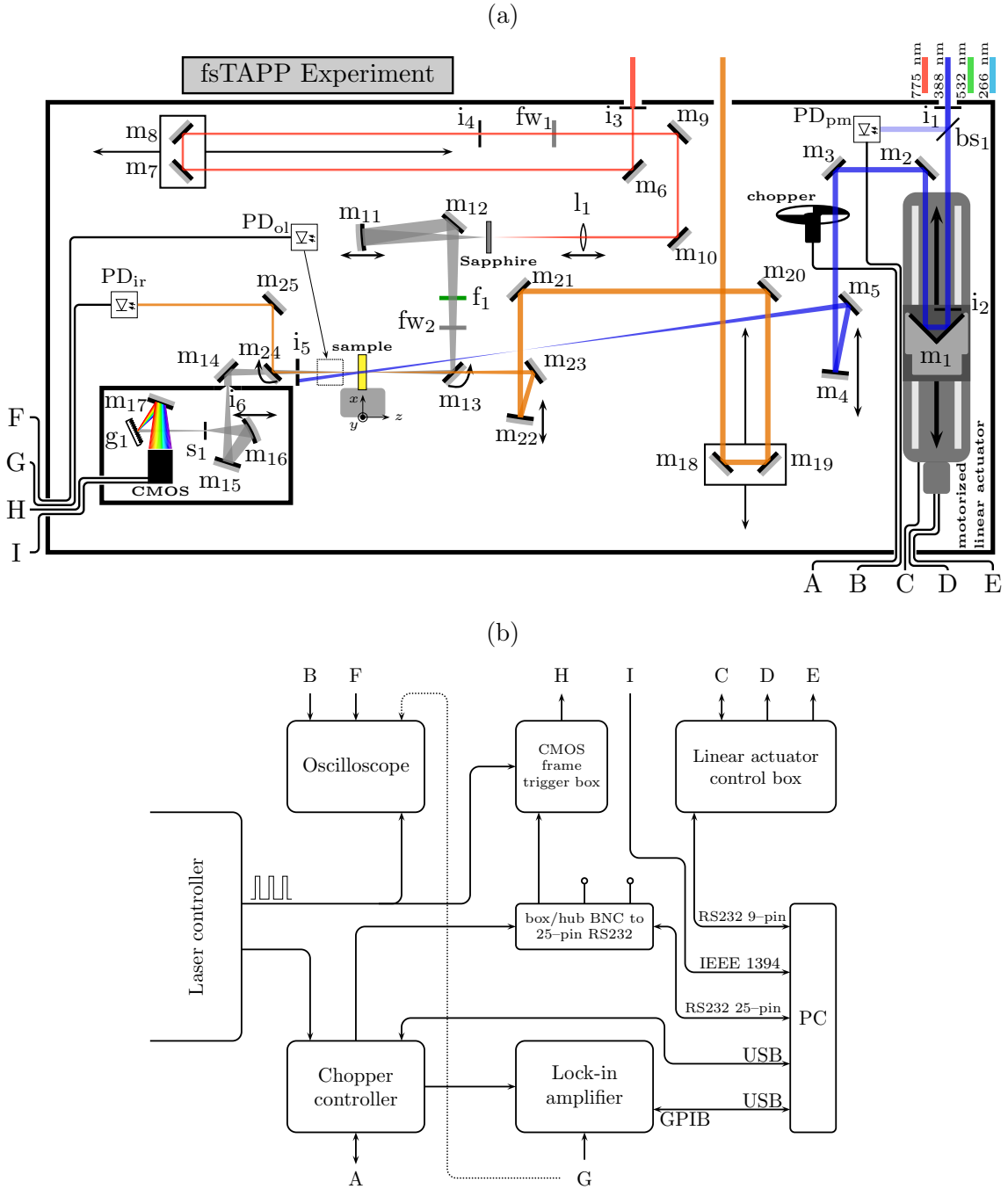
Figure 2.6: (a) Schematics of the optical layout of the femtosecond transient absorption pump–probe (fsTAPP) apparatus. (b) Simplified layout of the wiring connections and controllers within the fsTAPP apparatus. Leads A–I shown in (a) and (b) depicted the wiring connections between the mechanical and electrical components of the apparatus.

This beam entered the apparatus through the upper, intermediate entrance hole onto mirror m_{18}. It was then steered by mirrors m_{19-23} into the sample container. Mirrors $m_{18,19}$ acted as a retroreflector mounted on a variable stage to allow for temporal compensation between the pump and probe pulses. Mirror m_{22} focused the beam inside the sample container. The variable mounting of m_{22} allowed for proper positioning of the focal point with respect to the pump and the sample. In this single wavelength probe configuration, m_{13} was flipped down to allow for clear passage of the probe beam to the sample. After the sample, the probe was passed through the center of the iris i_5 to minimize any pump scattering or artifacts. It was then collected and refocused by mirror m_{24} through m_{25} onto a biased InGaAs photodetector (DET10C, Thorlabs), PD_{ir}.

The broadband probe mode utilized a supercontinuum generated by pumping a Al_2O_3 plate with $<15\,\mu J$ of the fundamental $775\,nm$. Briefly, those $\sim 15\,\mu J$ were directed through the upper, left entrance hole into an iris, i_3, at which the beam diameter was reduced. Steered by mirrors m_{6-8}, the beam was passed through a variable neutral density filter, fw_1, in order to attenuate its intensity. Iris i_4 served as a reference point when the beam would move out of alignment. Mirrors $m_{7,8}$ acted as a retroreflector mounted on a variable stage to allow for temporal compensation between the pump and probe pulses. After being attenuated, the beam was steered by mirrors $m_{9,10}$ into a bi–convex lens l_1 to be focused into the Al_2O_3 plate. The generated supercontinuum was collected and refocused by m_{11} then steered by mirrors $m_{12,13}$ into the sample container. Mirror m_{11} was mounted on a variable stage to allow for proper positioning of the probe focal point with respect to the sample container and the pump focal point. The supercontinuum is passed through a narrow–band filter f_1 centered around to $775\,nm$ to eliminate the fundamental residuals within the supercontinuum. The variable neutral density filter, fw_2, allowed for attenuating the supercontinuum intensity to avoid detector saturation. After passing through the

sample, the supercontinuum was passed through an iris, i_5, to minimize any pump scattering or artifacts. It was then steered by m_{14} into the spectrograph box near the lower left corner of the apparatus.

The spectrograph incorporated in the ShapeShifter's fsTAPP apparatus was based on a single, curved reflective grating. It was user–accessible to allow for fine–tuning and calibration when needed. The beam traveled into the spectrograph through an iris, i_6, for additional blockage of ambient light and pump scattering. It was then steered by m_{15} onto a concave mirror, m_{16}. Mirror m_{16} refocused the beam through a slit, s_1. Mirror m_{16} was mounted on a variable stage to allow for proper positioning of the focal point with respect to the slit, s_1. The diffracted beam through s_1 was then met with the reflective grating, g_1, to fully disperse the spectral components of the supercontinuum. The first order of the dispersed beam was reflected off of g_1 onto m_{17} which steered it onto the linear array camera, CMOS. This CMOS linear array camera (LW–ELIS–1024A-1394, LightWise) had 1024 active pixels and 1 kHz frame rate.

2.5.4 DATA ACQUISITION LOGIC OF THE PUMP–PROBE EXPERIMENT

A brief explanation of the data acquisition sequences for the single wavelength and broadband detection in the fsTAPP apparatus were listed below. This description detailed the inner workings and communication steps the apparatus took to collect the temporal differential absorbance spectra. The wiring connections between the various components at work in these sequence were depicted in Figure 2.6b. The alphabetical labeling in Figure 2.6b and b indicated the wiring connections between the electrical and mechanical parts of the apparatus.

SINGLE WAVELENGTH PROBE

In preparation for the acquisition sequence, the chopper frequency was stabilized at half of the laser frequency, i.e. 500 Hz. The chopper synthesized a TTL logic signal

associated with its running frequency through an LED–PD pair mounted around the blade. That TTL signal was sent back to the chopper controller through lead "A". The chopper controller sent a confirmation signal to the software through its USB connection. The software then sent a command to the linear actuator controller to move to the position associated with the desired temporal delay through its RS–232 connection. The actuator control box communicated the desired position with the actuator through leads "C", and "D". Once the actuator was positioned properly, it sent a confirmation handshake signal to its controller which in turn confirmed the position to the software through its RS–232 connection. The data acquisition started by sending a command to the lock–in amplifier through the GPIB–to–USB connector to start its demodulation process. Lock–in reference frequency was sent from the chopper controller at $500\,\mathrm{Hz}$, while the signal itself was sent from the IR photodiode PD_{ir} through lead "G". When the demodulation was done, the resulting signal was sent back to the computer from the lock–in amplifier through the GPIB–to–USB connector. The software then calculated the differential absorbance by using two consecutive demodulation events. The final step was for the software to accumulate the desired number of points required to produce the average, then store it in an array and present it in the live graph. The scan parameters set in the software determined the next delay position, which initiate the sequence again by moving the actuator to the new delay position.

BROADBAND PROBE

Much like the single wavelength probe sequence, the broadband required the chopper and stage to be locked at the desired frequency and position, respectively. Once that was achieved, the software sent a command to the 1024–pixel CMOS to begin the integration sequence. However, the triggering scheme of the CMOS was of a different nature. The CMOS was triggered in its "C–type" scheme, which constituted

of a main event trigger that was generated by the chopper TTL logic, see [107] for details. This TTL was sent from the chopper controller through the BNC–to–RS–232 hub to the CMOS frame trigger box, Figure 2.6b. The integration window was set to 2 ms as per the 500 Hz chopper frequency. The second event was the frame integration event, which was set to 1 ms as per the 1 kHz TTL logic signal generated by the laser controller. The grabbed, integrated frames were accumulated on the camera buffer then sent to the computer via the IEEE 1394 port, lead "I" Figure 2.6a and b. The software processed the received frames in two different ways depending on the requested way of operation. When presenting the "white light" information, it simply averaged all the frames, then presented the intensity spectra with respect to the wavelength. However, when acquiring the transient absorption data, it calculated the differential absorbance spectra between two consecutive frames based on Equation 2.3: At any given time delay point(Δt), the number of frames integrated was determined by the number of pulse pairs, and the number of differential absorbance spectra to average set by the user. In a typical measurement sequence, 50 pulse pairs were acquired, and 10 spectra were averaged, i.e. 500 pulse pairs were accumulated and averaged to produce one differential absorbance spectra. Once the required number of frames were acquired, the camera sent a handshake signal to the software to indicate the end of this acquisition cycle. This signal was communicated via its 15–pin micro–D connector, lead "H", through the CMOS frame trigger box, and the BNC–to–RS–232 hub, to the 25–pin RS–232 connector, Figure 2.6a and b. Finally, the software initiated the next acquisition sequence by sending a command to the linear actuator control box to move to the next time delay point within the temporal scan parameters.

$$\Delta OD = -\log \left(\frac{I^*(\lambda, \Delta t)}{I_0(\lambda)} \right) \qquad (2.3)$$

ΔOD was the intensity of the differential absorbance, $I^*(\lambda, \Delta t)$ was the intensity of the pumped frame at a given time delay, and $I_0(\lambda)$ was the intensity of the unpumped

frame.

2.6 FEMTOSECOND TRANSIENT ABSORPTION PUMP–PROBE (FSTAPP) SPECTROSCOPY

Two types of fsTAPP experiments were carried out within this work to detect transitions from the maximum number of excited state possible. These experiments employed "typical" and "extended" broadband supercontinuum probe sources. The pump–probe delay profile resulting from these experiments was used to unravel the lifetimes of the short and long–lived excited state.

2.6.1 DATA ACQUISITION

Herein, was an elaboration on the experimental and technical conditions under which fsTAPP data acquisition was carried out.

TYPICAL BROADBAND SUPERCONTINUUM PROBE

Primarily, the samples were studied using a limited broadband supercontinuum probe. This probe was generated using a Al_2O_3 plate, as described in the apparatus above. This probe choice was used because of its superior stability, and higher signal–to–noise ratio. The usable range in this probe type extended from $420\,nm$ to $775\,nm$ ($1.6\,eV$ to $3\,eV$). The scans were carried out on a sample solution placed in a $1\,mm$ path–length cuvette (Starna, Spectrosil 21–Q–1). These solutions were at $0.5\,mmol\,L^{-1}$ concentration, as described in Section 2.1. The pump fluence in these measurements was maintained around $500\,\mu J\,cm^{-2}$. The time–axis was scanned in a semi–logarithmic manner. Scan range from $-1\,ps$ to $1\,ps$ was spaced linearly with $10\,fs$ step between each differential spectrum. The range $<1\,ps$ was spaced logarithmically such that 200 differential spectra were acquired within each order of magnitude. i.e. logarithmically spaced 200 spectra from $1\,ps$ to $10\,ps$ and another 200 spectra from $10\,ps$ to $100\,ps$

and so on. The upper limit of the time–axis scan was constricted by the motion range of the linear actuator at ∼1.66 ns. This limit allowed the accumulation of a total of 845 differential spectra along the scanned time–axis. Averaging parameters were set to 50 "Pairs of Laser Shots" and 10 "Grabs to average" to a total of 500 pulse pairs per acquired spectrum. Each sample was scanned five times sequentially, dubbed as "passes", to ensure data reproducibility and improve the final signal–to–noise ratio. All five passes were averaged to produce the spectra presented in this work. Ultimately, the averaging parameters totaled to 2500 pulse pairs per each differential spectra. Finally, Using the same overlap configuration, and pump fluence, the same cuvette was filled with pure $CHCl_3$ and measured to produce the background data. The background scan the same semi–logarithmic scan configuration but within a limited range from −1 ps to 5 ps. This solvent background provided a reliable source that revealed the coherent artifacts typically present in the early time of any fsTAPP measurements. Sample and solvent data were exported as "tab delimited" text format, for processing and further analysis.

EXTENDED BROADBAND SUPERCONTINUUM PROBE

The typical, Al_2O_3–generated supercontinuum probe had superior stability and signal–to–noise ratio along the time–axis. However, it lacked the spectral range to reveal details of certain bands of interest in this work. Therefore, an alternative probe source, with wider spectral range, was utilized to explore these bands. This alternative supercontinuum was generated using a 2 mm thick, continuously moving CaF_2 plate. The continuous linear motion was achieved using a reciprocating cycle motor assembly pushing a linear translation stages onto which the plate was mounted. The generator was incorporated into the existing system, such that only the Al_2O_3 plate was replaced without altering the existing optical configuration. The supercontinuum generation using CaF_2 required higher fundamental pump power density compared to the one

41

generated using Al_2O_3. Therefore, significant adjustments to the existing power density controllers were required. Namely, i_3, fw_1, and l_1 in Figure 2.6 on page 35. The CaF_2 supercontinuum extended the probe range from 420 nm to 325 nm (3 eV to 3.8 eV). Comparative spectral profiles of these two supercontinuum probes were depicted in Figure 2.7.
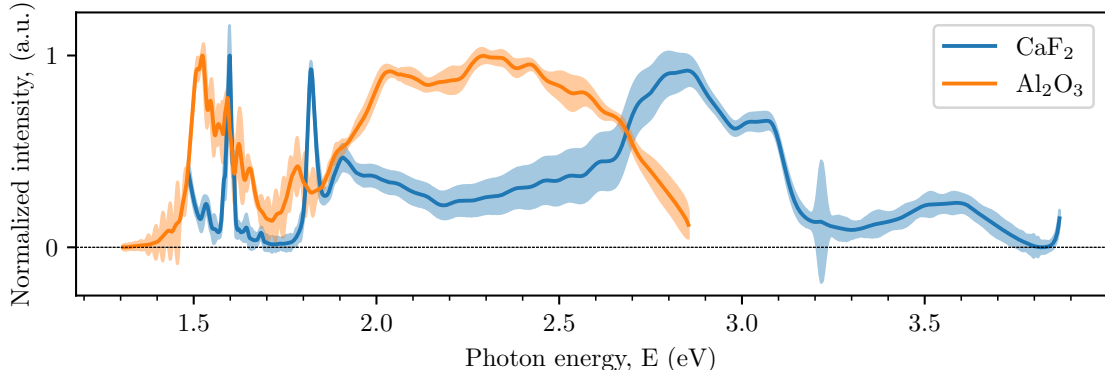
Figure 2.7: Spectral profiles of the supercontinuum probes generated using Al_2O_3 and CaF_2 plates. Solid lines represented the average of 100 individual curves. The shaded area was the standard deviation of these 100 curves multiplied by 4 for visibility.

Detection was also expanded into the NIR region in these experiments. The range was expanded to $\sim$1010 nm ($\sim$1.22 eV) by realigning the CaF_2–generated super-continuum on the CMOS linear array camera. The realignment involved shifting the diffracted beam horizontally on the CMOS using mirror m_{17}. The intensity distribution was then fine–tuned using mirrors m_{16} and m_{17}. Finally, The wavelength calibration was reinstated using a 533 nm notch filter as the reference point. Refer to Figure 2.6 on page 35. However, due to the limited number of pixels on the CMOS, both ends of the extended probe range can not be detected simultaneously. Therefore, two separate scans were carried out, then stitched together using the overlapping spectral region from 600 nm to 800 nm (1.55 eV to 2.0 eV). Due to the nature of the supercontinuum generation, the resolved spectral shape around the fundamental wavelength 775 nm (1.6 eV) was highly unreliable. This NIR expansion effort aimed at showing the extent of the signal presence, rather than resolving its spectral shape.

The extended probe data acquisition parameters were nearly identical to the ones under which the typical probe was acquired. Only the number of passes were increased to ten instead of five in order to improve the usability of the acquired data. Only solutions of BDODC and HTRMR were investigated using this extended probe. Ultimately, detected bands from the HTRMR were identical to those of the OLGMR and PLYMR from a spectral standpoint. Moreover, and due to the exploratory nature of this part of the investigation, the samples concentrations were not tightly controlled, but rather approximated around $0.5\,\mathrm{mmol\,L^{-1}}$. Finally, both spectral segments, and their solvent's background were exported as "tab delimited" text format, for processing, and visualization.

2.6.2   INITIAL DATA PROCESSING AND ARTIFACT REMOVAL

Python 3.x scripts were employed to process, correct, and refine the various fsTAPP experimental data, Script B.10 and Script B.11. These scripts employed functions from numpy [93], scipy [94], and h5py [95] libraries. Herein, a detailed outline of these scripts operations, and the types of processing and corrections carried out on the data files.

AL$_2$O$_3$–GENERATED BROADBAND PROBE

The data processing of the Al$_2$O$_3$–generated broadband probe was straight forward. The main objectives were from this processing was to remove the ambient light and coherent artifacts. Additionally, the processing would need to correct for the group velocity dispersion (GVD) curve artifact in the spectra. Script B.10 was able to achieve these objectives through a series of nested "for" loops. Prior to executing the script, data points representing the GVD curve were extracted from a representative spectrum, manually. Then a third order polynomial curve fitting was carried out to estimate the GVD curve parameters.

The script started by processing the solvent passes. The processing involved importing the data file into a numpy array then subtracting the spectra from an estimate of the ambient background. The ambient background curve was estimated by averaging ten spectral lines from the temporal region prior to the signal appearance, $<-0.5\,\text{ps}$. The corrected passes were then averaged. The script then imported each individual pass of the particular sample. The ambient light background for these passes were corrected in the same manner as solvent passes corrections. The coherent artifact was then removed by subtracting the averaged solvent data from the samples' data within the range from $-1\,\text{ps}$ to $5\,\text{ps}$. The next step was to compensate for the GVD curve. The script started by rearranging the data array into a three column XYZ format. During the rearrangement, a correction was applied to the spectral and temporal coordinates using the GVD curve parameters previously estimated. Additionally, the spectral axis data were converted from nm to eV. The array format was then recreated using a predefined energy and time axes to introduce consistency. The new energy axis extended from $1.6\,\text{eV}$ to $3.1\,\text{eV}$ with a step size of $0.001\,\text{eV}$. The new time axis had a semi–logarithmic nature. The linear range was set from $-1\,\text{ps}$ to $1\,\text{ps}$ with step size of $10\,\text{fs}$. The range from $1\,\text{ps}$ to $1700\,\text{ps}$ was spaced logarithmically with two hundred spectra within each order of magnitude. Once all the passes were processed, the script calculated their average and standard deviation then stored them in a three–dimensional numpy array. Finally, the data arrays were exported to a centralized HDF5 file for future analysis and visualization.

CAF_2–GENERATED BROADBAND PROBE

The processing of the CaF_2–generated broadband probe followed the same outlines described in the Al_2O_3–generated section above. However, due to the segmentation of the spectral range, steps were rearranged, and more steps were added to the processing script, Script B.11. The first loop in this script imported both segments of

44

the solvent background into separate numpy arrays. The subtraction of background ambient light was carried out on each individual segment. Following which was trimming of the spectral edges of both segments and stacking them into one array. Once all passes were processed, the average was calculated and stored into an identifiable array. The subsequent loops performed the same steps for the samples spectra. However, additional steps involving solvent background correction and GVD correction were included. The merging of the actual segments was embedded into the GVD correction procedure. During the array–to–XYZ rearrangement, data points from both segments at the spectral overlapping region were included. Subsequently, when the corrected XYZ–to–array conversion took place, the data points within the overlapping region from both segments were considered. The unified energy axis was set from $1.22\,\text{eV}$ to $3.87\,\text{eV}$ with a $0.002\,\text{eV}$ step size. The was axis was semi–logarithmic, with $20\,\text{fs}$ spacing in the linear region from $-1\,\text{ps}$ to $1\,\text{ps}$. The logarithmic range from $1\,\text{ps}$ to $1700\,\text{ps}$ was spaced so that it placed one hundred spectra in each order of magnitude. Once all sample passes were processed, the average and standard deviation were calculated and stored into a three–dimensional numpy array. Finally, the processed data arrays were exported to a centralized HDF5 file for future visualization.

2.6.3 DATA FITTING AND VISUALIZATION

Multi–exponential fitting of the kinetic traces of the main fsTAPP features was carried out in an in–house python 3.x script, Script B.12, Script B.13, and Script B.14. The data from the Al_2O_3–generated broadband probe experiment was used in these analyses. The fitting routine employed the nonlinear least-square minimization method as implemented in lmfit [96] package. The mathematical modeling used the same ExpGaus function described in Section 2.4. It also used a Gaussian distribution function to simulate the leftover coherent artifact component in the kinetic traces. A linear combination of exponential decays and growths was used to simulate the kinetic

profiles. These combinations were based on the assumption that the excited species follow a sequential first–order reaction.

Briefly, the script imported the data into a numpy array from the centralized HDF5 file. It then defined the kinetic model components of this particular sample and selected probe energy. The coherent artifact width, representing the IRF, was fixed at 240 fs, 240 fs and 220 fs for PIA_1, SE, and PIA_2 features among all samples. Finally, then script carried out the fitting algorithm to extract the parameters of interest. The initial guesses for each signal in each sample was optimized through a trial–and–error process. Data and analysis plots were all constructed in python 3.x using Matplotlib [99] library.

CHAPTER 3

RESULTS: DENSITY FUNCTIONAL THEORY CALCULATIONS

This chapter highlighted the results obtained from the density functional theory (DFT) and the time–dependent density functional theory (TD–DFT) calculations. It started by providing a brief historical highlight of the introduction and development of these *ab initio* calculation methods in Section 3.1. Section 3.2 detailed the investigation methods and procedures utilized in this work. The section touched on the molecular structures of the investigated chromophore models. It also provided a brief explanation of the scripts used for post–processing and visualization.

Three isolated oxanthrene chromophore models were investigated. Namely, the unsubstituted [1,4]benzodioxino[3,2-b]oxanthrene (BDO), the homosubstituted [1,4]benzodioxino[3,2–b]oxanthrene–6,13–dicarbonitrile (BDODC), and the hetero-substituted [1,4]benzodioxino[3,2–b]oxanthrene–6–(1,3,5–trimethylpyrazole–4-sulfo-nyl)–13–carbonitrile (BDOSC). Additionally, a model representing a hypothetical heterodimer sub–unit (HDIMR) was devised to explore the interactions of the two substituted chromophores through a spiro bridge. The inter–chromophore interaction was characterized as a type of homo–conjugation, also known as spiro–conjugation. This HDIMR model design resembled a micro environment found within the macro-molecules studied with spectroscopy techniques. It consisted of chromophores BDODC and BDOSC, linked through a 3,3,3′,3′-tetramethyl-1,1′-spirobiindan (SPIRO) bridge. The aforementioned bridge was the backbone of the third component in the macro-molecular synthesis, a 5,5′,6,6′-Tetrahydroxy-SPIRO, see Section 2.1 for more details.

In order to compare its parameters with those of the HDIMR the geometry of the isolated Tetrahydroxy-SPIRO was also explored. Sketches of these five models can be found in Figure 3.1. The chapter then presented a brief evaluation of the used DFT basis set and functional in Section 3.3. Section 3.4 detailed the geometrical and electrostatic properties of the investigated models. It elaborated on the geometrical characteristics of each investigated model, and drew parallels with similar molecules explored theoretically and experimentally in the literature. The subsequent section, Section 3.5, explored the frontier molecular orbitals (MOs) of these models. Finally, Section 3.6 presented a brief look into the vertical and adiabatic excitation energies of the isolated chromophores, as well as the HDIMR.

3.1 HISTORY OF DENSITY FUNCTIONAL THEORY (DFT) AND TIME–DEPENDENT DENSITY FUNCTIONAL THEORY (TD–DFT)

The principles and foundations of DFT was introduced by Kohn and co–workers in the mid 1960s [108, 109]. Since then, great deal of advancements were made, and still being made, to its approximations and applicability. Nowadays, DFT has become a primary theoretical tool for theoretical and experimental chemists alike. This theory came about as an alternative solution to the many–electron problem of the Schrödinger equation. It relied on the principles of electronic density distribution rather than the explicit many–electron wavefunction method [110]. In this vain, DFT can be considered an exact theory. A true DFT density functional can provide the exact solution to this many–electron problem [111]. However, this true functional can not be known for a chemical system of interest in any practical capacity. Therefore, a plethora of density functional approximations (DFAs) were introduced since the inception of DFT [111]. In the following decades, the enormous expansion of these DFAs prompted Perdew and Schmidt to introduce the "Jacob's Ladder" as a method of classification [112]. This ladder connected the "Hartree World" of non–interacting

electrons to the world of chemical accuracy [111, 112].

Local density approximation occupied the first tier on "Jacob's Ladder". These approximations employed the uniform electron gas theory. This theory depicted the molecular space as a negative, uniform electron density (ρ) cloud filled with evenly–spaced, freely moving, non–interacting electrons. The negative charge of this uniform cloud would be neutralized with a background positive potential. The second tier housed the generalized gradient approximation. This approximation introduced a density gradient component ($\nabla\rho$) to the local density approximation. Methods like BLYP [113–115] and BP86 [113, 116, 117] belonged to this tier. Energy contributions from both electron exchange [118] and correlation [119, 120] were part of these two tiers. Both of these contributions were included as separate mathematical expressions to the electron density approximation. The third tier included a form of non–separable gradient approximation that included higher–order density derivatives ($\nabla^2\rho$) [121]. In this "meta–generalized" gradient approximation, both exchanged and correlation contributions were combined into one mathematical expression [111].

Methods in the fourth tier improved on the previous approximations by introducing Fock exchange components in place of the local exchange. The rationale behind these modifications was the non–local nature of the exchange phenomenon. Some of the most famous methods like B3LYP [122, 123] and PBE0 [124, 125], also known as "hybrid" functionals, were classified within this tier. The final tier followed the same logic of the previous one. Here, semi–local correlation components were replaced with orbital–dependent, non–local terms [126–130]. Known as "double–hybrid", methods like B2PLYP [126], PWPB95 [127], and ωB97X–2 [131] were representatives of this tier [111].

While DFT excelled in describing the ground state electronic structure, it was invalid for describing the electronic structure of excited states [132]. The solution to this deficiency was introduced by Runge and Gross in 1984 in the form of TD–

DFT [133]. This solution was further refined into the linear-response TD–DFT by introducing the approximations including the interaction of electronic structures with weak electromagnetic fields [134, 135]. Including the same DFA found in DFT, TD–DFT has ascended to the rule of a primary tool for studying excited–state problems [132].

In order to assess excited states using TD–DFT methods, the ground state electronic structure must be established first. This would generally be done using the self–consistent field (SCF) of the Kohn–sham DFT. The total energy produced by DFT consisted of four components: electronic kinetic energy, attractive electron–nucleus energy, repulsive electron–electron Coulomb energy, and the exchange–correlation energy. The latter was introduced to account for any kinetic energy inaccuracies and the electronic self–interaction errors arose from the Coulomb term [136–140]. Similar to the density functional, this exchange–correlation term can not be known. Therefore, approximations for this term were introduced as part of the development of DFAs. These approximations were considered one of the differentiating factors between the tiers of "Jacob's Ladder" [132].

3.2 METHODS AND PROCEDURES OF DENSITY FUNCTIONAL THEORY CALCULATIONS

3.2.1 *AB INITIO* METHODS

DFT and TD–DFT calculations were carried out using Gaussian 16 software suite [141]. All calculation jobs were performed using the University of Louisville's Cardinal Research Cluster (CRC). Four structures were explored using DFT and TD–DFT. Namely, BDO, BDODC, BDOSC, and a HDIMR of the investigated macromolecules. The SPIRO bridge was also investigated as an isolated molecule. Depictions of these models can be found in Figure 3.1.

A brief evaluation of the DFT's functional and basis set parameters was performed

and compared with their available experimental counterparts. Energetics of BDODC was used as a reference value for the accuracy of six different basis sets. These basis sets were 6–31G(d), 6–31+G(d), 6–31G(3df,2p), 6–31+G(3df,2p), aug–cc–pVDZ, and aug–cc–pVTZ. On the other hand, the energetics of the two chromophores within the heterotrimer sub–model (HTRMR) were utilized to assess the accuracy of various functionals. In this framework, five exchange–correlation ratios within the framework of B3LYP* were investigated. Namely, the Hartree–Fock exchange ratios of 0%, 20%, 60%, and 80% were tested. The results of this brief method benchmarking were detailed in Section 3.3. The conclusion was that there was no significant benefit from increasing the size of the basis set, while sacrificing an increased calculation time. Similarly, B3LYP, at 20% Hartree–Fock exchange ratio, was found to produce the highest accuracy of the transition energy estimates. Therefore, B3LYP coupled with 6–31G(d) were adopted to carry out the DFT and TD–DFT calculations.

The calculation procedure was similar for the five investigated structures at the aforementioned B3LYP/6–31G(d) level of theory. Briefly, a semi–empirically (PM6) optimized geometry was used as an initial guess. The initial geometry was optimized to its singlet ground state (S_0) equilibrium geometry using Berny algorithm as implemented in Gaussian 16. Frequency calculations confirmed that the equilibrium geometry reached was real. No Imaginary frequencies were found for the equilibrium geometries of the investigated structures. Then, a TD–DFT singlet and triplet vertical excitation calculations were carried out using the S_0 optimized geometry. After locating the states of interest, singlet and triplet excited–state optimizations were performed to locate their corresponding equilibrium geometries. These located geometries were also confirmed using frequency calculations. Using these same procedure detailed above, D_2h point group restrictions on BDO and BDODC were also explored for

---

*Becke's 3–parameter hybrid functional with Lee, Yang, and Parr's non–local correlation term and Vosko, Wilk, and Nusair's 1980 local correlation functional(III) (B3LYP) as implemented in Gaussian 16 A.01. [141]
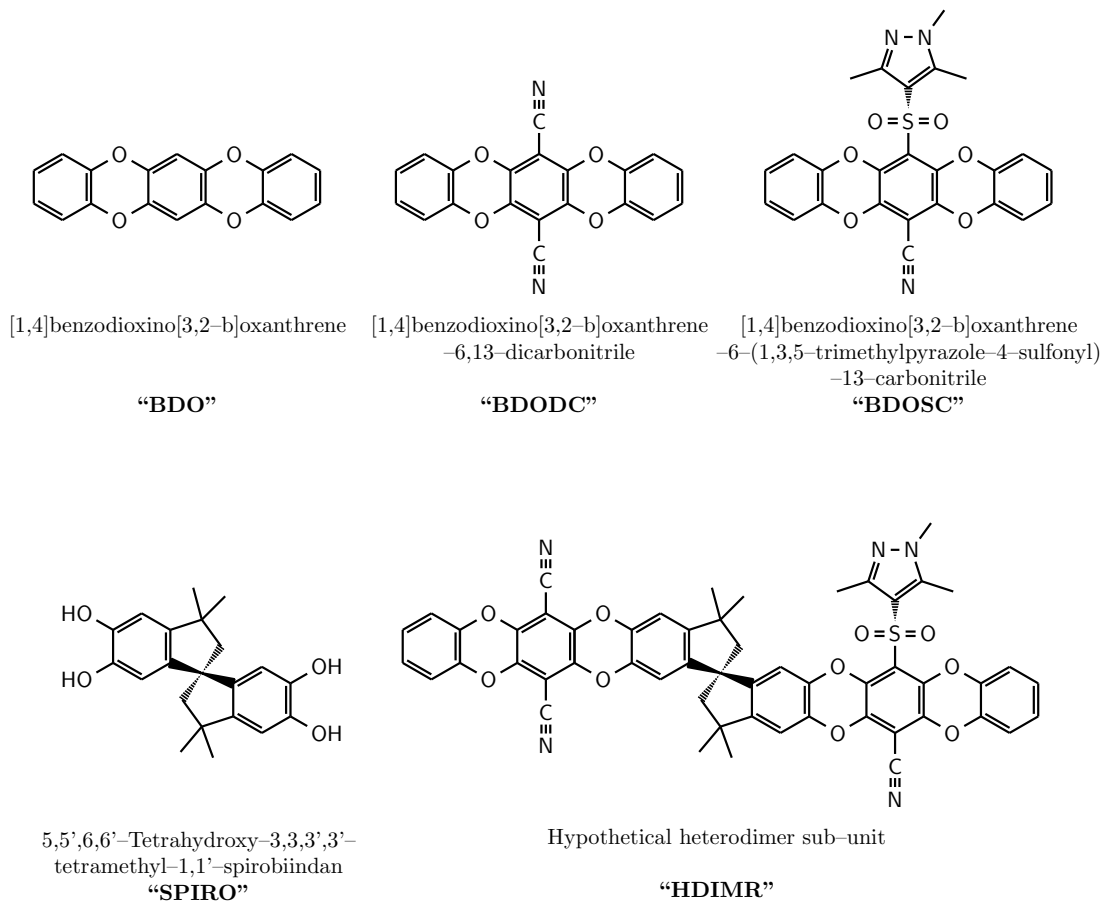
Figure 3.1: Structural outlines of the investigated models with DFT/TD–DFT studies.

comparison purposes. The integral equation formalism of the polarizable continuum model (IEFPCM) was used to accounted for the chloroform solvent effect. XYZ–coordinates of the ground and excited states' equilibrium geometries of all investigated models can be found in Section C.1.

For reference purposes, ionization potential (IP) values of the four investigated models were also calculated. Calculations of the IPs started with locating the S_0 equilibrium geometry of each model in the gas phase. These optimized models did not carry any charge, i.e. they were neutral. Then energy of the positively charged model at the neutral equilibrium geometry was calculated. IPs represented the subtraction between the energy of the positively charged form and the neutral form.

3.2.2 POST–PROCESSING AND VISUALIZATION

Python 3.x scripts were employed to process the DFT calculation output files and extract the information presented in this work. These scripts utilized functions from numpy [93] and cclib [142] libraries. Script B.17 and Script B.18 were used to calculate the IP values and extract the vertical excitation energies, respectively. Molecular geometries, MO isosurfaces, and electrostatic potential map (ESP) isosurfaces for the investigated models were visualized using Gabedit software [143]. Finally, all data, analysis, and molecular visualization plots were constructed in python 3.x using Matplotlib [99] library.

3.3 EVALUATION OF THE LEVEL OF THEORY SELECTED

The hybrid functional B3LYP [114, 115, 119, 122] was primarily used for DFT and TD–DFT calculations in conjunction with 6–31G(d) basis set. However, a brief comparative evaluation was needed to assess the validity of the results as well as the computational cost compared with compositions of larger basis sets and other functional variations. Singlet vertical excitation energies were the only experimentally available parameter to benchmark these calculations. Each comparison group presented here utilized the same types of computational resources available from the CRC.

3.3.1 BASIS SET

Six different basis sets with various sizes, some included diffuse functions, were compared. The calculation jobs utilized B3LYP functional. The basis sets were tested using the two isolated chromophore models, BDODC and BDOSC, that constituted the investigated macromolecules. Each job started with a S_0 geometry optimization, confirmed to be a real minimum by frequency calculations. The located equilibrium geometries were then used by single–point, TD–DFT, singlet vertical excitation

calculation to locate the first singlet excited state (S_1). Two criteria were assessed from the results of these TD–DFT calculations. The first was the single–CPU run time in hours shown in Figure 3.2a. The second was the S_1 vertical excitation energy estimation error depicted in Figure 3.2b. The energy estimation errors were calculated using the ultraviolet–visible absorption (UV–VIS) analysis presented in Section 4.1.2. Experimental excitation energy of BDOSC were indirectly estimated using the UV–VIS data analysis of BDODC and the HTRMR.
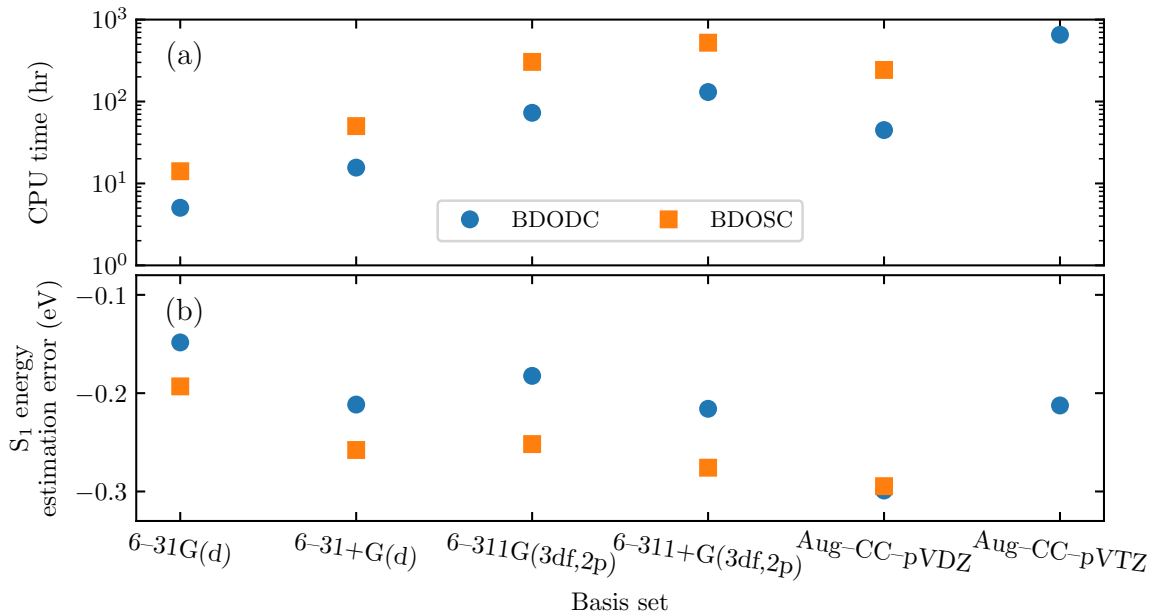
Figure 3.2: Basis sets evaluation summary. (a) Single–CPU run time in hours. The y–axis was drawn on a logarithmic scale. (b) Estimation error of the S_1 excitation energy. The negative sign indicated underestimation.

Predictably, a near exponential increase in the computational cost emerged when comparing the size of these basis sets. Most notably, triple-ζ basis sets, 6–311+G(3df,2p) and aug-cc-pVTZ. The BDOSC's job of the latter failed to converge within the 1–week limit of a continuous calculation run. As for the second criterion, the increase in basis set size decreased the overall S_1 vertical excitation energy estimates. This observed trend was likely due to the decrease in the total energy estimates as the size of the basis set increased. The observed correlation between the basis set size and

the total energy estimation was described by the variational principle [144]. However, the overall standard deviation among all S_1 energy estimates was ~0.046 eV. Such variation do not justify the increase in computational cost associated with using a larger basis set. Therefore, 6–31G(d) basis set was deemed sufficient to study these systems of chromophores and macromolecules.

3.3.2   FUNCTIONAL

The validity of the results produced by the functional B3LYP were evaluated from an electronic transition standpoint. The evaluation explored variations of the Hartree–Fock–to–Slater exchange–correlation ratio (XC) within the framework of the hybrid B3LYP. [113, 114, 119, 122, 123] Namely, XC 0:100 (=BLYP[†]), XC 20:80 (=B3LYP), XC 40:60, XC 60:80, and XC 80:20. What was being tested in these calculations was the vertical excitation energy of the individual chromophore moieties within the environment of the macromolecule. Therefore, these tests employed the representative model of the macromolecules, the HDIMR. These DFT and TD–DFT calculations employed 6–31G(d) as the basis set. They utilized the S_0 equilibrium geometry predicted using B3LYP and confirmed with frequency calculations. The excitation energy estimates were compared to the experimentally determined excitation energies from the decomposition analysis of UV–VIS shown in Section 4.1.2. Estimation errors at each functional and correction method variation were summarized in Figure 3.3.

The increase in the exchange contribution within the BLYP functional prompted an increase in the S_1 energy estimates of both chromophores. However, when considering the energy error estimates, B3LYP produced the highest accuracy at an underestimation error of ~0.11 eV. The second lowest estimation error was produced by BLYP(XC 40:60) at ~0.36 eV. The rest of the functional variations showed estimation errors that ranged from 0.57 eV to 1.18 eV. Since B3LYP showed the highest

---

[†]Becke's 1988 exchange functional with Lee, Yang, and Parr correlation functional (BLYP) as implemented in Gaussian 16 A.01. [141]
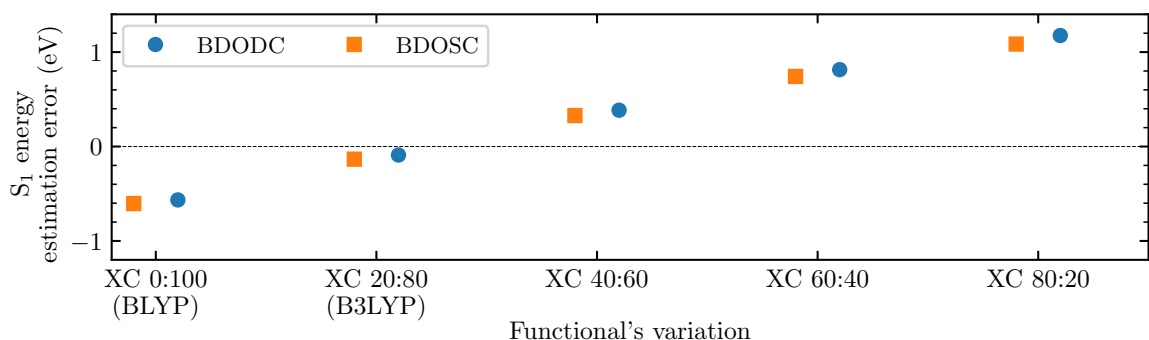
Figure 3.3: Functional evaluation summary of the singlet excitation energies of BDODC and BDOSC within the HDIMR framework. Initial S_0 equilibrium geometry was estimated by B3LYP. "XC" is Hartree–Fock to Slater exchange–correlation ratio.

accuracy, it was adopted as the DFA of choice to study these chromophores and macromolecules.

TD–DFT utilization of the B3LYP functional is known to have an over–polarisation problem that leads to spurious charge–transfer states (CTSs) and large errors in their transition energy estimates. [145–149] This limitation was not addressed in this work. The designated CTS discussed in the following chapters may be a result of this error despite various evidence of its existence drawn from the experimental data. Adamo and Jacquemin recommended the use of range–separated hybrid functionals such as CAM–B3LYP and ωB97X–D to overcome this limitation. [149] Further computational modeling using the recommended functionals is required to resolve this limitation.

Bulk solvation effects are one of the known detriments to the TD–DFT calculations of excited state geometries and transition energies. [149, 150] Mennucci and co–workers demonstrated the extent of these effects on several hybrid functionals. [150] In their study, B3LYP hybrid functional showed an error range of $\pm 0.27\,\text{eV}$. Since the purpose of this study is the general description of geometrical parameters and estimations of electronic transition energies an error range of this magnitude is acceptable. Adamo and Jacquemin noted that the IEFPCM scheme used here lacks description of specific solute–solvent interactions such as hydrogen bonds, ion

pairing, and π–interactions. [149] However, none of these interactions is expected to be prominent in the solvent–solute combination of this work.

3.4 GEOMETRIES AND CHARGE DISTRIBUTION

The primary goal of this theoretical part was understanding the nature of the electronic transitions of these chromophores. The influence of the substituents on the backbone of these chromophores was also needed some consideration. Therefore, the molecular geometries of all four models at equilibrium with respect to various electronic states were compared. However, due to the high complexity of these models, an atom numbering convention was devised to allow for clear and consistent referencing in the text, figures, and tables. This numbering convention was depicted in Figure 3.4 and was used throughout this document.

3.4.1 GEOMETRIES OF THE ISOLATED CHROMOPHORES

The principle backbone of all chromophores in this study was a linearly–fused, pentacyclic, six–membered ring heterocycle, see BDO in Figure 3.5. Its polyaromatic hydrocarbon equivalent was Pentacene, with oxygen atoms replacing the *para*–carbons in the second and fourth rings, $R_{2/9}$ and $R_{4/11}$, on positions: 6/20, 48/35, 10/24, and 44/31. This backbone, can also be described as an Oxanthrene, known as Dibenzo–*p*–dioxin, linearly–fused to a 1,4–Benzodioxin. The S_0 equilibrium geometry of both Oxanthrene and 1,4–Benzodioxin were found to be planar[151–153], by extension BDO was also expected to be planar.

These aforementioned bicyclic and tricyclic dioxins were classified as antiaromatic as they contained $[4n]\,\pi$ electrons [154]. In contrast, BDO at $26\,\pi$ electrons (Hückel's rule of $[4n+2]\,\pi$) would be classified as aromatic [7, 155–157]. The planarity and by extension the π–conjugation, of all of these dioxin–containing heterocycles were attributed to an effective overlap between the $2p_z$ orbital of the oxygen atom and
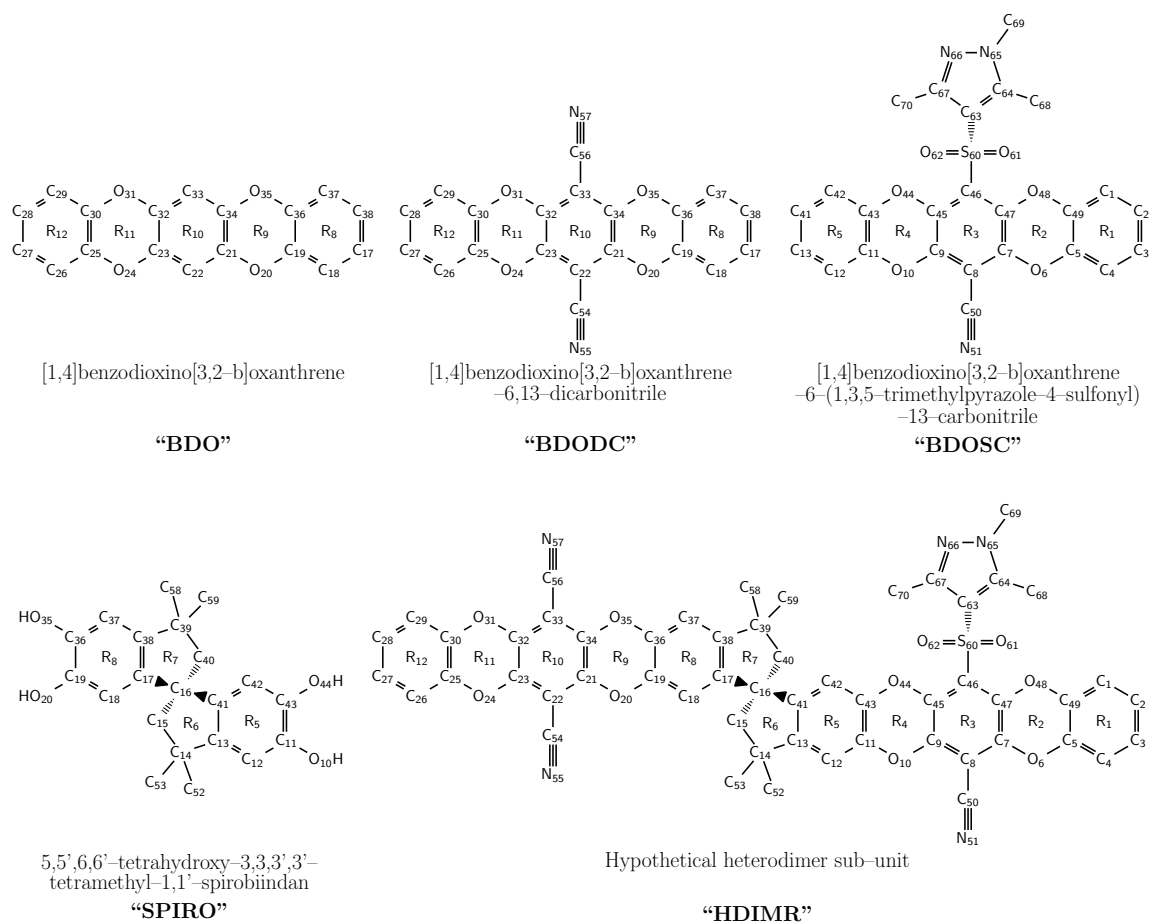
Figure 3.4: Atom numbering convention for the models studied with DFT/TD–DFT.

the π_{CC} of the neighboring benzene rings [158]. This overlap facilitated the electron delocalization across the heterocyclic system that allowed enough conformational stabilization for the planarity to be favored [7, 158–160]. However, it was noted that this type of delocalization leading to the planarity was quite fragile. The reports indicated that the energy barriers between the planar and distorted the dioxin ring through folding or puckering were low [156, 158].

The ground and excited states properties of both bi– and tricyclic dioxin components of BDO have been discussed extensively in the literature [7, 156, 160–169]. This was not the case for the backbone investigated here, i.e. BDO. As such, these studies can provide a foundation from which extrapolation can be made to interpret the results obtained in this work.

SINGLET GROUND STATE

The S_0 equilibrium geometry of BDO predicted by DFT was planar. The dihedral angles of all rings in the backbone sat at a flat 0° or 180°. See Figure 3.5 and Table 3.1. Optimization of the chromophore with symmetry restriction at D_{2h} point group resulted in identical total energy compared to the unrestricted optimization. The outermost rings, R_8 and R_{12}, showed typical Catechol ring geometrical parameters [170, 171]. Their C–C bond lengths averaged 1.395 ± 0.004 Å and their C–C–C bond angles averaged $119.99 \pm 0.12°$. The outer vertical C–C bond, 38–17, was shorter than its inner counterpart, 19–36, by $\sim$0.002 Å. In agreement with the expected bond lengths influenced by the cross–conjugation observed in fused aromatic polycycles [172]. On the other hand, the outer horizontal C–C bonds, 37–38 and 17–18, exhibited a slight elongation by $\sim$0.007 Å compared to their inner counterparts, 36–37 and 18–19. Distortions of these bond lengths were indicative of the heteroatoms' lone–pair delocalization over the π–system of the neighboring rings [7, 158].

The central ring, R_{10}, showed a slightly shorter C–C bond lengths average at 1.393 ± 0.003 Å. Its bond lengths were identical on both sides. Bonds 21–21, 22–23, 32–33, and 33–34, were estimated at $\sim$1.3914 Å and bonds 21–34 and 23–32 at $\sim$1.3971 Å. This similarity was attributed to the symmetrical two–sided oxygen atom lone–pairs delocalization over the π–system of this ring compared to the loop–sided effect exerted on the outer rings, R_8 and R_{12}. The geometrical parameters of the heterocycles', R_9 and R_{11}, were comparable to those of the unsaturated Dioxin ring more so than the saturated Dioxane ring [152, 153]. C–O bond lengths were relatively consistent at an average of 1.382 ± 0.001 Å. All C–O–C bond angles were estimated at 116.15°. Comparatively, crystal structures of various substituted planar Dioxins showed a C–O bond lengths average of 1.389 ± 0.011 Å. The crystal structure of the boat conformer of Dioxane showed an average C–O bond lengths of 1.425 ± 0.002 Å [173]. Similarly, the average of C–O–C bond angles of planar Dioxins was $117.43 \pm 1.45°$ and that of

Table 3.1: Truncated list of geometrical parameter values of the isolated chromophores, BDO, BDODC, and BDOSC, predicted by DFT. Atom numbering convention can be found in Figure 3.4. Full list of parameter values for all models can be found in Table C.3.

No.	ring label	Geometrical Parameters Length, Angle, Dihedral (Å,°) BDO/DC	BDOSC	isolated BDO S_0	S_1	isolated BDODC S_0	S_1	isolated BDOSC S_0	S_1
1		34–35	47–48	1.3803	1.3548	1.3647	1.3729	1.3705	1.3760
2		35–36	48–49	1.3828	1.3709	1.3900	1.3662	1.3883	1.3683
3		19–36	05–49	1.3995	1.4209	1.3955	1.4087	1.3943	1.4050
4		19–20	05–06	1.3828	1.3709	1.3900	1.3662	1.3872	1.3681
5		20–21	06–07	1.3803	1.3548	1.3647	1.3729	1.3668	1.3727
6		36–19–20	49–05–06	121.85	120.87	121.44	120.94	120.84	120.73
7	R2,R9	19–20–21	05–06–07	116.15	118.64	116.40	117.65	116.28	117.68
8		20–21–34	06–07–47	121.98	120.48	122.15	121.39	122.54	121.95
9		21–34–35	07–47–48	121.98	120.48	122.15	121.39	120.51	120.34
10		34–35–36	47–48–49	116.15	118.64	116.40	117.65	116.80	118.22
11		35–36–19	48–49–05	121.85	120.87	121.44	120.94	121.21	120.99
12		35–36–19–20	48–49–05–06	000.00	000.00	000.00	-000.00	-000.86	-000.11
13		35–34–21–20	48–47–07–06	000.00	000.00	-000.00	-000.00	000.76	-000.36
14		36–35–20–21	49–48–06–07	180.00	180.00	-179.99	-179.99	168.82	178.03
15		33–34	46–47	1.3914	1.3876	1.4062	1.4260	1.4084	1.4258
16		21–34	07–47	1.3971	1.4532	1.3930	1.3832	1.3937	1.3873
17		21–22	07–08	1.3914	1.3876	1.4063	1.4260	1.4026	1.4217
18		22–23	08–09	1.3914	1.3876	1.4062	1.4260	1.4014	1.4249
19		23–32	09–45	1.3971	1.4532	1.3930	1.3832	1.4010	1.3858
20		32–33	45–46	1.3914	1.3876	1.4062	1.4260	1.4089	1.4296
21	R3,R10	34–21–22	47–07–08	120.10	120.18	119.98	122.52	120.08	122.17
22		21–22–23	07–08–09	119.78	119.63	120.02	114.95	119.64	114.83
23		22–23–32	08–09–45	120.10	120.18	119.98	122.52	120.60	122.78
24		23–32–33	09–45–46	120.10	120.18	119.98	122.52	119.70	122.19
25		32–33–34	45–46–47	119.78	119.63	120.02	114.95	119.39	114.44
26		33–34–21	46–47–07	120.10	120.18	119.98	122.52	120.55	122.90
27		33–34–21–22	46–47–07–08	000.00	000.00	000.00	000.00	-000.35	000.27
28		33–32–23–22	46–45–09–08	000.00	000.00	000.00	000.00	-000.28	-000.34
29		34–33–22–23	47–46–08–09	180.00	180.00	180.00	-179.99	-179.13	-173.04
30		23–24	09–10	1.3803	1.3548	1.3647	1.3729	1.3661	1.3770
31		24–25	10–11	1.3828	1.3709	1.3900	1.3662	1.3873	1.3622
32		25–30	11–43	1.3995	1.4209	1.3955	1.4087	1.3929	1.4090
33		30–31	43–44	1.3828	1.3709	1.3900	1.3662	1.3848	1.3601
34		31–32	44–45	1.3803	1.3548	1.3647	1.3729	1.3665	1.3772
35		32–23–24	45–09–10	121.98	120.48	122.15	121.39	122.65	121.95
36	R4,R11	23–24–25	09–10–11	116.15	118.64	116.40	117.65	116.84	117.87
37		24–25–30	10–11–43	121.85	120.87	121.44	120.94	120.73	117.87
38		25–30–31	11–43–44	121.85	120.87	121.44	120.94	121.56	121.04
39		30–31–32	43–44–45	116.15	118.64	116.40	117.65	117.66	118.64
40		31–32–23	44–45–09	121.98	120.48	122.15	121.39	120.25	119.88
41		31–32–23–24	44–45–09–10	000.00	000.00	-000.00	000.00	-000.74	-000.96
42		31–30–25–24	44–43–11–10	000.00	000.00	-000.00	-000.00	000.07	-000.11
43		32–31–24–25	45–44–10–11	180.00	179.99	-179.99	-179.99	175.38	176.67
44		22–54	08–50			1.4270	1.4012	1.4274	1.4025
45		54–55	50–51			1.1628	1.1737	1.1628	1.1734
46		33–56	46–60			1.4270	1.4012	1.8334	1.7972
47		56–57	60–61			1.1628	1.1737	1.4717	1.4804
48			60–62					1.4679	1.4754
49			60–63					1.7555	1.7639
50		21–22–54	07–08–50			119.98	122.52	120.16	122.56
51	R3,R10	22–54–55	08–50–51			179.99	179.99	179.89	178.89
52	Subst-	34–33–56	47–46–60			119.98	122.52	117.85	118.86
53	ituents	33–26–57	46–60–63			179.99	179.99	103.83	105.09
54			61–60–62					118.38	118.15
55		34–21–22–54	47–07–08–50			179.99	-179.99	-179.38	-176.42
56		21–34–33–56	07–47–46–60			179.99	-179.99	177.86	151.80
57			47–46–60–63					067.58	079.72
58			47–46–60–61					-048.81	-035.70
59			47–46–60–62					-177.48	-165.37
60			46–60–63–64					-115.79	-119.58

60

the Dioxane's boat conformer was 109°. Aggregated list of values for the geometrical parameters of the aforementioned Dioxin and Dioxane crystal structures can be found in Table C.1.
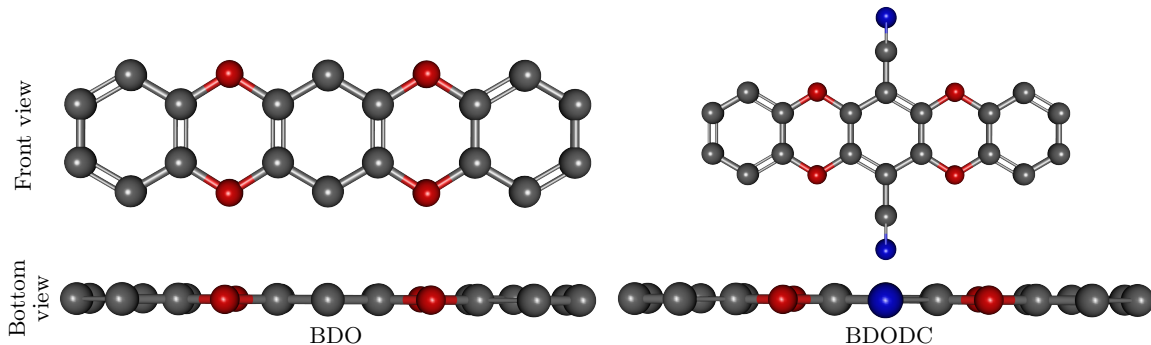
Figure 3.5: DFT–predicted singlet ground state (S_0) equilibrium geometry of BDO and BDODC in the isolated form. Structural outlines and atom numbering can be found in Figure 3.4. Values of geometrical parameters can be found in Table 3.1 and Table C.3. Hydrogen atoms were removed for clarity.

Similar to BDO, the S_0 equilibrium geometry of BDODC was planar, see Figure 3.5 and Table 3.1. Its optimization with symmetry restriction at D_{2h} point group also resulted in identical total energy compared to the unrestricted optimization. The predicted geometrical parameters of BDODC were in good agreement with its previously reported crystal structure [13]. The bond lengths of the carbonitrile group, 22–54 and 54–55, were comparable to their counterparts in the crystal structures of BDODC and Pentacene-6,13-dicarbonitrile [13, 174]. However, these lengths deviated from values reported in the crystal structure of p-dicyanobenzene [175]. The aforementioned agreement indicated that the conjugation across the heterocycles and its influence on the backbone and the carbonitrile substitute was comparable to the fully conjugated Pentacene.

The addition of the two carbonitrile groups to the central ring prompted few mild bond elongations to the backbone of BDODC compared to the backbone of BDO described earlier. Horizontal bonds between atoms 31 to 35, and between atoms 20 to 24 were elongated by ~ 0.015 Å on average. These elongations were most likely

61

due to the influence of the electron–withdrawing group (EWG), carbonitrile, exerted on the π–conjugation within the three central rings, R_9, R_{10}, and R_{11}. Depletion of the π–electrons from these rings resulted in a decrease in their bond character which manifested as elongations in the noted bond lengths. The extent of this elongation also implied that the EWG effect exerted by the carbonitrile groups on the backbone π–system was limited to these three central rings. The limited extent of conjugation was likely due to the type of conjugation expected in these π–systems, i.e. cross–conjugation. In this specific case, the cross–conjugation helped extent the π–cloud across all five rings. However, it introduced a semi–isolation effect between the two outer rings and the three central rings.
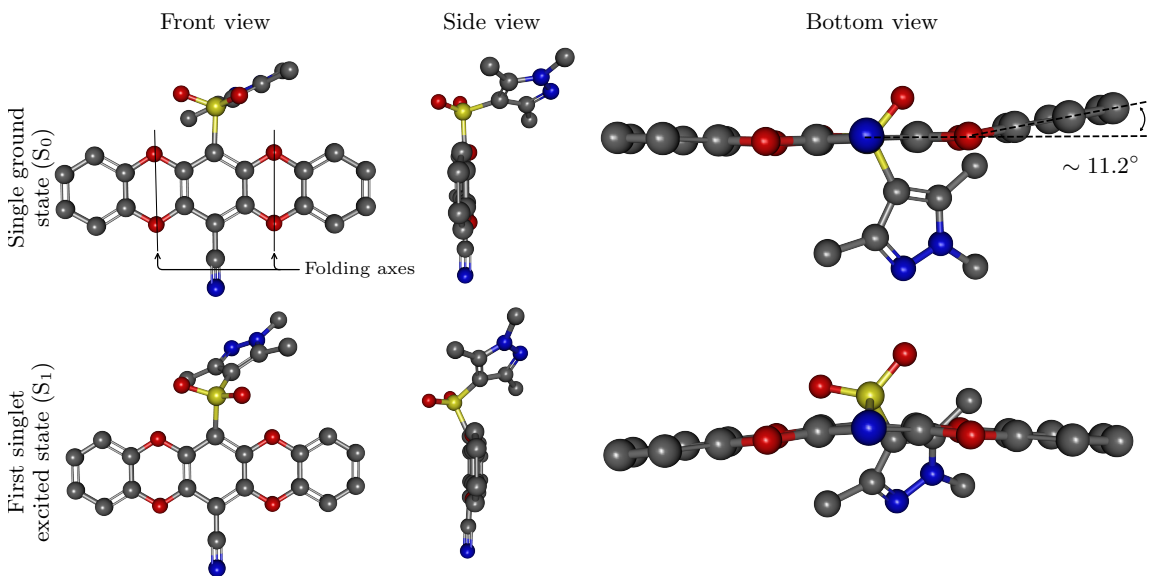
Figure 3.6: DFT–predicted singlet ground state (S_0) and first singlet excited state (S_1) equilibrium geometries of BDOSC in the isolated form. Structural outlines and atom numbering are listed in reffig:r-dft-gm-lbl. Values of geometrical parameters were listed in Table 3.1 and Table C.3. Hydrogen atoms were removed for clarity.

In contrast, the S_0 geometry of BDOSC predicted by DFT was non–planar, see Figure 3.6 and Table 3.1. The replacement of one of the carbonitrile groups with a pyrazol substituted sulfonyl group prompted some profound distortions to the backbone of this chromophore. These distortion included elongations of the horizontal

bonds between atoms 44 to 48, and between atoms 6 to 10, similar to the case of BDODC. However, these bond elongations were asymmetrical. The right–hand side C–O bonds, 47–48 and 6–7, were elongated by $0.0098\,\text{Å}$ and $0.0135\,\text{Å}$, respectively. While the left–hand side C–O bonds, 44–45 and 9–10, were elongated by $0.0138\,\text{Å}$ and $0.0142\,\text{Å}$, respectively. The central ring, R_3, experienced bond length elongations differently than its BDODC counterpart, R_{10}. Bonds closer the carbonitrile group, 7–8 and 8–9, were elongated by $0.0112\,\text{Å}$ and $0.01\,\text{Å}$, respectively. While the ones closer to the sulfonyl group, 45–46 and 46–47, were elongated by $0.0175\,\text{Å}$ and $0.017\,\text{Å}$, respectively. Finally, the largest distortion in the backbone was a folding–like deformity appeared around the O–O axis within both dioxin rings, see the "Front view" and "Bottom view" of the "singlet ground state" in Figure 3.6. Both sides folded away from the pyrazol substituted sulfonyl group in an asymmetrical fashion. The right hand side folding angle, 49–48–6–7, was $\sim$11.2° while its left–hand counterpart 45–44–10–11, was $\sim$4.6°. The observations listed above revealed two types of disparities in the observed distortions of the backbone of BDOSC. The first was between the carbonitrile side and the sulfonyl side, designated as "vertical disparity". The second was between the left– and right–hand sides of the backbone, denoted as "horizontal disparity". It was theorized that the cause of these disparities was a combination of the conformational orientation of the substituents and their electronic interactions with the backbone. Therefore, a closer inspection into these factors was conducted.

The backbone folding of BDOSC was oriented away from the pyrazol group. This indicated that the steric hindrance may have played a rule in the shaping of the backbone, see the "Bottom view" of the "singlet ground state" in Figure 3.6. The right–hand side, closer to the pyrazol ring, and its substitiuents, folded by a larger degree $\sim$11.2° compared to the $\sim$4.6° on the left–hand side. However, another observation can be drawn from the orientation of the oxygen atoms of the sulfonyl group. These two oxygen atoms oriented so that each fell within the plane of either the central

ring or the pyrazol, see the "Bottom view" and "Front view" of the "singlet ground state" in Figure 3.6, respectively. This was unfavorable from a steric perspective. It also reduced the extent of conjugation between these two aromatic rings through the sulfonyl group. Woollins and co–workers noted that the maximum conjugation between an aromatic ring and its sulfonyl substituent occurred when the angle between that ring and the C–S–C plane equaled 90° [176]. This certainly was not the case here. The sulfonyl angles with respect to the pyrazol ring and the central ring were −115.79° and 67.58°, respectively, entries 57 and 60 in Table 3.1. Woollins argued that a soft H···O bonding was the reason behind this orientation [176]. In their case, this H···O bonding would form between an *ortho*–aryl hydrogen and the in–plane sulfonyl oxygen. However, an *ortho*–aryl hydrogen was not available in neither of the cases here. Woollins and co–workers also proposed a possible weak C···O interaction in the absence of an *ortho*–aryl hydrogen [176]. This was likely the reasoning behind the unusual orientation of the sulfonyl oxygen atoms in BDOSC. Charge delocalization through this interaction would result in a minor charge disparity between the right– and left–hand carbons, 45 and 47, respectively. The charge depleted side would promote strong interaction with its corresponding dioxin oxygen atom, bringing its side of the backbone closer to planarity. This was observed in the backbone of BDOSC, ∼4.6° versus ∼11.2° for the right– and left–hand sides, respectively. Both steric and electronic interactions explained the overall horizontal disparity mentioned earlier.

The vertical disparity in the backbone can be explained using the strength difference in the EWG effect between the sulfonyl and the carbonitrile groups. Sulfonyl and sulfonic acid groups were expected to exhibit stronger EWG effect compared to the carbonitrile [177, 178]. The pK_a values[‡] of *p*–Phenylsulfonylphenol and *p*–Hydroxybenzonitrile were reported at 7.35 and 7.79, respectively. These values further supported the notion that the sulfonyl group can exert more EWG effect on its side.

[‡]Listed pK_a values were calculated using Advanced Chemistry Development (ACD/Labs) Software V11.02, these values were extracted manually from the SciFinder database as of January 15, 2020.

This effect was expected to extend throughout the three central rings of the backbone due to their conjugation. The imbalance in the EWG effect manifested as a depletion of the π–cloud on the stronger EWG side. The depletion of the π–cloud created smaller bond order values that corresponded to longer C–C bonds.

FIRST SINGLET EXCITED STATE

The S_1 equilibrium geometry of BDO chromophore exhibited minor distortions from its S_0 equivalent. List of the relevant geometrical parameters can be found in Table 3.1 on page 60. The chromophore's backbone remained planar. However, bond length shrinkage of all C–C bonds along the short axis were observed, with an overall reduction average of 0.0337 ± 0.0174 Å. The most severe of these reductions were bonds 21–34 and 23–32 shared between the central ring, R_{10}, and the heterocycles, R_9 and R_{11}, both of which decreased by 0.0561 Å. Additionally, the heterocycles showed elongation of all C–O bonds, expansion of all O–C–C bond angles, and shrinkage of all C–O–C bond angles. C–O bonds connected to the central ring, 34–35, 20–21, 23–24, and 31–32 expanded by 0.0255 Å, while the ones connected to the terminal rings expanded by 0.0119 Å. All the C–O–C angles decreased by $\sim 2.5°$, and the O–C–C angles expanded by $\sim 1.5°$ on the central ring side, and $\sim 1°$ on the terminal rings side. These distortions are a result of the electronic transition that depopulated an occupied MO dominated by bonding character and populated an unoccupied MO dominated by anti–bonding character. Such transition prompted a shuffle in the bond character of the bonds associated with these MOs, which manifested as bond distortions.

Compared to BDO, the S_1 equilibrium geometry of the homosubstituted chromophore, BDODC, exhibited a different set of distortions from its S_0 equivalent. Relevant geometrical parameters were also listed in Table 3.1. The S_1 geometry of this chromophore also remained planar. The terminal rings, R_8 and R_{12}, were virtually unperturbed. However, C–C bonds within the central ring, R_{10}, were noticeably

distorted. Bonds parallel to the long axis, 21–22, 22–23, 32–33, and 33–34 shrunk by ~ 0.02 Å. Bonds along the short axis, 34–21, and 23–32 were elongated by ~ 0.01 Å. Additionally, horizontal C–C–C bond angles, 32–33–34 and 21–22–23, expanded by $\sim 5°$ and the rest within the ring shrunk by $\sim 2.5°$. These changes were noticeably inconsistent with the geometrical changes exhibited by the S_1 of BDO.

Within the heterocycles, R_9 and R_{11}, C–O bond lengths were distorted asymmetrically. C–O bonds on the terminal side were elongated by ~ 0.024 Å and the ones on the central ring side shrunk by < 0.009 Å. Contrary to the central ring, C–C bonds along the short axis within both heterocycles, and terminal benzene rings, shrunk by < 0.013 Å. In these rings, C–O–C bond angles expanded by $\sim 1.25°$, while O–C–C angles expanded by $\sim 0.75°$ on the central ring side, and $\sim 0.5°$ on the terminal rings side. The overall C–C bond distortions along the short axis of all rings were less dramatic than the ones observed in BDO. The maximum recorded distortion in these bonds was < 0.013 Å. Moreover, the carbonitrile C–C bonds, 22–54 and 33–56, were elongated by ~ 0.026 Å, while C–N bonds, 54–55 and 33–56, shrunk by ~ 0.011 Å. Unlike the BDO, the unoccupied MO associated with this transition in BDODC was localized over the central and the heterocycle rings, as well as the carbonitrile substituents. The MO localization explained the dramatic differences of geometrical distortions associated with the S_0 to S_1 transition between BDO and BDODC.

Similar to BDODC, the S_1 equilibrium geometry of the heterosubstituted BDOSC exhibited distortions concentrated on the substituents as well as the central and heterocycle rings, R_2, R_3, and R_4. The list of relevant geometrical parameters can be found in Table 3.1. In its S_1, the geometrical parameters of BDOSC showed disparities similar to the ones discussed in Section 3.4.1. C–O bonds on the terminal rings' side were asymmetrically elongated ~ 0.02 Å and 0.025 Å on the right– and left–hand sides, respectively Their counterparts on the central ring side shrunk by ~ 0.005 Å and 0.01 Å, respectively. Moreover, C–O–C bond angles contracted by $\sim 1.4°$ and $1°$ on

the right– and left–hand sides, respectively. All O–C–C bond angle expansions on the right–hand side were under 0.6°, while their counterparts on the left–hand side were under 0.7°. The one exception was the unusual expansion of bond angle 10–11–43 by ∼2.9°.

The original backbone folding pattern of BDOSC nearly disappeared in its S_1 equilibrium geometry. The folding dihedral angles of both heterocycles receded back from ∼11.2° and 4.6° to ∼2° and 3.3°, respectively. A butterfly–like folding took its place where the central ring folded in the direction of the pyrazol group by ∼6.1°. See "Bottom view" of S_1 in Figure 3.6. In addition to the butterfly folding, the central ring showed disproportional C–C bond elongation along the short axis where bonds 7–47 and 9–45 stretched by ∼0.006 Å and 0.015 Å, respectively. Length of bonds 7–8, 8–9, 45–46, and 46-47 decreased by 0.019 Å, 0.024 Å, 0.021 Å and 0.017 Å, respectively. The highest shrinkage on the left–hand of the carbonitrile side was 8–9, and the lowest on the right–hand sulfonyl side was 46–47.

The C–C bond distortions of BDOSC along the short axis were similar to the ones observed in BDODC. Outer bonds, 2–3, 5–49, 11–43, and 13-41, shrunk by ∼0.007 Å, 0.011 Å, 0.016 Å and 0.010 Å, while central bonds, 7–47 and 9–45, expanded by ∼0.006 Å and 0.015 Å, respectively. Noticeably, these bond distortions were symmetrical in BDODC and asymmetrical in BDOSC, keeping in line with aforementioned horizontal disparity. C–S bond of the sulfonyl, 46–60, exhibited an elongation by ∼0.036 Å, while the carbonitrile's C–C bond, 8–50, elongated less prominently by ∼0.025 Å. On the other hand, S–O and S–C bonds of the sulfonyl, 60–61, 6–62, and 60–63, shrunk by ∼0.008 Å and their carbonitrile's counterpart, 50–51, shrunk by ∼0.011 Å. The carbonitrile group remained in the plane of the main backbone while the sulfonyl group moved out of the plane, evident by the increase of the dihedral angle 7–47–46–60 by ∼26°. See "Side view" in Figure 3.5.

As a consequence of these distortions, the oxygen atoms of the sulfonyl that was

67

within the plane of the backbone was forced out of that plane. The other oxygen remained within the plane of the pyrazol, indicating an effective $C \cdots O$ interaction in this particular instance. These changes increased the angle between the backbone and the sulfonyl plane to $\sim 80°$. This angle was much closer to the ideal $90°$ at which the conjugation would be maximized. These changes also allowed the butterfly folding to occur, since it minimized the pyrazol steric hindrance on the backbone. The nature and distribution of these geometrical distortions were consistent with the nature of the electronic transition itself. The unoccupied molecular orbital involved in this transition was delocalized over the backbone heteroatoms and the central ring and its substituents.

3.4.2 GEOMETRIES OF THE HYPOTHETICAL HETERODIMER SUB–UNIT SINGLET GROUND STATE

The principle chromophores, BDODC and BDOSC, largely retained their isolated S_0 geometries within the S_0 of the HDIMR. See "singlet ground state" column in Figure 3.7 and reftab:r-dft-gm-hdimr-par. The only exception being few rotations within the sulfonyl substituent on the BDOSC moiety. The sulfonyl group, as a whole, rotated along the 46–60 bond by $\sim 48°$, placing oxygen atom 61 within the backbone plane instead of 62. As a consequence, the folding pattern of the backbone of BDOSC was reversed. Folding across the axis 44–10 increased to $\sim 9.3°$ and the folding across the axis 48–6 shrunk to $\sim 3.7°$. An additional rotation along the 60–63 bond by $\sim 127°$ occurred. This rotation placing the oxygen atom 62 within the pyrazol ring plane in order to maximize the second $C \cdots O$ interaction. These changes were not expected to impact the energy of BDODC moiety compared to its isolated form.

The presence of the SPIRO linker in the HDIMR introduced a diagonal distance of $11.4 \, \text{Å}$ between the centers of the two chromophores. With respect to this SPIRO linker, the most influential geometrical parameter in this sub–structure was the

dihedral angle between the two benzene rings directly adjacent to the spiro center, R_5 and R_8. Experimentally, this angle was extracted from X–ray crystallography measurements on several occasions [38, 179–182]. The reported values varied depending on the type and extent of substituents on these benzene rings. These substituents and their interactions also influenced the structure in the lattice and by extension the reported angles. Whitcomb and co–workers reported this angle at 95° for the *bis*–Catechol variety [179]. In contrast, Zhou and co–workers reported a 70.0° for a 1,1'-Spirobiindane-7,7'-diol [180, 183]. Later, Zhang and co–workers reported a value of 71.9° for the combination of Catechol and dibenzo–*p*–dioxane [181]. Finally, Merkel and co–workers reported a value of 77.8° for the *bis*–dibenzo–*p*–dioxane [182]. Whitcomb noted that a strong hydrogen bonding resulted in an eight–Catechol tunnel configuration within the crystal lattice. Restricted configuration like the one Whitcomb noted would be the primary cause of expanding this angle by such large margins compared to the later reports. These reports demonstrated the unlikely high level of flexibility exhibited by this spiro bridge.

McKeown and co–workers recalculated the angle reported by Whitcomb at 85° in order to compare it with their own *bis*–ketone variety at 86° [38]. McKeown likely used different reference points in their calculation efforts resulting in the discrepancy with Whitcomb's reported. Therefore, the Benzene–Benzene angle around the SPIRO center were all recalculated using the reported crystal structures and a variety of reference points to clarify the comparison. Using three alternating carbons from each ring, atoms 42–11–13—37–19–17, the angles were estimated at 95.4°, 69.3°, 72.0° and 78.1°. These estimates were consistent with the reports of Whitcomb, Zhou, Zhang, and Merkel, respectively. In this framework, McKeown's angle was estimated at 92.7°, deviating significantly from the values reported in their study [38]. Notably, the significant variation in the calculated angles from these crystal structures reaffirmed the relative flexibility of the SPIRO bridge. Therefore, establishing a comparative

Table 3.2: Isolated chromophores' geometrical parameters. Atoms numbering convention can be found in Figure 3.4. Full list of parameters for all models can be found in Table C.3.

No.	location label	Geometrical Parameters Length, Angle,Dihedral (Å,°) BDO/DC	BDOSC	SPIRO	isolated SPIRO S_0	BDODC within HDIMR framework S_0	S_1	S_2	BDOSC within HDIMR framework S_0	S_1	S_2	SPIRO within HDIMR framework S_0	S_1	S_2
01	R2,R9	34–35	47–48			1.3643	1.3800	1.3922	1.3667	1.3661	1.3428			
02		35–36	48–49	35–36	1.3684	1.3908	1.3572	1.3753	1.3847	1.3849	1.3803			
03		19–36	05–49	19–36	1.4092	1.3979	1.4208	1.4048	1.3930	1.3929	1.3937			
04		19–20	05–06	19–20	1.3778	1.3911	1.3579	1.3758	1.3871	1.3873	1.3837			
05		20–21	06–07			1.3639	1.3796	1.3916	1.3664	1.3658	1.3420			
06		36–19–20	49–05–06	36–19–20	114.71	121.32	120.81	121.70	120.74	120.73	119.87			
07		19–20–21	05–06–07			116.55	117.77	115.81	116.84	116.86	118.81			
08		20–21–34	06–07–47			122.12	121.40	122.14	122.68	122.67	121.65			
09		21–34–35	07–47–48			122.12	121.39	122.14	120.25	120.23	119.22			
10		34–35–36	47–48–49			116.55	117.79	115.90	117.67	117.71	119.75			
11		35–36–19	48–49–05	35–36–19	119.96	121.31	120.81	121.52	121.58	121.56	120.66			
12		35–36–19–20	48–49–05–06	35–36–19–20	000.00	000.09	000.11	-000.10	-000.11	-000.12	000.00			
13		35–34–21–20	48–47–07–06			000.09	000.11	-000.16	000.66	000.67	000.29			
14		36–35–20–21	49–48–06–07			-179.02	-179.18	172.51	176.33	176.29	179.39			
15	R3,R10	33–34	46–47			1.4063	1.4289	1.4327	1.4091	1.4089	1.4024			
16		21–34	07–47			1.3931	1.3740	1.3657	1.4008	1.4014	1.4270			
17		21–22	07–08			1.4064	1.4287	1.4331	1.4013	1.4011	1.3973			
18		22–23	08–09			1.4063	1.4241	1.4335	1.4027	1.4027	1.4014			
19		23–32	09–45			1.3929	1.3867	1.3680	1.3938	1.3932	1.4161			
20		32–33	45–46			1.4062	1.4241	1.4333	1.4087	1.4087	1.4047			
21		34–21–22	47–07–08			119.96	122.54	121.96	120.58	120.58	120.97			
22		21–22–23	07–08–09			120.01	115.04	116.16	119.67	119.63	118.52			
23		22–23–32	08–09–45			120.00	122.40	121.86	120.09	120.14	120.57			
24		23–32–33	09–45–46			119.98	122.38	121.88	120.48	120.50	121.27			
25		32–33–34	45–46–47			120.00	115.00	116.20	119.44	119.39	118.12			
26		33–34–21	46–47–07			120.01	122.61	121.91	119.69	119.71	120.51			
27		33–34–21–22	46–47–07–08			000.08	000.09	-000.02	000.24	000.24	000.16			
28		33–32–23–22	46–45–09–08			000.04	000.05	-000.03	000.29	000.27	000.56			
29		34–33–22–23	47–46–08–09			179.95	-179.99	-179.42	-178.93	-178.93	-179.92			
30	R4,R11	23–24	09–10			1.3649	1.3718	1.3891	1.3658	1.3666	1.3414			
31		24–25	10–11	10–11	1.3775	1.3898	1.3734	1.3784	1.3878	1.3859	1.3783			
32		25–30	11–43	11–43	1.4093	1.3955	1.4031	1.4005	1.3967	1.3974	1.4022			
33		30–31	43–44	43–44	1.3687	1.3899	1.3735	1.3785	1.3897	1.3882	1.3796			
34		31–32	44–45			1.3649	1.3718	1.3891	1.3695	1.3704	1.3455			
35		32–23–24	45–09–10			122.14	121.49	122.32	122.61	122.57	121.60			
36		23–24–25	09–10–11			116.41	117.44	115.87	116.53	116.56	119.01			
37		24–25–30	10–11–43	10–11–43	114.66	121.44	121.05	121.80	120.80	120.78	119.84			
38		25–30–31	11–43–44	11–43–44	119.97	121.43	121.05	121.80	121.19	121.19	120.30			
39		30–31–32	43–44–45			116.40	117.43	115.87	117.04	117.04	119.59			
40		31–32–23	44–45–09			122.15	121.50	122.31	120.59	120.55	119.62			
41		31–32–23–24	44–45–09–10			000.01	000.02	000.04	-000.84	-000.85	-000.23			
42		31–30–25–24	44–43–11–10	44–43–11–10	-000.11	000.00	000.00	-000.01	000.52	000.62	000.14			
43		32–31–24–25	45–44–10–11			-179.93	-179.99	-179.70	170.73	170.47	179.39			
44	R3,R10	22–54	08–50			1.4270	1.4013	1.3989	1.4274	1.4274	1.4270			
45	Subst-	54–55	50–51			1.1628	1.1736	1.1758	1.1628	1.1628	1.1616			
46	ituent	33–56	46–60			1.4270	1.4010	1.3993	1.8325	1.8330	1.8486			
47		56–57	60–61			1.1629	1.1739	1.1755	1.4679	1.4677	1.4649			
48			60–62						1.4716	1.4715	1.4676			
49			60–63						1.7559	1.7559	1.7467			
50		21–22–54	07–08–50			120.00	122.40	121.72	120.19	120.22	120.74			
51		22–54–55	08–50–51			179.86	179.86	179.64	179.87	179.84	179.76			
52		34–33–56	47–46–60			119.96	122.36	121.83	122.69	122.69	123.07			
53		33–26–57	46–60–63			179.93	179.78	179.84	103.86	103.81	103.95			
54			61–60–62						118.39	118.45	119.74			
55		34–21–22–54	47–07–08–50			179.73	179.70	-179.21	-179.81	-179.85	179.69			
56		21–34–33–56	07–47–46–60			-179.98	-179.89	179.40	177.53	177.57	176.18			
57			47–46–60–63						114.21	113.81	118.86			
58			47–46–60–61						-000.69	-001.11	003.46			
59			47–46–60–62						-129.41	-129.85	-124.94			
60			46–60–63–64						116.73	116.75	120.02			
61	Param-			33–46								11.386	11.436	11.176
62	meters			22–08								11.344	11.300	11.215
63	around			42–16–18	085.32							085.44	085.22	084.01
64	the			33–22–08								120.18	120.41	119.56
65	SPIRO			46–08–22								056.65	057.00	054.76
66	bridge			42–41–17–18	-071.28							-071.71	-071.34	-070.17
67				42–41–16–17	-045.73							-045.86	-046.82	-043.13
68				42–41–16—16–17–18*	105.62							105.25	105.61	107.08
69				13–41–16—16–17–38*	107.81							107.53	107.83	107.91
70				42–11–13—37–19–17*	074.53							075.07	074.81	073.14

* Angles 68,69, and 70 were calculated between plane (P_1) containing atoms (A_1,B_1,C_1) and plane (P_2) containing atoms (A_2,B_2,C_2). see text for details.

theoretical reference to the hypothetical HDIMR model was necessary to deduce the influence of the chromophores on the spiro center. The *bis*–Catechol variety, SPIRO in Figure 3.4, was chosen and investigated using DFT at an identical level of theory used for the HDIMR. Using the same framework established earlier, calculated angles around the SPIRO center for the isolated SPIRO as well as the S_0 of the HDIMR produced values of 74.5° and 75.0°, respectively. Which was consistent with Zhang's, and Merkel's reports, and less so with the highly constrained structure of Whitcomb. For a complete list of calculated angles see Table C.2.
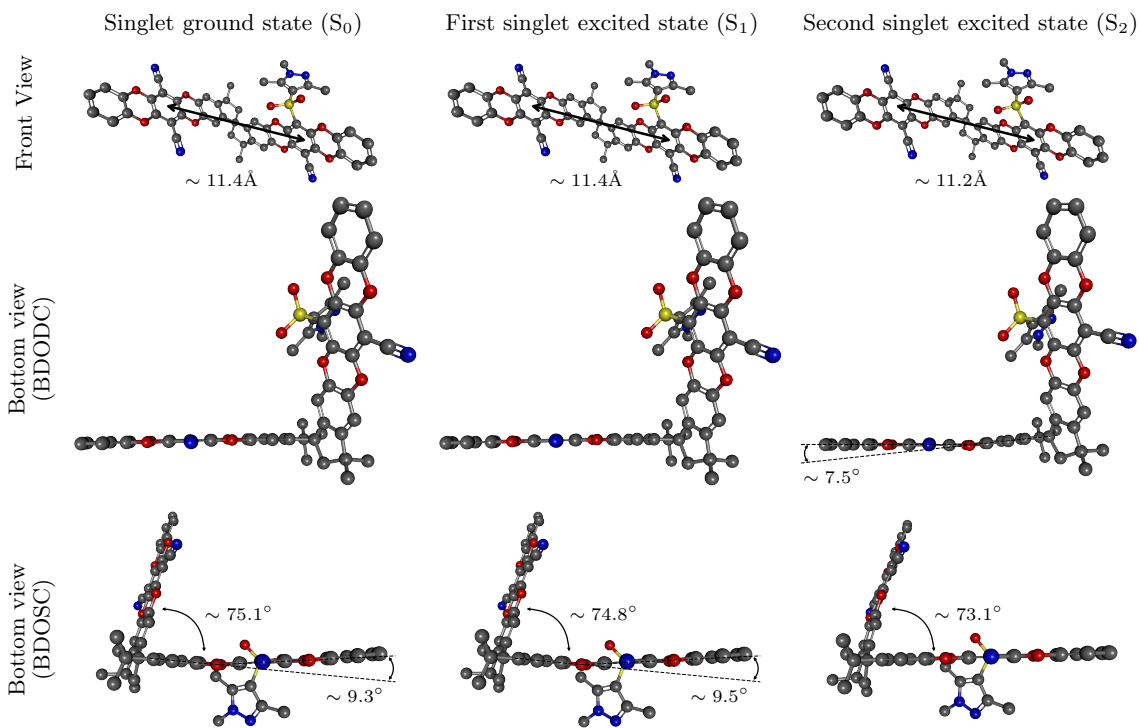
Figure 3.7: Molecular geometries of HDIMR at the equilibrium of its singlet ground state (S_0), first singlet excited state (S_1), and second singlet excited state (S_2). Structure outline can be found in Figure 3.4. Hydrogen atoms were removed for clarity.

Another metric established by Hofmann and co–workers for this geometrical parameter was the dihedral angle, 42–41–16–17, through the SPIRO center [33]. This metric was also used to demonstrate the degree of flexibility around the spiro center by evaluating potential energy curves estimated by molecular dynamics (MD)

simulations and DFT calculations. Hofmann reported an energy minimum at an angle of $-52°$ in vacuum from MD simulation for the infamous homo–polymer, polymer of intrinsic microporosity "1" (PIM–1), [33]. Later, McKeown and co–workers showed the minimum to be at an angle of $-45°$ for the same polymer [40]. Colina and co–workers and Müller and co–workers further evaluated the MD simulation methods [61, 184]. Finally, Jin and co–workers re–evaluated the MD simulation methods and compared them with DFT calculations at low and high levels of theory [185]. Jin reported minima at angle values of $-44.0°$, $-41.6°$ and $-46.5°$ from MD, B3LYP/6–21G, and B3LYP/6–311G+ DFT calculations, respectively [185].

In this work, Hofmann's metric was also evaluated for all crystal structures mentioned earlier as well as the geometries of the SPIRO and the HDIMR predicted by DFT. Whitcomb, Zhuo, McKeown, Zhang, and Merkel crystal structures [38, 179–182] showed angle values of $-57.5°$, $-79.2°$, $-63.0°$, $-43.1°$ and $56.2°$, respectively. While the angles from the DFT–predicted structures of the SPIRO and the HDIMR were $-45.7°$ and $-45.9°$, respectively. When considering the angles listed above, it is clear that Hofmann's metric has a much wider range of variability compared to the calculated Benzene–Benzene dihedral angle mentioned earlier. The large variability indicated that this metric, while useful, was not as representative of the true nature of flexibility exhibited by the inherently rigid spiro center.

FIRST AND SECOND SINGLET EXCITED STATES

The equilibrium geometry of the HDIMR in its S_1, showed in Figure 3.7, exhibited several changes compared to its S_0 equilibrium geometry. The BDOSC moiety of the HDIMR virtually showed no change compared to its S_0 counterpart. However, there were several observable changes in the BDODC moiety of the HDIMR. These observable changes, similar to the ones detailed in Section 3.4.1, indicated a localized excitation within the BDODC moiety. The average disparity of the S_0–to–S_1 changes

between the isolated BDODC and its HDIMR counterpart were 0.004 ± 0.003 Å and $0.07 \pm 0.06°$, for the measured bond lengths and angles, respectively. The chromophore–chromophore distance remained the same at 11.4 Å, while the benzene–benzene angle around the SPIRO center decreased by a negligible $0.3°$.

The second singlet excited state (S_2) equilibrium geometry exhibited higher degree of distortion compared to the S_0 equilibrium geometry. Unlike S_1, the S_2 distortions spread across both chromophore domains, revealing that the nature of this transition involved both moieties in the HDIMR. The geometrical distortions within the BDODC domain exhibited similar trends to those observed in the S_1 equilibrium geometry but to a higher degree of severity. The only exceptions to this severity trend were the outer bonds of the heterocycles, 35–36, 19–36, 19–20, 24–25, 25–30, and 30–31. Additionally, a folding by $\sim 7.5°$ around the 35–20 axis was observed, see Figure 3.7. Such folding was not observed in any other modeled BDODC domain, isolated or bound. Generally, this folding was expected to have unfavorable energetic consequences, as it broke the chromophore's planarity and subsequently the conjugation that stabilized backbone. However, in this particular instance, the folding aided in stabilizing the charge disparity created by these transitions, as discussed in Section 3.5 and Section 3.6. It was worth noting here that the two crystal structures reported by Merkel and co–workers [182] and Zhang and co–workers [181] exhibited similar and more sever folding with angles at $12°$ and $18°$, respectively. However, the reported crystal structure of the isolated BDODC [13] was similar to the isolated model studied here, i.e. had no detectable folding.

On the opposite side of the HDIMR model, the geometrical changes of the BDOSC moiety were unlike those observed in the S_1 of both the HDIMR and the isolated BDOSC, Section 3.4.1. Within the heterocycles, R_2 and R_4, the inner C–O bonds on both sides of the central benzene ring, 6–7, 47–48, 9–10, and 44–45 were elongated by ~ 0.024 Å. Their outer side counterparts closer to the SPIRO bridge,

10–11, and 43–44 were elongated by ∼0.01 Å. The same bonds away from the bridge, 5–6, and 48–49 changed by <0.0045 Å. The central ring, R_3, also showed a different set of distortions compared to the S_1 of the isolated BDODC. Bond contractions along the long axis of the backbone observed in the S_1 of the isolated form were absent here. Additionally, the elongations in the isolated form of the bonds along the short axis, 7–47, and 9–45, turned into contractions by ∼0.026 Å and 0.022 Å, respectively. The most notable change in this domain was the disappearance of the folding pattern around the 10–44 axis. The disappearance of this folding prompted the backbone to revert to a planar conformation. However, the sulfonyl substituent remained in its original conformation with both oxygen atoms, 61 and 62, sitting within the planes of the backbone and the pyrazol, respectively. Finally, the geometrical parameters around the SPIRO bridge exhibited several changes. The calculated benzene–benzene angle shrunk by ∼2° from its S_0 value of 75°. Additionally, the chromophore–chromophore distance shrunk by ∼0.2 Å. These changes indicated that the internal cavity of the HDIMR, and by extension the studied macromolecules, may exhibit some profound transient changes in pours volume upon photoexcitation.

3.4.3   ESTIMATED IONIZATION POTENTIALS

IPs of the four investigated models were estimated using DFT in vacuum at the same level of theory described earlier. In this context, IP was the energy required to completely remove an electron from the highest occupied molecular orbital (HOMO) orbital. It provided a reference point when comparing the ground and excited state energies of the various models, as well as a comparative indicator to these model's affinity to electron gain and loss. IPs of the isolated chromophores, BDO, BDODC, and BDOSC were estimated at 6.529 eV, 7.175 eV and 6.938 eV, respectively. The trend of these IPs indicated that the EWGs, i.e. the sulfonyl and the carbonitrile substituents, generally stabilize HOMOs these chromophores. However, the higher

IP value of BDODC compared to BDOSC was inconsistent with the expected EWG strength of these substituents [177, 178].

Predicted pK_a values[§] of Phenylsulfonylphenol and Hydroxybenzonitrile were reported at 7.17 and 6.87 for the *ortho–* position, 8.58 and 8.58 for the *meta–* position, and 7.35 and 7.79 the *para–* position, respectively. These pK_a values indicated that the sulfonyl group should exhibit a slightly stronger EWG properties than that of the carbonitrile group. The observed discrepancy in these IPs can be attributed to the profound geometrical distortions observed in the backbone of the BDOSC. These distortions, which directly effected the conjugation within the backbone, would destabilize the HOMO of BDOSC counteracting the stabilizing effect of the stronger EWG, the sulfonyl substituent.

The IP of the HDIMR was estimated at 6.517 eV. This lower IP compared to either of the constituting chromophores in their isolated form signaled a degree of destabilization induced by the chromophore–chromophore coupling through the SPIRO bridge. A destabilization like the one demonstrated here can be attributed to the increase in structural rigidity and steric hindrance in the HDIMR compared to the unhindered isolated forms.

3.4.4 ELECTROSTATIC POTENTIAL MAPS

ESPs were employed to evaluate the charge distribution across the topology of the four models investigated in this work. See Figure 3.8 for the isolated chromophores and Figure 3.9 for the HDIMR. Benzene rings in the backbone of BDO, R_8, R_{10}, and R_{12}, followed the general charge distribution behavior of aromatic rings. A partial negative charge was localized within the π–cloud above and below the ring's plane. The opposite partial positive charge was localized throughout the C–C and C–H σ–bonds of the backbone within the ring's plane [186–188].

[§]Listed pK_a values were calculated using Advanced Chemistry Development (ACD/Labs) Software V11.02, these values were extracted manually from the SciFinder database as of January 15, 2020.

The charge distribution of unsubstituted benzene rings were uniform [187, 188]. However, the presence of a substituent disrupted the negative charge localization in the π–cloud through resonance and inductive effects [177]. Phenols and Catechols showcased this disruption when an electron–donating groups (EDGs) was present. In Phenols, there was a mild increase of the electron density in the π–cloud over the *ortho*– and *para*– positions [186, 189]. It was worth noting that the carbon atom bonded to the hydroxyl substituent suffered from a mild electron depletion due to the conductive effect. Resonance structures of phenol were in agreement with these observations [177]. In the Catechol case, The effect was more pronounced. The *ortho*–hydroxyl substituents offered a larger and more uniform electron donation into the π–cloud. However, the two hydroxyl substituents slightly depleted the electron density from the carbon atoms they were bonded to through the conductive effect. Additionally, the relative *ortho*– positioning of both of these hydroxyl groups destabilized the resonance structures in which the negative charge is localized over the substituted carbon atoms. The result was a larger electron density that was skewed away from the two hydroxyl group [190, 191]. The same effect can be seen in both benzene rings in the ESP of dibenzo-*p*-dioxin [192].

Benzene rings of the unsubstituted chromophore, BDO, exhibited similar behavior. Terminal rings, R_8 and R_{12}, showed an ESP that strongly resembled that of the Catechol. This suggested that the oxygen atoms of the dioxin rings acted as an EDGs through resonance. The central ring, R_{10}, showed additional depletion compared to the terminal rings due to the substituents being on four positions rather than two. Electron density of R_{10} resembled an oval shape that was parallel to the short axis of the backbone. The regions of the ESP encompassing the oxygen atoms within the backbone were characterized by high electron density, due to the presence of two lone–pairs on each of these atoms. Regardless of the aforementioned depletion effect, and the various charge redistribution, the faces of the backbone of BDO were overall

electron–rich. See S_0 of BDO in Figure 3.8.

Following photoexcitation of BDO, very little change can be observed in the electron density of its S_1. Most noticeably, the central ring, R_{10}, exhibited a slight increase in its electron density compared to the picture of S_0. This increase was likely due to the redistribution of the lone–pairs of the oxygen atoms during the excitation, which effected their EDG abilities. See Section 3.5 for more details regarding the contribution of the lone–pairs of the oxygen atoms in the MOs.
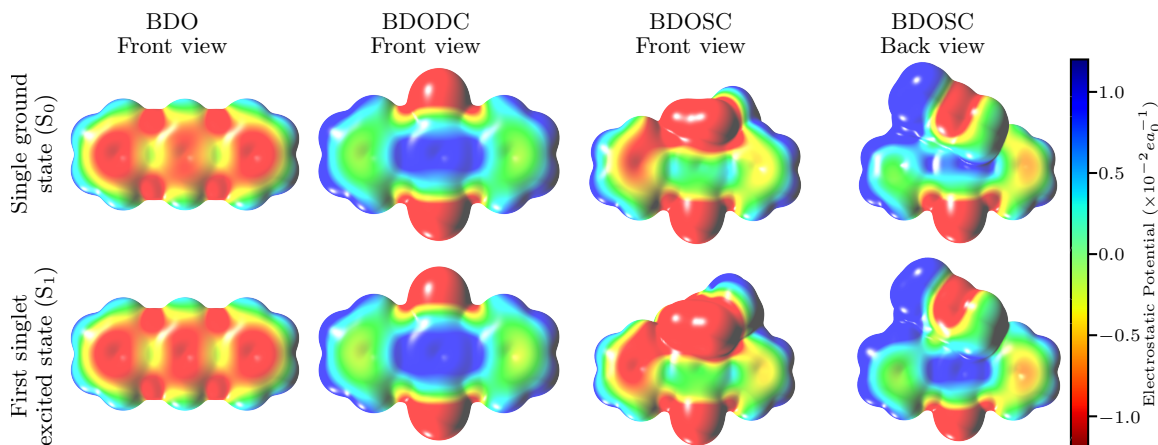
Figure 3.8: Visualization of the ESP isosurfaces of the isolated chromophores, BDO, BDODC, and BDOSC. Density surfaces were plotted at isovalue of $1 \times 10^{-4}\, e\, a_0^{-3}$. Electrostatic potential mapping was scaled to $\pm 0.012\, e\, a_0^{-1}$. Positive and negative potentials represented electron poor and rich regions, respectively.

In BDODC, the introduction of the two carbonitrile substituents to the central ring, R_{10}, redistributed the electron density throughout the whole chromophore. Being a strong EWG, the carbonitrile substituents alongside the neighboring oxygen atoms held the majority of the electron density of the entire chromophore. The three central rings, R_9, R_{10} and R_{11}, suffered most of the electron depletion to become highly electron poor sites. The two terminal rings, R_8 and R_{12}, were also effected and transformed to near neutral electrostatic potential sites. The more pronounced EWG effect on the central rings versus the terminal rings was rationalized by their closer proximity to the EWGs. Additionally, direct conjugation linking the EWGs to the

central rings had a higher electron transport efficiency than the cross–conjugation linking the terminal rings to the rest of the backbone. The ESP of BDODC in its S_1 showed further electron depletion within the backbone. This depletion was indicated by the expansion of the electron poor region on the central ring, as well as the mild electrostatic potential decrease on the terminal rings.

Similar behavior to BDODC was observed in the heterosubstituted chromophore, BDOSC, Figure 3.9. However, due to the loss of backbone planarity there were noticeable variations in the ESP between the front and the back sides. Both of which show electron depletion on the three central rings compared to the unsubstituted BDO. The front side of the backbone, facing away from the sulfonyl group, showed less electron depletion compared to the back side. This was likely due to the better orbital overlap between the sulfonyl substituent and the π–cloud of the central ring on the back side compared to the front side. This overlap effectively reduced the EWG effect of the sulfonyl substituent on the front side.

The disparity between the left–hand and right–hand terminal rings was observed here, too. The side with larger folding angle, right–hand in the front view, showed higher level of electron depletion compared to the less folded side, left–hand in the front view. This was an indicative of the minimal influence the backbone folding exerted on the cross–conjugation. The high electron density on the left terminal ring was possibly due to a stronger EDG effect exerted by the upper oxygen atom in the left dioxin ring. This higher EDG effect was likely due to the interaction between the sulfonyl oxygen atom parallel to the backbone and the neighboring rings, R_3 and R_4. Finally, the S_1 of BDOSC maintained the general characteristics observed in its S_0. The only obvious discrepancies were the higher electron depletion in the central ring, and the higher electron density in the left terminal ring.

The ESP isosurfaces of the HDIMR model were also inspected, Figure 3.9. In the S_0, both chromophores largely maintained the ESP of their isolated form. It was
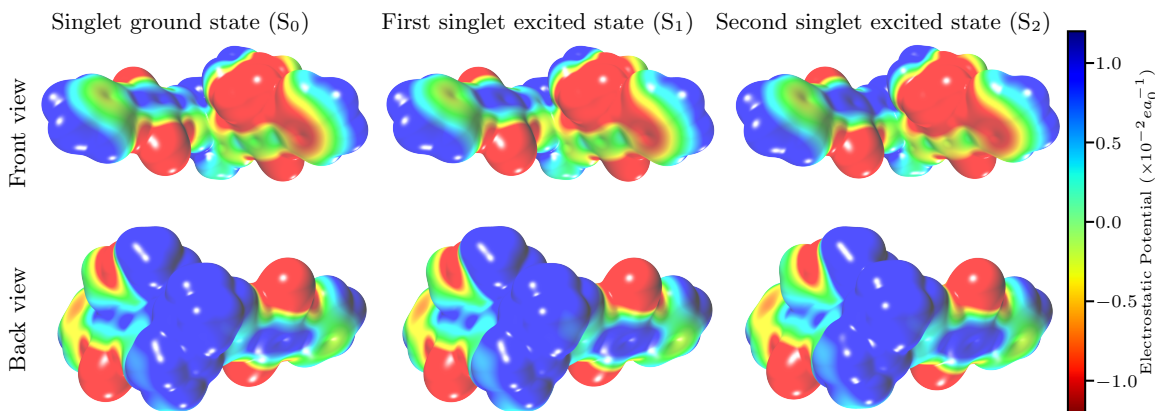
Figure 3.9: Visualization of the ESP isosurfaces of the HDIMR. Density surfaces were plotted at isovalue of $1 \times 10^{-4}\, e\, a_0{}^{-3}$. Electrostatic potential mapping was scaled to $\pm 0.012\, e\, a_0{}^{-1}$. Positive and negative potentials represented electron poor and rich regions, respectively.

worth noting here that the conformational changes of the sulfonyl substituent in the BDOSC moiety resulted in placing the electron rich terminal ring on the outer side of the backbone, right–hand side in the front view. This reversal showed that the electron rich terminal ring was always located on the side where the sulfonyl's oxygen was parallel to the backbone. In the S_1, the observable ESP changes were localized on the BDODC moiety, and were consistent with the ones observed in the S_1 of the isolated BDODC model. Predominantly, there was a further electron density depletion from the central ring, which was observable in both front and back views. In the BDOSC moiety, there were no appreciable changes in the ESP between the S_0 and S_1 of the HDIMR.

Unexpectedly, the S_2 showed a different pattern in its ESP compared to the S_1. The BDODC domain indicated further electron density depletion from the central ring, observable in both front and back views. In the BDOSC domain, on the other hand, less electron depletion can be observed on the central ring, as well as the right terminal ring. This pattern was indicative of a transfer of electron density between the two chromophores upon photoexcitation of the HDIMR to its S_2.

3.5 FRONTIER MOLECULAR ORBITALS

3.5.1 MOLECULAR ORBITALS OF THE ISOLATED CHROMOPHORE MODELS

The Kohn–Sham frontier MOs of the investigated models were inspected to aid in understanding the nature of the electronic transitions leading to the observed excited–states in Section 3.6. The HOMO, the lowest unoccupied molecular orbital (LUMO), and the LUMO+1 were considered for the isolated chromophores, shown in Figure 3.10. The HOMOs of all isolated chromophore models were identical. They were dominated by a π–like character delocalized over the C–C bonds along the short axis. They also featured electronic contribution from the non–bonding electrons of the oxygen atoms in the dioxin rings within the backbone. The oxygen atom contribution to the electronic structure of these chromophores took the form of π–electron conjugation with the neighboring benzene rings. The orbitals' nodal structure within the backbone's benzene rings resembled those of the two degenerate HOMOs of an isolated benzene ring [193]. Both LUMOs of all three chromophores showed similarities to the two degenerate LUMOs of the isolated benzene ring [193]. Additionally, the LUMO of BDO was identical to the LUMO+1 of both BDODC and BDOSC. Similarly, the LUMO+1 of BDO was identical to the LUMOs of BDODC and BDOSC. See Figure 3.10. The LUMO of BDO exhibited a π^* character localized over C–C bonds along the long axis of the backbone. The LUMO+1 of BDO exhibited a π^* character localized over C–C bonds within central ring along the short axis of the backbone. Additionally, it showed contributions from the virtual orbitals of the heteroatoms as well as the upper and lower carbon atoms of the central rings. The latter electron density was extended to the EWG substituents in the LUMOs of BDODC and BDOSC.

The estimated orbital energies of the HOMOs were relatively close at $-5.123\,\mathrm{eV}$, $-5.692\,\mathrm{eV}$ and $-5.545\,\mathrm{eV}$, for BDO, BDODC, and BDOSC, respectively. A small
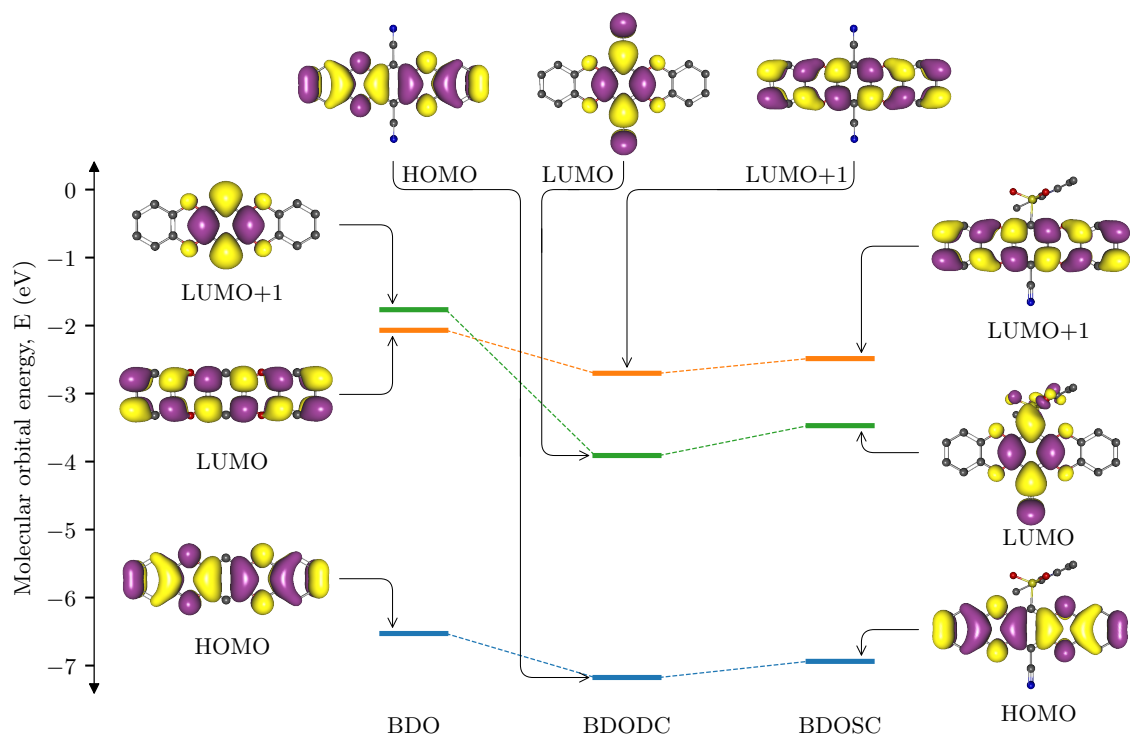
Figure 3.10: Kohn–Sham frontier molecular orbitals (MOs) of the isolated chromophores in their S_0. Surfaces were plotted at isovalue of $0.02\,e\,a_0{}^{-3}$. The vertical axis to the left indicated the estimated energies of the depicted orbitals. Dashed lines connecting the orbitals were placed to guide the reader to the LUMOs orbital reorder observed. Hydrogen atoms were removed for clarity.

decrease in the HOMOs orbital energies by $\sim$0.5 eV was evident for the BDODC and BDOSC compared to BDO. This energy decrease confirmed the stabilization effect introduced by the EWG substituents to these chromophores [193–195]. Orbital energy estimates of BDO's LUMO along with BDODC's and BDOSC's LUMO+1 were -0.663 eV, -1.218 eV and -1.132 eV, receptively. While the energies of BDO's LUMO+1 along with BDODC's and BDOSC's LUMOs were -0.360 eV, -2.427 eV and -2.118 eV, receptively. The first group showed a substituent–induced stabilization of $\sim$0.5 eV, in agreement with the HOMOs trend discussed earlier. The second group, however, exhibited a substituent–induced stabilization of nearly 2 eV. The location and nature of the EWG introduced to the backbone were the likely reason for this superior stabilization to these LUMOs. This stabilization introduced an orbital reorder

81

in the LUMOs of the substituted chromophores compared to the unsubstituted BDO. The effect of this orbital reorder in these chromophores was profound, and will be further discussed in Section 3.6.

3.5.2   MOLECULAR ORBITALS OF THE HETERODIMER SUB–UNIT MODEL
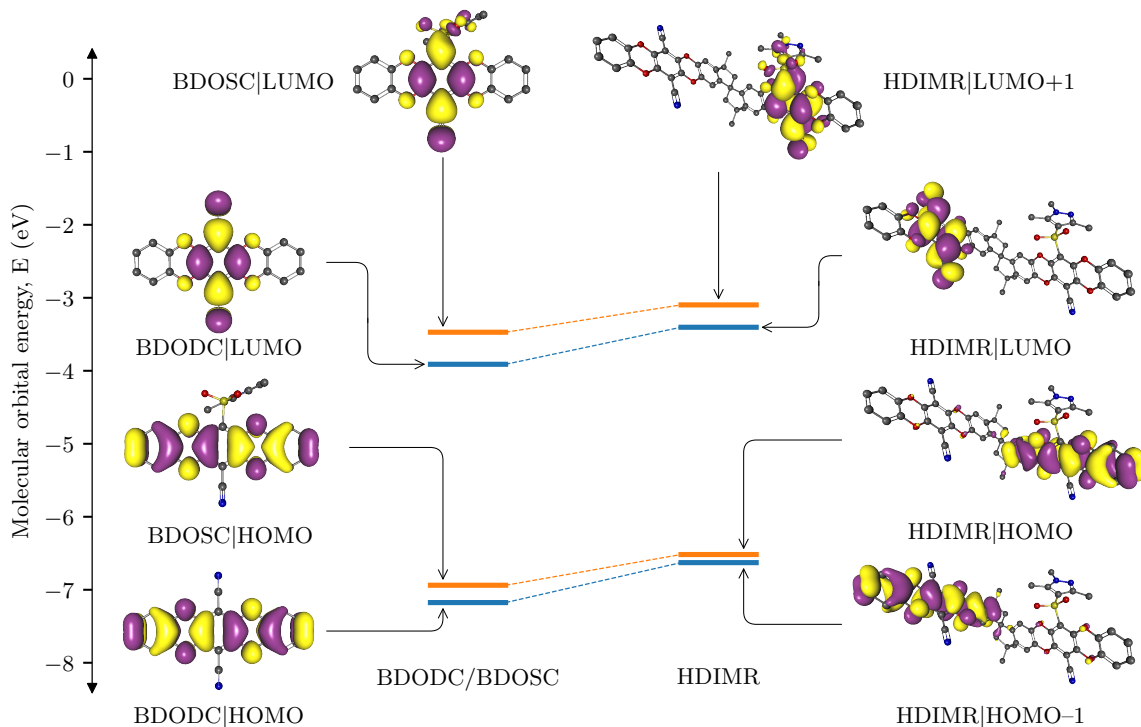
Figure 3.11: Kohn–Sham frontier molecular orbitals (MOs) of the HDIMR in its S_0 compared to their counterparts in the isolated chromophore models. Surfaces were plotted at isovalue of $0.02\,e\,a_0^{-3}$. The vertical axis to the left indicates the estimated energies of the depicted orbitals. Dashed lines were added to connect the similar orbitals between the isolated chromophore models and the HDIMR. Hydrogen atoms were removed for clarity.

Kohn–Sham frontier MOs of BDODC and BDOSC were then explored in the context of the HDIMR model, depicted in Figure 3.11. The HOMO−1 and HOMO of the HDIMR were very similar to the HOMOs of their corresponding isolated chromophores, BDODC and BDOSC, respectively. Also, the HDIMR's LUMO and LUMO+1 matched the LUMOs of their corresponding chromophores, BDODC and BDOSC, respectively. See Figure 3.10.

In addition to the similarities in their electron density localization, the DFT–estimated energies of these MOs were also similar. Energies of HOMO-1, HOMO, LUMO, and LUMO+1 were estimated at $-5.626\,\text{eV}$, $-5.515\,\text{eV}$, $-2.402\,\text{eV}$ and $-2.095\,\text{eV}$, respectively. The HOMOs exhibited destabilization of $\sim$0.7\,eV and the LUMOs of $\sim$0.25\,eV from their isolated chromophore counterparts. While the LUMOs remained strictly localized on their corresponding chromophores, the HOMOs hinted at electron density delocalization across the entire HDIMR model. Strictly speaking, at the isovalue presented in Figure 3.11, that delocalization was hardly noticeable. However, upon inflating the isosurfaces with a smaller isovalue, the extent of that delocalization was revealed, see Figure 3.12. The inflated depiction pointed at a possible mixing between the two HOMOs. Such mixing offered a pathway for the inter–chromophore excitation. These inflated HOMO depictions did not represent a quantitatively accurate electron density distribution. However, they did provide a qualitative picture to the extent of the electron density in these MOs [196].

HOMO–1   HOMO
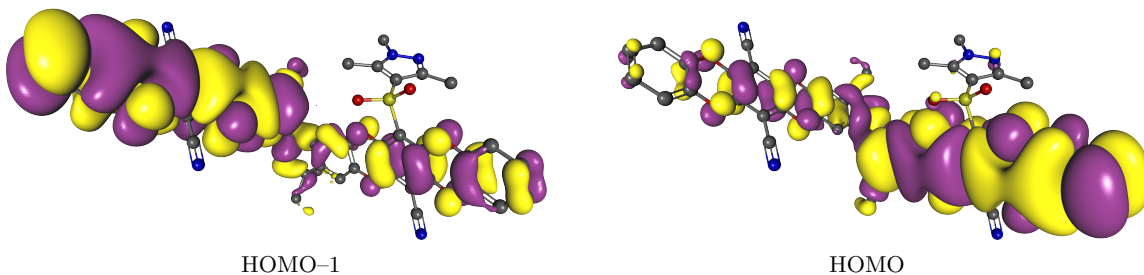
Figure 3.12: Inflated highest occupied molecular orbitals (HOMOs) of the HDIMR in its S_0. The inflation emphasized the delocalization of the electron density over both chromophores. Surfaces were plotted at isovalue of $0.005\,e\,a_0{}^{-3}$. Hydrogen atoms were removed for clarity.

3.6   ELECTRONIC TRANSITIONS

Singlet vertical excitation characteristics of the aforementioned model structures were estimated using TD–DFT. Calculations were carried out using the same level of theory used in DFT, see details in Section 3.2. Results were depicted as stick

plots in Figure 3.13a–c. The S_1 of all isolated chromophore models, BDO, BDODC, and BDOSC was characterized by a pure HOMO to LUMO transition. Their S_2 transition was dominated by a HOMO to LUMO+1 transition. The models' S_1 transition energies were predicted at 3.74 eV, 2.77 eV and 2.96 eV, respectively. Their S_2 transition energies were estimated at 4.11 eV, 3.55 eV and 3.73 eV, respectively.

The S_1 of BDO was revealed as a dark state with an oscillator strength value equal to zero. Its S_2 was predicted as a bright state with an oscillator strength of 0.2374. This observation was reversed in both of the substituted chromophores, BDODC and BDOSC. Their S_1 was predicted as a bright state with oscillator strengths of 0.2387 and 0.2285, respectively. Their S_2 was dark or near–dark state with oscillator strengths of zero and 0.0004, respectively. This reversal was clearly due to the order flip of LUMO and LUMO+1 in these models compared to BDO, Section 3.5.1. Additionally, the small oscillator strength associated with S_2 of BDOSC was likely due to the loss of its backbone planarity compared to BDODC. It was worth noting here that the stabilization introduced by the EWG substituents in BDODC and BDOSC, compared with unsubstituted BDO, resulted in a red shift of the S_1 excitation energy by near 1 eV. This shift was consistent with the stabilization energy observed in the LUMO of these models discussed in Section 3.5.1. This shift was sufficient to move the excitation energy of these chromophores from the ultraviolet (UV) region (>4.1 eV) to the visible (VIS) region (<3.1 eV) of the electromagnetic spectrum.

Singlet vertical excitation transitions of the HDIMR were presented in Figure 3.13d. Two of the first four excited states, the S_1 and the third singlet excited state (S_3), were revealed as bright states, while the other two, the S_2 and the fourth singlet excited state (S_4), were near–dark states. The oscillator strength values of S_1, S_2, S_3, and S_4 were estimated as 0.2713, 0.0042, 0.2640, and 0.0007, respectively. These states vertical excitation energies were estimated at 2.72 eV, 2.86 eV, 2.91 eV and 3.27 eV, respectively. The two bright states were dominated by localized transitions

between the MOs of the model's constituting chromophores. The S_1 was associated with a transition between the HDIMR's HOMO–1 to LUMO, equivalent to BDODC's HOMO to LUMO transition. Similarly, S_3 was characterized with a transition between HOMO to LUMO+1, equivalent to BDOSC's HOMO to LUMO transition. The excitation energies of these states were in agreement with the vertical excitation energies predicted for their isolated counterparts.
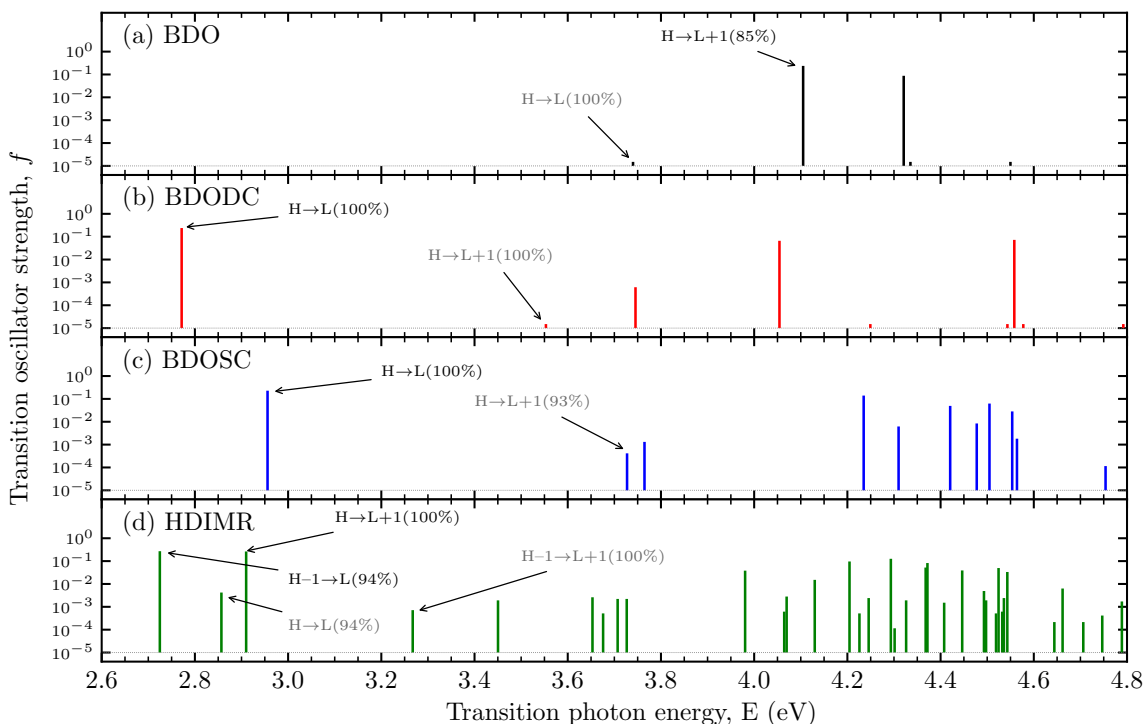
Figure 3.13: Summary of singlet vertical excitation transitions of the investigated models. Arrows point at the transitions of interest, and the labeling indicates the dominant transition and its percentage. Oscillator strength axis was plotted in logarithmic scale to improve visibility of the weak transitions. Transitions of zero oscillator strength were given a value of 1.5×10^{-5} to force their visibility.

The two near–dark states were associated with inter–chromophore transitions between the two constituting chromophores across the HDIMR. The S_2 was dominated by a HOMO to LUMO transitions, equivalent to BDOSC's HOMO to BDODC's LUMO. And the S_4 was a pure HOMO–1 to LUMO+1 transitions, equivalent to BDODC's HOMO to BDOSC's LUMO. The low, but non–zero oscillator strength

values of these transitions was in agreement with the MOs discussed in Section 3.5.2 and depicted in Figure 3.12. The limited special overlap between the participating MOs in these transitions was evident in their estimated oscillator strength values. However, these same values indicated that the delocalization of both HOMOs across the entire HDIMR should be a facilitating factor for these transitions. From the Frenkel–Davydov model, Section 1.2, these two near–dark states can be characterized as CTSs, while the bright states can be characterized as visible states (VSs). Characteristics of these states were further discussed in Section 5.2.
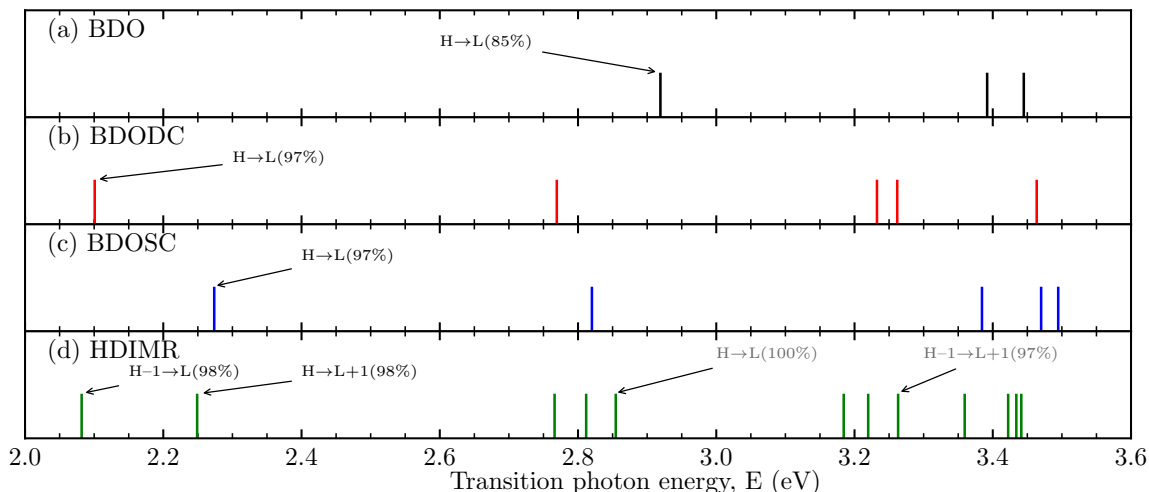
Figure 3.14: Summary of triplet vertical excitation transitions of the investigated models. Line heights do not reflect transition intensity.

Singlet adiabatic transitions were also investigated to aid in assigning the experimentally observed photoluminescence (PL) spectra, Section 4.2. The TD–DFT method successfully located the S_1 minima for all three isolated chromophore models, BDO, BDODC, and BDOSC. In consistence with the vertical excitation characteristics, it predicted a near–dark S_1 for BDO, and bright state for the substituted variants. The energies of these transition were estimated at 3.25 eV, 2.34 eV and 2.29 eV, respectively. Their oscillator strengths were estimated at 0.0003, 0.2574 and 0.2534, respectively. The HDIMR adiabatic transitions were partially located. The state minima of the lowest bright state S_1 and the lowest dark state S_2 were located. The other two states,

S_3 and S_4, were not located despite several trials of geometry optimization. These trials did not converge, or converged to a state resembling either S_1 or S_2. The transition energies of S_1 and S_2 were both estimated at $\sim 2.27\,\text{eV}$. Their oscillator strengths were estimated at 0.2699 and 0.0015, respectively. The close energy proximity between these two states indicated a possible significant overlap between their potential energy curves. Additionally, this proximity, if accurate, can introduce significant hurdles to distinguish between them using spectroscopic techniques. However, the dark versus bright nature of their transitions can lend clues that help distinguish between them spectroscopically. Specifically, the spectrum of the hypothetical HDIMR would be dominated by contributions from S_1 transition alongside a minor contribution from the S_2 transition. Additionally, the proximity would introduce inter–state transitions that can be detected in time–spectroscopy spectroscopy.

Both steady–state, Section 4.2.3, and time–resolved, Section 4.4.2, experimental measurements hinted at a possible presence of triplet transitions in these molecules. Therefore, triplet state excitation characteristics were also explored in these calculations. Triplet vertical excitation energies of the isolated chromophore models were presented as stick plots in Figure 3.14a–c. The first triplet excited state (T_1) of all isolated models, BDO, BDODC, and BDOSC were dominated by a HOMO to LUMO transition. Their vertical excitation energies were estimated as $2.92\,\text{eV}$, $2.10\,\text{eV}$ and $2.27\,\text{eV}$, respectively. Their adiabatic excitation energies were located at $2.21\,\text{eV}$, $1.74\,\text{eV}$ and $1.63\,\text{eV}$, respectively Similarly, triplet vertical excitation transitions of the HDIMR model were also estimated, Figure 3.14d. The T_1 and second triplet excited state (T_2) of the HDIMR were dominated by chromophore–localized transitions, similar in nature to S_1 and S_3, respectively. Their excitation energies were estimated at $2.08\,\text{eV}$ and $2.25\,\text{eV}$, respectively. The adiabatic excitation energy of T_1 was estimated at $1.84\,\text{eV}$. The transitions equivalent to the dark singlet transitions, S_2 and S_4, were predicted as higher triplet states at T_5 and T_8, respectively. Their respective excita-

tion energies were estimated at $2.85\,\text{eV}$ and $3.26\,\text{eV}$. The aforementioned predicted transitions indicated that the triplet so–called CTS may not play any significant rule in the electronic structure of the HDIMR.

CHAPTER 4

RESULTS: STEADY–STATE AND TIME–RESOLVED SPECTROSCOPY

This chapter presented an overview of the results obtained from the experimentally acquired spectra of the macromolecules. The heterotrimer sub–model (HTRMR), short–chain oligomer (OLGMR), and long–chain polymer (PLYMR). All of which contained chromophores [1,4]benzodioxino[3,2–b]oxanthrene–6–(1,3,5–trimethylpyrazole–4-sulfonyl)–13–carbonitrile (BDOSC) and [1,4]benzodioxino[3,2–b]oxanthrene–6,13–dicarbonitrile (BDODC). The latter was also investigated experimentally. Section 4.1 summarized the results obtained from ultraviolet–visible absorption (UV–VIS) spectroscopy. It discussed the observed features in all spectra and the results obtained from their spectral decomposition analysis.

Section 4.2 presented the acquired photoluminescence (PL) spectra. Excitation and emission spectra were discussed in addition to the excitation–emission matrix (EEM) of the samples. Additionally, it summarized the results obtained from emission spectral decomposition analysis. The section wrapped up by discussing the delayed photoluminescence (dPL) measurements of BDODC, the OLGMR, and the PLYMR. Section 4.3 showed the PL kinetics obtained from the time–resolved photoluminescence (TRPL) measurements. And it discussed the results of their fitting routine with a single exponential decay. Section 4.4 elaborated on the observed spectral features and kinetics in the femtosecond transient absorption pump–probe (fsTAPP) spectra. Finally, it summarized the results from the multi–exponential analysis routines employed to unravel their kinetic profiles.

4.1 ULTRAVIOLET–VISIBLE ABSORPTION SPECTROSCOPY

4.1.1 SPECTRAL FEATURES AND EXTINCTION COEFFICIENT

The four investigated molecules exhibited similar spectral features in their UV–VIS spectra, see Figure 4.1a. Spectra of the HTRMR and the PLYMR were nearly identical. Evidently, the HTRMR, representing a sub–unit of the longer PLYMR, was able to reproduce its UV–VIS spectrum. Spectral band widths of the macromolecules were sufficiently different from that of the isolated chromophore, BDODC. These observations indicated that the electronic transitions contributing to these spectra were "semi–localized" in nature. I.e., these transitions likely originated from within the domain of each chromophore or by interacting with their immediate neighbors.

Table 4.1: Summary of the UV–VIS spectral characteristics of the investigated molecules. "N° of chr" referred to the number of chromophore units within each macromolecule. These values were estimated using gel permeation chromatography (GPC) from [85]. "Conc" was the estimated chromophore unit concentration in the solutions prepared. E was the transition energy at the peak maximum. ε was the estimated molar extinction coefficient at the peak maximum. Listed errors referred to the error propagation estimates from the fundamental physical measurements.

Molecule	N° of chr	Conc (µM)	$E_{\text{Peak 1}}$ (eV)	$\varepsilon_{\text{Peak 1}}$ $(\text{mM}^{-1}\,\text{cm}^{-1})$	$E_{\text{Peak 2}}$ (eV)	$\varepsilon_{\text{Peak 2}}$ $(\text{mM}^{-1}\,\text{cm}^{-1})$
BDODC	1	50.3±06.3	2.897	3.92±0.49	4.567	4.62±0.58
HTRMR	3	50.0±33.8	2.897	3.26±2.21	4.246	5.47±3.70
OLGMR	6±2	66.7±24.8	2.942	2.27±0.84	4.320	3.76±1.40
PLYMR	121±54	51.8±33.9	2.896	2.00±1.31	4.246	2.55±1.67

Two main features, peak 1 and peak 2, were observed within the measured spectral range, Figure 4.1a. Peak 1, the low energy band, was centered ∼2.9 eV while peak 2 center ranged from 4.2 eV to 4.6 eV. Peak 1 center was consistent among all samples aside from OLGMR which showed a blue shift by ∼0.05 eV. On the other hand, peak 2 exhibited more variability among these molecules. For the macromolecules, the HTRMR and PLYMR were identical, yet again, at ∼4.246 eV. Following the same
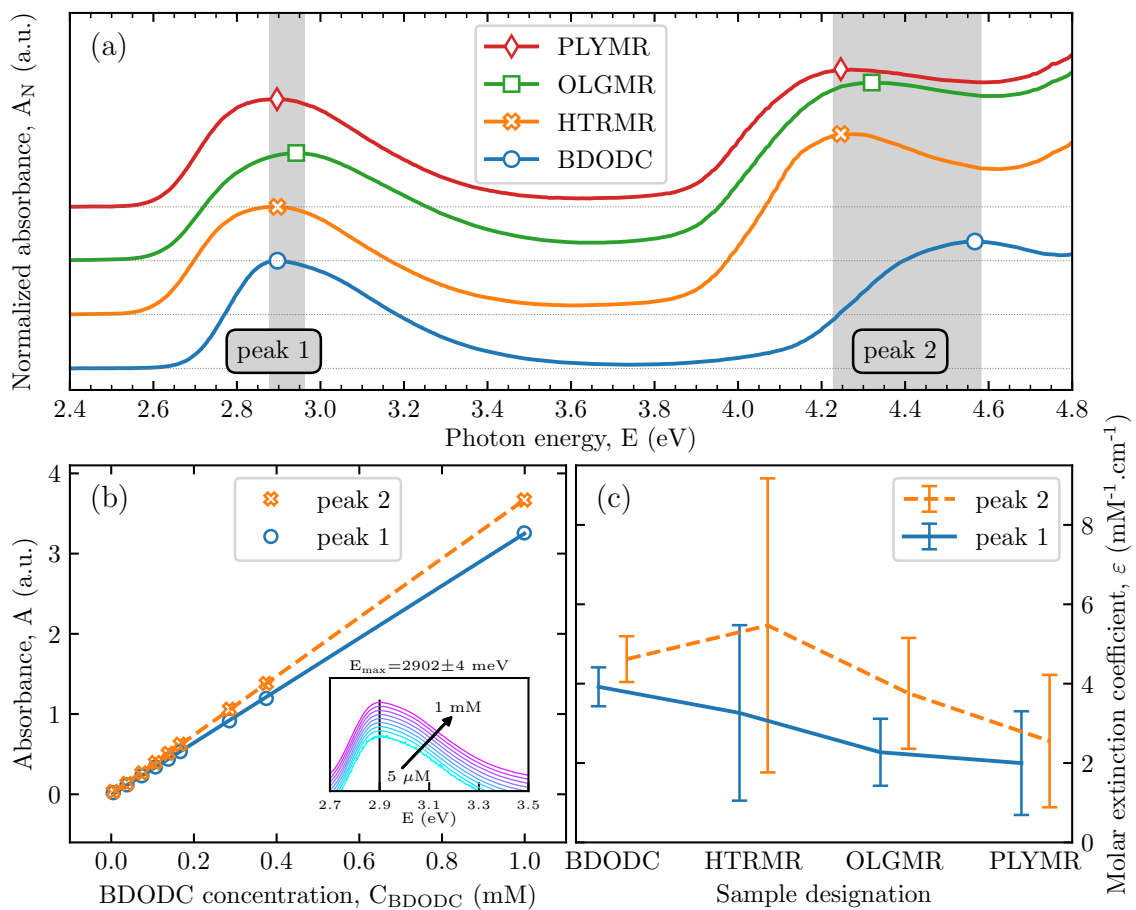
Figure 4.1: Summary of the results obtained from the UV–VIS spectra of the investigated molecules and macromolecules. These were BDODC, HTRMR, OLGMR, and PLYMR. (a) Normalized UV–VIS spectra at $\sim$50 µM chromophore unit concentration in $CHCl_3$. Spectra were normalized at peak 1, and vertically spaced for clarity. Markers indicated the maximum intensity location of peak 1 and peak 2. Shaded regions highlighted the extent of the spread of peak 1 and peak 2 within these spectra. (b) Beer's optical linearity of BDODC covering the concentration range from $0.005\,\mathrm{mmol\,L^{-1}}$ to $1.000\,\mathrm{mmol\,L^{-1}}$. Parameters of the Linear regression shown were listed in Table 4.2. Inset: Spectra of different concentrations of BDODC around peak 1 maximum. Data were normalized at peak 1 center and vertically spaced for clarity. (c) Molar extinction coefficients (ε) calculated from spectra in Figure 4.1a. Error bars represented the error propagation estimates from the fundamental physical measurements.

trend observed in the low energy band, here, the OLGMR was blue shifted $\sim$0.07 eV. On the other hand, the isolated chromophore, BDODC, was dramatically blue shifted by $\sim$0.32 eV.

A basic assumption can be made here that both bands correlated with the chromophoric composition of each solution. Each of these bands would contain transitions from both chromophore moieties in the macromolecules. The spectral agreement between the PLYMR and the HTRMR indicated that both macromolecules had very similar chromophoric composition. I.e. The BDODC:BDOSC ratio of the PLYMR was very similar to the 2:1 ratio of the HTRMR. Additional observations can be drawn when comparing the spectrum of BDODC to the rest of the macromolecules. Around peak 1, BDODC shared similar peak maximum with the rest of the macromolecules but had a narrow bandwidth. This meant that peak 1 was dominated by transitions from BDODC moiety. Also, that transition was on the lower energy side of the band. Using this logic, the OLGMR must contain higher content of BDOSC compared to the PLYMR. This was consistent with our previous report [85].

Table 4.2: Linear regression results of BDODC optical linearity experiment. Data and fit lines were depicted in Figure 4.1b. Error bars represented the fit standard error at 1σ.

	slope (mM^{-1})	intercept	R^2
Peak 1	3.26±0.58	-0.010±0.004	0.99991
Peak 2	3.67±0.45	0.004±0.003	0.99996

Linearity of the optical response of BDODC was also evaluated using a series of standard concentrations. BDODC was selected as a test subject due to its well–defined molar mass and geometry. These properties permitted more accurate concentration preparations and measurements. Furthermore, the small structure and expected planar geometry, Section 3.4.1, increased the possibility of observable non–linear behaviors. Non–linear behaviors may be caused by various types of possible intermolecular interactions such as solvent–solute interaction and π–stacking. Results of these

experiments were presented in Figure 4.1b and Table 4.2. Indeed, the optical response of BDODC was linear within the explored concentration range from $0.005\,\mathrm{mmol\,L^{-1}}$ to $1.000\,\mathrm{mmol\,L^{-1}}$. There was no observable shift in the peak 1 center due to an increase in the concentration of the chromophore, inset of Figure 4.1b. Slopes of the Beer's Law linear fits, Table 4.2, produced the molar extinction coefficients (ε) of BDODC at peak 1 and peak 2. Their values were $3.26 \pm 0.58\,\mathrm{mM^{-1}\,cm^{-1}}$ and $3.67 \pm 0.45\,\mathrm{mM^{-1}\,cm^{-1}}$, respectively. This litmus test ruled out possible intermolecular interactions of BDODC within this concentration range. By extension, there were no expectations of inter–macromolecular interactions between the macromolecules in their solution phase within this concentration range.

Molar extinction coefficients (ε) of the four investigated molecules were also calculated at their respective maxima, peak 1 and peak 2. The values were extracted for each of them from a single spectral measurement at a known concentration. These values were utilized to compare the optical response of the molecules and investigate any discrepancies. Notably, the results from this method for BDODC were in good agreement with the values extracted from the concentration–dependence experiment described earlier. These values revealed a trend of an inverse relationship, in both peaks, when associated with the number of chromophores in the investigated macromolecules, Figure 4.1c. In general terms, as the number of chromophores increased the value of ε decreased. This inverse relationship was likely due a state mixing between the adjacent chromophores within the macromolecules. It was possible that PLYMR showed the strongest deviation from the isolated chromophore due to its high molar mass. If this was the case, then the proposed state mixing may have a larger extent than just few adjacent chromophores. It was also possible that the composition of PLYMR contained a better alternation between the two constituting chromophores, maximizing this state mixing. A larger sample size of various chain lengths and more controlled chromophore alternation were required to answer this question definitively.

However, the current observation was enough of an indicator to the presence of inter–chromophore interactions within the three macromolecules.

4.1.2   LINE FITTING AND DECOMPOSITION ANALYSIS

The UV–VIS spectral data of BDODC was simulated with a single logarithmic–normal distribution (Logn) function, Equation 2.1, designated as Logn function of BDODC (Logn$_{\text{BDODC}}$). The three macromolecules, HTRMR, OLGMR, and PLYMR were simulated with a linear combination of two Logn functions, designated as Logn$_{\text{BDODC}}$ and Logn function of BDOSC (Logn$_{\text{BDOSC}}$). Each Logn function was used to represent the band containing transitions associated with one of the two different chromophores constituting the macromolecules, i.e. BDODC and BDOSC. See Section D.1 for more details on this Logn function. Results from the decomposition analysis were summarized in Figure 4.2 and Table 4.3. Parameter correlation tables of the fits can be found in Section D.3, Table D.1 to Table D.4. Parameter correlations in these fits were relatively high indicating a high ambiguity between the model and the data. [197, 198] This ambiguity arises from the poor spectral resolution of the UV–VIS data coupled with high overlap between the constituting components. However, the theoretical bases of the model lends validity to the results extracted from these fit. Moreover, the ambiguity may be elevated with low temperature UV–VIS measurements

The fit quality of all three macromolecules was higher than that of BDODC. The spectrum of BDODC exhibited a shoulder on the higher energy side of the peak maximum that deviated from the Logn curve. This shoulder was attributed to a partially resolved vibronic feature that was not observable in any of the other larger macromolecules. From the decomposition results, the trend of decreasing intensities observed earlier was also apparent in the individual chromophores. See Figure 4.2e–f and Table 4.3. The decrease in the maximum intensity (I_o) of BDODC appeared
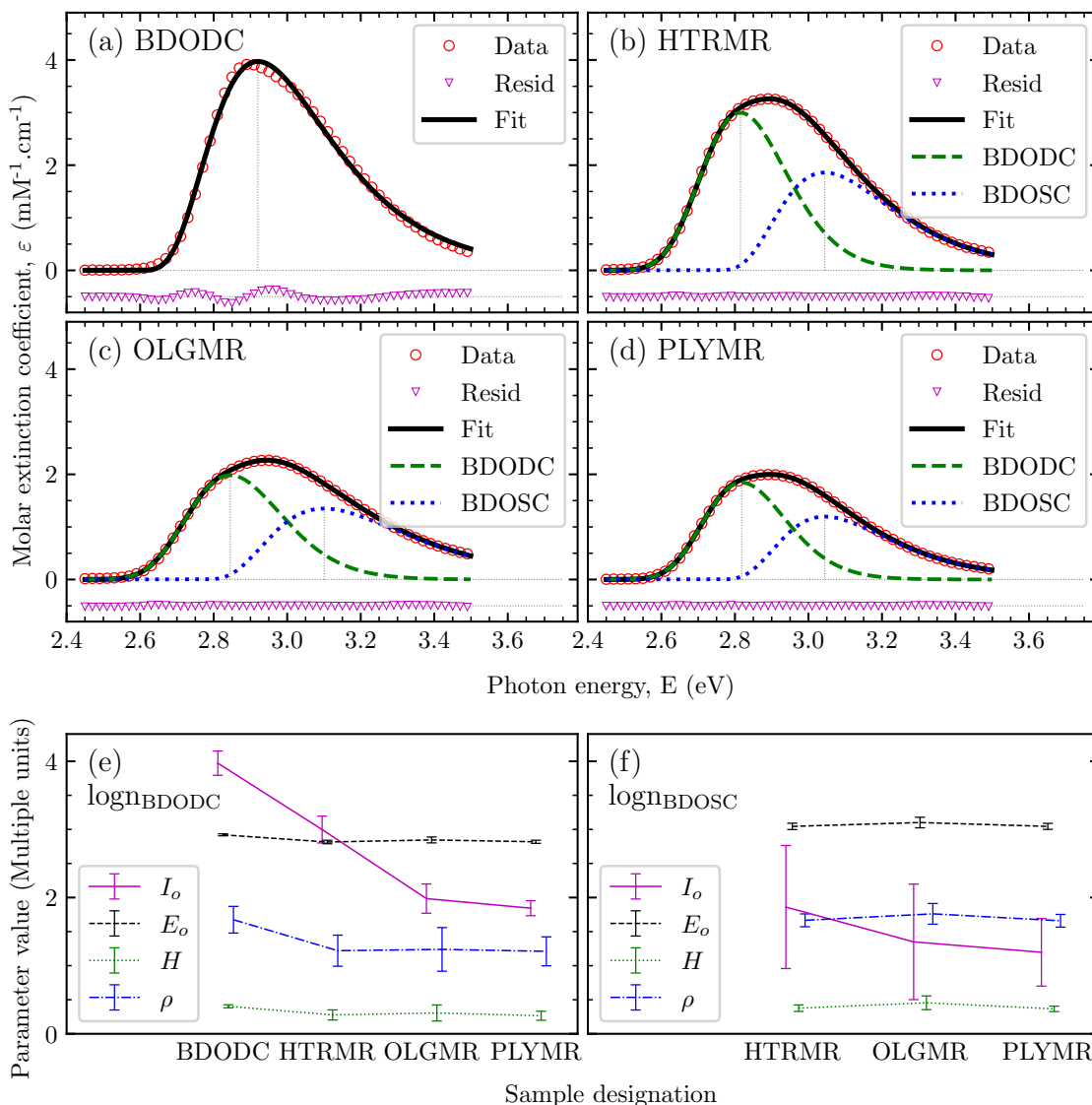
Figure 4.2: Summary of the results from the UV–VIS spectral decomposition analysis using Logn functions. (a) Decomposition of BDODC with one Logn function. (b–d) Decomposition of the HTRMR, the OLGMR, and the PLYMR with a linear combination of two Logn functions, Logn$_{\text{BDODC}}$ and Logn$_{\text{BDOSC}}$. (e–f) Visual depiction of the parameter values resulted from the decomposition analysis. All spectra were normalized to their respective maxima, then multiplied by the extinction coefficient calculated in Section 4.1.1. Data points in these plots were down–sampled by a factor of 20 to improve curve visibility. Parameters in (e) and (f) referred to Equation 2.1 on page 17. The associated error bars represented the fit confidence interval at 4σ multiplied by 10 for visibility. I_o was in $\text{mM}^{-1}\,\text{cm}^{-1}$, E_o and H were in eV, and ρ was unitless.

stronger than the one associated with BDOSC. It was reasonable to assume that this effect was more pronounced in the BDODC because of its higher presence ratio, $\sim$1:2, in the macromolecules.

Table 4.3: Summary of the UV–VIS spectral decomposition analysis results. Parameters referred to Equation 2.1 on page 17. I_o was in $\mathrm{mM^{-1}\,cm^{-1}}$, E_o and H were in eV, and ρ was unitless. Error bars represented the fit confidence interval at 4σ.

Parameter	BDODC	HTRMR	OLGMR	PLYMR
$I_{o,BDODC}$	3.972±0.018	2.998±0.020	1.984±0.021	1.843±0.011
$E_{o,BDODC}$	2.920±0.001	2.815±0.003	2.845±0.004	2.818±0.002
H_{BDODC}	0.404±0.002	0.277±0.007	0.306±0.012	0.265±0.007
ρ_{BDODC}	1.674±0.020	1.220±0.023	1.239±0.032	1.210±0.021
$I_{o,BDOSC}$		1.860±0.090	1.350±0.085	1.197±0.050
$E_{o,BDOSC}$		3.044±0.005	3.101±0.008	3.044±0.004
H_{BDOSC}		0.376±0.005	0.455±0.010	0.366±0.004
ρ_{BDOSC}		1.666±0.009	1.761±0.015	1.659±0.009
$\Delta E_{\mathrm{UV\text{–}VIS}}$		0.229	0.256	0.226
$I_{o,BDODC}/I_{o,BDOSC}$		1.488	1.332	1.423
BDODC/BDOSC		2	1.79	1.91

It was possible to evaluate the chromophoric compositions of the macromolecules using the results of the decomposition analysis. For a solution of a single chromophoric type, the molar extinction coefficient (ε) was directly related to the transition oscillator strength (f):

$$\varepsilon = f \times n$$

Where n was the number of chromophores contributing to the transition. Assuming the detected bands originated exclusively from localized transitions with a chromophore moiety, the evaluation can be carried out using a simple proportional relation as the following:

$$\varepsilon_1/\varepsilon_2 = f_1/f_2 \times n_1/n_2$$

Where f_1, f_2 were the oscillator strengths of BDODC and BDOSC, respectively. n_1, n_2 were the number of chromophore units of BDODC and BDOSC in any given macromolecule, respectively. And ε_1, ε_2 were the molar extinction coefficients of BDODC and BDOSC, respectively. ε_1, ε_2 were represented by the extracted transition intensities $I_{o,BDODC}$, $I_{o,BDOSC}$, respectively. Using the relation above, and the known HTRMR ratio n_1/n_2 of 2:1:

$$(\varepsilon_1/\varepsilon_2)_{\text{HTRMR}} = (f_1/f_2)_{\text{HTRMR}} \times (n_1/n_2)_{\text{HTRMR}}$$

$$2.998/1.86 = (f_1/f_2)_{\text{HTRMR}} \times 2/1$$

$$(f_1/f_2)_{\text{HTRMR}} = 0.806$$

Using this ratio

$$(n_1/n_2)_{\text{OLGMR}} = \frac{(\varepsilon_1/\varepsilon_2)_{\text{OLGMR}}}{0.806} = 1.82$$

And

$$(n_1/n_2)_{\text{PLYMR}} = \frac{(\varepsilon_1/\varepsilon_2)_{\text{PLYMR}}}{0.806} = 1.91$$

Indeed, the chromophoric composition ratio of the PLYMR at 1.91:1 was closer to the expected ratio of 2:1. On the other hand, the chromophoric composition of the OLGMR was sufficiently lower at 1.82:1. This low composition ratio provided additional support for the observed blue shift discussed in Section 4.1.1.

The extracted central transition energies (E_o) of BDODC within the HTRMR and the PLYMR were identical at $\sim$2.82 eV. This value was red–shifted from the E_o of the isolated form by $\sim$0.1 eV. The E_o of BDODC within the OLGMR fell between

the above values at $\sim$2.85 eV. Similarly, E_o values of BDOSC within the HTRMR and the PLYMR were approximately 3.04 eV. The same parameter was evaluated at $\sim$3.10 eV within the OLGMR. A minor discrepancy in the relative red–shifting between the two chromophores within the macromolecules was observed. Depicted as $\Delta E_{\text{UV–VIS}}$, Table 4.3, the relative red–shift within the OLGMR was lower than the other two macromolecules by $\sim$0.03 eV. These E_o and $\Delta E_{\text{UV–VIS}}$ values further supported the hypothesis of state mixing between the two chromophores within the framework of the macromolecules. These values indicated that the degree of mixing was more dependent on the chromophoric composition than the total molar mass.

4.2 PHOTOLUMINESCENCE SPECTROSCOPY

4.2.1 SPECTRAL FEATURES AND EXCITATION–EMISSION MATRICES

The EEMs of the four molecules were presented as pseudo–color contours shown in Figure 4.3a–d. All contours showed an asymmetric single feature within the investigated energy ranges of the excitation and the emission. The asymmetry of this feature constituted a tail extending to higher excitation and lower emission energies. This asymmetry was attributed to the vibronic progression of the absorption and emission transitions in these molecules, respectively. The feature associated with BDODC, Figure 4.3a, had a narrower excitation tail compared to the other macromolecules. The maximum of this feature was also blue–shifted by $\sim$0.1 eV on its emission axis compared to the other macromolecules.

The corresponding excitation and emission lines of these molecules were drawn in the adjacent plots, Figure 4.3e–h, respectively. Summary of their spectral features were listed in Table 4.4. Excitation spectra of all molecules resembled their respective UV–VIS spectra in broadness and peak positioning, Figure 4.1 and Table 4.1. However, the blue shift observed in the UV–VIS band of OLGMR was less pronounced here. As demonstrated in 4.1.2, the UV–VIS spectra of all macromolecules were a linear
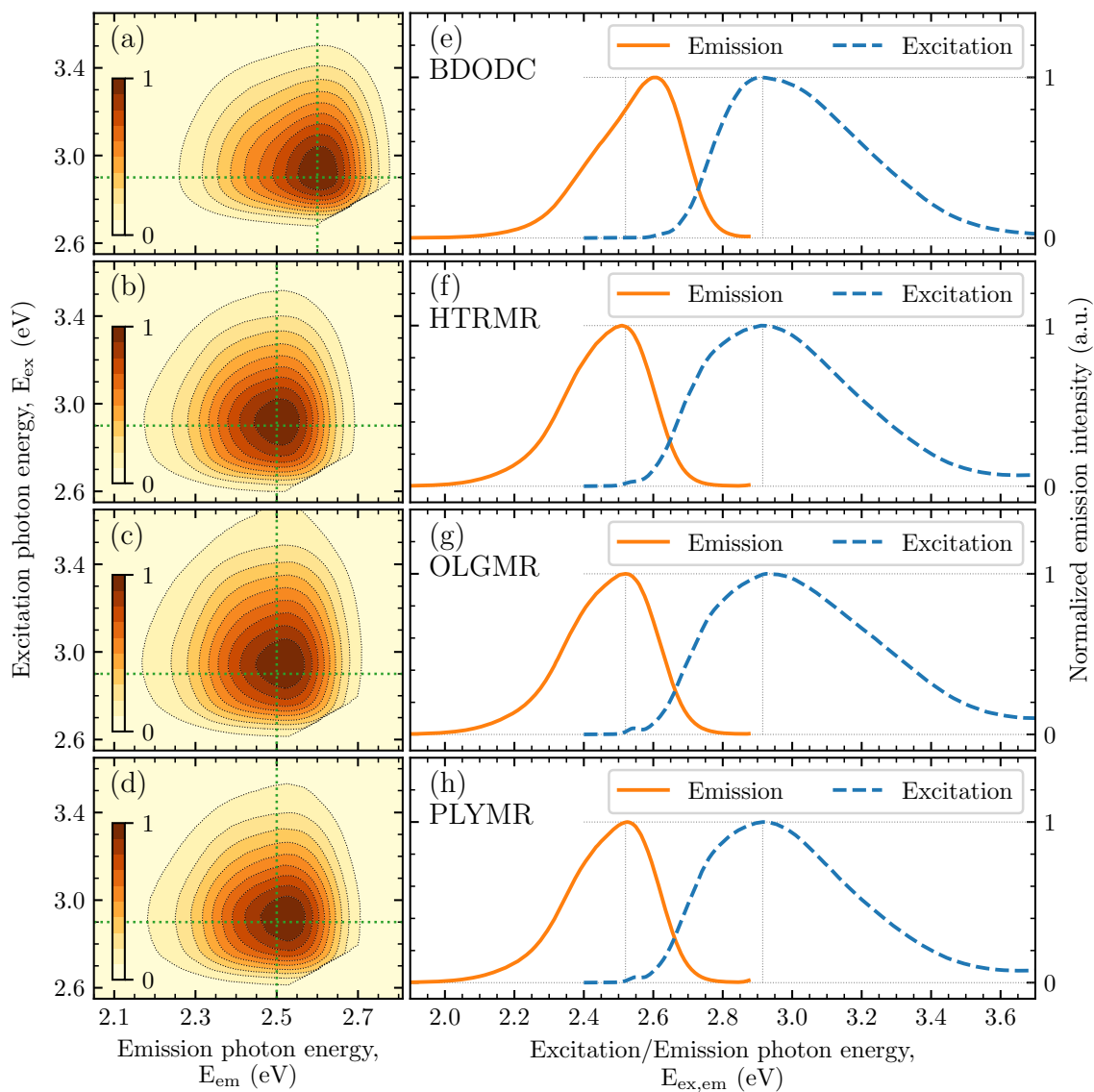
Figure 4.3: Summary of the PL spectra collected for the four molecules of interest. (a–d) Pseudo–color map of the normalized EEM. Data was normalized to the overall maximum in the two–dimensional array of each sample. (e–h) Normalized excitation and emission spectral lines. Excitation and emission data were normalized to their corresponding maximum. Emission lines were collected at excitation of 2.9 eV, represented by the horizontal dashed lines overlaid on the EEM maps. Excitation lines were collected at emission of 2.6 eV for BDODC and 2.5 eV for the other macromolecules, represented by the vertical dashed lines overlaid on the EEM maps.

combination of the UV–VIS bands of each chromophoric moiety. The excitation spectra shown here were measured at the emission band maxima of each macromolecule. The similarity between the UV–VIS and excitation spectra implied that the excitation of each chromophore moiety contributed to the measured emission spectra.

Table 4.4: Summary of the PL spectral characteristics. "Conc" was the estimated chromophore unit concentration. $I_{max,corr}$ was the maximum emission intensity divided by the molar extinction coefficient at the excitation photon energy (2.90 eV). E_{max} was the photon energy of the band maximum. ΔE_s was the Stokes shift. Error bars of the concentration represented the error propagation estimates from the fundamental physical measurements.

Molecule	Conc (μM)	$I_{max,corr}$ (mM cm)	$E_{\text{max, ex}}$ (eV)	$E_{\text{max, em}}$ (eV)	ΔE_s (eV)
BDODC	50.3±06.3	198	2.910	2.605	0.305
HTRMR	50.0±33.8	178	2.915	2.510	0.405
OLGMR	66.7±24.8	70	2.925	2.520	0.405
PLYMR	51.8±33.9	132	2.920	2.525	0.395

Emission spectra of all molecules showed a single band with maxima at $\sim$2.61 eV for BDODC and $\sim$2.52 eV for the other macromolecules. All of these bands had a tail extending toward the lower energy side corresponding to their vibronic progression. The emission spectra of all macromolecules had a relatively broader bandwidth compared to BDODC, especially near their peak maxima. Furthermore, the lower energy side of the emission spectra all macromolecules exhibited a small shoulder unlike the narrower emission spectrum of BDODC. These observations indicated that the emission spectra of the macromolecules was composed of more than one distinct transition. Kasha's rule stated that the emission of a chromophore or a macromolecule must originate from its lowest energy state [199]. Therefore, complex emissions such as the ones shown here could be a result of one of two possibilities. Isolated, non–interacting chromophores within a macromolecule may produce their own individual emission bands from their own lowest energy states. Consequently, the overall emission spectrum would be the linear combination of each chromophore's emission band, similar to the UV–VIS

spectra presented earlier. On the other hand, interacting chromophores may produce mixed states, such as electron–transfer states (ETSs), charge–transfer states (CTSs), and charge–separated states (CCSs). These "new" states could exhibit their own emission in addition to the emission from the macromolecule's overall lowest energy state. As demonstrated in 4.1.1, the chromophores within these macromolecules showed various degrees of interaction and state mixing. Therefore, the shoulder observed in their emission spectra was likely originating from a new state produced by inter–chromophore interactions and state mixing. Worth noting here that emission lines collected using higher excitation energies were identical to the ones shown here. This similarity supported the hypothesis that exciting either chromophore will eventually populate the lowest excited state(s), from which the emission originated.

4.2.2 LINE FITTING AND DECOMPOSITION ANALYSIS

Line fitting and decomposition analysis routines similar to that of UV–VIS spectra were carried out on the excitation and emission spectra of the investigated molecules. These analyses were required to unravel the properties of the components and states present in these molecules. The excitation spectrum of the isolated chromophore, BDODC, was simulated with a single, Logn function, Equation 2.1, labeled as $Logn_{BDODC}$. The emission spectrum of this chromophore was simulated with a single, mirror–symmetric Logn function, Equation 2.2, designated as Logn function of the first excited state ($Logn_{S_1}$). The excitation spectra of the other three macromolecules were simulated with a linear combination of two ordinary Logn functions, $Logn_{BDODC}$ and $Logn_{BDOSC}$. Their emission spectra were simulated with a linear combination of two, mirror–symmetric Logn functions, $Logn_{S_1}$ and Logn function of the second excited state ($Logn_{S_2}$). Results of these analyses were summarized in Table 4.5. Line fits of the excitation spectra were shown in Figure 4.4 and the emission spectra in Figure 4.5. Parameter correlation tables of the fits can be found in

Section D.3, Table D.5 to Table D.12. Similar to UV–VIS fits, parameter correlations of the excitation spectra were high indicating a high degree of ambiguity between the data and the fitting model. [197, 198] This ambiguity arises from the highly overlapping components and poor spectral resolution of the PL data. On the other hand, emission spectral fittings produced acceptable parameter correlations. These correlations further validate the model used and the conclusions drawn from these analyses.

Table 4.5: Summary of the PL's excitation and emission spectral line fit analysis. Parameters referred to Equation 2.1 for excitation and Equation 2.2 for emission. $\Delta E_{ex,BDODC}$ was the red–shift of E_o of BDODC between the isolated and the macromolecular environments. $\Delta E_{s,S_x}$ was the Stokes shift of state "x". This Stokes shift was calculated between the lowest excitation band maximum and the emission band maximum of that state. E_o, H, $\Delta E_{ex,BDODC}$, and ΔE_s are in eV, while I_o and ρ are unitless. Error bars represent the confidence interval of the fit at 3σ.

Parameter	BDODC	HTRMR	OLGMR	PLYMR
		Excitation spectra		
$I_{o,BDODC}$	1.009±0.012	0.906±0.025	0.907±0.031	0.931±0.018
$E_{o,BDODC}$	2.904±0.004	2.773±0.007	2.797±0.008	2.791±0.006
H_{BDODC}	0.405±0.006	0.239±0.015	0.249±0.018	0.236±0.015
ρ_{BDODC}	1.625±0.048	1.156±0.058	1.129±0.072	1.111±0.054
$I_{o,BDOSC}$		0.713±0.056	0.715±0.060	0.687±0.057
$E_{o,BDOSC}$		2.998±0.013	3.034±0.016	3.005±0.013
H_{BDOSC}		0.358±0.009	0.389±0.014	0.342±0.009
ρ_{BDOSC}		1.607±0.049	1.679±0.080	1.687±0.048
		Emission spectra		
I_{o,S_1}	1.005±0.013	1.009±0.005	1.009±0.006	1.009±0.005
E_{o,S_1}	2.575±0.003	2.487±0.002	2.496±0.002	2.502±0.002
H_{S_1}	0.301±0.005	0.287±0.002	0.297±0.004	0.287±0.004
ρ_{S_1}	1.455±0.044	1.397±0.013	1.397±0.016	1.412±0.019
I_{o,S_2}		0.093±0.010	0.111±0.012	0.115±0.013
E_{o,S_2}		2.369±0.005	2.376±0.005	2.376±0.004
H_{S_2}		0.113±0.013	0.126±0.018	0.129±0.021
ρ_{S_2}		1.255±0.207	1.399±0.265	1.427±0.276
$\Delta E_{ex,BDODC}$		0.131	0.107	0.113
$\Delta E_{s,S_1}$	0.329	0.286	0.301	0.289
$\Delta E_{s,S_2}$		0.404	0.421	0.415
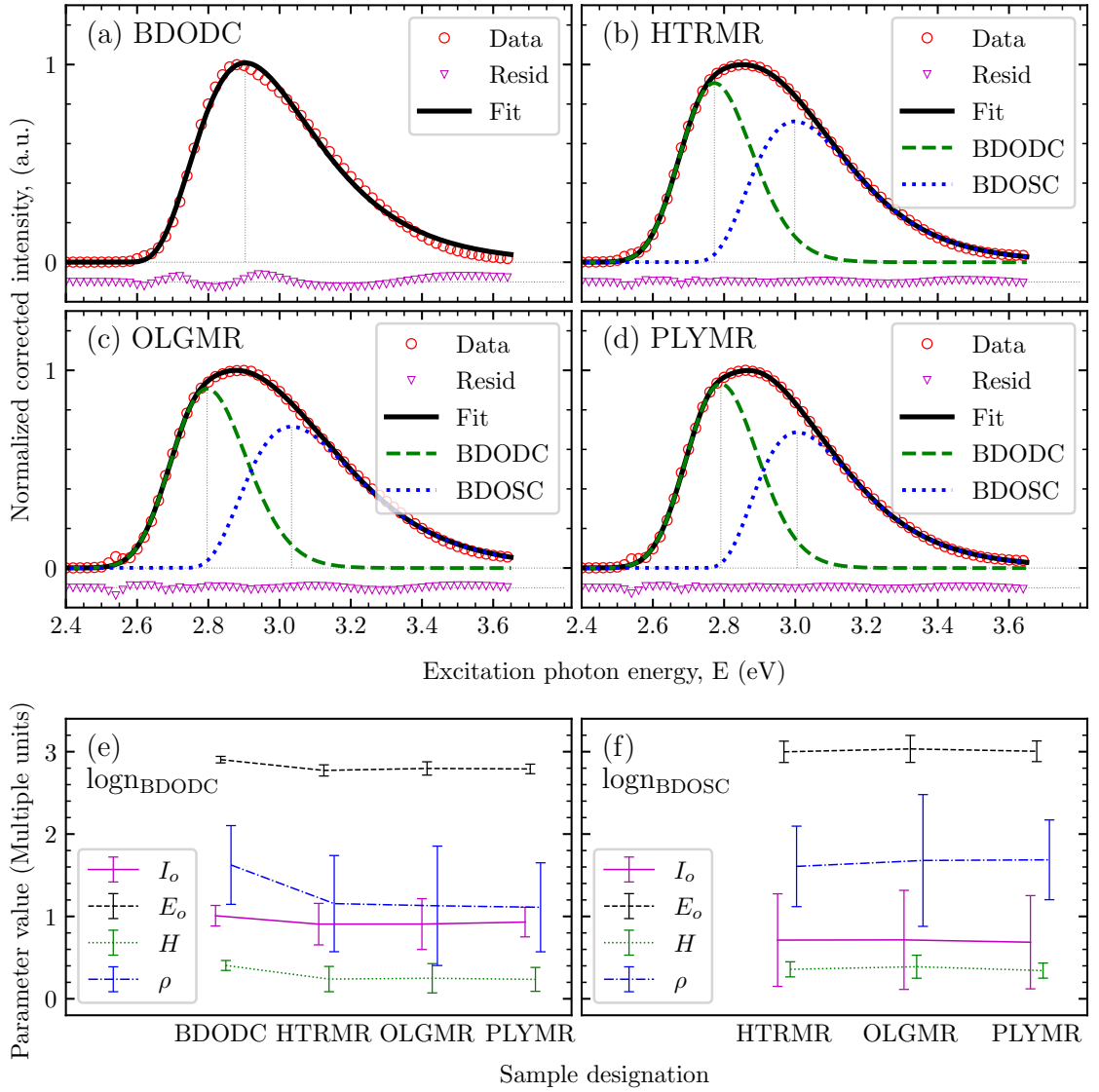
Figure 4.4: Summary of the decomposition analysis the PL's excitation spectra with Logn functions. (a) Decomposition of BDODC with one Logn function, $\text{Logn}_{\text{BDODC}}$. (b–d) Decomposition of the HTRMR, the OLGMR, and the PLYMR with a linear combination of two Logn functions, $\text{Logn}_{\text{BDODC}}$ and $\text{Logn}_{\text{BDOSC}}$. (e–f) Visual depiction of the parameter values resulted from the decomposition analysis. All spectra were normalized to their respective maxima. Data points in these plots were down–sampled by a factor of 4 to improve data curve visibility. Parameters in (e) and (f) referred to Equation 2.1. Error bars represented the fit confidence interval at 4σ multiplied by 10 for visibility. E_o and H were in eV, while I_o and ρ were unitless.
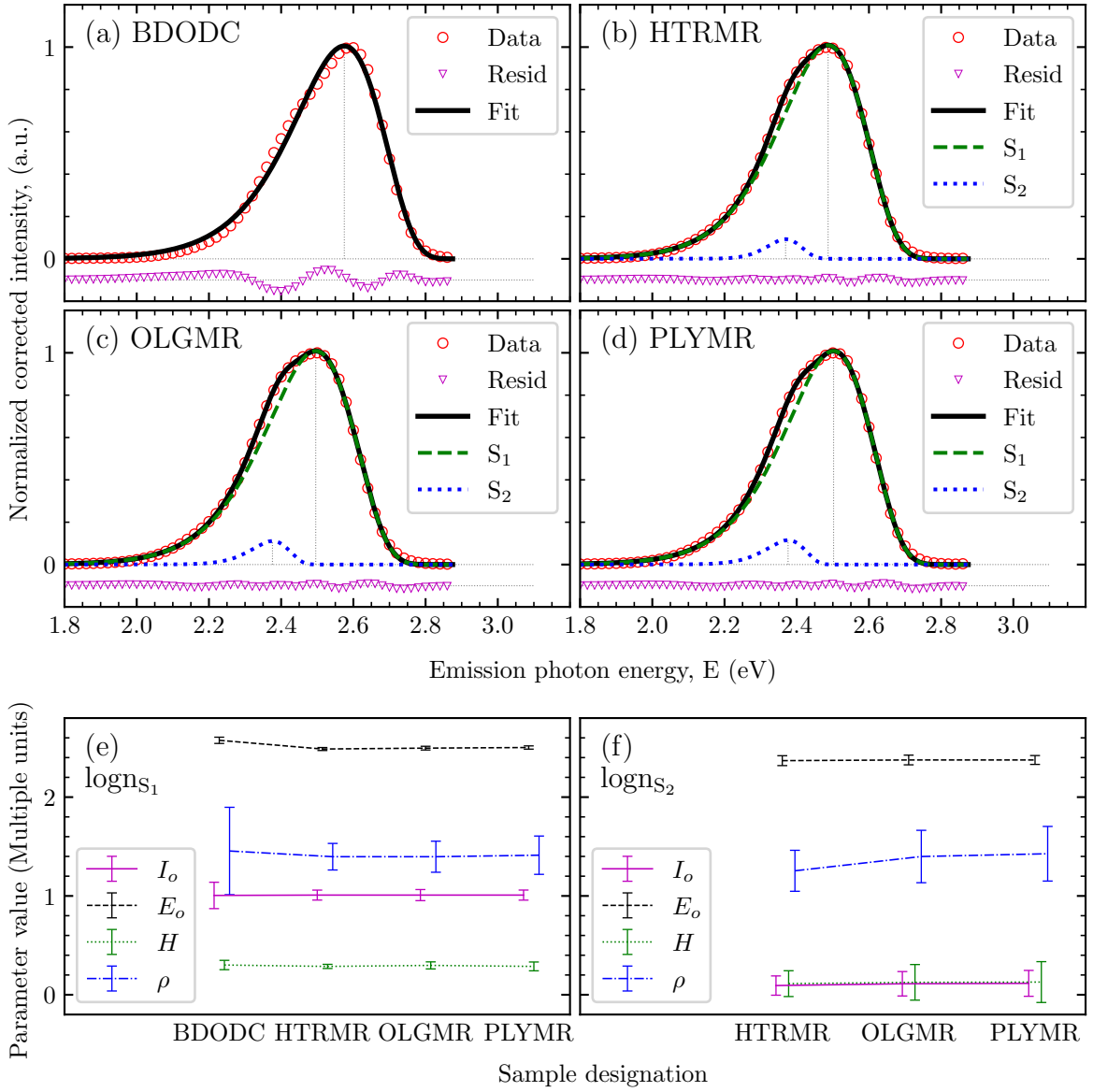
Figure 4.5: Summary of the PL's emission spectra decomposition analysis with a mirror-symmetric Logn functions. (a) Decomposition of BDODC with one mirror-symmetric Logn function, Logn_{S_1}. (b–d) Decomposition of the HTRMR, the OLGMR, and the PLYMR with a linear combination of two mirror-symmetric Logn functions, Logn_{S_1} and Logn_{S_2}. (e–f) Visual depiction of the parameter values resulted from the decomposition analysis. All spectra were normalized to their respective maxima. Data points in these plots were down–sampled by a factor of 4 to improve data curve visibility. Parameters in (e) and (f) referred to Equation 2.2. Error bars represented the fit confidence interval at 4σ multiplied by 10 for visibility. E_o and H were in eV, while I_o and ρ were unitless.

The results from the decomposition analysis of all excitation spectra were in good agreement with their UV–VIS counterparts. Central transition energy (E_o) of BDODC was estimated at $\sim$2.9 eV in its isolated form and averaged $\sim$2.79 eV within the macromolecules. These values were estimated at $\sim$2.92 eV and $\sim$2.83 eV from the UV–VIS analysis, respectively. Similar to the UV–VIS results, the OLGMR showed the lowest degree of red–shift of the BDODC transition from its isolated form. This supported the notion that the OLGMR exhibited the lowest degree of state mixing due to its poor chromophore alternation. Finally, the characteristics of band corresponding to the BDOSC moiety was relatively consistent across all macromolecules. The OLGMR, yet again, showed the highest E_o, further indicating a lower degree of inter–chromophore interaction.

The decomposition analysis of the emission spectra differed slightly from the UV–VIS and excitation spectra. Emission of all three macromolecules were dominated by a single component. This emission, as per Kasha's rule, was dubbed as the emission from the overall first singlet excited state (S_1) of the macromolecule. The S_1 band characteristics were similar to the S_1 band of the isolated BDODC with a slight red–shift of <0.090 eV. All macromolecules showed a much smaller band centered on the lower energy side of the dominant band. Contribution and location of this band was consistent with the emission shoulder referenced earlier. Characteristics of this shoulder band were relatively comparable among all macromolecules tested. This shoulder band was attributed to an emission from a CTS that laid slightly below the S_1 of the these macromolecules. The results also indicated that the macromolecular size have a small impact on the characteristics of this CTS band.

Both UV–VIS and PL analysis pointed at two factors effecting the electronic structure of these macromolecules. The first was the molecular size and by extension the number of chromophores present in each macromolecule. This factor effected the overall optical response of the macromolecule as indicated by the trend of the molar

extinction coefficient observed in the UV–VIS data. It also effected the relative energy position and characteristics of the CTS. In this context, the larger the molecular size was the higher the contribution of the CTS to the emission spectrum. This can either be viewed as a better emission efficiency from the CTS or higher overall population of the CTS following the photoexcitation. The second factor was the chromophoric composition of the macromolecule and the quality of alteration between the two chromophores within the backbone. The impact of this factor manifested on the relative energies of the composing chromophores within the backbone. The impact of both factors must be considered when designing a macromolecule targeting maximum efficiency of the CTS.

4.2.3   DELAYED PHOTOLUMINESCENCE

A brief procedure of DPL experiments were carried out under both ambient and degassed conditions. These experiments aimed at detecting emissions with long lifetime characteristics. These experiments would not produce time–dependent kinetic profiles. However, they can aid in isolating emission events of long lifetimes from the early time emissions. The detectable temporal range of these experiments was on a scale of µs to ms. States with such long lifetimes can be characterized as triplet excited states, CTSs, or emissions following a reverse intersystem crossing (ISC) [200, 201]. These experiments utilized the PL instrument described earlier, Section 2.3.1. It introduced a temporal delay of known magnitude between the instance of excitation and the start of the emission signal integration. In addition to the delay, the temporal signal integration window, dubbed as "gate", was controlled. The combination of both parameters could isolate emissions of longer lifetimes and emissions with initial lag time from early time emissions. The delay would minimize the contribution from early emission, generally fluorescence. The gate would differentiate between longer and shorter emission lifetimes. Furthermore, the effect of O_2 quenching of the triplet

excited state was explored. Emissions from two solutions, under ambient conditions and deoxygenated, were compared. The deoxygenation was carried out by purging with N_2 for >20 min prior to the data acquisition. Results from these experiments were summarized in Figure 4.6.
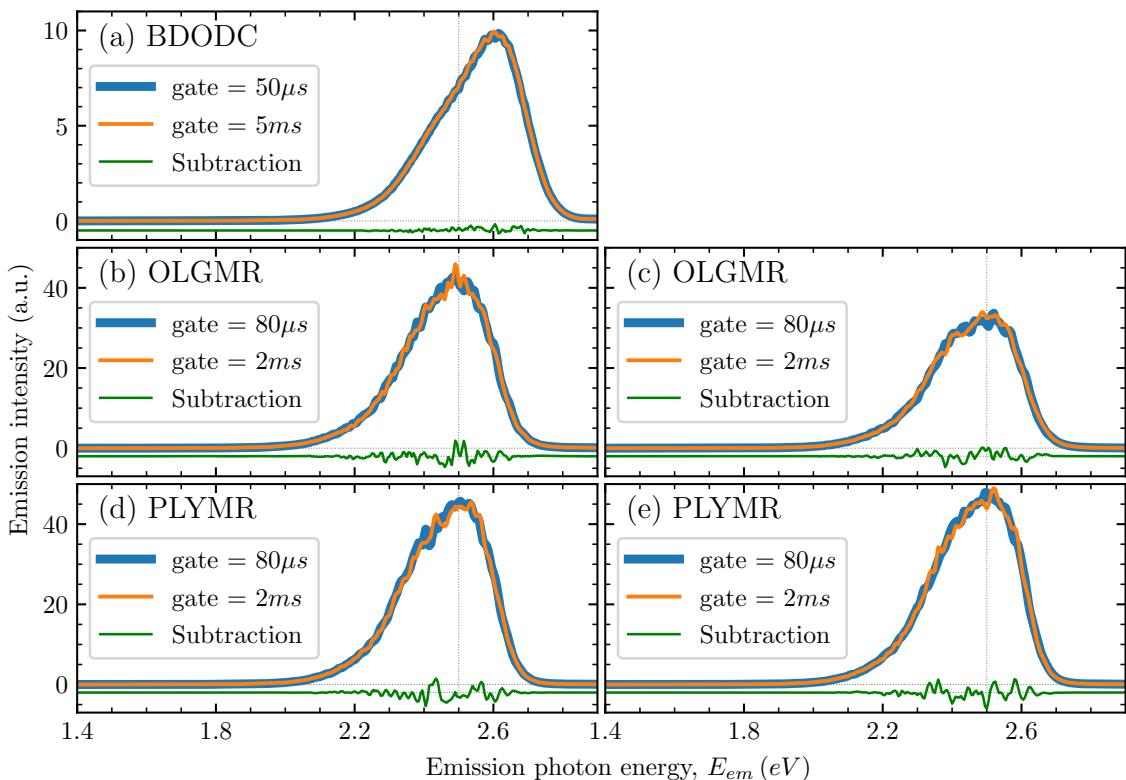
Figure 4.6: Comparison of dPL spectra with varying gaseous conditions, excitation-detection delay, and signal integration gate. (a, b, d) Measured under ambient conditions. (c, e) Measured after N_2 purge for over 20 min. (a) Measured with excitation (E_{ex}) at 2.91 eV, and a delay of 30 µs. (b-e) Measured with excitation (E_{ex}) at 3.02 eV, and a delay of 10 µs. Intensity was scaled by a factor of 10 without any normalization.

Each plot in the Figure 4.6 showed an overlay of two emission spectra acquired with identical delay values and different gate values. The plots also contained subtraction of the long gate spectrum from the short gate spectrum. The isolated chromophore, BDODC, was tested only under ambient conditions, Figure 4.6a. Under these conditions, the spectra acquired using gate values of 50 µs and 5 ms were nearly identical. The difference being a noise level elevation within the long gate spectrum

observable in the subtraction line. The subtraction line showed a minute elevation from the zero line, Figure 4.6a. This deviation was located on the lower energy side of the band center. Inconclusively, it indicated the presences of an emission with a lifetime longer than 50 µs.

The OLGMR and the PLYMR under ambient and deoxygenated conditions showed results similar to BDODC. However, in their case, the deviation of the long gate spectra was even less visible. The long gate spectra were plagued with higher levels of noise. It was worth noting here that the deoxygenation did not improve the visibility of these underlying long–lived bands.

The observations from these dPL experiments hinted at the presence of emission from long–lived state(s). This long lifetime emission was slightly more visible in the isolated chromophore BDODC compared to the macromolecules. The origin of this feature was expected to be of a triplet nature due to its presence in both isolated and bound chromophores, The efficiency of this state decreased when the chromophore was embedded in a macromolecule with inter–chromophore interactions. Unfortunately, the incompleteness of the data set hindered the effort to draw conclusive conclusions about the properties of these states. Low temperature and further deoxgynation experiments coupled with higher temporal resolution or dedicated time–resolved instruments would be necessary to support the above observations.

4.3   TIME–RESOLVED PHOTOLUMINESCENCE SPECTROSCOPY

The dPL experiments indicated that a long–lived states with a triplet character may be part of the energy structure of the investigated molecules. Therefore, a TRPL experiment was carried out to further characterize the lifetime of the emission spectrum. To that end, a simplified apparatus was constructed and used for these experiments. Details of the apparatus and the experimental procedures can be found in Section 2.4. The apparatus utilized a femtosecond laser pulse for excitation and

a photodiode–oscilloscope configuration for detection. Unfortunately, the detection scheme lacked adequate sensitivity to detect weak emission from the aforementioned long–lived states. However, it proved useful in providing information about the stronger emission from the singlet states.

Four time–dependent traces were collected for the molecules of interest. A fifth trace representing the instrument response function (IRF) was collected using a pure solvent, $CHCl_3$. The acquired IRF trace was fitted with a Gaussian function of the form:

$$G(t; I_o, \mu, \sigma) = \frac{I_o}{\sigma\sqrt{2\pi}} e^{-0.5\left(\frac{t-\mu}{\sigma}\right)^2} \tag{4.1}$$

Where I_o was the intensity, μ was the center, and σ was the width. The full width at half maximum (FWHM) of this Gaussian curve equaled $2\sigma\sqrt{2\ln 2}$. The width of the IRF, σ_{IRF} was estimated at $\sim$0.65 ns and its FWHM was $\sim$1.53 ns. These values were considered adequate to resolve the lifetimes of the TRPL profiles.

The TRPL traces were fitted with an exponentially modified gaussian (ExpGaus) function of the form:

$$EG(t; I_o, \mu, \sigma, \tau) = I_o e^{-\frac{1}{\tau}\left(t-\mu-\frac{\sigma^2}{2\tau}\right)} \left[1 + \text{erf}\left(\frac{t-\mu-\frac{\sigma^2}{\tau}}{\sqrt{2}\sigma}\right)\right] \tag{4.2}$$

Where I_o was the intensity, μ was the IRF center, σ was the width of the IRF, τ was the decay time constant The erf was the error function. Details on this error function and the ExpGaus function can be found in Section D.2. The σ value was fixed at 0.65 ns for all fitted profiles.

Fit results were summarized in Table 4.6. Data and fit lines were depicted in Figure 4.7. Parameter correlation tables of these fits can be found in Section D.3, Table D.13 to Table D.17. All correlation values were within the acceptable range of ±0.9. [197, 198] Lifetime of the isolated chromophore, BDODC, was evaluated near

Table 4.6: Summary of TRPL lifetimes (τ_{PL}) extracted from the single exponential fit. IRF was fitted with a Gaussian function of which the width (σ_{IRF}) is reported here. Error bars represent the confidence interval of the fit at 4σ.

Parameter		IRF	BDODC	HTRMR	OLGMR	PLYMR
σ_{IRF}	(ns)	0.65±0.03				
τ_{PL}	(ns)		12.95±0.15	11.27±0.10	9.49±0.10	10.64±0.08
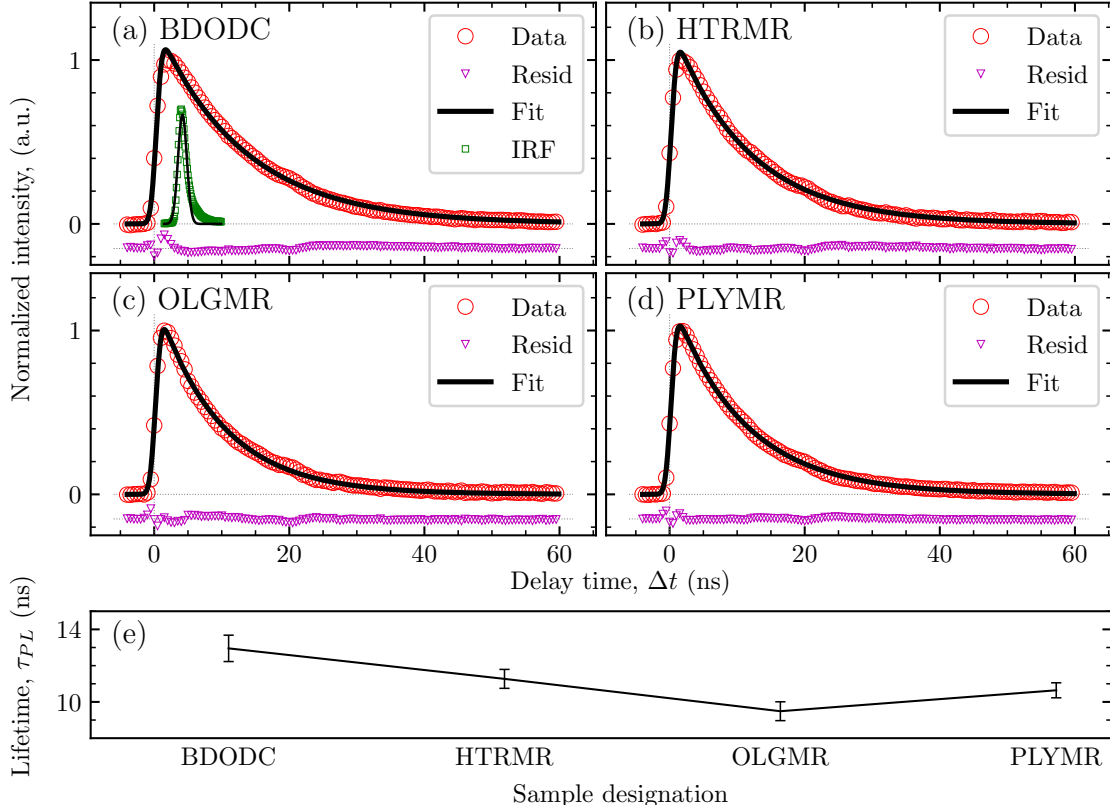
Figure 4.7: Summary of TRPL data and their fit with a single exponential fit. Data and fit of the IRF were shown under the BDODC trace in (a). Error bars shown in (e) were the confidence interval of the fit at 4σ multiplied by 10 for visibility. Data were down–sampled by a factor of 5 to improve visibility, too.

13 ns. This value was consistent with the reports of Fritsch and co–workers at 11.8 ns in CH_2Cl_2 [10]. The values for the other three macromolecules, the HTRMR, the OLGMR, and the PLYMR were estimated at 11.3 ns, 9.5 ns and 10.6 ns, respectively. These were also consistent with Fritsch's dominant lifetime reported at 10.8 ns for the polymer of intrinsic microporosity "1" (PIM–1). However, the macromolecules

studied here showed a trend in the estimated lifetimes with respect to their molar mass and chromophoric composition. There was a general decrease in the extracted lifetime as the size of the macromolecule increased. This trend was consistent with the observations from the UV–VIS and the PL data and analysis. I.e. The larger the macromolecule, the higher the degree of state mixing and the stronger the inter–chromophore interaction. But this interaction was also dependent of the chromophoric composition of the macromolecule. Here, the poor chromophoric composition of the OLGMR effected the observed lifetime even further, bringing the value below 10 ns. The consistent lifetime of the higher quality HTRMR and PLYMR indicated that the inter–chromophore interaction reached a plateau. This Indicated that the inter–chromophore interaction was limited to a small set of chromophores within the backbone.

4.4 FEMTOSECOND TRANSIENT ABSORPTION PUMP–PROBE SPECTROSCOPY

The fsTAPP data and analysis were discussed in this section. The data was highly overlapping in the spectral and temporal domains. Therefore, the spectral domain was discussed qualitatively in Section 4.4.1. Analysis and exponential fits were carried out on kinetic profiles representing the major spectral bands observed. Results of these analyses were summarized and discussed in Section 4.4.2.

4.4.1 SPECTRAL FEATURES IN THE UV TO NIR PROBE

The isolated chromophore, BDODC and the HTRMR were considered representatives of the molecules of interest in this work. Therefore, these molecules were selected for an extended probing experiment from $1.2\,\mathrm{eV}$ to $3.9\,\mathrm{eV}$ using CaF_2 supercontinuum. This extended probe aimed at exposing any uncovered bands from the standard Al_2O_3 supercontinuum probe that ranged from $1.6\,\mathrm{eV}$ to $3.0\,\mathrm{eV}$. However,

the temporal data in these measurements were unreliable for quantitative analysis due to various beam drifting artifacts. Therefore, all four molecules were also probed with the standard Al_2O_3 supercontinuum for quantitative data analysis. Spectral features from the extended probe of BDODC and the HTRMR were shown in Figure 4.8a and b, respectively. Standard probe results of the OLGMR and the PLYMR were shown in Figure 4.8c and d, respectively.

The detected signals from both BDODC and the HTRMR largely exhibited the same spectral features. A slight blue shift can be observed in the transition energies of the BDODC features compared to HTRMR. These features included a positive band from a photoinduced absorption (PIA) process, labeled as first photoinduced absorption (PIA_1). The feature started around 2.1 eV and extended beyond the lower detection limit at 1.2 eV. A negative feature was apparent from 2.2 eV to 2.5 eV. This feature was designated as a stimulated emission (SE) due to its similarity with the PL spectra. A second positive feature centered around 2.7 eV and 2.55 eV for BDODC and the HTRMR, respectively. This feature was labeled as second photoinduced absorption (PIA_2). A second negative signal appeared around 2.9 eV and 3.0 eV that matched UV–VIS spectra of BDODC and HTRMR, respectively. This feature originated from a photobleach (PB) process and therefore labeled as PB. Finally, a third positive feature, that started around 3.2 eV and stretched beyond the upper detection limit at 3.9 eV. This feature was designated as third photoinduced absorption (PIA_3).

Macromolecules OLGMR and PLYMR were probed only in the visible region from 1.6 eV to 3.0 eV. This probe range exposed all possible features detected by the CaF_2 supercontinuum except PIA_3 feature. PIA_3 feature in both BDODC and the HTRMR showed the same kinetic profile as that of PIA_2 feature, see Figure 4.9. This indicated that both of these features probed the same population from the same excited state. As such, and due to its reliability, the visible probe was used to explore the kinetic profile of all samples. It was worth noting that the visible probe distorted
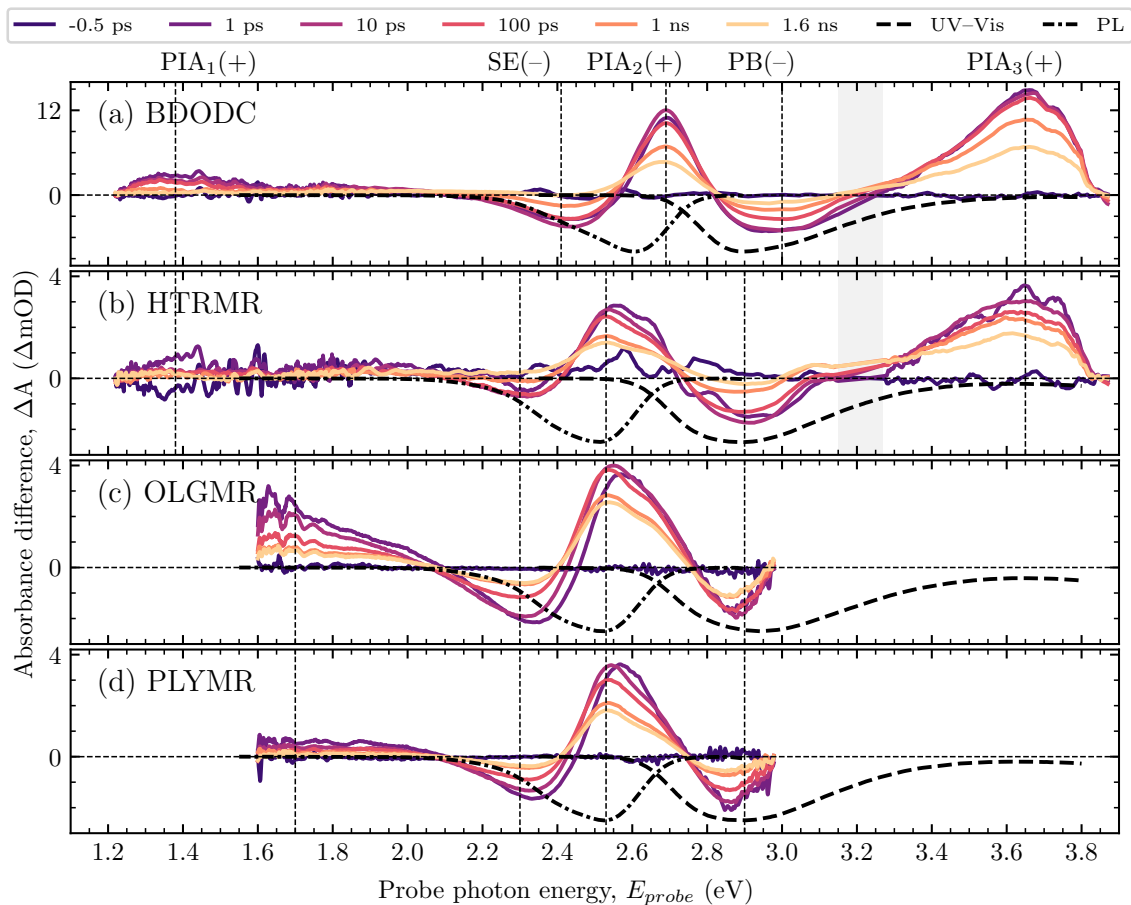
Figure 4.8: Summary of the fsTAPP spectral data. (a) and (b) were the CaF$_2$ extended probe range of BDODC and the HTRMR, respectively. The spectra presented here were two separate scans stitched together using an overlapping range from 1.6 eV to 1.8 eV. The data points in the shaded area around 3.2 eV were a result of linear interpolation following the removal of the pump scattering contaminant. The chromophore unit concentration of these samples were approximated around 0.5 mM. (c) and (d) were the standard, Al$_2$O$_3$ probe range of the OLGMR and the PLYMR samples, respectively. The chromophore unit concentration of these samples were maintained around 0.5 mM. Each plot contained transient spectral lines at pump–probe delay times of −0.5 ps, 1 ps, 10 ps, 100 ps, 1000 ps and 1600 ps. Overlaid dashed lines represented the scaled, inverted UV–VIS spectra of the corresponding molecule. The dashed–dotted lines represented their scaled, inverted PL spectra. Vertical dashed lines represented the apparent band maximum for each feature detected.

the high energy edge of PB signal due to the limited probe beam intensity near $3.0\,\text{eV}$. This was demonstrated in the supercontinuum spectral profiles shown in Figure 2.7 on page 42. Additionally, the PB feature was mostly overlapping with PIA_2 and PIA_3 features. This overlap was clear when comparing the positioning this feature with respect to the UV–VIS spectra shown. This overlap introduced a high level of contamination to the lifetimes extracted from this kinetic profile fittings. Therefore, the kinetics of PB feature were not considered in the lifetime analysis below.
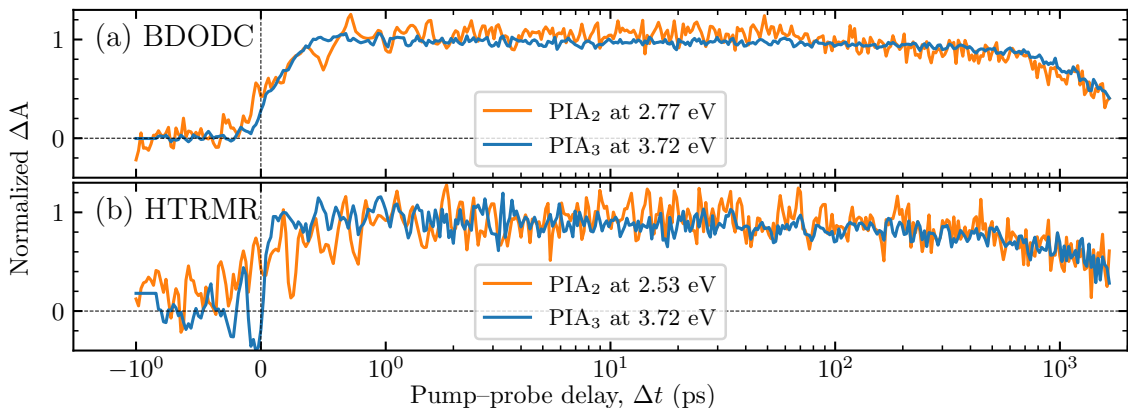
Figure 4.9: Comparison of the kinetic profiles of PIA_2 and PIA_3 features from the fsTAPP spectra of (a) BDODC and (b) HTRMR. Features were extracted from the spectra depicted in Figure 4.8a and b, respectively.

4.4.2   FITTING OF KINETIC PROFILES AND LIFETIME ANALYSIS

Three features, PIA_1, SE, and PIA_2 were analyzed for the four molecules of interest. The analysis explored single, double, and triple exponential decay fits for the three features. An additional exponential growth component was necessary for all SE and PIA_2 kinetic profiles. Exponential decay and growth features were simulated using the ExpGaus described in Equation 4.2. More details of this function can be found in Section D.2. Details of the fitting routine can be found in Section 2.6. Kinetic profiles of the isolated BDODC were fitted adequately with a double exponential decay. However, the other three macromolecules required a third exponential decay component for an adequate fit. The lifetime of the longest decay component, τ_{d_3}, for each sample

was fixed at its corresponding TRPL lifetime value listed in Section 4.3. Graphical depiction of these fits can be found in Figure 4.10, Figure 4.11, and Figure 4.12 for PIA_1, SE, and PIA_2 features, respectively. Summary of the lifetimes extracted from these fits were listed in Table 4.7. Parameter correlation tables of these fits can be found in Section D.3, Table D.18 to Table D.29. Parameter correlations for PIA_1 and SE fits were within the acceptable range. However, few correlations of PIA_2 fits exceeded ± 0.9 in few instances. These values indicate that the model was unable to reproduce the decay profile unambiguously. [197, 198] This ambiguity likely raises from the contamination of this decay profile by the PB decay profile. Global analysis is likely to remove this ambiguity and produce time constants with higher quality.

Table 4.7: Summary of the lifetimes extracted from the multi–exponential fits applied to the kinetic profile of fsTAPP spectra. All values listed here were in (ps). Error bars represented the fit error estimates.

Feature	Component	BDODC	HTRMR	OLGMR	PLYMR
PIA_1	τ_{d_1}	25.5±1.8	3.6±0.3	6.7±0.5	5.1±0.6
	τ_{d_2}		170.4±19.7	101.9±6.1	117.2±21.5
	τ_{d_3}	12950	11270	9490	10640
SE	τ_g	2.9±0.1	0.9±0.1	0.6±0.1	0.6±0.1
	τ_{d_1}	76.3±1.0	29.0±4.2	27.1±1.6	20.5±1.2
	τ_{d_2}		365.4±18.7	280.0±19.0	302.9±18.9
	τ_{d_3}	12950	11270	9490	10640
PIA_2	τ_g	4.6±0.2	1.4±0.1	3.4±0.2	1.5±0.2
	τ_{d_1}	86.2±1.6	114.3±17.6	158.0±87.2	63.7±7.7
	τ_{d_2}		893.2±290.2	951.7±609.4	737.5±116.8
	τ_{d_3}	12950	11270	9490	10640

All Kinetic profiles of the three features from BDODC were fitted adequately to the $\sim 13\,000\,\text{ps}$ component, τ_{d_3}, extracted from its TRPL experiment. Additionally, these profiles required a fast decay component, τ_{d_1}, with values ranging from $25\,\text{ps}$ to $85\,\text{ps}$. Both SE and PIA_2 features of this sample contained a growth component estimated at $<5\,\text{ps}$. Disparity between the value of τ_{d_1} among the three features was evident. In PIA_1, it was $\sim 25\,\text{ps}$, while in SE and PIA_2 it was $>75\,\text{ps}$.
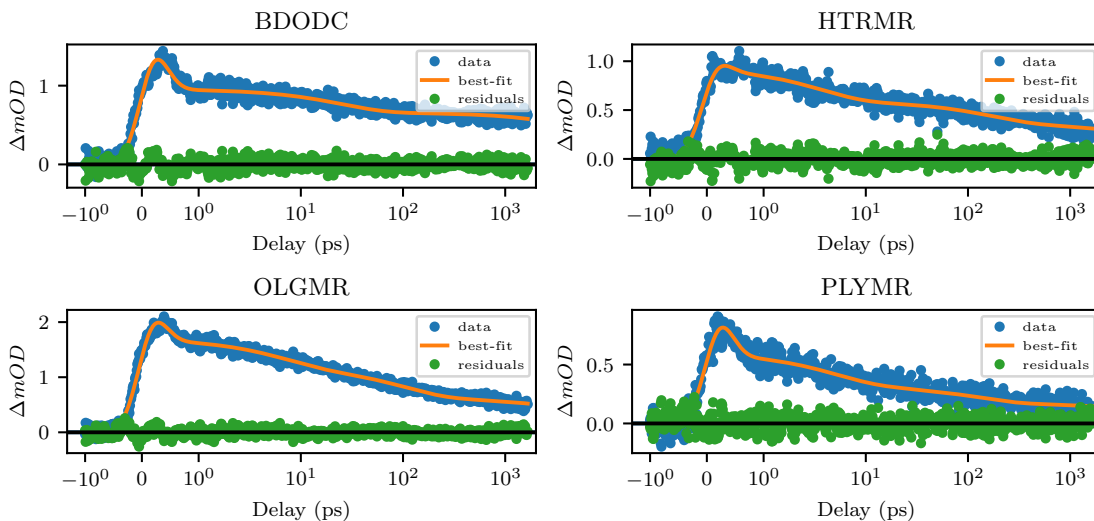
Figure 4.10: Depiction of kinetic fitting quality of the low energy PIA_1 feature. Kinetic profiles were extracted at $E_{probe} = 1.8\,eV$.

This disparity was likely the result of kinetics contamination between the highly overlapping positive and negative features in the observed spectra. The kinetic profile from the PIA_1 feature was likely the purest among the three profiles analyzed. However, the low signal–to–noise ratio in that region elevated the uncertainty associated with its lifetimes. The absence of the growth component from the aforementioned feature further supported this notion. In this spectral region, the growth component was compromised by the strong coherent artifact that dominated the early delay time.

The three macromolecules shared a similar trend of lifetimes among themselves. Their PIA_1 feature exhibited a fast decay component, τ_{d_1}, ranging from $3.6\,ps$ to $6.7\,ps$. These values were a significant decrease from their BDODC's counterpart at $\sim 25\,ps$. In addition to the fast component, an intermediate decay component, τ_{d_2}, estimated at $< 130\,ps$ was observed. Similar to the PIA_1 feature in BDODC, this feature in all three macromolecules lacked any growth component. The wide range of values for τ_{d_1} and τ_{d_2} was a result of the low signal–to–noise ratio and high coherent artifact contamination in this spectral range.

The SE feature of the three macromolecules was fitted adequately with a growth
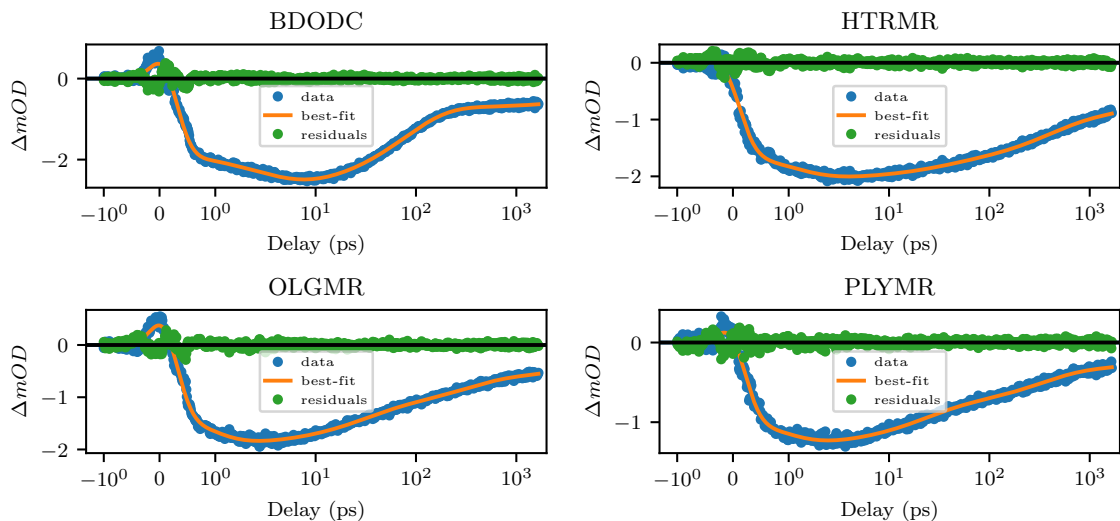
Figure 4.11: Depiction of kinetic fitting quality of the SE feature. Kinetic profiles were extracted at E_{probe} =2.3 eV for BDODC and E_{probe} =2.26 eV for the other three macromolecules.

component and three exponential decay components. The growth component, τ_g, had a relatively consistent estimate at <1 ps. These values were noticeably lower than their BDODC counterparts. In these molecules, the intermediate decay component, τ_{d_2}, ranged from 280 ps to 365 ps. Finally, the estimates of the fast decay component, τ_{d_1}, ranged from 20 ps to 29 ps. These values were also a significant decrease from their BDODC counterparts.

The kinetics of the last feature considered, PIA_2, showed a growth component, τ_g, with closer lifetime values compared to its BDODC counterpart. Values of this growth component ranged from 1.5 ps to 3.4 ps versus $\sim$4.5 ps for BDODC. The values of the intermediate component, τ_{d_2}, ranged from 737 ps to 951 ps. The fast decay component, τ_{d_1}, was estimated in a wide range between 63 ps to 158 ps for the three macromolecules. Nonetheless, these values remained comparable to their BDODC equivalent at $\sim$86 ps. Time constants extracted from this feature showed less consistency compared to the values extracted from both PIA_1 and SE features. The contamination of the kinetics from the PB feature overlapping with the PIA_2 feature was the reason behind this
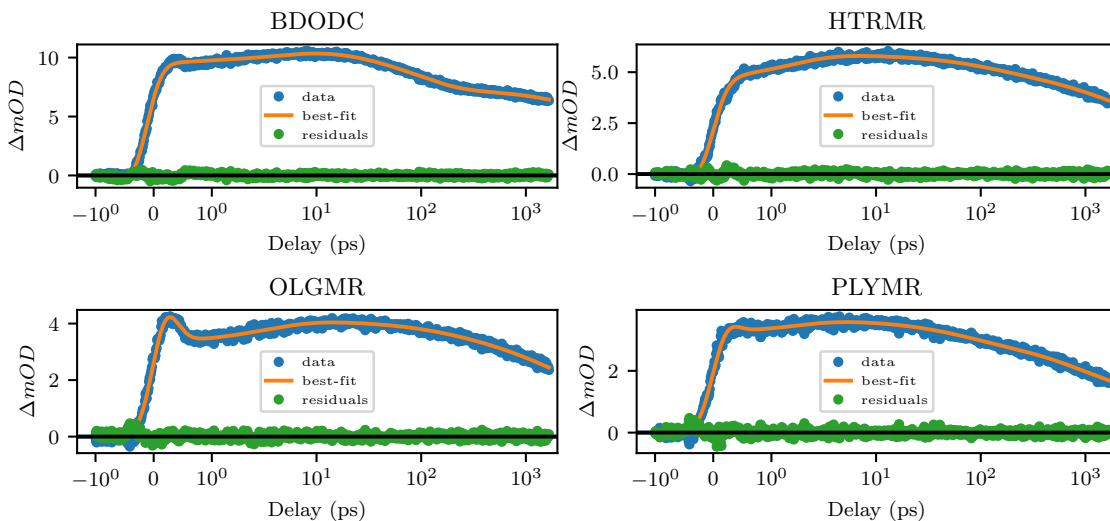
Figure 4.12: Depiction of kinetic fitting quality of the high energy PIA_1 feature. Kinetic profiles were extracted at E_{probe} =2.7 eV for BDODC and E_{probe} =2.55 eV for the other three macromolecules.

departure.

The overall fsTAPP picture from this work deviated from the one previously reported by our group. [85] In the previous report, the PIA_2 band was assumed to originate from the CTS. Therefore, the growth component of PIA_2, τ_g, was assigned to the population process of the CTS. The evidence presented here contradict this assumption as PIA_2 is also present in the isolated BDODC. Based on this evidence, PIA_2 along with SE and PIA_1 were assigned to originate from S_1 instead. As a result, the intermediate decay component, τ_{d_2}, was designated as the CTS population process. Naturally, the growth component of PIA_2, τ_g, was assigned to the internal conversion (IC) and vibrational relaxation (VR) process toward the equilibrium geometry of S_1. Worth noting here that τ_g values of PIA_2 reported in the paper [85] were consistent with the values extracted from the analysis presented here.

The general qualitative picture in these macromolecules remained true despite the poor separation of features that plagued their kinetic profiles. The trends observed in the three explored features indicated a complex depopulation kinetics for the excited

state(s) probed with the fsTAPP measurements. The consistency among the analyzed features for each molecule indicated that all three features originated from the same excited state, likely the S_1. The few picoseconds growth component represented the IC and VR to the S_1 minimum following the photoexcitation. Subsequently, the state depopulated to its triplet excited state via ISC, evident by the presence of the fast component, τ_{d_1}, in all investigated molecules. Simultaneously, S_1 depopulated to the ground state via the PL channel, τ_{d_3}. The introduction of the intermediate component in the macromolecules pointed to a third depopulation channel not present in the isolated BDODC. This channel was likely the CTS observed in the density functional theory (DFT) calculations discussed in Chapter 3. Further discussion, analysis, and proposed energy diagram can be found in Section 5.2.

CHAPTER 5

DISCUSSION AND CONCLUSIONS

This chapter elaborates on the implications of binding and mixing the two [1,4]benzodioxino[3,2-b]oxanthrene (BDO)–based chromophores within the framework of the three investigated macromolecules. These macromolecules were the heterotrimer sub–model (HTRMR), the short–chain oligomer (OLGMR), and the long–chain polymer (PLYMR). Their constituting chromophores were [1,4]benzodioxino[3,2–b]oxanthrene–6,13–dicarbonitrile (BDODC) and [1,4]benzodioxino[3,2–b]oxanthrene–6–(1,3,5–trimethylpyrazole–4-sulfonyl)–13–carbonitrile (BDOSC). Section 5.1 discusses the effects of this binding on the geometry of the two constituting chromophore moieties. This geometry centered discussion is primary based on the results obtained from the density functional theory (DFT) and time–dependent density functional theory (TD–DFT) calculations of the hypothetical heterodimer sub–unit (HDIMR). Section 5.2 focuses on the electronic structure aspects of isolated BDODC and BDOSC and their aforementioned binding. This section utilizes the theoretical modeling of the HDIMR and the spectroscopic studies of the macromolecules. The section summarizes the energies of the ground states and the energies and lifetimes of the excited states of interest. Finally, Section 5.3 lays out the overall observations and conclusions drawn from this work.

5.1 GEOMETRY OF THE CHROMOPHORES AND THE MACROMOLECULES

Chromophores of BDO class investigated in this work displayed several geometrical characteristics of interest. DFT and TD–DFT methods affirmed the ground state planarity of the backbone of BDO, Figure 3.5 in Section 3.4.1. This planarity extended to the homosubstituted BDODC which showed consistent planarity in both isolated and bound environments [13, 33, 38, 40, 85, 168, 181, 182, 184, 185]. The planarity is a result of the effective overlap between the $2p_z$ orbital of the oxygen atoms of the heterocycles and the π_{CC} of the neighboring benzene rings, [7, 158]. This interaction occurs through cross–conjugation which offers a sufficient amount of stability to the backbone; locking it in this planar conformation [172, 202–206]. Planarity of BDOs is one of the factors contributing to the efficient gas permeability and structural stability the polymer of intrinsic microporosity "1" (PIM–1) [33, 57, 64, 207, 208].

This work introduces the heterosubstituted chromophore BDOSC to the PIM–1–like macromolecule. DFT and TD–DFT showed that BDOSC deviates from the typical planarity of BDOs discussed earlier. A folding conformation appeared around the axis passing through the two oxygen atoms within each heterocycle, Figure 5.1a. This folding mounted to about 11° on one side and about 4.5° on the other. Structural analysis of the backbone of BDOSC indicated that the sulfonyl substituent is the major planarity disturber, Section 3.4.1.

In the S_0 of BDOSC, one of the oxygen atoms in the sulfonyl substituent was in the plane with the backbone. The second oxygen atom was in plane the pyrazol ring in the sulfonyl substituent. From Figure 5.1a, the pyrazol and its in–plane oxygen sandwiched the prominently folded side of the backbone. The folding of the opposite side of the backbone was shallower. It was hypothesized that the presence of the in–plane oxygen atom retained the backbone planarity on that side. The in–plane oxygen atom possibly contributed to the conjugation of the backbone. Additionally,
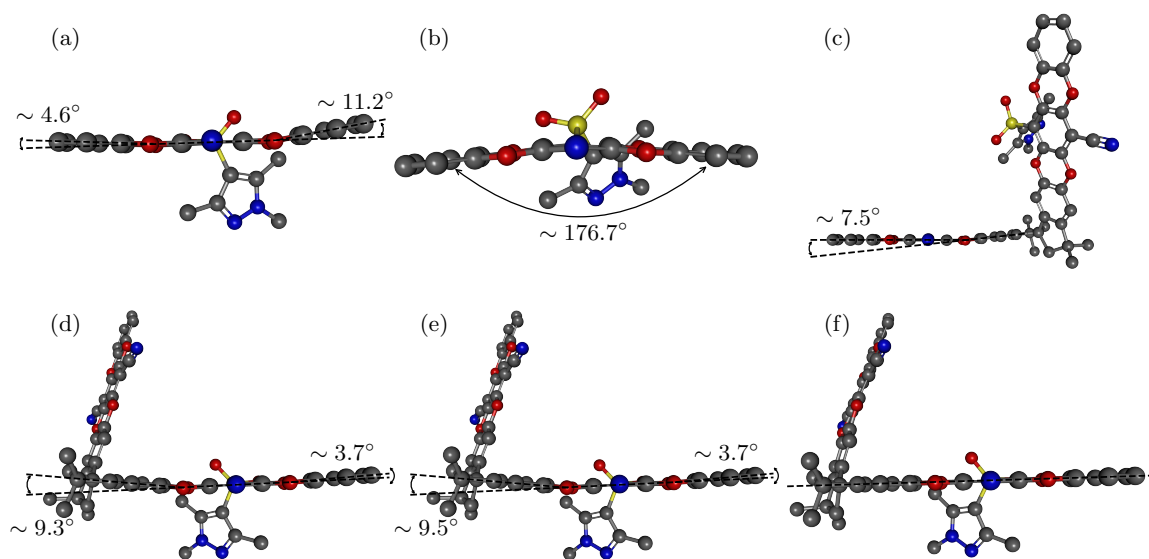
Figure 5.1: Backbone folding of BDOs observed with DFT and TD–DFT. Folding of BDOSC in its singlet ground state (S_0) (a) and first singlet excited state (S_1) (b). (c) Folding of BDODC within the HDIMR in its second singlet excited state (S_2). Folding of BDOSC within the HDIMR in its S_0 (d) S_1 (e) and S_2 (f).

this oxygen atom may exhibit a $C \cdots O$ interaction with the central ring carbon atom similar to the one proposed by Woollins and co–workers [176]. Both of these interactions farther increased the backbone's ability to retain its planarity on that side. On the contrary, the steric and electronic effects of the out–of–plane pyrazol and oxygen atom proved to be strong enough to induce the observed folding. This hypothesis was farther supported by the vertical and lateral disparities of bond lengths and angles between the two sides of the backbone discussed in Section 3.4.1.

The homosubstituted chromophore BDODC retained its planarity in its S_1. Few mild changes were observed in the bond lengths and angles of its backbone corresponding to the charge redistribution across the backbone following the electronic transition. On the contrary, BDOSC underwent significant geometrical changes in its backbone and sulfonyl substituent, Figure 5.1b. In addition to the aforementioned distortions observed in BDODC, the backbone of BDOSC folded in the opposite direction from its S_0 geometry. The folding situated around the axis passing through

the center of the molecule, while the dioxin–centered folding nearly vanished. However, the angle of this central folding was shallower at about 7° compared the dioxin–centered folding of the S_0 at about 11°. Finally, both oxygen atoms of the sulfonyl substituent moved out of the plane of the backbone. This shift came about as the bond of the sulfur atom with the central ring titled out of the plane of the backbone, Figure 5.1b.

The macromolecules, HTRMR, OLGMR, and PLYMR were modeled through the hypothetical HDIMR, Section 3.4.2. The individual chromophore moieties retained their geometrical characteristics within the framework of the HDIMR in its S_0, Figure 5.1d. The prominent folding of BDOSC favored the side closer to the bridge between the two chromophores, i.e. the 3,3,3′,3′-tetramethyl-1,1′-spirobiindan (SPIRO). However, the folding angle decreased from 11° to 9°. In the S_1 of HDIMR, characterized by a localized transition within the BDODC moiety, the geometrical parameters remained consistent with this transition characterization, Figure 5.1e. The vast majority of the geometrical distortions were confined within the BDODC moiety. These distortions were tied to the charge redistribution across the backbone of BDODC following a localized electronic transition.

The S_2 of the HDIMR showed a different set of geometrical distortions compared to the S_1. Most notably was the folding of the backbone of the BDODC moiety by about 7°, Figure 5.1f. Simultaneously, the backbone of BDOSC became planar while the orientation of the sulfonyl substituent remained unchanged, Figure 5.1f. These geometrical distortions were consistent with the predicted charge–transfer state (CTS) nature of S_2, 3.5 and 3.6. Transition to S_2 shifted the electron density from the BDOSC moiety (Donor) to the BDODC moiety (Acceptor). As a result, the depleted electron density within the BDOSC moiety allowed backbone to reverse to the planar conformation. On the other hand, the increased electron density within the BDODC moiety forced the backbone to a folded conformation. The aforementioned observations indicated that the backbone folding of BDOSC was likely due to an

electronic effect more so than a steric effect.

The geometrical characteristics of PIM–1–like macromolecules are of significant importance to their gas separation and permeability applications. The geometry of these macromolecules has been characterized experimentally [13, 15, 16, 19–24] and theoretically [16, 55, 57, 209]. However, none of these studies explored the geometrical implications of introducing a folded BDOSC moiety to the backbone. The closest were theoretical [209] and experimental [210] gas separation studies of sulfonated PIM–1–like polymers. All the aforementioned studies addressed the geometrical characteristics of these macromolecules' S_0, exclusively. TD–DFT, albeit inaccurate, provide one of the few viable methods to explore these characteristics in the excited state(s). As demonstrated earlier, BDODC–BDOSC co–polymer exhibits various conformational states due electronic excitation. When understood, the optically active backbone of these macromolecules can be exploited to fine–tune the pore size of PIM–1–like membranes. The advantage of these procedures arises from the noninvasive, nondestructive, and temporary nature of these electronic states. This work provides a theoretical proof of viability for these procedures. However, additional experimental and theoretical investigations are necessary to validate the predicted outcomes of this work.

5.2 ELECTRONIC TRANSITIONS OF THE CHROMOPHORES AND THE MACROMOLECULES

The importance of understanding the optical characteristics and excited state properties of BDO–based chromophores and macromolecules stem from their potential wide range of applications, Section 1.1. This understanding provide necessary tools to improve their utilization in applications such organic photocatalysis, photovoltaics, and memory devices. The work presented here aims at characterizing the energy and temporal properties of the low–laying excited states of these chromophores. This aim

is achieved through thorough analysis of spectral data acquired from several techniques in conjunction with DFT and TD–DFT calculations.

The properties of the electronic structure of these chromophores can be classified into two main categories. The first is the localized transitions spanning the extent of the five rings of the backbone of the fundamental BDO chromophore. These transitions are characterized as singlet state transitions in the isolated chromophores and visible state (VS) transitions in the macromolecules. Additionally, the analysis found experimental and theoretical indications of triplet excited states of the same transition localization.

The second category includes inter–chromophore transitions. These transitions only exist in the macromolecules and are characterized as CTS transition. This characterization relay on the Frenkel–Davydov exciton model detailed in Section 1.2. CTS transitions involve multiple chromophores throughout the backbone of the macromolecules including the SPIRO bridge. They are influenced by the types of the interacting chromophores as well as their geometrical state. Herein, these transition categories are detailed, with a focus on their characteristics and the underlying mechanisms that govern their population.

5.2.1 TRANSITIONS OF SINGLET (S), TRIPLET (T), AND VISIBLE STATES (VS)

Electronic transition within the BDO–based chromophores in their isolated form are confined to the five rings constituting their backbone. Ultraviolet–visible absorption (UV–VIS) experiments at high concentrations, up to $1\,\text{mM}$, showed no evidence of unbound inter–chromophore interactions. When substituted, the central ring substituents also contribute to the electronic transitions of these chromophores. Additionally, these central ring substituents stabilize one of the two frontier lowest unoccupied molecular orbitals (LUMOs) significantly more than the other. This

disproportional stabilization results in an order flip of the frontier LUMOs. The flip introduces a bright state as S_1 in the place of the dark S_1 found in the unsubstituted BDO.

DFT and TD–DFT calculations revealed the nature of these localized transitions. In the unsubstituted form, both molecular orbitals (MOs) contributing to the transition to S_1 are localized across all five rings of the backbone. Non–bonding orbitals of the oxygen atoms and π–character on the C–C bonds along the short axis of the backbone dominates the contributing highest occupied molecular orbital (HOMO). On the other hand, π^*–character on the C–C bonds along the long axis of the backbone dominates the LUMO of this transition. Details of these MOs are shown in Figure 3.10 on page 81. As mentioned earlier, the S_1 resulting from this transition is characterized as a dark state with a transition oscillator strength value equal to zero. This transition is located in the ultraviolet (UV) region of the electromagnetic spectrum at a vertical excitation energy of $\sim$3.74 eV. Following the transition to S_1, the central ring carries a slightly higher electron density compared to the density of the S_0. This deviation is likely the by–product of the contribution of the oxygen atoms to the HOMO involved in this transition.

Table 5.1: Summary of transition energy estimates from the theoretical and experimental methods. "Bound" represented the chromophore moiety in the HDIMR or the macromolecules. $CTS_{BDOSC \to BDODC}$ represented the lowest inter–chromophore transition. In this configuration BDOSC was the donor and BDODC was the acceptor. All energy estimates were in eV.

Type		Vertical ($S_0 \to S_1$)		Adiabatic ($S_1 \to S_0$)	
		Experimental	Theoretical	Experimental	Theoretical
BDO	Isolated		3.74		3.25
BDODC	Isolated	2.92	2.77	2.58	2.34
	Bound	2.83	2.72	2.50	2.27
BDOSC	Isolated		2.96		2.29
	Bound	3.06	2.91		
$CTS_{BDOSC \to BDOSC}$			2.86	2.37	2.27

The S_1 transition of the homosubstituted BDODC is characterized differently. The order flip of the frontier LUMOs in this chromophore compared to the unsubstituted BDO resulted in a bright S_1. Here, the HOMO contributing to the transition to S_1 is identical to the one in the unsubstituted BDO. However, the newly introduced LUMO is localized primarily on the central ring. This MO is dominated by π^*–character on the C–C bonds along the short axis of the backbone. The π^* of the carbonitrile substituents also contributes to this LUMO. Additionally, the non–bonding orbitals of the oxygen atoms in the heterocycles contributes to this LUMO unlike the LUMO of BDO. Table 5.1 summarizes transition energies of all investigated BDO chromophores.

TD–DFT estimated the S_1 vertical excitation energy of the homosubstituted BDODC at $\sim 2.77\,\text{eV}$ with an oscillator strength of ~ 0.2387. Experimentally, this transition energy was estimated from the UV–VIS line fitting at $\sim 2.92\,\text{eV}$. These values mark a significant shift to the visible (VIS) electromagnetic region compared to the unsubstituted BDO. This shift, in addition to this state's bright nature, is the primary reasons behind the usability of substituted BDOs in photocatalysis and photovoltaics applications. UV–VIS data and TD–DFT calculations reported by Zheng and co–workers indicated a similar behavior in terminally substituted BDOs. [21]

The adiabatic, S_1 to S_0, transition energy of BDODC was estimated at $\sim 2.34\,\text{eV}$. Its experimental equivalent, extracted from photoluminescence (PL) data, was estimated at $\sim 2.57\,\text{eV}$. Here, TD–DFT exhibited a larger underestimation error of $\sim 0.23\,\text{eV}$ compared to the vertical excitation error of $\sim 0.15\,\text{eV}$. The electrostatic potential maps (ESPs) of the S_0 and S_1 of this chromophore, Figure 3.8 on page 77, revealed an electron density depletion on the central ring following the photoexcitation. Additionally, the terminal rings seemed to carry higher electron density in the S_1 state compared to the S_0 state. Both of these observations were tied to the contribution of

the oxygen atoms to this transition.

Characteristics of the S_1 of BDOSC were largely similar to its BDODC counterparts. The MOs of this chromophore retained the LUMOs flip from the unsubstituted version. Similar to the dicarbonitrile case, this LUMO extended throughout most of the sulfonyl–pyrazol and carbonitrile substituents. This expansion was an indication of the extended conjugation overlap between the backbone of the chromophore and the pyrazol. However, the stabilization of the LUMOs here was less dramatic. Therefore, the S_1 vertical excitation energy was estimated at a higher value, $\sim$2.96 eV, with an oscillator strength of $\sim$0.2285. The adiabatic transition energy in this chromophore was estimated at $\sim$2.29 eV. Charge redistribution due to this electronic transition was similar to that of the homosubstituted form, BDODC. An increase in the electron localization on the terminal rings was evident, while the central ring suffered more electron depletion. These changes were consistent with the localization of the MOs involved in these transitions as well as the contribution from the oxygen atoms in the heterocycles.

The macromolecules studied in this work were modeled using the hypothetical HDIMR. This model contained the substituted chromophores, BDODC and BDOSC, bound through a SPIRO bridge. The electronic transitions of interest in this model, predicted by TD–DFT, were of two different natures: dark and bright. In this section, only the bright states, the S_1 and the third singlet excited state (S_3), were discussed. These bright states were characterized as localized transitions. The BDODC moiety was responsible for the S_1 transition, while BDOSC moiety was responsible for the S_3 transition. The topological localization of these transitions was primarily inferred through the MOs involved in each transition, Figure 3.11 on page 82. This interpretation was additionally supported by the ESP comparisons between the ground and excited states of these transitions. See Figure 3.9 on page 79.

The vertical excitation energy of the BDODC moiety in the HDIMR was predicted

by TD–DFT at $\sim$2.72 eV. This transition energy deviated by $<$0.02 eV from the isolated form. The oscillator strength of this transition was estimated at $\sim$0.2713, indicating a transition intensity enhancement from the isolated form by $\sim$0.033. These values suggested a minimal perturbation to the localized vertical excitation of BDODC between the isolated and bound forms. However, the transition probability seemed to exhibit a significant enhancement when bound in the HDIMR. Vertical excitation energy estimates, extracted from the decomposition analysis of the UV–VIS data of the three macromolecules, averaged $\sim$2.82 eV. Here, the underestimation error from the TD–DFT of the HDIMR compared to the experimental estimates average was $\sim$0.1 eV. This value was comparable to the estimation error associated with the isolated BDODC, further indicating a successful modeling with TD–DFT. Adiabatic transition energy of the BDODC moiety was located by TD–DFT at $\sim$2.27 eV. Its experimental equivalent, extracted from the PL decomposition analysis was estimated at $\sim$2.50 eV. The underestimation of the adiabatic transition energy in TD–DFT was $\sim$0.23 eV. This underestimation was consistent with the values computed for the isolated form. The ESPs of the HDIMR in its S_0 and S_1 revealed charge redistribution confined to the BDODC moiety. This confined charge redistribution was similar to that of the isolated form.

The bright electronic transition associated with BDOSC moiety was predicted as S_3. Its vertical excitation energy was estimated by TD–DFT at $\sim$2.91 eV. Experimentally, this transition was estimated from UV–VIS decomposition analysis at an average of $\sim$3.06 eV. Underestimation error of this transition energy was also consistent with the underestimations discussed earlier at $\sim$0.15 eV. The equilibrium geometry of this excited state was not located through TD–DFT calculations. Therefor, no direct adiabatic excitation energy nor ESP was formulated for this state. However, if an assumption of consistent underestimation error for both moieties can be made, a rough estimation of this transition energy may be drawn. The adiabatic excitation energy of

the isolated form of BDODC was blue shifted by $\sim 0.07\,\text{eV}$ from its isolated form. On the other hand, the adiabatic excitation energy of the isolated form of BDOSC was located at $\sim 2.29\,\text{eV}$. Therefore, the adiabatic excitation energy of the bound form of BDOSC may be estimated at $\sim 2.22\,\text{eV}$. The large Stokes shift associated with this chromophore can be explained by the significant geometrical changes associated with its excited state. It was worth noting here that this state may be inaccessible in the bound form due to the presence of less hindered relaxation pathways. Some of these pathways involved the first VS state, S_1, and the first CTS, S_2, present in the HDIMR.

The first triplet excited state (T_1) was located using TD–DFT in the isolated chromophores and the HDIMR. In both BDODC and the HDIMR, the transition nature was localized within the backbone of the BDODC. Vertical excitation energies of these states were estimated at $\sim 2.10\,\text{eV}$ for the isolated BDODC and $\sim 2.08\,\text{eV}$ for the HDIMR. Their adiabatic transition energies were estimated at $1.74\,\text{eV}$ and $1.84\,\text{eV}$, respectively. Similar to the singlet excited states, this transition was not significantly perturbed due to the binding of the two chromophores. Experimentally, there was no conclusive evidence of the location of the T_1 from either the PL or the delayed photoluminescence (dPL) spectra. However, the femtosecond transient absorption pump–probe (fsTAPP) spectroscopy experiments showed indications of intersystem crossing (ISC) from the S_1 to the T_1.

5.2.2   TRANSITIONS OF THE CHARGE–TRANSFER STATES (CTS)

In the HDIMR, two states, the S_2 and the fourth singlet excited state (S_4), were characterized as CTSs. This characterization was inferred from the MOs involved in these transitions as well as their dark nature. Frenkel–Davydov exciton model can be utilized to explain the underlying phenomenon responsible for their presence, Section 1.2. Briefly, the model approximates the wavefunction of S_0 of the HDIMR as the dot product of the wavefunctions of the two ground states of the constituting

chromophores. The model also predicts four different excited states resulting from inter–chromophore interactions within the HDIMR. The wavefunctions of these four states are represented using the dot products of the ground, excited, donor, and acceptor wavefunctions of the two constituting chromophores. The first two, S_1 and S_3 discussed in the previous section, are localized on each chromophore moiety and denoted as VSs. The other two, characterized as inter–chromophore transitions, appeared as S_2 and S_4 in the excited states manifold of the HDIMR

The upper state, S_4, seems to be inaccessible due to its high energy and geometrical requirements associated with the excitation of BDOSC moiety. On the other hand, the lower state, S_2, was predicted to have significant involvement in the electronic structure of the HDIMR and by extension the investigated macromolecules. Vertical excitation energy of this state was estimated at ~2.86 eV, just ~0.14 eV above the first VS, S_1. Its near–dark nature with an oscillator strength of ~0.0042, prevented its detection in the UV–VIS experiments. The adiabatic transition energy of this state was estimated at ~2.27 eV, identical to the energy associated with the first visible state S_1. However, the molecular geometry of this state was vastly different from that of S_1. As discussed in Section 5.1, the CTS exhibited folding of the planar moiety, BDODC, and planarity of the folded moiety, BDOSC. Charge redistribution across the entire backbone of the HDIMR was evident in the ESP of this state compared to the S_0.

A minor emission component was isolated using the decomposition analysis of the PL spectra of the macromolecules. This component contributed <5% of the total emission collected for each macromolecule. The central transition energy of this component averaged at ~2.37 eV. This component was assigned as emission from the CTS. This assignment was rationalized by the consistent contribution of this component across PL spectra collected using various excitation energies, 2.6 eV to 3.6 eV. Additionally, TD–DFT failed to locate the equilibrium geometry of the S_3.

This failure indicated that localized excitation in the BDOSC moiety relaxes to either S_1 or S_2 prior to radiative relaxation to the S_0. Transitions energies of the CTS were summarized in Table 5.1.

5.2.3 PROPOSED ENERGY DIAGRAMS AND THE SEQUENCES OF PROCESSES

The presented results, experimental and theoretical, formulates a clear picture for the processes in the excited state manifold of the isolated chromophores. In the homosubstituted chromophore, BDODC, the processes followed a straight forward path. Following the photoexcitation, the chromophore relaxes to its S_1 equilibrium geometry through a series of internal conversions (ICs) and vibrational relaxations (VRs). These processes unfold within the first 5 ps after the photoexcitation. Once the chromophore relaxes to its S_1, this excited state deactivates through two main pathways: ISC and PL. The time constant of the ISC pathway was approximated at $\sim$60 ps. This rate was relatively fast compared to a typical ISC in organic chromophores, indicating an efficient population of the T_1. The time constant of the second pathway, PL, was approximately at 13 ns. No detection was made for the time constant of the deactivation of the T_1. However, based on the dPL measurements, the value may be assumed larger than few microseconds. These time constants are summarized in Table 5.2. Depiction of these processes and the overall energy diagram is presented under BDODC in Figure 5.2.

The macromolecules posed a bigger challenge due to their geometrical and energetic inter–chromophore interactions. The DFT modeling of these macromolecules using the HDIMR proved beneficial. When utilizing the picture formulated from the HDIMR, coupled with the experimental results of the macromolecules, a simplified picture can be drawn. See HDIMR in Figure 5.2. Similar to BDODC, a series of IC and VR processes carry the macromolecules to their S_1 after the photoexcitation.

Table 5.2: Summary of time constant estimates extracted from fsTAPP and time–resolved photoluminescence (TRPL) experiments. Time constant labels referred to the usage in Figure 5.2. Listed values of τ_g, τ_{d_1}, and τ_{d_2} represented the average of all similar time constants extracted from the three features analyzed from the fsTAPP.

transition	label	unit	BDODC	HTRMR	OLGMR	PLYMR
$S_{1(IC/VR)}$	τ_g	(ps)	3.75	1.15	2.00	1.05
$S_1 \rightarrow T_{1(ISC)}$	τ_{d_1}	(ps)	62.7	49.0	64.0	29.8
$S_1 \rightarrow S_{2(charge–transfer\ (CT))}$	τ_{d_2}	(ps)		476.3	444.5	385.9
$S_1 \rightarrow S_{0(PL)}$	τ_{d_3}	(ns)	13.0	11.3	9.5	10.6
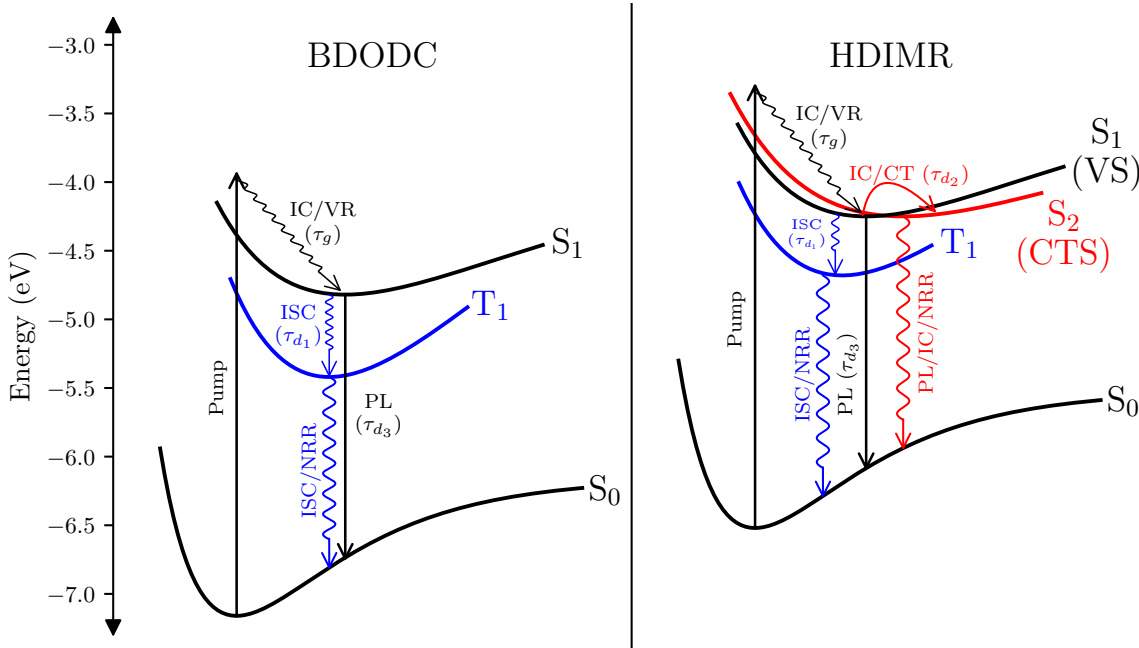
Figure 5.2: Proposed energy diagrams and excited state processes observed in the studied models. Energy level positioning was scaled according to the results obtained from DFT and TD–DFT calculations. Arrows indicated processes expected or observed from the steady–state and time–dependent spectroscopy measurements and analysis. The time constants (τ) associated with these processes were listed in Table 5.2.

Compared to the isolated BDODC, the overall time constant for these processes was relatively smaller in the macromolecules at <2 ps. The smaller time constant in the macromolecules implies more accessible relaxation pathways from the higher electronic and vibrational excited states to the equilibrium geometry of S_1. Once these relaxations are completed, S_1 deactivation occurs through the two pathways observed in the isolated chromophore: ISC and PL. Time constants of the ISC for the HTRMR,

OLGMR, and PLYMR were 49 ps, 64 ps and 30 ps, respectively. Table 5.2 lists these relevant time constants. The ISC rate is dependent on the size and chromophoric composition of the macromolecule. The fastest ISC was observed in the PLYMR. On the other hand, the slowest was observed in the OLGMR, which was comparable to that of the isolated chromophore.

All macromolecules showed enhancement of their second deactivation pathway, PL, time constant compared to the isolated chromophore, BDODC. The fastest was the OLGMR at $\sim$9.5 ns. The PLYMR was next at $\sim$10.5 ns, then the HTRMR at $\sim$11.3 ns. The trend here showed a relation between the size and chromophoric composition of the macromolecules and their PL time constant. While the size seemed to slow the PL deactivation pathway, the chromophoric composition played a more significant role in its enhancement.

A third deactivation pathway of the S_1 is observed in these macromolecules, labeled as a CT process. This pathway is the result of the inter–chromophore interactions across the backbone. In this particular CT process, the BDOSC moiety acts as a donor and the BDODC is the acceptor. The time constants of this process are approximated at 476 ps, 445 ps and 386 ps for the HTRMR, the OLGMR, and the PLYMR, respectively. These values are considered similar, due to the significant error associated with their approximation from fsTAPP spectroscopy experiments. While they fall with an order of magnitude higher than the ISC deactivation pathway, they are still considered competitive with the long lifetime of the PL pathway. Analysis of the steady–state PL experiments showed that the position of the CTS was $\sim$0.1 eV higher than predicted value from TD–DFT. On the other hand, the error in main state estimation, S_1, was $\sim$0.23 eV. These analyses also indicated that the population of the CTS was consistent regardless of the excitation energy used. Both of these observations further supported the notion that the deactivation of S_1 through the CT process was competitive with the other two deactivation pathways.

The overall picture assembled from this work offers the necessary explanation for the catalytic activity observed for the BDO–based macromolecules. [85] Evidence suggests the presence of both long–lived CTS and T_1 in these macromolecules' excited state manifold. Population of these states via photoexcitation allows electron extraction with external acceptors during a catalyzed reaction. Similarly, depopulation of the ground state following a photoexcitation allows for electron extraction from external donors during the catalytic process. See Figure 5.3.
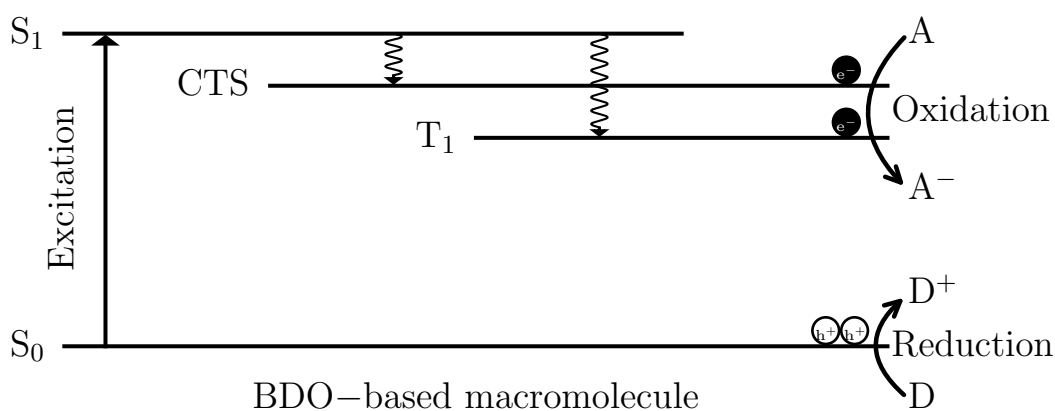
Figure 5.3: Diagram depicting the photocatalytic activity of BDO–based polymers.

5.3 CONCLUSIONS

The geometry and electronic structure of three isolated chromophores of the BDO class were studied theoretically using DFT and TD–DFT methods. These chromophores were the unsubstituted BDO, the homosubstituted BDODC, and the heterosubstituted BDOSC. The electronic structure of BDODC was also studied experimentally using various types of steady–state and time–dependent spectroscopy techniques. Theoretical methods predicted a planar geometry and a dark S_1 for the unsubstituted BDO. This state was approximated to be in the UV region of the electromagnetic spectrum. Simulation of the ESP of BDO indicated an electron–rich backbone with electron density distributed across all five rings of its backbone.

The introduction of electron–withdrawing groups (EWGs) in the substituted variants, BDODC and BDOSC, lowered their overall total energy. Their ESPs showed electron–depleted backbone compared to the unsubstituted variant. This depletion was higher on the central ring compared to the terminal rings. The majority of the electron density was located on the substituents. The homosubstituted form, BDODC, remained planar while the heterosubstituted form, BDOSC, lost its planarity to a backbone folding. This folding, located within the heterocycles of the backbone, was more prominent on one side versus the other. Evidence suggested that the oxygen atoms in the sulfonyl substituent in BDOSC played a major role in the observed folding. This type of backbone folding have been observed experimentally in similar BDO–based chromophores and macromolecules. [15, 19, 23, 24] This folding provides a rationale to the improved gas selectivity observed for sulfonated PIM–1–like polymers reported by Ma and co–workers. [210]

TD–DFT methods predicted that the S_1 of both substituted variants was bright. This dramatic change of S_1 characteristics was explained by an order flip of the two lowest LUMOs induced by the EWG effect of the substituents. This order flip coupled with the stabilization effect of the EWGs red–shifted vertical excitation of the substituted BDOs by $>1\,\text{eV}$ compared to BDO. The red–shit placed these S_1 transition in the VIS region of the electromagnetic spectrum. Therefore, substituents on the central ring of BDO chromophores represent the primary tool to tune their electronic transitions for photocatalytic and photovoltaic applications.

Time–dependent spectroscopy measurements of BDODC indicated that its S_1 deactivates through PL and ISC pathways. Evidence suggests that the ISC pathway is efficient in this class of chromophores. The presence and efficiency of T_1 in these chromophores indicate their ability to perform well in photocatalytic and photovoltaic applications. Population of the long–lived T_1 can be extracted by external acceptors such as reactants and electrodes. This photocatalytic efficiency of BDODC was

demonstrated in our recent report. [85]

The substituted variants BDODC and BDOSC were also studied in the framework of larger macromolecules using theoretical and spectroscopic methods. These macromolecules took the form of short and long PIM–1–like co–polymers. These co–polymers contained both BDODC and BDOSC bound together through a SPIRO bridge. Three macromolecules, the HTRMR, the OLGMR, and the PLYMR were investigated using spectroscopic methods. DFT and TD–DFT methods utilized a hypothetical HDIMR to elucidate the geometries and electronic structures of these macromolecules.

Modeling of the HDIMR indicated a minimal perturbation to the localized geometries and electronic transitions of these chromophores within the framework of the macromolecules. These perturbations included a less dramatic folding of the backbone of BDOSC compared to its isolated form. Additionally, these methods revealed inter–chromophore interactions between the constituting chromophores. These interactions included the delocalization of the HOMO of each chromophore over its neighboring chromophores through the SPIRO bridge. Subsequently, TD–DFT methods predicted an inter–chromophore electronic transition with a CT character.

TD–DFT methods showed that the excited states manifold of the macromolecules was dominated by localized electronic transitions within the domains of each chromophore. These methods predicted that all higher excited state eventually relaxed to the S_1 of these macromolecules, which was localized on the BDODC moiety. Deactivation of this S_1 was similar to that of the isolated form in which PL and ISC pathways were observed. The rates of these deactivation processes were comparable to the ones in the isolated BDODC. However, the rates of these processes appeared to vary slightly among the three macromolecules. These variations were dependent on the size and chromophoric composition of the macromolecule, with the latter playing a more significant role. Overall, these factors proportionally enhanced the rate of deactivation

137

through the ISC pathway. They also improved the rate of VR and IC to the S_1 from higher vibrational and electronic states. Poor chromophoric composition appeared to further enhance the deactivation through the PL pathway compared to the effect of the macromolecular size. These trends showed that the control of chromophoric composition take priority over molecular size when designing and manufacturing these macromolecules for photocatalytic and photovoltaic applications.

The inter–chromophore electronic transition with CT character was strictly observed in the bound form of the chromophores. Experiments with the isolated form of BDODC indicated that no such interaction existed when the chromophore was not bound. Frenkel–Davydov exciton model, Section 1.2, rationalized the presence of this CTS in the excited state manifold of the HDIMR. This state appeared to have strong interaction with the S_1 of the HDIMR which is localized over the BDODC moiety. In this state, the BDOSC acted as a donor and BDODC was the acceptor. Deactivation of S_1 to the CTS was independent of the chromophoric composition or the size of the macromolecule. This suggested that the CTS was primary confined to two or three neighboring chromophore moieties. The rate of deactivation to this state was slower than that of the T_1. However, experimental data suggested this deactivation pathway was efficient and competitive with the other two pathways.

Photocatalysis and photovoltaic applications value the experimental and theoretical characterizations presented in this work and our previous report. [85] Understanding the origins of the strong red–shift exhibited by substituted BDOs provide the necessary tools to fine–tune their electronic structure. Various EWG substituents on the central and terminal rings can position BDOs' excited states for optimal catalytic performance. Furthermore, a fine–tuned mix of substituted BDOs may provide the necessary spectral coverage for high–performance photovoltaic applications. The presence of efficiently populated and long–lived T_1 and CTS offers a rationale for the observed photocatalytic activity of these macromolecules. [85] Electronic population of these

states may be extracted by external acceptors such as reactants and electrodes in photocatalytic applications and photovoltaic devices.

Conformational analysis of the isolated chromophores and their macromolecules are of value to the gas separation applications of BDO–based co–polymers. The analysis of the sulfonated BDOSC offers a rationale to the enhanced gas selectivity demonstrated by Ma and co–workers. [210] Additionally, the optically active backbone of the macromolecules can be exploited to fine–tune the pore size of PIM–1–like membranes through direct photoexcitation. This procedure is advantageous for being noninvasive, nondestructive, and temporary in nature. While a theoretical proof of viability for these procedures is offer in this work, additional experimental and theoretical investigations are necessary to validate the predicted outcomes.

The work presented here represents the first steps in a comprehensive understanding of the electronic structure of BDO–based chromophores and macromolecules. Further experimental and theoretical characterization of the T_1 and CTS is necessary. Low temperature spectroscopy studies are need to locate and characterize the T_1. Additionally, comparative study on a larger macromolecular set is needed to understand the energy and lifetime trends observed among the macromolecules. Finally, quantum chemical calculations with higher level of theory is required to provide an undisputed evidence of the CTS characteristics.

REFERENCES

[1] Darsow, G.; Schnell, H. Chlorine-containing aromatic dioxine compounds and process for the production thereof, US3799944, 1974, eprint: https://www.freepatentsonline.com/3799944.html.

[2] Oliver, J. E.; Lusby, W. R. 2,3,9,10-Tetrachlorobenzo[1,2-b:4,5-b']bis[1,4]benzodioxin, a homologue of TCDD. *Journal of Heterocyclic Chemistry* **1978**, *15*, 689–690, DOI: 10.1002/jhet.5570150436.

[3] Dembek, A. A.; Fagan, P. J. Synthesis of (η5-Pentamethylcyclopentadienyl)ruthenium π-Complexes of Heterocycles by Nucleophilic Substitution†. *Organometallics* **1996**, *15*, 1319–1322, DOI: 10.1021/om9507686.

[4] Hellberg, J.; Pelcman, M. E. Synthesis of annulated dioxins and their use as donors for cation radical salts. *Tetrahedron Letters* **1994**, *35*, 1769–1772, DOI: 10.1016/0040-4039(94)88342-4.

[5] Hellberg, J.; Dahlstedt, E.; Pelcman, M. E. Synthesis of annulated dioxins as electron-rich donors for cation radical salts. *Tetrahedron* **2004**, *60*, 8899–8912, DOI: 10.1016/j.tet.2004.07.017.

[6] Woldegiorgis, A.; von Kieseritzky, F.; Dahlstedt, E.; Hellberg, J.; Brinck, T.; Roeraade, J. Polymer-assisted laser desorption/ionization analysis of small molecular weight compounds. *Rapid Communications in Mass Spectrometry* **2004**, *18*, 841–852, DOI: 10.1002/rcm.1412.

[7] Vidal, B. Near UV Spectroscopy and Electronic Structure of Dibenzo-p-dioxin, the Parent Compound of Highly Food-Polluting Agents. *Chemical Papers-Slovak Academy of Sciences* **2003**, *57*, 112–118, eprint: https://chempap.org/file_access.php?file=572a112.pdf.

[8] Apell, J. N.; Kliegman, S.; Solá-Gutiérrez, C.; McNeill, K. Linking Triclosan's Structural Features to Its Environmental Fate and Photoproducts. *Environmental Science & Technology* **2020**, *54*, 14432–14441, DOI: 10.1021/acs.est.0c05121.

[9] Mason, C. R.; Maynard-Atem, L.; Al-Harbi, N. M.; Budd, P. M.; Bernardo, P.; Bazzarelli, F.; Clarizia, G.; Jansen, J. C. Polymer of Intrinsic Microporosity Incorporating Thioamide Functionality: Preparation and Gas Transport Properties. *Macromolecules* **2011**, *44*, 6471–6479, DOI: 10.1021/ma200918h.

[10] Chen, S.; Yi, W.; Duhamel, J.; Heinrich, K.; Bengtson, G.; Fritsch, D. Effect of the Porosity of a Polymer of Intrinsic Microporosity (PIM) on Its Intrinsic Fluorescence. *The Journal of Physical Chemistry B* **2013**, *117*, 5249–5260, DOI: 10.1021/jp307173k.

[11] Santoso, B.; Yanaranop, P.; Kang, H.; Leung, I. K. H.; Jin, J. A Critical Update on the Synthesis of Carboxylated Polymers of Intrinsic Microporosity (C-PIMs). *Macromolecules* **2017**, *50*, 3043–3050, DOI: 10.1021/acs.macromol.7b00344.

[12] Wang, X.; Liu, Y.; Ma, X.; Das, S. K.; Ostwal, M.; Gadwal, I.; Yao, K.; Dong, X.; Han, Y.; Pinnau, I.; Huang, K.-W.; Lai, Z. Soluble Polymers with Intrinsic Porosity for Flue Gas Purification and Natural Gas Upgrading. *Advanced Materials* **2017**, *29*, 1605826, DOI: 10.1002/adma.201605826.

[13] Zhang, B.; Wei, M.; Mao, H.; Pei, X.; Alshmimri, S. A.; Reimer, J. A.; Yaghi, O. M. Crystalline Dioxin-Linked Covalent Organic Frameworks from Irreversible

Reactions. *Journal of the American Chemical Society* **2018**, *140*, 12715–12719, DOI: 10.1021/jacs.8b08374.

[14] Guan, X.; Li, H.; Ma, Y.; Xue, M.; Fang, Q.; Yan, Y.; Valtchev, V.; Qiu, S. Chemically stable polyarylether-based covalent organic frameworks. *Nature Chemistry* **2019**, *11*, 587–594, DOI: 10.1038/s41557-019-0238-5.

[15] Ponomarev, I. I.; Lyssenko, K. A.; Razorenov, D. Y.; Volkova, Y. A.; Ponomarev, I. I.; Skupov, K. M.; Klemenkova, Z. S.; Starannikova, L. E.; Alentiev, A. Y.; Yampolskii, Y. P. New approach to chemical modification of PIM-1 for gas separation membranes. *Mendeleev Communications* **2019**, *29*, 663–665, DOI: 10.1016/j.mencom.2019.11.020.

[16] Hiscock, L. K.; Yao, C.; Skene, W. G.; Dawe, L. N.; Maly, K. E. Synthesis of Emissive Heteroacene Derivatives via Nucleophilic Aromatic Substitution. *The Journal of Organic Chemistry* **2019**, *84*, 15530–15537, DOI: 10.1021/acs.joc.9b02523.

[17] Foster, A. B.; Tamaddondar, M.; Luque-Alled, J. M.; Harrison, W. J.; Li, Z.; Gorgojo, P.; Budd, P. M. Understanding the Topology of the Polymer of Intrinsic Microporosity PIM-1: Cyclics, Tadpoles, and Network Structures and Their Impact on Membrane Performance. *Macromolecules* **2020**, *53*, 569–583, DOI: 10.1021/acs.macromol.9b02185.

[18] Lai, J.; Fianchini, M.; Pericàs, M. A. Development of Immobilized SPINOL-Derived Chiral Phosphoric Acids for Catalytic Continuous Flow Processes. Use in the Catalytic Desymmetrization of 3,3-Disubstituted Oxetanes. *ACS Catalysis* **2020**, *10*, 14971–14983, DOI: 10.1021/acscatal.0c04497.

[19] Taylor, R. G. D.; Bezzu, C. G.; Carta, M.; Msayib, K. J.; Walker, J.; Short, R.; Kariuki, B. M.; McKeown, N. B. The Synthesis of Organic Molecules of Intrinsic

Microporosity Designed to Frustrate Efficient Molecular Packing. *Chemistry - A European Journal* **2016**, *22*, 2466–2472, DOI: 10.1002/chem.201504212.

[20] Maly, K. E.; Buck, W.; Dawe, L. N. Open network structures from 2D hydrogen bonded networks: diaminotriazyl tetraoxapentacenes. *CrystEngComm* **2017**, *19*, 6401–6405, DOI: 10.1039/c7ce01247k.

[21] Yuan, Y.-X.; Wu, B.-X.; Xiong, J.-B.; Zhang, H.-C.; Hu, M.; Zheng, Y.-S. Exceptional aggregation-induced emission from one totally planar molecule. *Dyes and Pigments* **2019**, *170*, 107556, DOI: 10.1016/j.dyepig.2019.107556.

[22] Hiscock, L. K.; Raycraft, B. M.; Wałęsa-Chorab, M.; Cambe, C.; Malinge, A.; Skene, W. G.; Taing, H.; Eichhorn, S. H.; Dawe, L. N.; Maly, K. E. Synthesis and Characterization of Liquid-Crystalline Tetraoxapentacene Derivatives Exhibiting Aggregation-Induced Emission. *Chemistry – A European Journal* **2018**, DOI: 10.1002/chem.201804215.

[23] Short, R.; Carta, M.; Bezzu, C. G.; Fritsch, D.; Kariuki, B. M.; McKeown, N. B. Hexaphenylbenzene-based polymers of intrinsic microporosity. *Chemical Communications* **2011**, *47*, 6822, DOI: 10.1039/c1cc11717c.

[24] Taylor, R. G. D.; Carta, M.; Bezzu, C. G.; Walker, J.; Msayib, K. J.; Kariuki, B. M.; McKeown, N. B. Triptycene-Based Organic Molecules of Intrinsic Microporosity. *Organic Letters* **2014**, *16*, 1848–1851, DOI: 10.1021/ol500591q.

[25] Mckeown, N. B.; Makhseed, S. (of Manchester, U.). Organic microporous materials, US20040198587A1, 2004, eprint: https://www.freepatentsonline.com/y2004/0198587.html.

[26] Budd, P. M.; Ghanem, B. S.; Makhseed, S.; McKeown, N. B.; Msayib, K. J.; Tattershall, C. E. Polymers of intrinsic microporosity (PIMs): robust, solution-

processable, organic nanoporous materials. *Chemical Communications* **2004**, 230, DOI: 10.1039/b311764b.

[27] Budd, P. M.; Msayib, K. J.; Tattershall, C. E.; Ghanem, B. S.; Reynolds, K. J.; McKeown, N. B.; Fritsch, D. Gas separation membranes from polymers of intrinsic microporosity. *Journal of Membrane Science* **2005**, *251*, 263–269, DOI: 10.1016/j.memsci.2005.01.009.

[28] McKeown, N. B.; Budd, P. M. Polymers of intrinsic microporosity (PIMs): organic materials for membrane separations, heterogeneous catalysis and hydrogen storage. *Chemical Society Reviews* **2006**, *35*, 675, DOI: 10.1039/b600349d.

[29] Budd, P. M.; McKeown, N. B.; Fritsch, D. Polymers of Intrinsic Microporosity (PIMs): High Free Volume Polymers for Membrane Applications. *Macromolecular Symposia* **2006**, *245-246*, 403–405, DOI: 10.1002/masy.200651356.

[30] Budd, P. M.; Butler, A.; Selbie, J.; Mahmood, K.; McKeown, N. B.; Ghanem, B.; Msayib, K.; Book, D.; Walton, A. The potential of organic polymer-based hydrogen storage materials. *Physical Chemistry Chemical Physics* **2007**, *9*, 1802, DOI: 10.1039/b618053a.

[31] De Miranda, R. L.; Kruse, J.; Rätzke, K.; Faupel, F.; Fritsch, D.; Abetz, V.; Budd, P. M.; Selbie, J. D.; McKeown, N. B.; Ghanem, B. S. Unusual temperature dependence of the positron lifetime in a polymer of intrinsic microporosity. *physica status solidi (RRL) – Rapid Research Letters* **2007**, *1*, 190–192, DOI: 10.1002/pssr.200701116.

[32] Mackintosh, H. J.; Budd, P. M.; McKeown, N. B. Catalysis by microporous phthalocyanine and porphyrin network polymers. *Journal of Materials Chemistry* **2008**, *18*, 573–578, DOI: 10.1039/b715660j.

[33] Heuchel, M.; Fritsch, D.; Budd, P. M.; McKeown, N. B.; Hofmann, D. Atomistic packing model and free volume distribution of a polymer with intrinsic

microporosity (PIM-1). *Journal of Membrane Science* **2008**, *318*, 84–99, DOI: `10.1016/j.memsci.2008.02.038`.

[34] Carta, M.; Msayib, K. J.; Budd, P. M.; McKeown, N. B. Novel Spirobisindanes for Use as Precursors to Polymers of Intrinsic Microporosity. *Organic Letters* **2008**, *10*, 2641–2643, DOI: `10.1021/ol800573m`.

[35] Carta, M.; Msayib, K. J.; McKeown, N. B. Novel polymers of intrinsic microporosity (PIMs) derived from 1,1-spiro-bis(1,2,3,4-tetrahydronaphthalene)-based monomers. *Tetrahedron Letters* **2009**, *50*, 5954–5957, DOI: `10.1016/j.tetlet.2009.08.032`.

[36] McKeown, N. B.; Budd, P. M. Exploitation of Intrinsic Microporosity in Polymer-Based Materials. *Macromolecules* **2010**, *43*, 5163–5176, DOI: `10.1021/ma1006396`.

[37] Emmler, T.; Heinrich, K.; Fritsch, D.; Budd, P. M.; Chaukura, N.; Ehlers, D.; Rätzke, K.; Faupel, F. Free Volume Investigation of Polymers of Intrinsic Microporosity (PIMs): PIM-1 and PIM1 Copolymers Incorporating Ethanoanthracene Units. *Macromolecules* **2010**, *43*, 6075–6084, DOI: `10.1021/ma1008786`.

[38] Carta, M.; Raftery, J.; McKeown, N. B. Crystal Structures of 5,6,5',6'-Tetramethoxy-1,1'-spirobisindane-3,3'-dione and two of its Fluorene Adducts. *Journal of Chemical Crystallography* **2011**, *41*, 98–104, DOI: `10.1007/s10870-010-9844-1`.

[39] Carta, M.; Helliwell, M.; McKeown, N. B. Crystal Structures of a Series of 1,1-Spiro-bis(1,2,3,4-tetrahydronaphthalene)-Based Derivatives. *Journal of Chemical Crystallography* **2011**, *42*, 111–118, DOI: `10.1007/s10870-011-0211-7`.

[40] Bezzu, C. G.; Carta, M.; Tonkins, A.; Jansen, J. C.; Bernardo, P.; Bazzarelli, F.; McKeown, N. B. A Spirobifluorene-Based Polymer of Intrinsic Microporosity

with Improved Performance for Gas Separation. *Advanced Materials* **2012**, *24*, 5930–5933, DOI: `10.1002/adma.201202393`.

[41] McKeown, N. B. Polymers of Intrinsic Microporosity. *ISRN Materials Science* **2012**, *2012*, 1–16, DOI: `10.5402/2012/513986`.

[42] Satilmis, B.; Budd, P. M. Base-catalysed hydrolysis of PIM-1: amide versus carboxylate formation. *RSC Adv.* **2014**, *4*, 52189–52198, DOI: `10.1039/c4ra09907a`.

[43] Razali, M.; Kim, J. F.; Attfield, M.; Budd, P. M.; Drioli, E.; Lee, Y. M.; Szekely, G. Sustainable wastewater treatment and recycling in membrane manufacturing. *Green Chemistry* **2015**, *17*, 5196–5205, DOI: `10.1039/c5gc01937k`.

[44] Konnertz, N.; Ding, Y.; Harrison, W. J.; Budd, P. M.; Schönhals, A.; Böhning, M. Molecular Mobility of the High Performance Membrane Polymer PIM-1 as Investigated by Dielectric Spectroscopy. *ACS Macro Letters* **2016**, *5*, 528–532, DOI: `10.1021/acsmacrolett.6b00209`.

[45] Konnertz, N.; Ding, Y.; Harrison, W. J.; Budd, P. M.; Schönhals, A.; Böhning, M. Molecular mobility and gas transport properties of nanocomposites based on PIM-1 and polyhedral oligomeric phenethyl-silsesquioxanes (POSS). *Journal of Membrane Science* **2017**, *529*, 274–285, DOI: `10.1016/j.memsci.2017.02.007`.

[46] Madrid, E.; Lowe, J. P.; Msayib, K. J.; McKeown, N. B.; Song, Q.; Attard, G. A.; Düren, T.; Marken, F. Triphasic Nature of Polymers of Intrinsic Microporosity Induces Storage and Catalysis Effects in Hydrogen and Oxygen Reactivity at Electrode Surfaces. *ChemElectroChem* **2018**, *6*, 252–259, DOI: `10.1002/celc.201800177`.

[47] Yin, H.; Chua, Y. Z.; Yang, B.; Schick, C.; Harrison, W. J.; Budd, P. M.; Böhning, M.; Schönhals, A. First Clear-Cut Experimental Evidence of a Glass

Transition in a Polymer with Intrinsic Microporosity: PIM-1. *The Journal of Physical Chemistry Letters* **2018**, *9*, 2003–2008, DOI: 10.1021/acs.jpclett.8b00422.

[48] Issam, A. M.; Shahabuddin, S.; Kareem, H. S.; Mohamad, S.; Saidur, R. Synthesis of a Novel Ladder Poly(azomethine-ester) Based on PET Waste Bottles. *International Polymer Processing* **2019**, *34*, 296–306, DOI: 10.3139/217.3595.

[49] Rong, Y.; Large, M. J.; Tripathi, M.; Ogilvie, S. P.; Graf, A. A.; Mao, B.; Tunesi, J.; Salvage, J. P.; King, A. A. K.; Pasquazi, A.; Peccianti, M.; Malpass-Evans, R.; McKeown, N. B.; Marken, F.; Dalton, A. B. Charge Transfer Hybrids of Graphene Oxide and the Intrinsically Microporous Polymer PIM-1. *ACS Applied Materials & Interfaces* **2019**, *11*, 31191–31199, DOI: 10.1021/acsami.9b09832.

[50] Longo, M.; Santo, M. P. D.; Esposito, E.; Fuoco, A.; Monteleone, M.; Giorno, L.; Comesaña-Gándara, B.; Chen, J.; Bezzu, C. G.; Carta, M.; Rose, I.; McKeown, N. B.; Jansen, J. C. Correlating Gas Permeability and Young's Modulus during the Physical Aging of Polymers of Intrinsic Microporosity Using Atomic Force Microscopy. *Industrial & Engineering Chemistry Research* **2019**, *59*, 5381–5391, DOI: 10.1021/acs.iecr.9b04881.

[51] Zorn, R.; Lohstroh, W.; Zamponi, M.; Harrison, W. J.; Budd, P. M.; Böhning, M.; Schönhals, A. Molecular Mobility of a Polymer of Intrinsic Microporosity Revealed by Quasielastic Neutron Scattering. *Macromolecules* **2020**, *53*, 6731–6739, DOI: 10.1021/acs.macromol.0c00963.

[52] Felemban, S. A.; Bezzu, C. G.; Comesaña-Gándara, B.; Jansen, J. C.; Fuoco, A.; Esposito, E.; Carta, M.; McKeown, N. B. Synthesis and gas permeation proper-

ties of tetraoxidethianthrene-based polymers of intrinsic microporosity. *Journal of Materials Chemistry A* **2021**, *9*, 2840–2849, DOI: `10.1039/d0ta10134f`.

[53] Kricheldorf, H. R.; Lomadze, N.; Fritsch, D.; Schwarz, G. Cyclic and telechelic ladder polymers derived from tetrahydroxytetramethylspirobisindane and 1,4-dicyanotetrafluorobenzene. *Journal of Polymer Science Part A: Polymer Chemistry* **2006**, *44*, 5344–5352, DOI: `10.1002/pola.21627`.

[54] Du, N.; Robertson, G. P.; Song, J.; Pinnau, I.; Guiver, M. D. High-Performance Carboxylated Polymers of Intrinsic Microporosity (PIMs) with Tunable Gas Transport Properties†. *Macromolecules* **2009**, *42*, 6038–6043, DOI: `10.1021/ma9009017`.

[55] Larsen, G. S.; Lin, P.; Siperstein, F. R.; Colina, C. M. Methane adsorption in PIM-1. *Adsorption* **2010**, *17*, 21–26, DOI: `10.1007/s10450-010-9281-7`.

[56] Laghari, G. M. Preparation and Properties of polybenzodioxane PIM-1 and its copolymers with poly(ethylene glycol), Ph.D. Thesis, The University of Manchester, 2011, 211 pp., eprint: `https://www.research.manchester.ac.uk/portal/files/54508324/FULL_TEXT.PDF`.

[57] Larsen, G. S.; Lin, P.; Hart, K. E.; Colina, C. M. Molecular Simulations of PIM-1-like Polymers of Intrinsic Microporosity. *Macromolecules* **2011**, *44*, 6944–6951, DOI: `10.1021/ma200345v`.

[58] Li, F. Y.; Xiao, Y.; Ong, Y. K.; Chung, T.-S. UV-Rearranged PIM-1 Polymeric Membranes for Advanced Hydrogen Purification and Production. *Advanced Energy Materials* **2012**, *2*, 1456–1466, DOI: `10.1002/aenm.201200296`.

[59] Li, F. Y.; Chung, T.-S. Physical aging, high temperature and water vapor permeation studies of UV-rearranged PIM-1 membranes for advanced hydrogen purification and production. *International Journal of Hydrogen Energy* **2013**, *38*, 9786–9793, DOI: `10.1016/j.ijhydene.2013.05.056`.

[60] Yong, W. F.; Li, F. Y.; Chung, T. S.; Tong, Y. W. Molecular interaction, gas transport properties and plasticization behavior of cPIM-1/Torlon blend membranes. *Journal of Membrane Science* **2014**, *462*, 119–130, DOI: `10.1016/j.memsci.2014.03.046`.

[61] Frentrup, H.; Hart, K.; Colina, C.; Müller, E. In Silico Determination of Gas Permeabilities by Non-Equilibrium Molecular Dynamics: CO2 and He through PIM-1. *Membranes* **2015**, *5*, 99–119, DOI: `10.3390/membranes5010099`.

[62] Liao, K.-S.; Lai, J.-Y.; Chung, T.-S. Metal ion modified PIM-1 and its application for propylene/propane separation. *Journal of Membrane Science* **2016**, *515*, 36–44, DOI: `10.1016/j.memsci.2016.05.032`.

[63] Ponomarev, I. I.; Blagodatskikh, I. V.; Muranov, A. V.; Volkova, Y. A.; Razorenov, D. Y.; Ponomarev, I. I.; Skupov, K. M. Dimethyl sulfoxide as a green solvent for successful precipitative polyheterocyclization based on nucleophilic aromatic substitution, resulting in high molecular weight PIM-1. *Mendeleev Communications* **2016**, *26*, 362–364, DOI: `10.1016/j.mencom.2016.07.033`.

[64] Kupgan, G.; Demidov, A. G.; Colina, C. M. Plasticization behavior in polymers of intrinsic microporosity (PIM-1): A simulation study from combined Monte Carlo and molecular dynamics. *Journal of Membrane Science* **2018**, *565*, 95–103, DOI: `10.1016/j.memsci.2018.08.004`.

[65] Dong, G.; Zhang, J.; Wang, Z.; Wang, J.; Zhao, P.; Cao, X.; Zhang, Y. Interfacial Property Modulation of PIM-1 through Polydopamine-Derived Submicrospheres for Enhanced CO2/N2 Separation Performance. *ACS Applied Materials & Interfaces* **2019**, *11*, 19613–19622, DOI: `10.1021/acsami.9b02281`.

[66] Wang, P.; Liu, Z.; Li, X.; Peng, J.; Hu, W.; Liu, B. Toward enhanced conductivity of high-temperature proton exchange membranes: development of novel

PIM-1 reinforced PBI alloy membranes. *Chemical Communications* **2019**, *55*, 6491–6494, DOI: 10.1039/c9cc02102g.

[67]   Jin, J.; Zhang, J. Polymers of intrinsic microporosity (PIMs) containing locked spirobisindane structures and methods of synthesis of PIMs polymers, 20190153154, 2019, eprint: http://www.freepatentsonline.com/y2019/0153154.html.

[68]   Wang, S.; Shi, K.; Tripathi, A.; Chakraborty, U.; Parsons, G. N.; Khan, S. A. Designing Intrinsically Microporous Polymer (PIM-1) Microfibers with Tunable Morphology and Porosity via Controlling Solvent/Nonsolvent/Polymer Interactions. *ACS Applied Polymer Materials* **2020**, *2*, 2434–2443, DOI: 10.1021/acsapm.0c00386.

[69]   Ranjith, K. S.; Satilmis, B.; Huh, Y. S.; Han, Y.-K.; Uyar, T. Highly selective surface adsorption-induced efficient photodegradation of cationic dyes on hierarchical ZnO nanorod-decorated hydrolyzed PIM-1 nanofibrous webs. *Journal of Colloid and Interface Science* **2020**, *562*, 29–41, DOI: 10.1016/j.jcis.2019.11.096.

[70]   Anstine, D. M.; Demidov, A. G.; Mendez, N. F.; Morgan, W. J.; Colina, C. M. Screening PIM-1 performance as a membrane for binary mixture separation of gaseous organic compounds. *Journal of Membrane Science* **2020**, *599*, 117798, DOI: 10.1016/j.memsci.2019.117798.

[71]   Li, J.; Zhang, M.; Feng, W.; Zhu, L.; Zhang, L. PIM-1 pore-filled thin film composite membranes for tunable organic solvent nanofiltration. *Journal of Membrane Science* **2020**, *601*, 117951, DOI: 10.1016/j.memsci.2020.117951.

[72]   Liu, M.; Lu, X.; Nothling, M. D.; Doherty, C. M.; Zu, L.; Hart, J. N.; Webley, P. A.; Jin, J.; Fu, Q.; Qiao, G. G. Physical Aging Investigations of

a Spirobisindane-Locked Polymer of Intrinsic Microporosity. *ACS Materials Letters* **2020**, *2*, 993–998, DOI: `10.1021/acsmaterialslett.0c00184`.

[73]   Hiscock, L. K. Synthesis, Properties, and Solid-State Structures of a Series of 6,13-Dicyanoheteropentacene Analogues: Towards New Liquid Crystalline Materials, MA thesis, Wilfrid Laurier University, 2018, eprint: `https://scholars.wlu.ca/etd/2073`.

[74]   Hiscock, L. K.; Maly, K. E.; Dawe, L. N. Crystal Packing of a Series of 1,2,3,4-Substituted Phenoxazine and Dibenzodioxin Heterocycles. *Crystal Growth & Design* **2019**, *19*, 7298–7307, DOI: `10.1021/acs.cgd.9b01184`.

[75]   Aliyev, E.; Warfsmann, J.; Tokay, B.; Shishatskiy, S.; Lee, Y.-J.; Lillepaerg, J.; Champness, N. R.; Filiz, V. Gas Transport Properties of the Metal–Organic Framework (MOF)-Assisted Polymer of Intrinsic Microporosity (PIM-1) Thin-Film Composite Membranes. *ACS Sustainable Chemistry & Engineering* **2020**, *9*, 684–694, DOI: `10.1021/acssuschemeng.0c06297`.

[76]   Han, J.; Bai, L.; Jiang, H.; Zeng, S.; Yang, B.; Bai, Y.; Zhang, X. Task-Specific Ionic Liquids Tuning ZIF-67/PIM-1 Mixed Matrix Membranes for Efficient CO2 Separation. *Industrial & Engineering Chemistry Research* **2020**, *60*, 593–603, DOI: `10.1021/acs.iecr.0c04830`.

[77]   Chen, W.; Zhang, Z.; Hou, L.; Yang, C.; Shen, H.; Yang, K.; Wang, Z. Metal-organic framework MOF-801/PIM-1 mixed-matrix membranes for enhanced CO2/N2 separation performance. *Separation and Purification Technology* **2020**, *250*, 117198, DOI: `10.1016/j.seppur.2020.117198`.

[78]   Muldoon, P. F.; Venna, S. R.; Gidley, D. W.; Baker, J. S.; Zhu, L.; Tong, Z.; Xiang, F.; Hopkinson, D. P.; Yi, S.; Sekizkardes, A. K.; Rosi, N. L. Mixed Matrix Membranes from a Microporous Polymer Blend and Nanosized Metal–Organic

Frameworks with Exceptional CO2/N2 Separation Performance. *ACS Materials Letters* **2020**, *2*, 821–828, DOI: 10.1021/acsmaterialslett.0c00156.

[79] Ozcan, A.; Semino, R.; Maurin, G.; Yazaydin, A. O. Modeling of Gas Transport through Polymer/MOF Interfaces: A Microsecond-Scale Concentration Gradient-Driven Molecular Dynamics Study. *Chemistry of Materials* **2020**, *32*, 1288–1296, DOI: 10.1021/acs.chemmater.9b04907.

[80] Sánchez-Laínez, J.; Pardillos-Ruiz, A.; Carta, M.; Malpass-Evans, R.; McKeown, N. B.; Téllez, C.; Coronas, J. Polymer engineering by blending PIM-1 and 6FDA-DAM for ZIF-8 containing mixed matrix membranes applied to CO2 separations. *Separation and Purification Technology* **2019**, *224*, 456–462, DOI: 10.1016/j.seppur.2019.05.035.

[81] Xu, J.; Ma, S.; Li, Y.; Li, X.; Ou, J.; Ye, M. Thiol-functionalized PIM-1 for removal and sensing for mercury (II). *Journal of Environmental Chemical Engineering* **2020**, *8*, 104545, DOI: 10.1016/j.jece.2020.104545.

[82] Gu, P.-Y.; Zhou, F.; Gao, J.; Li, G.; Wang, C.; Xu, Q.-F.; Zhang, Q.; Lu, J.-M. Synthesis, Characterization, and Nonvolatile Ternary Memory Behavior of a Larger Heteroacene with Nine Linearly Fused Rings and Two Different Heteroatoms. *Journal of the American Chemical Society* **2013**, *135*, 14086–14089, DOI: 10.1021/ja408208c.

[83] Bonso, J. S.; Kalaw, G. D.; Ferraris, J. P. High surface area carbon nanofibers derived from electrospun PIM-1 for energy storage applications. *J. Mater. Chem. A* **2014**, *2*, 418–424, DOI: 10.1039/c3ta13779a.

[84] Molefe, L. Y.; Musyoka, N. M.; Ren, J.; Langmi, H. W.; Mathe, M.; Ndungu, P. G. Polymer-Based Shaping Strategy for Zeolite Templated Carbons (ZTC) and Their Metal Organic Framework (MOF) Composites for Improved Hydro-

gen Storage Properties. *Frontiers in Chemistry* **2019**, *7*, DOI: 10.3389/fchem.2019.00864.

[85] Smith, J. D.; Jamhawi, A. M.; Jasinski, J. B.; Gallou, F.; Ge, J.; Advincula, R.; Liu, J.; Handa, S. Organopolymer with dual chromophores and fast charge-transfer properties for sustainable photocatalysis. *Nature Communications* **2019**, *10*, DOI: 10.1038/s41467-019-09316-5.

[86] Frenkel, J. On the Transformation of light into Heat in Solids. I. *Physical Review* **1931**, *37*, 17–44, DOI: 10.1103/physrev.37.17.

[87] Davydov, A. S. The theory of molecular excitons. *Soviet Physics Uspekhi* **1964**, *7*, 145–178, DOI: 10.1070/pu1964v007n02abeh003659.

[88] Heid, C. G.; Ottiger, P.; Leist, R.; Leutwyler, S. TheS1/S2exciton interaction in 2-pyridone·6-methyl-2-pyridone: Davydov splitting, vibronic coupling, and vibronic quenching. *The Journal of Chemical Physics* **2011**, *135*, 154311, DOI: 10.1063/1.3652759.

[89] Zeng, T.; Hoffmann, R.; Ananth, N. The Low-Lying Electronic States of Pentacene and Their Roles in Singlet Fission. *Journal of the American Chemical Society* **2014**, *136*, 5755–5764, DOI: 10.1021/ja500887a.

[90] Morrison, A. F.; You, Z.-Q.; Herbert, J. M. Ab Initio Implementation of the Frenkel–Davydov Exciton Model: A Naturally Parallelizable Approach to Computing Collective Excitations in Crystals and Aggregates. *Journal of Chemical Theory and Computation* **2014**, *10*, 5366–5376, DOI: 10.1021/ct500765m.

[91] Cary 50 Spectrometer Hardware Manual, 9th ed.; Agilent Technologies, 2011, eprint: https://www.agilent.com/cs/library/usermanuals/public/1596.pdf.

[92] Reichardt, C., *Solvents and Solvent Effects in Organic Chemistry*; Wiley: 2002, DOI: 10.1002/3527601791.

[93] van der Walt, S.; Colbert, S. C.; Varoquaux, G. The NumPy Array: A Structure for Efficient Numerical Computation. *Computing in Science Engineering* **2011**, *13*, 22–30, DOI: 10.1109/MCSE.2011.37.

[94] Virtanen, P.; Gommers, R.; Oliphant, T. E.; Haberland, M.; Reddy, T.; Cournapeau, D.; Burovski, E.; Peterson, P.; Weckesser, W.; Bright, J.; van der Walt, S. J.; Brett, M.; Wilson, J.; Millman, K. J.; Mayorov, N.; Nelson, A. R. J.; Jones, E.; Kern, R.; Larson, E.; Carey, C. J.; Polat, İ.; Feng, Y.; Moore, E. W.; VanderPlas, J.; Laxalde, D.; Perktold, J.; Cimrman, R.; Henriksen, I.; Quintero, E. A.; Harris, C. R.; Archibald, A. M.; Ribeiro, A. H.; Pedregosa, F.; van Mulbregt, P. SciPy 1.0: fundamental algorithms for scientific computing in Python. *Nature Methods* **2020**, *17*, 261–272, DOI: 10.1038/s41592-019-0686-2.

[95] Koziol, Q.; Robinson, D. HDF5, en, 2018, DOI: 10.11578/DC.20180330.1.

[96] Newville, M.; Stensitzki, T.; Allen, D. B.; Ingargiola, A. LMFIT: Non-Linear Least-Square Minimization and Curve-Fitting for Python, 2014, DOI: 10.5281/zenodo.11813.

[97] Siano, D. B.; Metzler, D. E. Band Shapes of the Electronic Spectra of Complex Molecules. *The Journal of Chemical Physics* **1969**, *51*, 1856–1861, DOI: 10.1063/1.1672270.

[98] Burstein, E. A.; Emelyanenko, V. I. Log-Normal Description of Fluorescence Spectra of Organic Fluorophores. *Photochemistry and Photobiology* **1996**, *64*, 316–320, DOI: 10.1111/j.1751-1097.1996.tb02464.x.

[99] Hunter, J. D. Matplotlib: A 2D Graphics Environment. *Computing in Science Engineering* **2007**, *9*, 90–95, DOI: 10.1109/MCSE.2007.55.

[100] Strickland, D.; Mourou, G. Compression of amplified chirped optical pulses. *Optics Communications* **1985**, *56*, 219–221, DOI: `10.1016/0030-4018(85)90120-8`.

[101] Murray, J. E.; Lowdermilk, W. H. ND:YAG regenerative amplifier. *Journal of Applied Physics* **1980**, *51*, 3548–3556, DOI: `10.1063/1.328194`.

[102] Lowdermilk, W. H.; Murray, J. E. The multipass amplifier: Theory and numerical analysis. *Journal of Applied Physics* **1980**, *51*, 2436, DOI: `10.1063/1.328014`.

[103] Nelson, L. E.; Jones, D. J.; Tamura, K.; Haus, H. A.; Ippen, E. P. Ultrashort-pulse fiber ring lasers. *Applied Physics B: Lasers and Optics* **1997**, *65*, 277–294, DOI: `10.1007/s003400050273`.

[104] CPA–series user Manual; Clark–MXR, Inc., 2010.

[105] Manzoni, C.; Cerullo, G. Design criteria for ultrafast optical parametric amplifiers. *Journal of Optics* **2016**, *18*, 103501, DOI: `10.1088/2040-8978/18/10/103501`.

[106] NOPA user Manual; Clark–MXR, Inc., 2010.

[107] LightWise camera series specification and user guide, LW-5-S-1394 FireWire Smart Digital Imaging Module, 2nd ed.; Imaging Solutions Group of NY, Inc., 2004, eprint: `http://isgcameras.com/wp-content/uploads/2015/09/ISG_LW-5-S-1394-C_Datasheet_UG.pdf`.

[108] Hohenberg, P.; Kohn, W. Inhomogeneous Electron Gas. *Physical Review* **1964**, *136*, B864–B871, DOI: `10.1103/physrev.136.b864`.

[109] Kohn, W.; Sham, L. J. Self-Consistent Equations Including Exchange and Correlation Effects. *Physical Review* **1965**, *140*, A1133–A1138, DOI: `10.1103/physrev.140.a1133`.

[110] Kohn, W.; Becke, A. D.; Parr, R. G. Density Functional Theory of Electronic Structure. *The Journal of Physical Chemistry* **1996**, *100*, 12974–12980, DOI: 10.1021/jp960669l.

[111] Goerigk, L.; Mehta, N. A Trip to the Density Functional Theory Zoo: Warnings and Recommendations for the User. *Australian Journal of Chemistry* **2019**, *72*, 563, DOI: 10.1071/ch19023.

[112] Perdew, J. P. In *AIP Conference Proceedings*, AIP: 2001, DOI: 10.1063/1.1390175.

[113] Becke, A. D. Density-functional exchange-energy approximation with correct asymptotic behavior. *Physical Review A* **1988**, *38*, 3098–3100, DOI: 10.1103/physreva.38.3098.

[114] Lee, C.; Yang, W.; Parr, R. G. Development of the Colle-Salvetti correlation-energy formula into a functional of the electron density. *Physical Review B* **1988**, *37*, 785–789, DOI: 10.1103/physrevb.37.785.

[115] Miehlich, B.; Savin, A.; Stoll, H.; Preuss, H. Results obtained with the correlation energy density functionals of becke and Lee, Yang and Parr. *Chemical Physics Letters* **1989**, *157*, 200–206, DOI: 10.1016/0009-2614(89)87234-3.

[116] Perdew, J. P. Density-functional approximation for the correlation energy of the inhomogeneous electron gas. *Physical Review B* **1986**, *33*, 8822–8824, DOI: 10.1103/physrevb.33.8822.

[117] Perdew, J. P. Erratum: Density-functional approximation for the correlation energy of the inhomogeneous electron gas. *Physical Review B* **1986**, *34*, 7406–7406, DOI: 10.1103/physrevb.34.7406.

[118] Slater, J. C. A Simplification of the Hartree-Fock Method. *Physical Review* **1951**, *81*, 385–390, DOI: 10.1103/physrev.81.385.

[119]   Vosko, S. H.; Wilk, L.; Nusair, M. Accurate spin-dependent electron liquid cor-
relation energies for local spin density calculations: a critical analysis. *Canadian Journal of Physics* **1980**, *58*, 1200–1211, DOI: `10.1139/p80-159`.

[120]   Perdew, J. P.; Wang, Y. Accurate and simple analytic representation of the electron-gas correlation energy. *Physical Review B* **1992**, *45*, 13244–13249, DOI: `10.1103/physrevb.45.13244`.

[121]   Peverati, R.; Truhlar, D. G. Exchange–Correlation Functional with Good Accuracy for Both Structural and Energetic Properties while Depending Only on the Density and Its Gradient. *Journal of Chemical Theory and Computation* **2012**, *8*, 2310–2319, DOI: `10.1021/ct3002656`.

[122]   Becke, A. D. Density-functional thermochemistry. III. The role of exact ex-
change. *The Journal of Chemical Physics* **1993**, *98*, 5648–5652, DOI: `10.1063/1.464913`.

[123]   Stephens, P. J.; Devlin, F. J.; Chabalowski, C. F.; Frisch, M. J. Ab Initio Calculation of Vibrational Absorption and Circular Dichroism Spectra Using Density Functional Force Fields. *The Journal of Physical Chemistry* **1994**, *98*, 11623–11627, DOI: `10.1021/j100096a001`.

[124]   Ernzerhof, M.; Scuseria, G. E. Assessment of the Perdew–Burke–Ernzerhof exchange-correlation functional. *The Journal of Chemical Physics* **1999**, *110*, 5029–5036, DOI: `10.1063/1.478401`.

[125]   Adamo, C.; Barone, V. Toward reliable density functional methods without adjustable parameters: The PBE0 model. *The Journal of Chemical Physics* **1999**, *110*, 6158–6170, DOI: `10.1063/1.478522`.

[126]   Grimme, S. Semiempirical hybrid density functional with perturbative second-
order correlation. *The Journal of Chemical Physics* **2006**, *124*, 034108, DOI: `10.1063/1.2148954`.

[127] Goerigk, L.; Grimme, S. Efficient and Accurate Double-Hybrid-Meta-GGA Density Functionals—Evaluation with the Extended GMTKN30 Database for General Main Group Thermochemistry, Kinetics, and Noncovalent Interactions. *Journal of Chemical Theory and Computation* **2010**, *7*, 291–309, DOI: 10.1021/ct100466k.

[128] Kozuch, S.; Gruzman, D.; Martin, J. M. L. DSD-BLYP: A General Purpose Double Hybrid Density Functional Including Spin Component Scaling and Dispersion Correction. *The Journal of Physical Chemistry C* **2010**, *114*, 20801–20808, DOI: 10.1021/jp1070852.

[129] Kozuch, S.; Martin, J. M. L. DSD-PBEP86: in search of the best double-hybrid DFT with spin-component scaled MP2 and dispersion corrections. *Physical Chemistry Chemical Physics* **2011**, *13*, 20104, DOI: 10.1039/c1cp22592h.

[130] Kozuch, S.; Martin, J. M. L. Spin-component-scaled double hybrids: An extensive search for the best fifth-rung functionals blending DFT and perturbation theory. *Journal of Computational Chemistry* **2013**, n/a–n/a, DOI: 10.1002/jcc.23391.

[131] Chai, J.-D.; Head-Gordon, M. Long-range corrected double-hybrid density functionals. *The Journal of Chemical Physics* **2009**, *131*, 174105, DOI: 10.1063/1.3244209.

[132] Goerigk, L.; Casanova-Paéz, M. The Trip to the Density Functional Theory Zoo Continues: Making a Case for Time-Dependent Double Hybrids for Excited-State Problems. *Australian Journal of Chemistry* **2021**, *74*, 3, DOI: 10.1071/ch20093.

[133] Runge, E.; Gross, E. K. U. Density-Functional Theory for Time-Dependent Systems. *Physical Review Letters* **1984**, *52*, 997–1000, DOI: 10.1103/physrevlett.52.997.

[134] Gross, E.; Kohn, W. In *Advances in Quantum Chemistry*; Elsevier: 1990, pp 255–291, DOI: 10.1016/s0065-3276(08)60600-0.

[135] Bauernschmitt, R.; Ahlrichs, R. Treatment of electronic excitations within the adiabatic approximation of time dependent density functional theory. *Chemical Physics Letters* **1996**, *256*, 454–464, DOI: 10.1016/0009-2614(96)00440-x.

[136] Sim, E.; Song, S.; Burke, K. Quantifying Density Errors in DFT. *The Journal of Physical Chemistry Letters* **2018**, *9*, 6385–6392, DOI: 10.1021/acs.jpclett.8b02855.

[137] Bao, J. L.; Gagliardi, L.; Truhlar, D. G. Self-Interaction Error in Density Functional Theory: An Appraisal. *The Journal of Physical Chemistry Letters* **2018**, *9*, 2353–2358, DOI: 10.1021/acs.jpclett.8b00242.

[138] Hait, D.; Head-Gordon, M. Delocalization Errors in Density Functional Theory Are Essentially Quadratic in Fractional Occupation Number. *The Journal of Physical Chemistry Letters* **2018**, *9*, 6280–6288, DOI: 10.1021/acs.jpclett.8b02417.

[139] Vuckovic, S.; Song, S.; Kozlowski, J.; Sim, E.; Burke, K. Density Functional Analysis: The Theory of Density-Corrected DFT. *Journal of Chemical Theory and Computation* **2019**, *15*, 6636–6646, DOI: 10.1021/acs.jctc.9b00826.

[140] Lonsdale, D. R.; Goerigk, L. The one-electron self-interaction error in 74 density functional approximations: a case study on hydrogenic mono- and dinuclear systems. *Physical Chemistry Chemical Physics* **2020**, *22*, 15805–15830, DOI: 10.1039/d0cp01275k.

[141] Frisch, M. J.; Trucks, G. W.; Schlegel, H. B.; Scuseria, G. E.; Robb, M. A.; Cheeseman, J. R.; Scalmani, G.; Barone, V.; Petersson, G. A.; Nakatsuji, H.; Li, X.; Caricato, M.; Marenich, A. V.; Bloino, J.; Janesko, B. G.; Gomperts, R.; Mennucci, B.; Hratchian, H. P.; Ortiz, J. V.; Izmaylov, A. F.; Sonnenberg,

J. L.; Williams-Young, D.; Ding, F.; Lipparini, F.; Egidi, F.; Goings, J.; Peng, B.; Petrone, A.; Henderson, T.; Ranasinghe, D.; Zakrzewski, V. G.; Gao, J.; Rega, N.; Zheng, G.; Liang, W.; Hada, M.; Ehara, M.; Toyota, K.; Fukuda, R.; Hasegawa, J.; Ishida, M.; Nakajima, T.; Honda, Y.; Kitao, O.; Nakai, H.; Vreven, T.; Throssell, K.; Montgomery Jr., J. A.; Peralta, J. E.; Ogliaro, F.; Bearpark, M. J.; Heyd, J. J.; Brothers, E. N.; Kudin, K. N.; Staroverov, V. N.; Keith, T. A.; Kobayashi, R.; Normand, J.; Raghavachari, K.; Rendell, A. P.; Burant, J. C.; Iyengar, S. S.; Tomasi, J.; Cossi, M.; Millam, J. M.; Klene, M.; Adamo, C.; Cammi, R.; Ochterski, J. W.; Martin, R. L.; Morokuma, K.; Farkas, O.; Foresman, J. B.; Fox, D. J. Gaussian 16 Revision A.01, Gaussian Inc. Wallingford CT, 2016.

[142] O'boyle, N. M.; Tenderholt, A. L.; Langner, K. M. cclib: A library for package-independent computational chemistry algorithms. *Journal of Computational Chemistry* **2008**, *29*, 839–845, DOI: `10.1002/jcc.20823`.

[143] Allouche, A.-R. Gabedit-A graphical user interface for computational chemistry softwares. *Journal of Computational Chemistry* **2010**, *32*, 174–182, DOI: `10.1002/jcc.21600`.

[144] Koch, W.; Holthausen, M. C., *A Chemist's Guide to Density Functional Theory*, 2nd ed.; Wiley: 2001, DOI: `10.1002/3527600043`.

[145] Champagne, B.; Perpète, E. A.; van Gisbergen, S. J. A.; Baerends, E.-J.; Snijders, J. G.; Soubra-Ghaoui, C.; Robins, K. A.; Kirtman, B. Assessment of conventional density functional schemes for computing the polarizabilities and hyperpolarizabilities of conjugated oligomers: An ab initio investigation of polyacetylene chains. *The Journal of Chemical Physics* **1998**, *109*, 10489–10498, DOI: `10.1063/1.477731`.

[146] Gelabert, R.; Moreno, M.; Lluch, J. M. Charge-Transfer ππ∗ Excited State in the 7-Azaindole Dimer. A Hybrid Configuration Interactions Singles/Time-Dependent Density Functional Theory Description. *The Journal of Physical Chemistry A* **2006**, *110*, 1145–1151, DOI: 10.1021/jp055581z.

[147] Magyar, R. J.; Tretiak, S. Dependence of Spurious Charge-Transfer Excited States on Orbital Exchange in TDDFT: Large Molecules and Clusters. *Journal of Chemical Theory and Computation* **2007**, *3*, 976–987, DOI: 10.1021/ct600282k.

[148] Peach, M. J. G.; Benfield, P.; Helgaker, T.; Tozer, D. J. Excitation energies in density functional theory: An evaluation and a diagnostic test. *The Journal of Chemical Physics* **2008**, *128*, 044118, DOI: 10.1063/1.2831900.

[149] Adamo, C.; Jacquemin, D. The calculations of excited-state properties with Time-Dependent Density Functional Theory. *Chem. Soc. Rev.* **2013**, *42*, 845–856, DOI: 10.1039/c2cs35394f.

[150] Jacquemin, D.; Planchat, A.; Adamo, C.; Mennucci, B. TD-DFT Assessment of Functionals for Optical 0–0 Transitions in Solvated Dyes. *Journal of Chemical Theory and Computation* **2012**, *8*, 2359–2372, DOI: 10.1021/ct300326f.

[151] Cordes, A. W.; Fair, C. K. Dibenzo-p-dioxin. *Acta Crystallographica Section B Structural Crystallography and Crystal Chemistry* **1974**, *30*, 1621–1623, DOI: 10.1107/s0567740874005425.

[152] Mamedov, V. A.; Litvinov, I. A.; Kataeva, O. N.; Rizvanov, I. K.; Nuretdinov, I. A. Darzens reaction as a convenient method for the synthesis of α-chloroketones, α-chloroepoxides, and symmetrically substituted dioxines. *Monatshefte für Chemie Chemical Monthly* **1994**, *125*, 1427–1435, DOI: 10.1007/bf00811092.

[153] Mamedov, V. A.; Tsuboi, S.; Mustakimova, L. V.; Hamamoto, H.; Gubaidullin, A. T.; Litvinov, I. A.; Levin, Y. A. 1,4-dioxins from methyl phenylchloropyruvate. Competition of the Darzens, Favorskii, and Gabriel reactions. *Chemistry of Heterocyclic Compounds* **2000**, *36*, 911–922, DOI: 10.1007/bf02256975.

[154] Katritzky, A. R.; Ramsden, C. A.; Joule, J. A.; Zhdankin, V. V., *Handbook of Heterocyclic Chemistry*, 3rd ed.; Elsevier: Oxford, 2010, DOI: 10.1016/c2009-0-05547-0.

[155] Hückel, E. Quantentheoretische Beiträge zum Benzolproblem. *Zeitschrift für Physik* **1931**, *70*, 204–286, DOI: 10.1007/bf01339530.

[156] Podlogar, B. L.; Glauser, W. A.; Rodriguez, W. R.; Raber, D. J. A conformational criterion for aromaticity and antiaromaticity. *The Journal of Organic Chemistry* **1988**, *53*, 2127–2129, DOI: 10.1021/jo00244a059.

[157] Tarko, L. Aromatic molecular zones and fragments. *Arkivoc* **2008**, *2008*, 24, DOI: 10.3998/ark.5550190.0009.b03.

[158] Kim, S.; Kwon, Y.; Lee, J.-P.; Choi, S.-Y.; Choo, J. A theoretical investigation into the conformational changes of dibenzo-p-dioxin, thianthrene, and selenanthrene. *Journal of Molecular Structure* **2003**, *655*, 451–458, DOI: 10.1016/s0022-2860(03)00326-0.

[159] Banerjee, S.; Phadte, A. A.; Chattopadhyay, A.; Fernandes, J. R. D.; Savardekar, A. V.; Banerjee, A.; Singh, K. S. Synthesis and photophysical characterization of heterocyclic dihydrotetracenes and their utility in the fluorescence imaging of HeLa cells. *Tetrahedron Letters* **2018**, *59*, 3787–3791, DOI: 10.1016/j.tetlet.2018.09.013.

[160] Toldo, J.; El Bakouri, O.; Solà, M.; Norrby, P.-O.; Ottosson, H. Is Excited-State Aromaticity a Driving Force for Planarization of Dibenzannelated 8π-

Electron Heterocycles? *ChemPlusChem* **2019**, *84*, 712–721, DOI: `10.1002/cplu.201900066`.

[161] Pickett, L. W.; Sheffield, E. The Ultraviolet Absorption Spectra of Dioxadiene and Dioxene. *Journal of the American Chemical Society* **1946**, *68*, 216–220, DOI: `10.1021/ja01206a021`.

[162] Connett, J. E.; Creighton, J. A.; Green, J. H. S.; Kynaston, W. The vibrational spectra of 1,4-dioxadiene. *Spectrochimica Acta* **1966**, *22*, 1859–1867, DOI: `10.1016/0371-1951(66)80173-x`.

[163] Gastilovich, E. A.; Klimenko, V. G.; Korol'kova, N. V.; Nurmukhametov, R. N. Spectroscopic data on nuclear configuration of dibenzo-p-dioxin in S0, S1, and T1 electronic states. *Chemical Physics* **2002**, *282*, 265–275, DOI: `10.1016/s0301-0104(02)00719-x`.

[164] Lee, J. E.; Choi, W.; Odde, S.; Mhin, B. J.; Balasubramanian, K. Electron affinity and inversion distortion of dibenzo-p-dioxin. *Chemical Physics Letters* **2005**, *410*, 142–146, DOI: `10.1016/j.cplett.2005.05.018`.

[165] Ljubić, I.; Sabljić, A. Dibenzo-p-dioxin. An ab Initio CASSCF/CASPT2 Study of the π-π* and n-π* Valence Excited States. *The Journal of Physical Chemistry A* **2005**, *109*, 8209–8217, DOI: `10.1021/jp051867s`.

[166] Laane, J.; Yang, J. Spectroscopic determination of vibrational potential energy surfaces in ground and excited electronic states. *Journal of Electron Spectroscopy and Related Phenomena* **2007**, *156-158*, 45–50, DOI: `10.1016/j.elspec.2006.11.034`.

[167] Yang, J.; Choo, J.; Kwon, O.; Laane, J. Theoretical calculations and vibrational spectra of 1,4-benzodioxan in its S1(π, π*) electronic excited state. *Spectrochimica Acta Part A: Molecular and Biomolecular Spectroscopy* **2007**, *68*, 1170–1173, DOI: `10.1016/j.saa.2007.01.016`.

[168] Mazurek, A.; Dobrowolski, J. C. Heteroatom Incorporation Effect in σ- and π-Electron Systems: The sEDA(II) and pEDA(II) Descriptors. *The Journal of Organic Chemistry* **2012**, *77*, 2608–2618, DOI: 10.1021/jo202542e.

[169] Spanget-Larsen, J. Dibenzo-p-dioxin. Twisted and puckered excited state molecular geometries. *Computational and Theoretical Chemistry* **2019**, *1164*, 112551, DOI: 10.1016/j.comptc.2019.112551.

[170] Brown, C. J. The crystal structure of catechol. *Acta Crystallographica* **1966**, *21*, 170–174, DOI: 10.1107/S0365110X66002482.

[171] Wunderlich, H.; Mootz, D. Die Kristallstruktur von Brenzcatechin: eine Neubestimmung. *Acta Crystallographica Section B* **1971**, *27*, 1684–1686, DOI: 10.1107/S0567740871004618.

[172] Phelan, N. F.; Orchin, M. Cross conjugation. *Journal of Chemical Education* **1968**, *45*, 633, DOI: 10.1021/ed045p633.

[173] Buschmann, J.; Müller, E.; Luger, P. X-ray structure analysis of 1,4-dioxane, phase I at 279 K and phase II at 153 K. *Acta Crystallographica Section C* **1986**, *42*, 873–876, DOI: 10.1107/s0108270186094222.

[174] Glöcklhofer, F.; Lunzer, M.; Stöger, B.; Fröhlich, J. A Versatile One-Pot Access to Cyanoarenes from ortho - and para -Quinones: Paving the Way for Cyanated Functional Materials. *Chemistry - A European Journal* **2016**, *22*, 5173–5180, DOI: 10.1002/chem.201600004.

[175] Drück, U.; Littke, W. Packing studies in cyano-aromatic compounds: the structure of 1,4-benzenedicarbonitrile. *Acta Crystallographica Section B* **1978**, *34*, 3095–3096, DOI: 10.1107/s056774087801016x.

[176] Rudolph, F. A. M.; Fuller, A. L.; Slawin, A. M. Z.; Bühl, M.; Aitken, R. A.; Woollins, J. D. The X-ray Structures of Sulfones. *Journal of Chemical Crystallography* **2009**, *40*, 253–265, DOI: 10.1007/s10870-009-9643-8.

[177] Greeves, N.; Warren, S.; Clayden, J., *Organic Chemistry*; Oxford University Press: 2012; 1260 pp.

[178] Giuliano, R. M.; Carey, F. A., *Organic chemistry*, 10th ed.; McGraw-Hill Education: New York, NY, 2017.

[179] Bjork, J. A.; Brostrom, M. L.; Whitcomb, D. R. Molecular and supramolecular structure of 5,5′,6,6′-tetrahydroxy-3,3,3′,3′-tetramethyl-1,1′-spirobisindane, tetrahydrofuran solvate. *Journal of Chemical Crystallography* **1997**, *27*, 223–230, DOI: `10.1007/bf02575959`.

[180] Huo, X.-H.; Xie, J.-H.; Wang, Q.-S.; Zhou, Q.-L. The Synthesis of Spirobitetraline Phosphoramidite Ligands and their Application in Rhodium-Catalyzed Asymmetric Hydrogenation. *Advanced Synthesis & Catalysis* **2007**, *349*, 2477–2484, DOI: `10.1002/adsc.200700109`.

[181] Zhang, J.; Jin, J.; Cooney, R.; Zhang, S. Synthesis of polymers of intrinsic microporosity using an AB-type monomer. *Polymer* **2015**, *57*, 45–50, DOI: `10.1016/j.polymer.2014.12.010`.

[182] Zhang, J.; Jin, J.; Cooney, R.; Fu, Q.; Qiao, G. G.; Thomas, S.; Merkel, T. C. Synthesis of perfectly alternating copolymers for polymers of intrinsic microporosity. *Polymer Chemistry* **2015**, *6*, 5003–5008, DOI: `10.1039/c5py00570a`.

[183] Birman, V. B.; Rheingold, A. L.; Lam, K.-C. 1,1′-Spirobiindane-7,7′-diol: a novel, C2-symmetric chiral ligand. *Tetrahedron: Asymmetry* **1999**, *10*, 125–131, DOI: `10.1016/s0957-4166(98)00481-9`.

[184] Hart, K. E.; Abbott, L. J.; Colina, C. M. Analysis of force fields and BET theory for polymers of intrinsic microporosity. *Molecular Simulation* **2013**, *39*, 397–404, DOI: `10.1080/08927022.2012.733945`.

[185] Zhang, J.; Kang, H.; Martin, J.; Zhang, S.; Thomas, S.; Merkel, T. C.; Jin, J. The enhancement of chain rigidity and gas transport performance of polymers of intrinsic microporosity via intramolecular locking of the spiro-carbon. *Chemical Communications* **2016**, *52*, 6553–6556, DOI: 10.1039/c6cc02308h.

[186] Sinnokrot, M. O.; Sherrill, C. D. Substituent Effects in π-π Interactions: Sandwich and T-Shaped Configurations. *Journal of the American Chemical Society* **2004**, *126*, 7690–7697, DOI: 10.1021/ja049434a.

[187] Lo, R.; Švec, P.; Růžičková, Z.; Růžička, A.; Hobza, P. On the nature of the stabilisation of the E$\cdots\pi$ pnicogen bond in the SbCl3$\cdots$toluene complex. *Chemical Communications* **2016**, *52*, 3500–3503, DOI: 10.1039/c5cc10363k.

[188] Ikkanda, B. A.; Iverson, B. L. Exploiting the interactions of aromatic units for folding and assembly in aqueous environments. *Chemical Communications* **2016**, *52*, 7752–7759, DOI: 10.1039/c6cc01861k.

[189] Wang, C.; Li, M.; Fang, Y. Upgrading of pyrolytic lignin into hexamethylbenzene with high purity: demonstration of the "all-to-one" biochemical production strategy in thermo-chemical conversion. *Green Chemistry* **2019**, *21*, 1000–1005, DOI: 10.1039/c8gc03788d.

[190] Ortega-Moo, C.; Durán, R.; Herrera, B.; Gutiérrez-Oliva, S.; Toro-Labbé, A.; Vargas, R. Study of antiradical mechanisms with dihydroxybenzenes using reaction force and reaction electronic flux. *Physical Chemistry Chemical Physics* **2017**, *19*, 14512–14519, DOI: 10.1039/c7cp01304c.

[191] Polatoğlu, İ.; Karataş, D. Modeling of molecular interaction between catechol and tyrosinase by DFT. *Journal of Molecular Structure* **2020**, *1202*, 127192, DOI: 10.1016/j.molstruc.2019.127192.

[192] Wang, L.-L.; Tu, Y.-K.; Valkonen, A.; Rissanen, K.; Jiang, W. Selective Recognition of Phenazine by 2,6-Dibutoxylnaphthalene-Based Tetralactam Macro-

cycle. *Chinese Journal of Chemistry* **2019**, *37*, 892–896, DOI: `10.1002/cjoc.201900233`.

[193] Klessinger, M.; Michl, J., *Excited States and Photo-Chemistry of Organic Molecules*; Wiley-VCH: 1995; 564 pp.

[194] Mao, Y.; Head-Gordon, M.; Shao, Y. Unraveling substituent effects on frontier orbitals of conjugated molecules using an absolutely localized molecular orbital based analysis. *Chemical Science* **2018**, *9*, 8598–8607, DOI: `10.1039/c8sc02990c`.

[195] Mojica, M.; Méndez, F.; Alonso, J. The Diels-Alder Cycloaddition Reaction of Substituted Hemifullerenes with 1,3-Butadiene: Effect of Electron-Donating and Electron-Withdrawing Substituents. *Molecules* **2016**, *21*, 200, DOI: `10.3390/molecules21020200`.

[196] Stowasser, R.; Hoffmann, R. What Do the Kohn-Sham Orbitals and Eigenvalues Mean? *Journal of the American Chemical Society* **1999**, *121*, 3414–3420, DOI: `10.1021/ja9826892`.

[197] Motulsky, H.; Christopoulos, A. GraphPad Prism Version 4.0: Fitting models to biological data using linear and nonlinear regression, a practical guide to curve fitting, GraphPad Software Inc., San Diego CA: 2003, eprint: `https://cdn.graphpad.com/faq/2/file/Prism_v4_Fitting_Models_to_Biological_Data.pdf`.

[198] Stiltskin, R. Physics 133 lab manual; 2015, eprint: `https://scott.physics.ucsc.edu/pdf/133_draftman.pdf`.

[199] Kasha, M. Characterization of electronic transitions in complex molecules. *Discussions of the Faraday Society* **1950**, *9*, 14, DOI: `10.1039/df9500900014`.

[200] Noda, H.; Nakanotani, H.; Adachi, C. Excited state engineering for efficient reverse intersystem crossing. *Science Advances* **2018**, *4*, eaao6910, DOI: `10.1126/sciadv.aao6910`.

[201] Lyskov, I.; Marian, C. M. Climbing up the Ladder: Intermediate Triplet States Promote the Reverse Intersystem Crossing in the Efficient TADF Emitter ACRSA. *The Journal of Physical Chemistry C* **2017**, *121*, 21145–21153, DOI: `10.1021/acs.jpcc.7b06187`.

[202] Eisler, S.; Tykwinski, R. R. Expanded Radialenes: Modular Synthesis and Characterization of Cross-Conjugated Enyne Macrocycles. *Angewandte Chemie International Edition* **1999**, *38*, 1940–1943, DOI: `10.1002/(SICI)1521-3773(19990712)38:13/14<1940::AID-ANIE1940>3.0.CO;2-8`.

[203] Gholami, M.; Tykwinski, R. R. Oligomeric and Polymeric Systems with a Cross-conjugated π-Framework†. *Chemical Reviews* **2006**, *106*, 4997–5027, DOI: `10.1021/cr0505573`.

[204] Ricks, A. B.; Solomon, G. C.; Colvin, M. T.; Scott, A. M.; Chen, K.; Ratner, M. A.; Wasielewski, M. R. Controlling Electron Transfer in Donor-Bridge-Acceptor Molecules Using Cross-Conjugated Bridges. *Journal of the American Chemical Society* **2010**, *132*, 15427–15434, DOI: `10.1021/ja107420a`.

[205] Emanuelsson, R.; Wallner, A.; Ng, E. A. M.; Smith, J. R.; Nauroozi, D.; Ott, S.; Ottosson, H. Cross-Hyperconjugation: An Unexplored Orbital Interaction between π-Conjugated and Saturated Molecular Segments. *Angewandte Chemie International Edition* **2012**, *52*, 983–987, DOI: `10.1002/anie.201206030`.

[206] Zirzlmeier, J.; Casillas, R.; Reddy, S. R.; Coto, P. B.; Lehnherr, D.; Chernick, E. T.; Papadopoulos, I.; Thoss, M.; Tykwinski, R. R.; Guldi, D. M. Solution-based intramolecular singlet fission in cross-conjugated pentacene dimers. *Nanoscale* **2016**, *8*, 10113–10123, DOI: `10.1039/c6nr02493a`.

[207] Hart, K. E.; Colina, C. M. Estimating gas permeability and permselectivity of microporous polymers. *Journal of Membrane Science* **2014**, *468*, 259–268, DOI: 10.1016/j.memsci.2014.06.017.

[208] Abbott, L. J.; Hart, K. E.; Colina, C. M. Polymatic: a generalized simulated polymerization algorithm for amorphous polymers. *Theoretical Chemistry Accounts* **2013**, *132*, DOI: 10.1007/s00214-013-1334-z.

[209] Fang, W.; Zhang, L.; Jiang, J. Gas Permeation and Separation in Functionalized Polymers of Intrinsic Microporosity: A Combination of Molecular Simulations and Ab Initio Calculations. *The Journal of Physical Chemistry C* **2011**, *115*, 14123–14130, DOI: 10.1021/jp204193g.

[210] Dong, H.; Zhu, Z.; Li, K.; Li, Q.; Ji, W.; He, B.; Li, J.; Ma, X. Significantly improved gas separation properties of sulfonated PIM-1 by direct sulfonation using SO3 solution. *Journal of Membrane Science* **2021**, *635*, 119440, DOI: 10.1016/j.memsci.2021.119440.

[211] Maroncelli, M.; Fleming, G. R. Picosecond solvation dynamics of coumarin 153: The importance of molecular aspects of solvation. *The Journal of Chemical Physics* **1987**, *86*, 6221–6239, DOI: 10.1063/1.452460.

[212] Reinhardt, M.; Kirschke, K.; Baumann, H. UV-VIS spectra of some 3-arylazopropenoic acid esters. *Journal of Molecular Structure* **1995**, *348*, 417–420, DOI: 10.1016/0022-2860(95)08677-n.

[213] Mühlpfordt, A.; Schanz, R.; Ernsting, N. P.; Farztdinov, V.; Grimme, S. Coumarin 153 in the gas phase: optical spectra and quantum chemical calculations. *Physical Chemistry Chemical Physics* **1999**, *1*, 3209–3218, DOI: 10.1039/a902491c.

[214] Bouvier, B.; Gustavsson, T.; Markovitsi, D.; Millié, P. Dipolar coupling between electronic transitions of the DNA bases and its relevance to exciton states in

double helices. *Chemical Physics* **2002**, *275*, 75–92, DOI: 10.1016/s0301-0104(01)00523-7.

[215] Klymchenko, A. S.; Demchenko, A. P. Electrochromic Modulation of Excited-State Intramolecular Proton Transfer: The New Principle in Design of Fluorescence Sensors. *Journal of the American Chemical Society* **2002**, *124*, 12372–12379, DOI: 10.1021/ja027669l.

[216] Lanzi, M.; Bertinelli, F.; Paganin, L.; Costa-Bizzarri, P.; Cesari, G. Electronic Transitions of Polyalkylthiophenes Partially Derivatized with NLO Chromophores: A Theoretical and Experimental Study. *Macromolecular Chemistry and Physics* **2006**, *207*, 1253–1261, DOI: 10.1002/macp.200600192.

[217] Schwalb, N. K.; Temps, F. A femtosecond time-resolved investigation of dual fluorescence from N6,N6-dimethyladenine. *Physical Chemistry Chemical Physics* **2006**, *8*, 5229, DOI: 10.1039/b610003a.

[218] Gustavsson, T.; Sarkar, N.; Bányász, Á.; Markovitsi, D.; Improta, R. Solvent Effects on the Steady-state Absorption and Fluorescence Spectra of Uracil, Thymine and 5-Fluorouracil. *Photochemistry and Photobiology* **2007**, *83*, 595–599, DOI: 10.1111/j.1751-1097.2007.00052.x.

[219] Malkova, V. I.; Makotchenko, E. V. Analysis of composite bands in the electronic absorption spectra of compounds in solutions. *Russian Journal of General Chemistry* **2008**, *78*, 1161–1166, DOI: 10.1134/s1070363208060108.

[220] Marciniak, H.; Lochbrunner, S. On the interpretation of decay associated spectra in the presence of time dependent spectral shifts. *Chemical Physics Letters* **2014**, *609*, 184–188, DOI: 10.1016/j.cplett.2014.05.006.

[221] Beckwith, J. S.; Rumble, C. A.; Vauthey, E. Data analysis in transient electronic spectroscopy – an experimentalist's view. *International Reviews in Physical Chemistry* **2020**, *39*, 135–216, DOI: 10.1080/0144235x.2020.1757942.

[222] Wheldon, C. Convolution of a Gaussian with an exponential, and its application in programs halflife.c/nanofit.f, English, Online, United Kingdom: University of Birmingham, 2019, eprint: http://www.np.ph.bham.ac.uk/research_resources/programs/halflife/gauss_exp_conv.pdf.

[223] Telfah, H.; Jamhawi, A.; Teunis, M. B.; Sardar, R.; Liu, J. Ultrafast Exciton Dynamics in Shape-Controlled Methylammonium Lead Bromide Perovskite Nanostructures: Effect of Quantum Confinement on Charge Carrier Recombination. *The Journal of Physical Chemistry C* **2017**, *121*, 28556–28565, DOI: 10.1021/acs.jpcc.7b10377.

Appendices

APPENDIX A

ABBREVIATIONS

B3LYP   Becke's 3–parameter hybrid functional with Lee, Yang, and Parr's non–local correlation term and Vosko, Wilk, and Nusair's 1980 local correlation functional(III)

BBO   β–Barium borate

BDO   [1,4]benzodioxino[3,2-b]oxanthrene

BDODC   [1,4]benzodioxino[3,2–b]oxanthrene–6,13–dicarbo-nitrile

BDOSC   [1,4]benzodioxino[3,2–b]oxanthrene–6–(1,3,5–tri-methylpyrazole–4-sulfonyl)–13–carbonitrile

BLYP   Becke's 1988 exchange functional with Lee, Yang, and Parr correlation functional

CPA   femtosecond chirped pulse regenerative amplifier

CRC   University of Louisville's Cardinal Research Cluster

CSV   comma separated values

CT   charge–transfer

CTS   charge–transfer state

DFA   density functional approximation

DFT	density functional theory
dPL	delayed photoluminescence
EDG	electron–donating group
EEM	excitation–emission matrix
ESP	electrostatic potential map
EWG	electron–withdrawing group
ExpGaus	exponentially modified gaussian
fsTAPP	femtosecond transient absorption pump–probe
FWHM	full width at half maximum
GVD	group velocity dispersion
HDIMR	heterodimer sub–unit
HOMO	highest occupied molecular orbital
HTRMR	heterotrimer sub–model
IC	internal conversion
IEFPCM	integral equation formalism of the polarizable continuum model
IP	ionization potential
IRF	instrument response function
ISC	intersystem crossing
Logn	logarithmic–normal distribution
$\text{Logn}_{\text{BDODC}}$	Logn function of BDODC
$\text{Logn}_{\text{BDOSC}}$	Logn function of BDOSC
Logn_{S_1}	Logn function of the first excited state
Logn_{S_2}	Logn function of the second excited state
LUMO	lowest unoccupied molecular orbital
MD	molecular dynamics
MO	molecular orbital

NIR	near infrared
NOPA	non–collinear optical parametric amplifier
OLGMR	short–chain oligomer
PB	photobleach
PIA	photoinduced absorption
PIA_1	first photoinduced absorption
PIA_2	second photoinduced absorption
PIA_3	third photoinduced absorption
PIM–1	polymer of intrinsic microporosity "1"
PL	photoluminescence
PLYMR	long–chain polymer
PPLN	periodically poled lithium niobate
S_0	singlet ground state
S_1	first singlet excited state
S_2	second singlet excited state
S_3	third singlet excited state
S_4	fourth singlet excited state
SCF	self–consistent field
SE	stimulated emission
SHG	second harmonic generation
SPIRO	3,3,3′,3′-tetramethyl-1,1′-spirobiindan
T_1	first triplet excited state
T_2	second triplet excited state
TD–DFT	time–dependent density functional theory
TRPL	time–resolved photoluminescence
UV	ultraviolet
UV–VIS	ultraviolet–visible absorption

VIS   visible

VR   vibrational relaxation

VS   visible state

XC   Hartree–Fock–to–Slater exchange–correlation ratio

APPENDIX B

PYTHON 3.X SCRIPTS

Script B.1: System environment information

```
 1   2021-08-04 12:13 PM
 2   ====================
 3   OS and hardware
 4   ====================
 5   ajamhawi@aj-t1600-f33
 6   ---------------------
 7   OS: Fedora 33 (Workstation Edition) x86_64
 8   Host: Precision T1600 01
 9   Kernel: 5.13.5-100.fc33.x86_64
10   Uptime: 1 day, 17 hours, 3 mins
11   Packages: 3219 (rpm)
12   Shell: bash 5.0.17
13   Resolution: 1920x1080, 1680x1050
14   DE: GNOME 3.38.5
15   WM: Mutter
16   WM Theme: Adwaita
17   Theme: Adwaita [GTK2/3]
18   Icons: Adwaita [GTK2/3]
19   Terminal: gnome-terminal
20   CPU: Intel Xeon E31245 (8) @ 3.700GHz
21   GPU: NVIDIA Quadro 2000
22   Memory: 3904MiB / 11914MiB
23
24   ====================
25   Used Python packages
26   ====================
27   # packages in environment at /home/ajamhawi/.miniconda3:
28   # Name                    Version                   Build  Channel
29   astropy                   4.2.1            py38h27cfd23_1
30   cclib                     1.7                pyhd3deb0d_0    conda-forge
31   conda                     4.10.3           py38h06a4308_0
32   h5py                      3.2.1            py38h6c542dc_0
33   hdf5                      1.10.6               hb1b8bf9_0
34   ipython                   7.22.0           py38hb070fc8_0
35   jupyterlab                3.0.14             pyhd3eb1b0_1
36   lmfit                     1.0.2              pyhd8ed1ab_0    conda-forge
37   matplotlib                3.3.4            py38h06a4308_0
38   numpy                     1.20.3           py38hf144106_0
39   python                    3.8.10               h12debd9_8
40   scipy                     1.6.2            py38had2a1c9_1
```

B.1 ULTRAVIOLET–VISIBLE ABSORPTION SPECTROSCOPY SCRIPTS

Script B.2: UV–VIS spectral raw data processing and refining.

```python
import numpy as np
import os, gc, h5py
path = ['../1ab/','../0da/']
subs = ['20190119_AJ12_XXX_50uM_diss/'
        ,'20181112_AJ12_0XA-N2_abs/'
        ,'20181213_AJ12_10A-conc_abs/data_files/']
files = [sorted([x for x in os.listdir(path[0]+Sub) if 'csv' in x]) for sub, Sub in enumerate(subs)]
eV = np.arange(2300,4801,1)/1000
n_rows = [701,3327,1876]
header = ['Energy..eV']
for k in range(3):
    solvs = 2 if k==2 else 0
    for i,j in enumerate(files[k][solvs:]):
        data_i = np.genfromtxt(path[0]+subs[k]+files[k][i+solvs], delimiter=',', max_rows=n_rows[k],
        ↪ skip_header=2, dtype=float)[:,:-1]
        data_i = data_i[:,np.r_[[0],1:len(data_i[0,:]):2]]
        if k==2 and '1mm' in files[k][i+solvs]:
            solv = np.genfromtxt(path[0]+subs[k]+files[k][1], delimiter=',', max_rows=n_rows[k],
            ↪ skip_header=2, dtype=float)[:,1]
            for l in range(len(data_i[0,1:])):
                data_i[:,l+1] = (data_i[:,l+1] - solv)/0.1
        elif k==2 and '1cm' in files[k][i+solvs]:
            solv = np.genfromtxt(path[0]+subs[k]+files[k][0], delimiter=',', max_rows=n_rows[k],
            ↪ skip_header=2, dtype=float)[:,1]
            for l in range(len(data_i[0,1:])):
                data_i[:,l+1] = (data_i[:,l+1] - solv)
        data_i[:,0] = 1240/data_i[:,0]
        data_i[:,1:] = data_i[:,1:]-np.average(data_i[:20,1:], axis=0)
        for s in range(len(data_i[0,1:])):
            interp = np.interp(eV,data_i[:,0], data_i[:,s+1])
            if s==0:
                data_int = interp
            else:
                data_int = np.column_stack((data_int, interp))
        if i==0 and k==0:
            data_ave = eV; data_std = eV
        data_ave = np.column_stack((data_ave, np.mean(data_int, axis=1)))
        data_std = np.column_stack((data_std, np.std(data_int, axis=1)))
        header.append(files[k][i+solvs][14:-4])
np.savetxt(path[1]+'1ab_XXX_ave.txt', data_ave, delimiter='\t', header='\t'.join(header), fmt='%1.4e',
↪ comments='')
np.savetxt(path[1]+'1ab_XXX_std.txt', data_std, delimiter='\t', header='\t'.join(header), fmt='%1.4e',
↪ comments='')
hdf5_names = ['1ab_data', '0ds_data']
for i in range(len(hdf5_names)):
    hdf5_file = h5py.File(path[1]+hdf5_names[i]+'.hdf5', 'a')
    ab_data = hdf5_file.require_group('./1ab_data')
    ab_data.attrs.create('titles', header, dtype=h5py.special_dtype(vlen=str))
    aves = ab_data.require_dataset('./XXX_ave', shape=data_ave.shape, maxshape=(None, None),
    ↪ dtype=float, compression='gzip')
    stds = ab_data.require_dataset('./XXX_std', shape=data_std.shape, maxshape=(None, None),
    ↪ dtype=float, compression='gzip')
    aves[:,:] = data_ave; stds[:,:] = data_std
    hdf5_file.close()
gc.collect()
```

Script B.3: UV–VIS spectral decomposition analysis.

```python
import numpy as np
import os, gc, h5py
```

```python
from lmfit import Model, Parameters
from fit_funcs import logna

data_file = h5py.File('../0da/0ds_data.hdf5', 'r')
ave = data_file['1ab_data']['XXX_ave']
std = data_file['1ab_data']['XXX_std']
lbl = data_file['1ab_data'].attrs.get('titles')

sams = [4,3,1,2]
ep = np.array([3.92060851, 3.26271495, 2.27118516, 1.998269])
for i in range(4):
    if i==0:
        data = ave[150:1200, 0]
    data_i = (ave[150:1200, sams[i]] / np.amax(ave[150:1200, sams[i]])) * ep[i]
    data = np.column_stack((data, data_i))

model1 = Model(logna, prefix='l1_')
model2 = Model(logna, prefix='l1_') + Model(logna, prefix='l2_')
pars1 = Parameters()
pars2 = Parameters()
pars1.add_many(
                ('l1_e0', 5.0, True, None, None, None, None)
               ,('l1_v0', 2.9, True, None, None, None, None)
               ,('l1_H', 0.5, True, None, None, None, None)
               ,('l1_p', 2.0, True, None, None, None, None)
               )

pars2.add_many(
                ('l1_e0', 3.0, True, None, None, None, None)
               ,('l1_v0', 2.8, True, None, None, None, None)
               ,('l1_H', 0.4, True, None, None, None, None)
               ,('l1_p', 1.5, True, None, None, None, None)
               ,('l2_e0', 1.0, True, None, None, None, None)
               ,('l2_v0', 3.0, True, None, None, None, None)
               ,('l2_H', 0.5, True, None, None, None, None)
               ,('l2_p', 2.0, True, None, None, None, None)
               )

for i in range(4):
    model = model1 if i==0 else model2
    pars = pars1 if i==0 else pars2
    result = model.fit(data[:,i+1], v=data[:,0], params=pars, method='leastsq',
        nan_policy='propagate')
    print(result.fit_report(show_correl=False))
    result.conf_interval(sigmas=[4])
    print(result.ci_report())

gc.collect()
```

B.2   PHOTOLUMINESCENCE SPECTROSCOPY SCRIPTS

Script B.4: PL spectral raw data processing and refining.

```python
import numpy as np
import os, gc, h5py
path = ['../2pl/20190119_AJ12_XXX_50uM_diss/', '../0da/']
subs = ['04A_lines/', '07A_lines/', '08D_lines/', '10A_lines/']
files = [sorted(list(set([x[:-5] for x in os.listdir(path[0]+Sub) if 'txt' in x]))) for sub, Sub in
    enumerate(subs)]
ex_cor_fac = -10; em_cor_fac = 5
eV = np.arange(1550,4965,5)/1000
header = ['Energy...eV']
for k,l in enumerate(subs):
```

```
10        for i,j in enumerate(files[k]):
11            for f in range(5):
12                file = path[0]+subs[k]+files[k][i]+'%i.txt'%(f+1)
13                data_i = np.genfromtxt(file, delimiter='\t', comments='$', skip_header=54)
14                data_i = np.flip(data_i,axis=0)
15                data_i[:,1][data_i[:,1]<=0] = 0
16                fixed = float(np.genfromtxt(file, dtype=str,comments='$', delimiter='$')[10])
17                if 'em' in files[k][i]:
18                    data_i[:,0] = 1240/(data_i[:,0] + em_cor_fac)
19                    fixed = 1240/(fixed + ex_cor_fac)
20                elif 'ex' in files[k][i]:
21                    data_i[:,0] = 1240/(data_i[:,0] + ex_cor_fac)
22                    fixed = 1240/(fixed + em_cor_fac)
23                interp_i = np.interp(eV, data_i[:,0], data_i[:,1],left=0,right=0)
24                if f == 0:
25                    data_s = interp_i
26                data_s = np.column_stack((data_s,interp_i))
27            header.append('%s%0.1feV'%(files[k][i][-11:-5],fixed))
28            if i==0 and k==0:
29                data_ave = eV; data_std = eV
30            data_ave = np.column_stack((data_ave,np.average(data_s,axis=1)))
31            data_std = np.column_stack((data_std,np.std(data_s,axis=1)))
32  np.savetxt(path[1]+'2pl_XXX_li-ave.txt', data_ave, delimiter='\t', header='\t'.join(header),
    ↪  fmt='%1.5e', comments='')
33  np.savetxt(path[1]+'2pl_XXX_li-std.txt', data_std, delimiter='\t', header='\t'.join(header),
    ↪  fmt='%1.5e', comments='')
34  hdf5_names = ['2pl_data', '0ds_data']
35  for i in range(len(hdf5_names)):
36      hdf5_file = h5py.File(path[1]+hdf5_names[i]+'.hdf5', 'a')
37      pl_data = hdf5_file.require_group('./2pl_data')
38      pl_data.attrs.create('lines_labels', header, dtype=h5py.special_dtype(vlen=str))
39      li_ave = pl_data.require_dataset('lines_ave', shape=data_ave.shape, maxshape=(None, None),
        ↪  dtype=float, compression='gzip')
40      li_std = pl_data.require_dataset('lines_std', shape=data_std.shape, maxshape=(None, None),
        ↪  dtype=float, compression='gzip')
41      li_ave[:,:] = data_ave; li_std[:,:] = data_std
42      hdf5_file.close()
43  gc.collect()
```

Script B.5: dPL spectral raw data processing and refining.

```
1   import numpy as np
2   import os, gc, h5py
3   path = ['../2pl/', '../0da/']
4   subs = ['20181112_0XA-N2_pl/04A_02/'
5           ,'20181112_0XA-N2_pl/04A_N2/'
6           ,'20181112_0XA-N2_pl/07A_02/'
7           ,'20181112_0XA-N2_pl/07A_N2/'
8           ,'20190119_AJ12_XXX_50uM_diss/10A_ph/']
9   files = [sorted(list(set([x.split('.')[0] for x in os.listdir(path[0]+Sub) if 'ph' in x ]))) for sub,
    ↪  Sub in enumerate(subs)]
10  files = [sorted(list(set([x.split('#')[0] for x in files[i] if '_001-' in x or '#' in x]))) for i in
    ↪  range(len(subs))]
11  files = [sorted([x for x in files[i] if '-001' not in x]) for i in range(len(subs))]
12  ex_cor_fac = -10; em_cor_fac = 5
13  eV = np.arange(1400,2905,5)/1000
14  int_cor = [1,1.029873471915855,1,1.032565944919366,1]
15  header = ['Energy.........eV']; ex = ['energy.eV']
16  for k,l in enumerate(subs):
17      for i,j in enumerate(files[k]):
18          no_files = 5 if k>3 else 1
19          for f in range(no_files):
20              ext = '#0%s.txt'%str(f+1) if k>3 else '.txt'
21              file = path[0]+subs[k]+files[k][i]+ext
22              fixed = 1240/(float(np.genfromtxt(file, dtype=str,comments='$', delimiter='$')[10]) +
                  ↪  ex_cor_fac)
```

```
23              delay = float(np.genfromtxt(file, dtype=str,comments='$', delimiter='$')[17])*10
24              gate = float(np.genfromtxt(file, dtype=str,comments='$', delimiter='$')[16])*10
25              data_i = np.genfromtxt(file, delimiter='\t', comments='$', skip_header=54)
26              data_i[:,0] = 1240/(data_i[:,0] + em_cor_fac)
27              data_i[:,1][data_i[:,1]<=0] = 0
28              data_i = np.flip(data_i,axis=0)
29              interp_i = np.interp(eV, data_i[:,0], data_i[:,1]*int_cor[k],left=0,right=0)
30              if f == 0:
31                  data_s = interp_i
32              data_s = np.column_stack((data_s,interp_i))
33          head_add = '%s-d%ig%04dus'%(files[k][i].split('_')[2], delay, gate)
34          header.append(head_add)
35          ex.append('%s-ex%0.2feV'%(files[k][i].split('_')[2],fixed))
36          if i==0 and k==0:
37              data = eV
38          data = np.column_stack((data, np.average(data_s,axis=1)))
39  np.savetxt(path[1]+'2pl_XXX_ph.txt', data, delimiter='\t', header='\t'.join(header), fmt='%1.11e',
   ↪  comments='')
40  hdf5_names = ['2pl_data', '0ds_data']
41  for i in range(len(hdf5_names)):
42      hdf5_file = h5py.File(path[1]+hdf5_names[i]+'.hdf5', 'a')
43      pl_data = hdf5_file.require_group('./2pl_data')
44      pl_data.attrs.create('ph_labels', header, dtype=h5py.special_dtype(vlen=str))
45      pl_data.attrs.create('ph_ex', ex, dtype=h5py.special_dtype(vlen=str))
46      ph_data = pl_data.require_dataset('ph_data', shape=data.shape, maxshape=(None, None), dtype=float,
   ↪  compression='gzip')
47      ph_data[:,:] = data
48      hdf5_file.close()
49  gc.collect()
```

Script B.6: PL EEM raw data processing and refining.

```
1   import numpy as np
2   import os, gc, h5py
3   from scipy.interpolate import griddata
4   path = ['../2pl/20190119_AJ12_XXX_50uM_diss/', '../0da/']
5   subs = ['04A_3d/', '07A_3d/', '08D_3d/', '10A_3d/']
6   files = [sorted([x for x in os.listdir(path[0]+Sub) if 'sem' in x]) for sub, Sub in enumerate(subs)]
7   ex_cor_fac = -10; em_cor_fac = 5
8   em_eV = np.arange(1550,2955,5)/1000; ex_eV = np.arange(2550,3655,5)/1000
9   data_all = np.zeros((len(ex_eV)+1, len(em_eV)+1, len(subs)))
10  for k,l in enumerate(subs):
11      for i,j in enumerate(files[k]):
12          data_i = np.genfromtxt(path[0]+subs[k]+files[k][i], delimiter='\t', comments='$',
   ↪  skip_header=54)
13          delta = float(np.genfromtxt(path[0]+subs[k]+files[k][i], dtype=str,comments='$',
   ↪  delimiter='$')[10])
14          em = data_i[:,0] + delta + em_cor_fac
15          ex = data_i[:,0] + ex_cor_fac
16          pl = data_i[:,1]
17          pl[pl<=0] = 0
18          if i==0:
19              em_all = em; ex_all = ex; pl_all = pl
20          else:
21              em_all = np.hstack((em_all, em))
22              ex_all = np.hstack((ex_all, ex))
23              pl_all = np.hstack((pl_all, pl))
24      xyz_k = np.column_stack(([1240/em_all, 1240/ex_all,pl_all]))
25      data_all[1:,0,k] = ex_eV; data_all[0,1:,k] = em_eV
26      data_all[1:,1:,k] = griddata((xyz_k[:,0], xyz_k[:,1]), xyz_k[:,2], (em_eV[None,:], ex_eV[:,None]),
   ↪  method='linear', fill_value=0)
27  np.save(path[1]+'2pl_XXX_3dg.npy',data_all)
28  hdf5_names = ['2pl_data', '0ds_data']
29  for i in range(len(hdf5_names)):
30      hdf5_file = h5py.File(path[1]+hdf5_names[i]+'.hdf5', 'a')
31      pl_data = hdf5_file.require_group('./2pl_data')
```

```
32        details = ['1st_column=em_eV, 1st row=ex_eV']
33        pl_data.attrs.create('3d_details', details, dtype=h5py.special_dtype(vlen=str))
34        for k in range(len(subs)):
35            pl3d = pl_data.require_dataset('./%s'%subs[k][:-1], shape=data_all[:,:,k].shape,
          ↪    maxshape=(None, None), dtype=float, compression='gzip')
36            pl3d[:,:] = data_all[:,:,k]
37        hdf5_file.close()
38    gc.collect()
```

Script B.7: PL spectral decomposition analysis.

```
1    import numpy as np
2    from numpy import zeros, sqrt, log, exp, pi
3    import os, gc, h5py
4    from lmfit import Model, Parameters
5    from fit_funcs import lne, lna
6
7    data_file = h5py.File('../0da/0ds_data.hdf5', 'r')
8    ave = data_file['2pl_data']['lines_ave']
9
10   #excitation
11   sams = [12,9,3,6]
12   for i in range(4):
13       if i==0:
14           data = ave[150:421,0]
15       data_i = ave[150:421,sams[i]] / ave[150:421,0]**3
16       data_i = (data_i/np.amax(data_i))
17       data = np.column_stack((data,data_i))
18
19   model1 = Model(lna,prefix='l1_')
20   model2 = Model(lna,prefix='l1_') + Model(lna,prefix='l2_')
21   pars1 = Parameters()
22   pars2 = Parameters()
23   pars1.add_many(
24                   ('l1_I0', 5.0, True, None, None, None, None)
25                  ,('l1_v0', 2.7, True, None, None, None, None)
26                  ,('l1_H', 0.5, True, None, None, None, None)
27                  ,('l1_p', 2.0, True, None, None, None, None)
28                  )
29
30   pars2.add_many(
31                   ('l1_I0', 3.0, True, None, None, None, None)
32                  ,('l1_v0', 2.8, True, None, None, None, None)
33                  ,('l1_H', 0.4, True, None, None, None, None)
34                  ,('l1_p', 1.5, True, None, None, None, None)
35                  ,('l2_I0', 1.0, True, None, None, None, None)
36                  ,('l2_v0', 3.1, True, None, None, None, None)
37                  ,('l2_H', 0.5, True, None, None, None, None)
38                  ,('l2_p', 2.0, True, None, None, None, None)
39                  )
40   for i in range(4):
41           model = model1 if i==0 else model2
42           pars = pars1 if i==0 else pars2
43           result = model.fit(data[:,i+1], v=data[:,0], params=pars, method='leastsq',
          ↪    nan_policy='propagate')
44           comps = result.eval_components()
45           result.conf_interval(sigmas=[4])
46           print(result.fit_report(show_correl=False))
47           print(result.ci_report())
48
49   #emission
50   sams = [11,8,2,5]
51   for i in range(4):
52       if i==0:
53           data = ave[50:266,0]
54       data_i = ave[50:266,sams[i]] / ave[50:266,0]**3
```

```
55        data_i = (data_i/np.amax(data_i))
56        data = np.column_stack((data,data_i))
57
58    model1 = Model(lne,prefix='l1_')
59    model2 = Model(lne,prefix='l1_') + Model(lne,prefix='l2_')
60    pars1 = Parameters()
61    pars2 = Parameters()
62    pars1.add_many(
63                    ('l1_I0', 1, True, None, None, None, None)
64                   ,('l1_v0', 2.6, True, None, None, None, None)
65                   ,('l1_H', 0.3, True, None, None, None, None)
66                   ,('l1_p', 1.5, True, None, None, None, None)
67                    )
68
69    pars2.add_many(
70                    ('l1_I0', 1.0, True, 0.1, None, None, None)
71                   ,('l1_v0', 2.6, True, None, None, None, None)
72                   ,('l1_H', 0.3, True, None, None, None, None)
73                   ,('l1_p', 1.4, True, 1.01, None, None, None)
74                   ,('l2_I0', 0.1, True, 0.01, None, None, None)
75                   ,('l2_v0', 2.35, True, None, None, None, None)
76                   ,('l2_H', 0.15, True, None, None, None, None)
77                   ,('l2_p', 1.2, True, 1.01, None, None, None)
78                    )
79
80    for i in range(4):
81            model = model1 if i==0 else model2
82            pars = pars1 if i==0 else pars2
83            result = model.fit(data[:,i+1], v=data[:,0], params=pars, method='leastsq',
          ↪  nan_policy='propagate')
84            result.conf_interval(sigmas=[3])
85            print(result.fit_report(show_correl=False))
86            print(result.ci_report())
87    gc.collect()
```

B.3   TIME–RESOLVED PHOTOLUMINESCENCE SPECTROSCOPY SCRIPTS

Script B.8: TRPL kinetics raw data processing, refining, and jitter correction.

```
1    import numpy as np
2    import os, gc, h5py
3    from scipy.interpolate import interp1d
4    path = ['../0da/'
5           ,'../3tr/20180515_AJ12_0XA-N2_TRPL_388-470/'
6           ,'../3tr/20190122_AJ12_XXX-50uM_388_diss/']
7    subs = [['IRF/', '04A/', '07A/']
8           ,['00C/', '04A/', '07A/', '08D/', '10A/']]
9    times_i = np.arange(-200000,1000001,5)/10000
10   times_f = np.arange(-50,1001,1)/10
11   header = ['Delay....ns']
12   for k,l in enumerate(path[1:]):
13       for i,j in enumerate(subs[k]):
14           for m in range(9):
15               file = 'tek000%iCH1.csv'%m
16               data_i = np.genfromtxt(path[k+1]+subs[k][i]+file, delimiter=',', skip_header=22)
17               data_i[:,1] = data_i[:,1] - np.average(data_i[40:50,1])
18               data_i[:,0] = (data_i[:,0] * 1e9) - 51
19               interp_f = interp1d(data_i[:,0],data_i[:,1],kind=3)
20               interp_i = interp_f(times_i)
21               if i == 0:
22                   max_loc = np.argmax(interp_i)
23               else:
24                   max_loc = np.argmax(np.diff(interp_i,n=1))
```

```python
25                data_i[:,0] = (data_i[:,0] - times_i[max_loc])
26                interp_f = interp1d(data_i[:,0], data_i[:,1], kind=1)
27                interp_i = interp_f(times_f)
28                if m == 0:
29                    data_s = interp_i
30                else:
31                    data_s = np.column_stack((data_s, interp_i))
32            head_add = '..%s-N2..'%subs[k][i][:-1] if k==0 else '..%s-O2..'%subs[k][i][:-1]
33            header.append(head_add)
34            if k==0 and i==0:
35                data_ave = times_f; data_std = times_f
36            data_ave = np.column_stack((data_ave, np.average(data_s,axis=1)))
37            data_std = np.column_stack((data_std, np.std(data_s,axis=1)))
38    np.savetxt(path[0]+'3tr_XXX_ave.txt', data_ave, delimiter='\t', header='\t'.join(header), fmt='%1.4e',
   ↪    comments='')
39    np.savetxt(path[0]+'3tr_XXX_std.txt', data_std, delimiter='\t', header='\t'.join(header), fmt='%1.4e',
   ↪    comments='')
40    hdf5_names = ['3tr_data', '0ds_data']
41    for i in range(len(hdf5_names)):
42        hdf5_file = h5py.File(path[0]+hdf5_names[i]+'.hdf5', 'a')
43        tr_data = hdf5_file.require_group('./3tr_data')
44        tr_data.attrs.create('col_labels', header, dtype=h5py.special_dtype(vlen=str))
45        tr_ave = tr_data.require_dataset('XXX_ave', shape=data_ave.shape, maxshape=(None, None),
   ↪        dtype=float, compression='gzip')
46        tr_std = tr_data.require_dataset('XXX_std', shape=data_std.shape, maxshape=(None, None),
   ↪        dtype=float, compression='gzip')
47        tr_ave[:,:] = data_ave; tr_std[:,:] = data_std
48        hdf5_file.close()
49    gc.collect()
```

Script B.9: TRPL single exponential fit.

```python
1   import numpy as np
2   import os, gc, h5py
3   from lmfit import Model, Parameters
4   from fit_funcs import gaus_c, exp_c
5
6   data_file = h5py.File('../0da/0ds_data.hdf5', 'r')
7   ave = data_file['3tr_data']['XXX_ave']
8   lbl = data_file['3tr_data'].attrs.get('col_labels')
9
10  sams = [4,8,7,2,3]
11  colored=True
12  sam_lbl = ['irf','chr01','htrmr','olgmr','plymr']
13  lims = [100,-1]
14  for i in range(5):
15      if i==0:
16          data = ave[:,0]
17      data_i = (ave[:,sams[i]] / np.amax(ave[:,sams[i]]))
18      data = np.column_stack((data,data_i))
19
20  model1 = Model(gaus_c,prefix='g_')
21  model2 = Model(exp_c,prefix='d1_')
22  pars1 = Parameters()
23  pars2 = Parameters()
24  pars1.add_many(
25              ('g_I0', 1, True, None, None, None, None)
26             ,('g_c', 0, True, None, None, None, None)
27             ,('g_w', 0.7, True, 0.1, 1, None, None)
28              )
29
30  pars2.add_many(
31              ('d1_I0', 6, True, 0.1, None, None, None)
32             ,('d1_c', 0.5, True, -0.9, 0.9, None, None)
33             ,('d1_w', 0.4, True, 1e-4, None, None, None)
34             ,('d1_tau', 10, True, None, None, None, None)
```

```
35                )
36
37  for i in range(5):
38          if i==1:
39                  ir_w = result.params['g_w'].value
40                  pars2['d1_w'].set(value=ir_w, vary=False)
41                  ir_fit = result.best_fit
42          model = model1 if i==0 else model2
43          pars = pars1 if i==0 else pars2
44          result = model.fit(data[:,i+1], t=data[:,0], params=pars, method='leastsq',
            ↪ nan_policy='propagate')
45          cis = result.conf_interval(sigmas=[4])
46          print(result.fit_report(show_correl=False))
47          print(result.ci_report())
48  gc.collect()
```

B.4 FEMTOSECOND TRANSIENT ABSORPTION PUMP–PROBE SPECTROSCOPY SCRIPTS

Script B.10: Al_2O_3 fsTAPP spectral and kinetic raw data, refining, and GVD correction.

```
1   import numpy as np
2   import os, gc, h5py
3   from scipy.interpolate import griddata
4   from fit_funcs import gvd_quad, gvd_cubic
5   from lmfit import Model
6   path = ['../0da/'
7           , '4ta/20190503_CaF2_scans/']
8   subs = ['passes/']
9   files = sorted(list(set([x.split('i')[0][:-1] for x in os.listdir(path[1]+subs[0])])))
10  files += sorted(list(set([x.split('i')[0][:-1] for x in os.listdir(path[2]+subs[0])])))
11  ids = [['500_', '050_', '100_', '150_', '250_', '400_', '600_', '700_', '999_']
12         ,['00C', '04A', '07A', '08D', '10A']
13         ,['500uM', '050uM', '006mM']]
14  gvd_data = np.genfromtxt(path[1]+'gvd_curve.txt')
15  gvd_data[:,0] = 1240/gvd_data[:,0]
16  gvd_curve = Model(gvd_cubic).fit(gvd_data[:,1],x=gvd_data[:,0],a=1,b=1,c=1,d=1)
17  gvd_par = np.zeros(4)
18  for k,l in enumerate(['a','b','c','d']):
19      gvd_par[k] = gvd_curve.params[l].value
20  print(gvd_curve.fit_report(show_correl=False))
21  id_set = [[x,y,z] for x in ids[0] for y in ids[1] for z in ids[2]]
22  eV = np.arange(1600,3101,1)/1000
23  ps = np.hstack((np.arange(-100,101,1)/100,np.logspace(0,3.23,646)[1:]))
24  ta = np.zeros((len(ps)+1,len(eV)+1))
25  ta[1:,0] = ps; ta[0,1:] = eV
26  titles = []; counter=0
27  for i in id_set:
28      for f in files:
29          if all(x in f for x in i):
30              path_f = path[1] if '500_' in f else path[2]
31              file = path_f + subs[0] + f +'%ii.txt'
32              if '00C' in i[1]:
33                  for p in range(5):
34                      solv_i = np.genfromtxt(file%p)
35                      solv_i[1:,1:] = solv_i[1:,1:] - np.average(solv_i[1:5,1:], axis=0)
36                      solv_p = solv_i if p==0 else np.dstack((solv_p, solv_i))
37                  solv_p = np.average(solv_p, axis=2)
38                  leng = solv_p.shape[0]
39              else:
```

```
40                          for p in range(5):
41                              scan_i = np.genfromtxt(file%p)
42                              scan_i[1:,1:] = scan_i[1:,1:] - np.average(scan_i[1:5,1:], axis=0)
43                              scan_i[1:leng,1:] = scan_i[1:leng,1:] - solv_p[1:,1:]
44                              WL,TD,TA = [],[],[]
45                              for x,wl in enumerate(scan_i[0,1:]):
46                                  for y,td in enumerate(scan_i[1:,0]):
47                                      WL.append(1240/wl)
48                                      TD.append(td-gvd_cubic(1240/wl, gvd_par[0], gvd_par[1], gvd_par[2],
                                    ↪   gvd_par[3]))
49                                      TA.append(scan_i[1:,1:][y,x])
50                              XYZ = np.column_stack((TD,WL,TA))
51                              scan_gl = griddata((XYZ[:,0], XYZ[:,1]), XYZ[:,2], (ps[:,None], eV[None,:]),
                                ↪   rescale=True, method='linear')
52                              scan_gn = griddata((XYZ[:,0], XYZ[:,1]), XYZ[:,2], (ps[:,None], eV[None,:]),
                                ↪   rescale=True, method='nearest')
53                              scan_gl[:,-1], scan_gl[-1,:] = np.nan, np.nan
54                              scan_gl[np.isnan(scan_gl)] = scan_gn[np.isnan(scan_gl)]
55                              scan_g = np.copy(ta)
56                              scan_g[1:,1:] = scan_gl
57                              scan_p = scan_g if p==0 else np.dstack((scan_p, scan_g))
58                          if counter==0:
59                              data_ave = np.average(scan_p, axis=2)
60                              data_std = np.std(scan_p, axis=2)
61                          else:
62                              data_ave = np.dstack((data_ave, np.average(scan_p, axis=2)))
63                              data_std = np.dstack((data_std, np.std(scan_p, axis=2)))
64                          titles.append('%s.%s.%s'%(i[1],i[2],i[0][:-1]))
65                          counter += 1
66  np.save(path[0]+'4ta_XXX-XXX-XXX_ave.npy', data_ave)
67  np.save(path[0]+'4ta_XXX-XXX-XXX_std.npy', data_ave)
68  hdf5_names = ['4ta_data', '0ds_data']
69  for i in range(len(hdf5_names)):
70      hdf5_file = h5py.File(path[0]+hdf5_names[i]+'.hdf5', 'a')
71      ta_data = hdf5_file.require_group('./4ta_data')
72      details = ['1st_column=td_ps', '1st row=wl_eV']
73      ta_data.attrs.create('ta-main_details', details, dtype=h5py.special_dtype(vlen=str))
74      for k in range(len(titles)):
75          ta_ave = ta_data.require_dataset('./%s_ave'%titles[k], shape=data_ave[:,:,k].shape,
            ↪   maxshape=(None, None), dtype=float, compression='gzip')
76          ta_ave[:,:] = data_ave[:,:,k]
77          ta_std = ta_data.require_dataset('./%s_std'%titles[k], shape=data_std[:,:,k].shape,
            ↪   maxshape=(None, None), dtype=float, compression='gzip')
78          ta_std[:,:] = data_std[:,:,k]
79      hdf5_file.close()
80  gc.collect()
```

Script B.11: CaF$_2$ fsTAPP spectral and kinetic raw data, refining, and GVD correction.

```
1   import numpy as np
2   import os, gc, h5py
3   from scipy.interpolate import griddata
4   from fit_funcs import gvd_cubic
5   from lmfit import Model
6   path = ['../0da_test/'
7           , '../4ta/20190503_CaF2_scans/']
8   subs = ['Passes/']
9   files = sorted(list(set([x.split('i')[0][:-1] for x in os.listdir(path[1]+subs[0])])))
10  files = [[files[x] for x in [2,3]], [files[x] for x in [7,8]], [files[x] for x in [5,6]]]
11
12  gvd_data = np.genfromtxt(path[1]+'gvd_curve_sorted.txt')
13  gvd_data[:,0] = gvd_data[:,0]
14  gvd_curve = Model(gvd_cubic).fit(gvd_data[:,1],x=gvd_data[:,0],a=1,b=1,c=1,d=1)
15  gvd_par = np.zeros(4)
16  for k,l in enumerate(['a','b','c','d']):
17      gvd_par[k] = gvd_curve.params[l].value
```

```
18    gvd_curve.plot_fit(xlabel='eV',ylabel='ps')
19    gvd_curve.plot_residuals()
20    print(gvd_curve.fit_report(show_correl=False))
21
22    eV = np.arange(1220,3871,2)/1000
23    ps = np.hstack((np.arange(-100,101,2)/100,np.logspace(0,3.23,323)[1:]))
24    ta = np.zeros((len(ps)+1,len(eV)+1))
25
26    for s in range(3):
27        data_f = [[x for x in os.listdir(path[1] + subs[0]) if files[s][0] in x]
28                   ,[x for x in os.listdir(path[1] + subs[0]) if files[s][1] in x]]
29        for f in range(len(data_f[0])):
30            data_e_i = np.genfromtxt(path[1] + subs[0] + data_f[0][f])
31            data_l_i = np.genfromtxt(path[1] + subs[0] + data_f[1][f])
32            data_e_i[1:,1:] = data_e_i[1:,1:] - np.average(data_e_i[1:10,1:], axis=0)
33            data_l_i[1:,1:] = data_l_i[1:,1:] - np.average(data_l_i[1:10,1:], axis=0)
34            data_e_i[0, 1:] = 1240/data_e_i[0, 1:]
35            data_l_i[0, 1:] = 1240/data_l_i[0, 1:]
36            data_e_i = np.delete(data_e_i, np.r_[120:150, 845:940], axis=1)
37            data_l_i = np.delete(data_l_i, np.r_[1:300, 185:265], axis=1)
38            data_i = np.hstack((data_e_i,data_l_i[:,1:]))
39            if s > 0:
40                data_i[1:len(solv)+1,1:] = data_i[1:len(solv)+1,1:] - solv
41                WL,TD,TA = [],[],[]
42                for x,wl in enumerate(data_i[0,1:]):
43                    for y,td in enumerate(data_i[1:,0]):
44                        WL.append(wl)
45                        TD.append(td-gvd_cubic(wl, gvd_par[0], gvd_par[1], gvd_par[2], gvd_par[3]))
46                        TA.append(data_i[1:,1:][y,x])
47                XYZ = np.column_stack((TD,WL,TA))
48                scan_gl = griddata((XYZ[:,0], XYZ[:,1]), XYZ[:,2], (ps[:,None], eV[None,:]), rescale=True,
              ↪  method='linear')
49                scan_gn = griddata((XYZ[:,0], XYZ[:,1]), XYZ[:,2], (ps[:,None], eV[None,:]), rescale=True,
              ↪  method='nearest')
50                scan_gl[:,-1], scan_gl[-1,:] = np.nan, np.nan
51                scan_gl[np.isnan(scan_gl)] = scan_gn[np.isnan(scan_gl)]
52                data_i = np.copy(ta[:-1,:])
53                data_i[1:,1:] = scan_gl[:-1,:]
54            data_s = data_i if f == 0 else np.dstack((data_s,data_i))
55        if s == 0:
56            solv = np.average(data_s[1:,1:,:], axis=2)
57        else:
58            ave = np.average(data_s, axis=2); ave[0,1:] = eV; ave[1:,0] = ps[:-1]
59            std = np.std(data_s, axis=2); std[0,1:] = eV; std[1:,0] = ps[:-1]
60            data_ave = ave if s == 1 else np.dstack((data_ave, ave))
61            data_std = std if s == 1 else np.dstack((data_std, std))
62    np.save(path[0]+'4ta_XXX-388EL-500_ave.npy', data_ave)
63    np.save(path[0]+'4ta_XXX-388EL-500_std.npy', data_std)
64
65    hdf5_names = ['4ta_data', '0ds_data']
66    for i in range(len(hdf5_names)):
67        hdf5_file = h5py.File(path[0]+hdf5_names[i]+'.hdf5', 'a')
68        ta_data = hdf5_file.require_group('./4ta_data')
69        details = ['1st_column=td_ps', '1st row=wl_eV']
70        ta_data.attrs.create('ta-main-details', details, dtype=h5py.special_dtype(vlen=str))
71        for k in range(2):
72            title = files[k+1][0][14:-3].replace('_388E-','.caf2.')
73            ta_ave = ta_data.require_dataset('./%s_ave'%title, shape=data_ave[:,:,k].shape,
              ↪  maxshape=(None, None), dtype=float, compression='gzip')
74            ta_ave[:,:] = data_ave[:,:,k]
75            ta_std = ta_data.require_dataset('./%s_std'%title, shape=data_std[:,:,k].shape,
              ↪  maxshape=(None, None), dtype=float, compression='gzip')
76            ta_std[:,:] = data_std[:,:,k]
77        hdf5_file.close()
78    gc.collect()
```

Script B.12: Multi–exponential fit of the kinetic profile of first photoinduced absorption (PIA$_1$) feature extracted from fsTAPP data.

```python
1   import numpy as np
2   import matplotlib.pyplot as plt
3   from matplotlib import cm, colorbar, rc
4   import scipy.special as spsp
5   from mpl_toolkits.axes_grid1.inset_locator import inset_axes
6   from matplotlib.ticker import ScalarFormatter
7   from pprint import pprint
8   import os, gc, h5py, copy
9   from lmfit import CompositeModel, Model, Parameters
10  from matplotlib import interactive as mplint; mplint(False)
11  from matplotlib import use as mpluse; mpluse('agg')
12  from fit_funcs import exp_c, gaus, lna, lne, gausst, expg
13  from funcs import idx
14
15  plt.rcParams.update({'font.size': 8})
16  rc('font', **{'family': 'serif', 'serif': 'Computer Modern'})
17  rc('text', usetex=True)
18
19  data_file = h5py.File('../0da/0ds_data.hdf5', 'r')
20
21  path = './ta_linefit_results/'
22
23  sam_set = ['10A', '08D', '04A', '07A']
24  for i in sam_set:
25          ta_i = data_file['4ta_data']['%s.%s.%s_ave'%(i,'500uM','500')][:,:1331]
26          ta_i = np.delete(ta_i,np.r_[1:201],axis=1)
27          if i=='10A':
28                  data = np.copy(ta_i)
29          else:
30                  data = np.dstack((data,ta_i))
31  gc.collect()
32
33  #             1.8,2.25,2.55,2.7,2.9eV
34  slices = [
35              [1,500,900],
36              [1,460,750,1060],
37              [1,460,750,1060],
38              [1,460,750,1060]
39  ]
40  lolts = [12.95e3, 11.27e3, 9.49e3, 10.64e3]#long lifetimes from trpl (ps)
41  ###########functions#################
42  def gaus_ar(t, I0, t0, rf):
43          H = 2*(np.sqrt(2*np.log(2)))*rf
44          return I0*(np.exp((-4*np.log(2)*(t-t0)**2)/(H**2)))
45
46  def seco(t, I0, t0, rf, tu):
47          H = 2*(np.sqrt(2*np.log(2)))*rf
48          t = t-t0
49          t1 = t
50          t2 = np.linspace(t[0],t[(abs(-t[0]-t)).argmin()],201)
51          y1 = np.zeros(len(t1)+len(t2))
52          for i in range(len(y1)):
53                  if i >= len(t):
54                          y1[i] = (tu)/(tu+t[-1])
55                  elif i < len(t) and t[i] > 0:
56                          y1[i] = (tu)/(tu+t[i])
57          y2 = np.exp((-4*np.log(2)*(t2-t0)**2)/(H**2))
58          y = np.convolve(y1,0.1*y2,mode='same')
59          y = I0*(y/np.amax(y))
60          y = y[:len(t)]
61          return y
62
63  def expg(t, I0, t0, rf, tu):
64          t = t-t0
```

```
65          la = 1/tu
66          y = I0 * np.exp(-la*(t-(rf**2*la)/2)) * (1+spsp.erf((t-(rf**2*la))/((np.sqrt(2)*rf))))
67          return y
68  ##################################
69  #################models&params#####
70
71  sam_idx = 2
72  tu3 = lolts[sam_idx]
73  # artifacts model and parameters
74  AR  = Model(gaus_ar, prefix='AR_', independent_vars=['t'], nan_policy='propagate')
75  AR_p = Parameters()
76  AR_p.add_many(
77                  ('AR_I0', 1.000,  True,  None,  None,  None )
78                 ,('AR_t0', 0.000,  True,  None,  None,  None )
79                 ,('AR_rf', 0.250, False,  None,  None,  None )
80                 )
81  #PIA1 model
82  P1  = AR
83  P1 += Model(expg, prefix='P1a_', independent_vars=['t'], nan_policy='propagate')
84  P1 += Model(expg, prefix='P1c_', independent_vars=['t'], nan_policy='propagate')
85  P1_p = AR_p
86  P1_p.add_many(
87                  ('P1a_I0', 0.200,  True, 0.000, 1.000,  None)
88                 ,('P1a_t0', 0.000,  True,  None,  None, 'AR_t0')
89                 ,('P1a_rf', 0.200,  True,  None,  None, 'AR_rf')
90                 ,('P1a_tu', 10.00,  True, 0.000, 50.00,  None)
91                 ,('P1c_I0', 0.200,  True, 0.000,  None,  None)
92                 ,('P1c_t0', 0.000,  True,  None,  None, 'AR_t0')
93                 ,('P1c_rf', 0.200,  True,  None,  None, 'AR_rf')
94                 ,('P1c_tu', 1.0e3, False,  1e2,  None,  None)
95                 )
96  #######fit&plot################
97  sam_set = ['BDODC','HTRMR','OLGMR','PLYMR']
98
99  with open(path+'P1_results.txt','w') as f:
100         for i in range(4):
101                 P1_model = P1
102                 P1_pars = P1_p
103                 if i in [1,2,3]:
104                         P1_model += Model(expg, prefix='P1b_', independent_vars=['t'],
                         ↪  nan_policy='propagate')
105                         P1_pars.add_many(
106                                         ('P1b_I0',0.200,True,0.000, None, None)
107                                        ,('P1b_t0',0.000,True, None, None,'AR_t0')
108                                        ,('P1b_rf',0.200,True, None, None,'AR_rf')
109                                        ,('P1b_tu',1.0e2,True,0.000,1.0e3, None)
110                                        )
111                 P1_p['P1c_tu'].set(value=lolts[i],vary=False)
112                 P1_fit_results = P1_model.fit(data[1:,slices[i][0],i], params=P1_pars, t=data[1:,0,0],
                 ↪  method='leastsq', nan_policy='propagate')
113                 P1_fit_results.conf_interval(sigmas=[2])
114                 print(P1_fit_results.fit_report(show_correl=False, sort_pars=True))
115                 print(P1_fit_results.ci_report())
116                 f.write('##############{:s}#############'.format(sam_set[i])+'\n')
117                 f.write(P1_fit_results.fit_report(show_correl=False, sort_pars=True)+'\n')
118                 f.write(P1_fit_results.ci_report()+'\n')
119  f.close()
```

Script B.13: Multi–exponential fit of the kinetic profile of stimulated emission (SE) feature extracted from fsTAPP data.

```
1  import numpy as np
2  import matplotlib.pyplot as plt
3  from matplotlib import cm, colorbar, rc
4  import scipy.special as spsp
```

```
 5    from mpl_toolkits.axes_grid1.inset_locator import inset_axes
 6    from matplotlib.ticker import ScalarFormatter
 7    from pprint import pprint
 8    import os, gc, h5py, copy
 9    from lmfit import CompositeModel, Model, Parameters
10    from matplotlib import interactive as mplint; mplint(False)
11    from matplotlib import use as mpluse; mpluse('agg')
12    from fit_funcs import exp_c, gaus, lna, lne, gausst, expg
13    from funcs import idx
14
15    plt.rcParams.update({'font.size': 8})
16    rc('font', **{'family': 'serif', 'serif': 'Computer Modern'})
17    rc('text', usetex=True)
18
19    data_file = h5py.File('../0da/0ds_data.hdf5', 'r')
20
21    path = './ta_linefit_results/'
22
23    sam_set = ['10A', '08D', '04A', '07A']
24    for i in sam_set:
25            ta_i = data_file['4ta_data']['%s.%s.%s_ave'%(i,'500uM','500')][:,:1331]#[:,:1250]
26            ta_i = np.delete(ta_i,np.r_[1:201],axis=1)
27            #ta_i = np.delete(ta_i,np.r_[1:201],axis=0)
28            if i=='10A':
29                    data = np.copy(ta_i)
30            else:
31                    data = np.dstack((data,ta_i))
32    gc.collect()
33
34    #        1.8,2.25,2.55,2.7,2.9eV
35    slices = [
36             [1,500,900],
37             [1,460,750,1060],
38             [1,460,750,1060],
39             [1,460,750,1060]
40            ]
41
42    lolts = [12.95e3, 11.27e3, 9.49e3, 10.64e3]#long lifetimes from trpl (ps)
43    ##########functions#################
44    def gaus_ar(t, I0, t0, rf):
45            H = 2*(np.sqrt(2*np.log(2)))*rf
46            return I0*(np.exp((-4*np.log(2)*(t-t0)**2)/(H**2)))
47
48    def seco(t, I0, t0, rf, tu):
49            H = 2*(np.sqrt(2*np.log(2)))*rf
50            t = t-t0
51            t1 = t
52            t2 = np.linspace(t[0],t[(abs(-t[0]-t)).argmin()],201)
53            y1 = np.zeros(len(t1)+len(t2))
54            for i in range(len(y1)):
55                    if i >= len(t):
56                            y1[i] = (tu)/(tu+t[-1])
57                    elif i < len(t) and t[i] > 0:
58                            y1[i] = (tu)/(tu+t[i])
59            y2 = np.exp((-4*np.log(2)*(t2-t0)**2)/(H**2))
60            y = np.convolve(y1,0.1*y2,mode='same')
61            y = I0*(y/np.amax(y))
62            y = y[:len(t)]
63            return y
64
65    def expg(t, I0, t0, rf, tu):
66            t = t-t0
67            la = 1/tu
68            y = I0 * np.exp(-la*(t-(rf**2*la)/2)) * (1+spsp.erf((t-(rf**2*la))/((np.sqrt(2)*rf))))
69            return y
70    ################################
71    ###############models&params#####
72    sam_idx = 2
```

190

```
73    tu3 = lolts[sam_idx]
74    # artifacts model and parameters
75    AR  = Model(gaus_ar, prefix='AR_', independent_vars=['t'], nan_policy='propagate')
76    AR_p = Parameters()
77    AR_p.add_many(
78                  ('AR_I0',1.000, True, None, None, None)
79                 ,('AR_t0',0.000, True, None, None, None)
80                 ,('AR_rf',0.240,False, None, None, None)
81                 )
82    #SE model
83    SE  = AR
84    SE += Model(expg, prefix='SEa_', independent_vars=['t'], nan_policy='propagate')
85    SE += Model(expg, prefix='SEb_', independent_vars=['t'], nan_policy='propagate')
86    SE += Model(expg, prefix='SEd_', independent_vars=['t'], nan_policy='propagate')
87    SE_p = AR_p
88    SE_p.add_many(
89                  ('SEa_I0',0.200, True,0.000,2.000, None)
90                 ,('SEa_t0',0.000, True, None, None,'AR_t0')
91                 ,('SEa_rf',0.200, True, None, None,'AR_rf')
92                 ,('SEa_tu',1.000, True,0.000,1.0e1, None)
93                 ,('SEb_I0',-0.20, True,-2.00,0.000, None)
94                 ,('SEb_t0',0.000, True, None, None,'AR_t0')
95                 ,('SEb_rf',0.200, True, None, None,'AR_rf')
96                 ,('SEb_tu',10.00, True,0.100,1.0e2, None)
97                 ,('SEd_I0',-0.20, True,-2.00,0.000, None)
98                 ,('SEd_t0',0.000, True, None, None,'AR_t0')
99                 ,('SEd_rf',0.200, True, None, None,'AR_rf')
100                ,('SEd_tu',1.0e3,False,  1e2, None, None)
101                )
102   #######fit&plot###############
103   sam_set = ['BDODC','HTRMR','OLGMR','PLYMR']
104
105
106   with open(path+'SE_results.txt','w') as f:
107        for i in range(4):
108              SE_model = SE
109              SE_pars = SE_p
110              if i in [1,2,3]:
111                    SE_model += Model(expg, prefix='SEc_', independent_vars=['t'],
                      ↪  nan_policy='propagate')
112                    SE_pars.add_many(
113                                  ('SEc_I0',-0.20, True,-1.00,0.000, None)
114                                 ,('SEc_t0',0.000, True, None, None,'AR_t0')
115                                 ,('SEc_rf',0.200, True, None, None,'AR_rf')
116                                 ,('SEc_tu',100.0, True,0.000,1.0e3, None)
117                                 )
118              SE_p['SEd_tu'].set(value=lolts[i],vary=False)
119              SE_fit_results = SE_model.fit(data[1:,slices[i][1],i], params=SE_pars, t=data[1:,0,0],
                 ↪  method='leastsq', nan_policy='propagate')
120              print(SE_fit_results.fit_report(show_correl=False, sort_pars=True))
121              f.write('#############{:s}#############'.format(sam_set[i])+'\n')
122              f.write(SE_fit_results.fit_report(show_correl=False, sort_pars=True)+'\n')
123   f.close()
```

Script B.14: Multi–exponential fit of the kinetic profile of second photoinduced absorption (PIA_2) feature extracted from fsTAPP data.

```
1    import numpy as np
2    import matplotlib.pyplot as plt
3    from matplotlib import cm, colorbar, rc
4    import scipy.special as spsp
5    from mpl_toolkits.axes_grid1.inset_locator import inset_axes
6    from matplotlib.ticker import ScalarFormatter
7    from pprint import pprint
8    import os, gc, h5py, copy
```

```
 9    from lmfit import CompositeModel, Model, Parameters
10    from matplotlib import interactive as mplint; mplint(False)
11    from matplotlib import use as mpluse; mpluse('agg')
12    from fit_funcs import exp_c, gaus, lna, lne, gausst, expg
13    from funcs import idx
14
15    plt.rcParams.update({'font.size': 8})
16    rc('font', **{'family': 'serif', 'serif': 'Computer Modern'})
17    rc('text', usetex=True)
18
19    data_file = h5py.File('../0da/0ds_data.hdf5', 'r')
20
21    path = './ta_linefit_results/'
22
23    sam_set = ['10A', '08D', '04A', '07A']
24    for i in sam_set:
25            ta_i = data_file['4ta_data']['%s.%s.%s_ave'%(i,'500uM','500')][:,:1331]
26            ta_i = np.delete(ta_i,np.r_[1:201],axis=1)
27            if i=='10A':
28                    data = np.copy(ta_i)
29            else:
30                    data = np.dstack((data,ta_i))
31    gc.collect()
32
33    #           1.8,2.25,2.55,2.7,2.9eV
34    slices = [
35            [1,500,900],
36            [1,460,750,1060],
37            [1,460,750,1060],
38            [1,460,750,1060]
39            ]
40
41    lolts = [12.95e3, 11.27e3, 9.49e3, 10.64e3]#long lifetimes from trpl (ps)
42    ##########functions################
43    def gaus_ar(t, I0, t0, rf):
44            H = 2*(np.sqrt(2*np.log(2)))*rf
45            return I0*(np.exp((-4*np.log(2)*(t-t0)**2)/(H**2)))
46
47    def seco(t, I0, t0, rf, tu):
48            H = 2*(np.sqrt(2*np.log(2)))*rf
49            t = t-t0
50            t1 = t
51            t2 = np.linspace(t[0],t[(abs(-t[0]-t)).argmin()],201)
52            y1 = np.zeros(len(t1)+len(t2))
53            for i in range(len(y1)):
54                    if i >= len(t):
55                            y1[i] = (tu)/(tu+t[-1])
56                    elif i < len(t) and t[i] > 0:
57                            y1[i] = (tu)/(tu+t[i])
58            y2 = np.exp((-4*np.log(2)*(t2-t0)**2)/(H**2))
59            y = np.convolve(y1,0.1*y2,mode='same')
60            y = I0*(y/np.amax(y))
61            y = y[:len(t)]
62            return y
63
64    def expg(t, I0, t0, rf, tu):
65            t = t-t0
66            la = 1/tu
67            y = I0 * np.exp(-la*(t-(rf**2*la)/2)) * (1+spsp.erf((t-(rf**2*la))/((np.sqrt(2)*rf))))
68            return y
69    ##################################
70    ###############models&params#####
71    sam_idx = 2
72    tu3 = lolts[sam_idx]
73    # artifacts model and parameters
74    AR  = Model(gaus_ar, prefix='AR_', independent_vars=['t'], nan_policy='propagate')
75    AR_p = Parameters()
76    AR_p.add_many(
```

```
77                          ('AR_I0',1.000, True, None, None, None)
78                         ,('AR_t0',0.000, True, None, None, None)
79                         ,('AR_rf',0.220,False, None, None, None)
80                          )
81  #PIA2 model
82  P2  = AR
83  P2 += Model(expg, prefix='P2a_', independent_vars=['t'], nan_policy='propagate')
84  P2 += Model(expg, prefix='P2b_', independent_vars=['t'], nan_policy='propagate')
85  P2 += Model(expg, prefix='P2d_', independent_vars=['t'], nan_policy='propagate')
86  P2_p = AR_p
87  P2_p.add_many(
88                  ('P2a_I0',-0.20, True,-2.00,0.000, None)
89                 ,('P2a_t0',0.000, True, None, None,'AR_t0')
90                 ,('P2a_rf',0.200, True, None, None,'AR_rf')
91                 ,('P2a_tu',5.000, True,0.100, 1.0e1 None)
92                 ,('P2b_I0',0.200, True,0.000, 3.000 None)
93                 ,('P2b_t0',0.000, True, None, None,'AR_t0')
94                 ,('P2b_rf',0.200, True, None, None,'AR_rf')
95                 ,('P2b_tu',10.00, True,0.000,3.0e2, None)
96                 ,('P2d_I0',0.200, True,0.000, 5.000 None)
97                 ,('P2d_t0',0.000, True, None, None,'AR_t0')
98                 ,('P2d_rf',0.200, True, None, None,'AR_rf')
99                 ,('P2d_tu',1.0e3, True, 1e2, None, None)
100                 )
101  #######fit&plot################
102  sam_set = ['BDODC','HTRMR','OLGMR','PLYMR']
103
104  with open(path+'P2_results.txt','w') as f:
105      for i in range(4):
106          P2_model = P2
107          P2_pars = P2_p
108          if i in [1,2,3]:
109              P2_model += Model(expg, prefix='P2c_', independent_vars=['t'],
                  ↪ nan_policy='propagate')
110              P2_pars.add_many(
111                              ('P2c_I0',0.200, True,0.000,1.000, None)
112                             ,('P2c_t0',0.000, True, None, None,'AR_t0')
113                             ,('P2c_rf',0.200, True, None, None,'AR_rf')
114                             ,('P2c_tu',100.0, True,0.000,5.0e3, None)
115                              )
116          P2_p['P2d_tu'].set(value=lolts[i],vary=False)
117          P2_fit_results = P2_model.fit(data[1:,slices[i][2],i], params=P2_pars, t=data[1:,0,0],
              ↪ method='leastsq', nan_policy='propagate')
118          print(P2_fit_results.fit_report(show_correl=False, sort_pars=True))
119          f.write('#############{:s}#############'.format(sam_set[i])+'\n')
120          f.write(P2_fit_results.fit_report(show_correl=False, sort_pars=True)+'\n')
121  f.close()
```

B.5 DENSITY FUNCTIONAL THEORY RELATED SCRIPTS

Script B.15: Analysis of chromophores benchmark against various basis sets.

```
1  import cclib as cl
2  import numpy as np
3  import os
4  from matplotlib import rc
5  import matplotlib.pyplot as plt
6
7
8  paths = ['../5qc/01/Bs/','../5qc/03/Bs/']
9  print('Done')
10
11
```

```
12    bs_sym = [['X1', 'X2', 'X3', 'X4', 'X5','X6'], ['X1', 'X2', 'X3', 'X4', 'X5']]
13    for c in [0,1]:
14        files_f =[]
15        for bs in bs_sym[c]:
16            files_bs = []
17            files = [x for x in os.listdir(paths[c]) if '.log' in x]
18            for f in files:
19                if bs in f:
20                    files_bs += [f]
21            files_f += [files_bs[-1]]
22        file_a = files_f if c==0 else [file_a]+[files_f]
23
24    for c in [0,1]:
25        basis, s1en, hf = [], [], []
26        for i,j in enumerate(file_a[c]):
27            data_i = cl.io.ccread(paths[c]+j)
28            basis += [data_i.metadata['basis_set'].replace('-','--')]
29            s1en += [data_i.etenergies[0]/8065.54]
30            hf += [data_i.scfenergies[-1]/27.2114]
31            #print(data_i.getattributes().keys())
32        basis_a = basis if c==0 else [basis_a]+[basis]
33        s1en_a = s1en if c==0 else [s1en_a]+[s1en]
34        hf_a = hf if c==0 else [hf_a]+[hf]
35
36    s1en_merg = [s1en_a[0][i]-np.average(s1en_a[0]) for i in range(6)]+[s1en_a[1][i]-np.average(s1en_a[1])
      ↪  for i in range(5)]
37
38    #3.044+2.92-2.815 = 3.129
39    facs = [2.92,3.149]
40    hf_err = [[x-hf_a[c][0] for x in hf_a[c]] for c in [0,1]]
41    s1err = [[x-facs[c] for x in s1en_a[c]] for c in [0,1]]
42
43    lbl = ['BDODC','BDOSC']
44    marker = ['o','s']
45    fig_lbl = ['(a)', '(b)', '(c)']
46
47    cpu_t = [[18169.8, 56181.6, 262114.2, 470014.9, 161361.6, 2351011.5]
48            ,[50738.1, 180311.6, 1096684.1, 1880449.9, 874397.6]]
49    cpu_t = [[x/3600 for x in cpu_t[s]] for s in range(2)]
50    data_all = [cpu_t,s1err,hf_err]
51    print(basis_a)
52    print(data_all)
```

Script B.16: Analysis of heterodimer sub–unit (HDIMR) benchmark against various functionals.

```
1    import cclib as cl
2    import numpy as np
3    import os
4    from matplotlib import rc
5    import matplotlib.pyplot as plt
6
7    paths = ['../5qc/13/XC/']
8
9
10   data_xx = cl.io.ccread(paths[0]+'13ChOFTs0xxx.log')
11   trans_idx_all, esen_all, func_all = [], [], []
12   for func in [[0,50],[50,100],[100,150],[150,200],[200,250],[250,300],[300,350]]:
13       trans_idx, esen = [], []
14       for trans in [[-1,1],[0,2],[0,1],[-1,2]]:
15           trans_idx_i, ci_coef_i = [],[]
16           for i in range(func[0],func[1]):
17               for j in range(len(data_xx.etsecs[i])):
18                   if data_xx.etsecs[i][j][0][0]==data_xx.homos+trans[0] and
                     ↪  data_xx.etsecs[i][j][1][0]==data_xx.homos+trans[1]:
19                       trans_idx_i += [i]
```

```
20                         ci_coef_i += [abs(data_xx.etsecs[i][j][2])]
21             trans_loc = np.argmax(ci_coef_i)
22             trans_idx += [trans_idx_i[trans_loc]]
23         for es_no in trans_idx:
24             esen += [data_xx.etenergies[es_no]/8065.54]
25         esen_all += [esen]
26         trans_idx_all += [trans_idx]
27 eten_all = [[esen_all[i][j] for i in range(7)] for j in range(4)]
28 trans_en = np.array(eten_all).T
29 fn_sym = ['000', '020', '040', '060', '080', 'ca', 'lc']
30 files_a =[]
31 for fn in fn_sym:
32     files_fn = []
33     files = [x for x in os.listdir(paths[0]) if '.log' in x]
34     for f in files:
35         if fn in f:
36             files_fn += [f]
37     files_a += [files_fn[-1]]
38 for spin in [[0,50],[50,100]]:
39     trans_idx_all, esen_all, func_all = [], [], []
40     for file in files_a:
41         data_i = cl.io.ccread(paths[0]+file)
42         func_all += [data_i.metadata['functional']]
43         trans_idx, esen = [], []
44         for trans in [[-1,1],[0,2],[0,1],[-1,2]]:
45             trans_idx_i, ci_coef_i = [],[]
46             for i in range(spin[0],spin[1]):
47                 for j in range(len(data_i.etsecs[i])):
48                     if data_i.etsecs[i][j][0][0]==data_i.homos+trans[0] and
            ↪  data_i.etsecs[i][j][1][0]==data_i.homos+trans[1]:
49                         trans_idx_i += [i]
50                         ci_coef_i += [abs(data_i.etsecs[i][j][2])]
51             trans_loc = np.argmax(ci_coef_i)
52             trans_idx += [trans_idx_i[trans_loc]]
53         for es_no in trans_idx:
54             esen += [data_i.etenergies[es_no]/8065.54]
55         esen_all += [esen]
56         trans_idx_all += [trans_idx]
57     eten_all = [[esen_all[i][j] for i in range(7)] for j in range(4)]
58     trans_en = np.column_stack((trans_en,np.array(eten_all).T))
59
60 print('state/method',['BLYP', 'B3LYP', 'BLYP-60:40', 'BLYP-40:60', 'BLYP-20:80', 'CAM-B3LYP',
    ↪  'LC-BLYP'])
61 print('VS1(b3lyp)',['{:0.5f}'.format(i-2.815) for i in trans_en[:,0]])
62 print('VS2(b3lyp)',['{:0.5f}'.format(i-3.044) for i in trans_en[:,1]])
63 print('VS1(method)',['{:0.5f}'.format(i-2.815) for i in trans_en[:,4]])
64 print('VS2(method)',['{:0.5f}'.format(i-3.044) for i in trans_en[:,5]])
```

Script B.17: Calculations of the ionization potentials (IPs).

```
1  import cclib as cl
2  import numpy as np
3  import os
4  from matplotlib import rc
5  import matplotlib.pyplot as plt
6
7
8  paths = ['../5qc/00/Ga/','../5qc/01/Ga/','../5qc/03/Ga/','../5qc/13/Ga/']
9  print('Done')
10
11 ips = []
12 for i in paths:
13     f = [x for x in os.listdir(i) if '.log' in x][0]
14     data_i = cl.io.ccread(i+f)
15     ips.append(data_i.scfenergies[-2]-data_i.scfenergies[-1])
16 print(['BDO','BDODC','BDOSC','HDIMR'])
17 print(ips)
```

```python
1   import cclib as cl
2   import numpy as np
3   import os
4   from matplotlib import rc
5   import matplotlib.pyplot as plt
6
7   path = ['../5qc/']
8
9   strucs = ['00','01','03','13']
10  meths = ['Ch','Ga']
11  ve_files = sorted([x for y in strucs for x in os.listdir(path[0]+y+'/'+meths[0]+'/') if 'OFTx0.log' in
    ↪   x])
12  ip_files = sorted([x for y in strucs for x in os.listdir(path[0]+y+'/'+meths[1]+'/') if 'OFEx0.log' in
    ↪   x])
13  print(ve_files,ip_files)
14
15  mod_lbl = ['BDO', 'BDODC', 'BDOSC', 'HDIMR']
16
17
18  for i in range(4):
19      lims = 10 if i in [0,1,2] else 20
20      data_i = cl.io.ccread(path[0]+strucs[i]+'/'+meths[0]+'/'+ve_files[i])
21      print(mod_lbl[i])
22      print(data_i.etenergies[:lims]/8065.6)
```

B.6 GENERAL PURPOSE SCRIPTS

Script B.19: Definitions of mathematical functions employed in the fitting procedures presented in this work

```python
1   from numpy import zeros, sqrt, log, exp, pi, outer
2   from scipy.special import erf
3   from astropy.convolution import convolve_fft
4   from lmfit.lineshapes import gaussian
5
6   def exp_p(x,a,t,t0):
7       y = np.zeros(len(x))
8       for i,j in enumerate(x):
9           if j-t0 > 0:
10              y[i] = a * np.exp(- j / t)
11      return y
12
13
14  def irf(x, I0, c, w, tau):
15      x = x[np.argmin(abs(x-c+(5*w))):np.argmin(abs(x-c-(5*w)))]
16      return gaus_c(x, I0, c, w, tau)
17
18  def convolve(func, ker):
19      orig = len(func)
20      func = np.pad(func,(0,len(ker)*10), mode='linear_ramp', end_values=0)
21      con = convolve_fft(func,ker, boundary='fill', normalization_zero_tol=1e-12,
    ↪   normalize_kernel=True, nan_treatment='interpolate')
22      return con[:orig]
23
24
25  def gvd_cubic(x, a, b, c, d):
26      func=a+(b*x)+(c*x**2)+(d*x**3)
27      return func
```

```python
28
29  def gvd_quad(x, a, b, c):
30          func=a+(b*x)+(c*x**2)
31          return func
32
33  def gaus_c(t, I0, c, w):
34          t = t-c
35          y = (I0/(w*sqrt(2*pi)))  *exp(-0.5*((t/w)**2))
36          return y
37
38  def exp_c(t, I0, c, w, tau):
39          t = t-c
40          la = 1/tau
41          y = (I0) * exp(-la*(t-(w**2*la)/2)) * (1+erf((t-(w**2*la))/((sqrt(2)*w))))
42          return y
43
44  def expg(t, I0, t0, rf, tu):
45          t = t-t0
46          la = 1/tu
47          y = I0 * exp(-la*(t-(rf**2*la)/2)) * (1+erf((t-(rf**2*la))/((sqrt(2)*rf))))
48          return y
49
50
51  def lognat(v, t, I0, v0, H0, p0, tu, t0, t1, t2, t3, rf):
52          I= zeros((len(t), len(v))); la=1/tu
53          for i in range(len(t)):
54                  for j in range(len(v)):
55                          tv = t[i] - (t0 + (t1 * v[j]) + (t2 * v[j]**2) + (t3 * v[j]**3))
56                          a = v0 - (H0*(p0/((p0**2)-1)))
57                          w = rf/sqrt(8*log(2))
58                          w = w*(v[j]/v[j]) if v[j]>a else w
59                          if v[j] > a:
60                                  if w == 0:
61                                          if tv > 0:
62                                                  I[i, j]=exp(-la*tv)
63                                  else:
64                                          I[i, j] = (0.5 * exp(-la * (tv - (0.5 * la * w**2))) * (1 +
                                          ↪   erf((tv - (la * w **2))/( w *sqrt(2)))))
65                                  I[i, j] = (I0 * I[i, j] * exp(-(log(2) / (log(p0))**2) * (log((v[j] -
                                          ↪   a) / (v0-a))**2)))
66          return I
67
68  def lognet(v, t, I0, v0, H0, p0, tu, t0, t1, t2, t3, rf):
69          I= zeros((len(t), len(v))); la=1/tu
70          for i in range(len(t)):
71                  for j in range(len(v)):
72                          tv = t[i] - (t0 + (t1 * v[j]) + (t2 * v[j]**2) + (t3 * v[j]**3))
73                          a = v0 + (H0 * (p0 / ((p0**2) - 1)))
74                          w = rf / sqrt(8 * log(2))
75                          w = w * (v[j] / v[j]) if v[j] < a else w
76                          if v[j] < a:
77                                  if w == 0:
78                                          if tv > 0:
79                                                  I[i, j] = exp(-la * tv)
80                                  else:
81                                          I[i, j] = (0.5 * exp(-la * (tv - (0.5 * la * w**2))) * (1 +
                                          ↪   erf((tv - (la * w**2)) / (w * sqrt(2)))))
82                                  I[i, j] = (I0 * I[i, j] * exp(-(log(2) / (log(p0))**2) * (log((a -
                                          ↪   v[j]) / (a - v0))**2)))
83          return I
84
85  def gausstgvd(v, t, I0, v0, H0, tu, rf, t0, t1, t2, t3):
86          """
87          This function simulates a 2D (v,t) gaussian lineshape with center (v0),
88          FWHM (H0), intensity (I0). The gaussian decays in a single exponential
89          fashion with time constant (tu), that is convoluted with gaussiab IRF
90          of width (rf). The 2D function exhibits a simulated cubic GVD behavior
91          with the the cubic parameters being: t0, t1, t2, t3. The parameter's
```

197

```python
92              numebr represents the independent variable's order.
93              """
94          I= zeros((len(t), len(v))); la=1/tu
95          w0=H0/sqrt(8*log(2))
96          w=rf/sqrt(8*log(2))
97          for j in range(len(v)):
98                  tv0=t0+(t1*v[j])+(t2*v[j]**2)+(t3*v[j]**3)
99                  for i in range(len(t)):
100                         tv = t[i] - tv0
101                         if w == 0 and tv > 0:
102                                 I[i, j]=exp(-la*tv)
103                         else:
104                                 I[i, j]=(0.5*exp(-la*(tv-(0.5*la*w**2))) *
                                ↪  (1+erf((tv-(la*w**2))/(w*sqrt(2)))))
105                         I[i, j]=(I0*I[i, j]*exp(-((v[j]-v0)**2)/(2*w0**2)))
106         return I
107
108 def gausst_slow(v, t, I0, v0, H0, tu, t0, t1, t2, t3, rf):
109         """
110         This function simulates a 2D (v,t) gaussian lineshape with center (v0),
111         FWHM (H0), intensity (I0). The gaussian decays in a single exponential
112         fashion with time constant (tu), that is convoluted with gaussiab IRF
113         of width (rf). The 2D function exhibits a simulated cubic GVD behavior
114         with the the cubic parameters being: t0, t1, t2, t3. The parameter's
115         numebr represents the independent variable's order.
116         """
117         I= zeros((len(t), len(v))); la=1/tu
118         for i in range(len(t)):
119                 for j in range(len(v)):
120                         tv=t[i]-(t0+(t1*v[j])+(t2*v[j]**2)+(t3*v[j]**3))
121                         w0=H0/sqrt(8*log(2))
122                         w=rf/sqrt(8*log(2))
123                         w=w*(v[j]/v[j])
124                         if w == 0:
125                                 if tv > 0:
126                                         I[i, j]=exp(-la*tv)
127                         else:
128                                 I[i, j]=(0.5*exp(-la*(tv-(0.5*la*w**2))) *
                                ↪  (1+erf((tv-(la*w**2))/(w*sqrt(2)))))
129                         I[i, j]=(I0*I[i, j]*exp(-((v[j]-v0)**2)/(2*w0**2)))
130         return I
131
132 def gausst(v, t, I0, v0, H0, tu, rf, t0):
133         """
134         This function simulates a 2D (v,t) gaussian lineshape with center (v0),
135         FWHM (H0), intensity (I0). The gaussian decays in a single exponential
136         fashion with time constant (tu), that is convoluted with gaussiab IRF
137         of width (rf) and shifted by t0.
138         """
139         la=1/tu
140         w0=H0/sqrt(8*log(2))
141         w=rf/sqrt(8*log(2))
142         d = zeros(len(t))
143         for i in range(len(t)):
144                 tv = t[i] - t0
145                 if w == 0:
146                         if tv > 0:
147                                 d[i]=exp(-la*tv)
148                 else:
149                         d[i]=(0.5*exp(-la*(tv-(0.5*la*w**2))) * (1+erf((tv-(la*w**2))/(w*sqrt(2)))))
150         I=I0*(outer(d,exp(-((v-v0)**2)/(2*w0**2))))
151         return I
152
153
154 def logna(v, e0, v0, H, p):
155         y=zeros(len(v))
156         c=log(p)/sqrt(2*log(2))
157         b=(H*(p/((p**2)-1)))*exp(c**2)
```

```
158            a=v0-(H*(p/((p**2)-1)))
159            for i, j in enumerate(v):
160                    if j > a:
161                            y[i]=((e0*b)/(v[i]-a))*exp(-c**2) * exp((-1/c**2)*(log((v[i]-a)/b))**2)
162            return y
163
164    def logne(v, e0, v0, H, p):
165            y=zeros(len(v))
166            c=log(p)/sqrt(2*log(2))
167            b=(H*(p/((p**2)-1)))*exp(c**2)
168            a=v0+(H*(p/((p**2)-1)))
169            for i, j in enumerate(v):
170                    if j < a:
171                            y[i]=((e0*b)/(a-v[i]))*exp(-c**2) * exp((-1/c**2)*(log((a-v[i])/b))**2)
172            return y
173
174    def gaus(v, v0, H):
175            y=exp((-4*log(2)*(v-v0)**2)/(H**2))
176            return y
177
178    def lna(v, I0, v0, H, p):
179            y=zeros(len(v))
180            a=v0-(H*(p/((p**2)-1)))
181            for i, j in enumerate(v):
182                    if j > a:
183                            y[i]=I0*exp(-(log(2)/(log(p))**2) * (log((v[i]-a)/(v0-a)))**2)
184            return y
185
186    def lne(v, I0, v0, H, p):
187            y=zeros(len(v))
188            a=v0+(H*(p/((p**2)-1)))
189            for i, j in enumerate(v):
190                    if j < a:
191                            y[i]=I0*exp(-(log(2)/(log(p))**2) * (log((a-v[i])/(a-v0)))**2)
192            return y
```

APPENDIX C

ADDITIONAL INFORMATION FROM DFT CALCULATIONS

C.1   XYZ–COORDINATES OF THE INVESTIGATED MODELS

Ground and excited state XYZ–coordinates for the investigated models. S_0 of BDO on page 201. S_1 of BDO on page 201. S_0 of BDODC on page 202. S_1 of BDODC on page 202. S_0 of BDOSC on page 203. S_1 of BDOSC on page 204. S_0 of HDIMR on page 206. S_1 of HDIMR on page 208. S_2 of HDIMR on page 209.

XYZ–coordinates of [1,4]benzodioxino[3,2-b]oxanthrene (BDO) in its ground state.

```
-------------------------------------------------------------------
Center     Atomic     Atomic            Coordinates (Angstroms)
Number     Number      Type         X            Y            Z
-------------------------------------------------------------------
    1         6          0        5.961558     0.697647     0.000000
    2         6          0        5.961558    -0.697647     0.000001
    3         6          0        4.751937    -1.397423     0.000000
    4         6          0        3.549064    -0.699776     0.000000
    5         6          0        3.549064     0.699776     0.000000
    6         6          0        4.751937     1.397423     0.000000
    7         8          0        2.374516    -1.429730     0.000000
    8         6          0        1.203723    -0.698585     0.000000
    9         6          0        1.203723     0.698585     0.000000
   10         8          0        2.374516     1.429730     0.000000
   11         6          0        0.000000    -1.396538     0.000000
   12         6          0       -1.203723    -0.698585    -0.000000
   13         6          0       -1.203723     0.698585    -0.000000
   14         6          0        0.000000     1.396538    -0.000000
   15         8          0       -2.374516    -1.429730    -0.000000
   16         6          0       -3.549064    -0.699776    -0.000000
   17         6          0       -3.549064     0.699776    -0.000000
   18         8          0       -2.374516     1.429730    -0.000000
   19         6          0       -4.751937    -1.397423    -0.000000
   20         6          0       -5.961558    -0.697647    -0.000000
   21         6          0       -5.961558     0.697647    -0.000001
   22         6          0       -4.751937     1.397423    -0.000000
   23         1          0        6.897618     1.247458     0.000001
   24         1          0        6.897618    -1.247458     0.000001
   25         1          0        4.722852    -2.482564     0.000001
   26         1          0        4.722852     2.482564     0.000000
   27         1          0        0.000000    -2.480851     0.000000
   28         1          0        0.000000     2.480851    -0.000000
   29         1          0       -4.722852    -2.482564    -0.000000
   30         1          0       -6.897618    -1.247458    -0.000000
```

```
   31          1          0        -6.897618    1.247458   -0.000001
   32          1          0        -4.722852    2.482564   -0.000001
   --------------------------------------------------------------
```

XYZ–coordinates of BDO in its first excited state.

```
--------------------------------------------------------------
Center    Atomic     Atomic          Coordinates (Angstroms)
Number    Number     Type          X          Y          Z
--------------------------------------------------------------
    1          6          0         5.952333    0.709311    0.000001
    2          6          0         5.952333   -0.709311    0.000001
    3          6          0         4.752771   -1.409358    0.000001
    4          6          0         3.543854   -0.710448    0.000000
    5          6          0         3.543854    0.710448    0.000000
    6          6          0         4.752771    1.409358    0.000001
    7          8          0         2.367119   -1.413954   -0.000000
    8          6          0         1.199542   -0.726626   -0.000000
    9          6          0         1.199542    0.726626   -0.000000
   10          8          0         2.367119    1.413954   -0.000000
   11          6          0         0.000000   -1.424314   -0.000000
   12          6          0        -1.199542   -0.726626   -0.000001
   13          6          0        -1.199542    0.726626   -0.000001
   14          6          0         0.000000    1.424314   -0.000001
   15          8          0        -2.367119   -1.413954   -0.000001
   16          6          0        -3.543854   -0.710448   -0.000000
   17          6          0        -3.543854    0.710448   -0.000000
   18          8          0        -2.367119    1.413954   -0.000001
   19          6          0        -4.752771   -1.409358   -0.000000
   20          6          0        -5.952333   -0.709311    0.000000
   21          6          0        -5.952333    0.709311    0.000000
   22          6          0        -4.752771    1.409358   -0.000000
   23          1          0         6.891327    1.253370    0.000001
   24          1          0         6.891327   -1.253370    0.000002
   25          1          0         4.726157   -2.494973    0.000001
   26          1          0         4.726157    2.494973    0.000000
   27          1          0         0.000000   -2.508825   -0.000000
   28          1          0         0.000000    2.508825   -0.000001
   29          1          0        -4.726157   -2.494973   -0.000000
   30          1          0        -6.891327   -1.253370    0.000000
   31          1          0        -6.891327    1.253370    0.000001
   32          1          0        -4.726157    2.494973    0.000000
--------------------------------------------------------------
```

XYZ–coordinates of [1,4]benzodioxino[3,2–b]oxanthrene–6,13–dicarbonitrile (BDODC) in its ground state.

```
--------------------------------------------------------------
Center    Atomic     Atomic          Coordinates (Angstroms)
Number    Number     Type          X          Y          Z
--------------------------------------------------------------
    1          6          0         0.000000    1.399458    0.000040
    2          6          0         1.218014    0.696539    0.000044
    3          6          0        -1.218014    0.696539   -0.000002
    4          6          0         1.218014   -0.696539    0.000006
    5          8          0         2.373399    1.422860    0.000088
    6          6          0         0.000000    2.826519    0.000079
    7          6          0        -1.218014   -0.696539   -0.000041
    8          8          0        -2.373399    1.422860   -0.000005
    9          6          0         0.000000   -1.399458   -0.000037
   10          8          0         2.373399   -1.422860    0.000009
   11          6          0         3.559295    0.697774    0.000089
   12          7          0         0.000000    3.989374    0.000110
   13          8          0        -2.373399   -1.422860   -0.000084
```

```
14            6            0       -3.559295    0.697774   -0.000051
15            6            0        0.000000   -2.826519   -0.000076
16            6            0        3.559295   -0.697774    0.000051
17            6            0        4.756131    1.401160    0.000129
18            6            0       -3.559295   -0.697774   -0.000089
19            6            0       -4.756131    1.401160   -0.000056
20            7            0        0.000000   -3.989374   -0.000108
21            6            0        4.756131   -1.401160    0.000052
22            6            0        5.963838    0.697750    0.000131
23            6            0       -4.756131   -1.401160   -0.000133
24            6            0       -5.963838    0.697750   -0.000100
25            6            0        5.963838   -0.697750    0.000093
26            6            0       -5.963838   -0.697750   -0.000138
27            1            0        4.726603    2.485862    0.000158
28            1            0       -4.726603    2.485862   -0.000025
29            1            0        4.726603   -2.485862    0.000022
30            1            0        6.900344    1.246121    0.000163
31            1            0       -4.726603   -2.485862   -0.000162
32            1            0       -6.900344    1.246121   -0.000104
33            1            0        6.900344   -1.246121    0.000094
34            1            0       -6.900344   -1.246121   -0.000172
-------------------------------------------------------------------
```

XYZ–coordinates of BDODC in its first excited state.

```
-------------------------------------------------------------------
Center      Atomic       Atomic          Coordinates (Angstroms)
Number      Number       Type          X           Y           Z
-------------------------------------------------------------------
    1            6            0        0.000000    1.458340    0.000042
    2            6            0        1.202376    0.691639    0.000043
    3            6            0       -1.202376    0.691639   -0.000002
    4            6            0        1.202376   -0.691639    0.000005
    5            8            0        2.374329    1.406895    0.000087
    6            6            0        0.000000    2.859593    0.000078
    7            6            0       -1.202376   -0.691639   -0.000041
    8            8            0       -2.374329    1.406895   -0.000006
    9            6            0        0.000000   -1.458340   -0.000039
   10            8            0        2.374329   -1.406895    0.000008
   11            6            0        3.546080    0.704383    0.000090
   12            7            0        0.000000    4.033345    0.000109
   13            8            0       -2.374329   -1.406895   -0.000085
   14            6            0       -3.546080    0.704383   -0.000051
   15            6            0        0.000000   -2.859593   -0.000077
   16            6            0        3.546080   -0.704383    0.000050
   17            6            0        4.747792    1.409486    0.000131
   18            6            0       -3.546080   -0.704383   -0.000090
   19            6            0       -4.747792    1.409486   -0.000054
   20            7            0        0.000000   -4.033345   -0.000108
   21            6            0        4.747792   -1.409486    0.000052
   22            6            0        5.946472    0.702450    0.000133
   23            6            0       -4.747792   -1.409486   -0.000133
   24            6            0       -5.946472    0.702450   -0.000097
   25            6            0        5.946472   -0.702450    0.000094
   26            6            0       -5.946472   -0.702450   -0.000137
   27            1            0        4.719125    2.493720    0.000160
   28            1            0       -4.719125    2.493720   -0.000023
   29            1            0        4.719125   -2.493720    0.000021
   30            1            0        6.886380    1.244382    0.000164
   31            1            0       -4.719125   -2.493720   -0.000162
   32            1            0       -6.886380    1.244382   -0.000100
   33            1            0        6.886380   -1.244382    0.000095
   34            1            0       -6.886380   -1.244382   -0.000170
-------------------------------------------------------------------
```

XYZ–coordinates of [1,4]benzodioxino[3,2–b]oxanthrene–6–(1,3,5–trimethylpyrazole–4–sulfonyl)–13–carbonitrile (BDOSC) in its ground state.

```
--------------------------------------------------------------------
Center    Atomic    Atomic          Coordinates (Angstroms)
Number    Number    Type        X           Y           Z
--------------------------------------------------------------------
    1         6         0     -0.299525   -0.109583   -0.534846
    2        16         0      0.331915   -1.673860   -1.253023
    3         6         0     -1.667292    0.115843   -0.282831
    4         6         0      1.284197   -2.376841    0.043540
    5         8         0     -0.807809   -2.560588   -1.516691
    6         8         0      1.204181   -1.301935   -2.378540
    7         6         0      0.631894    0.909217   -0.255287
    8         6         0     -2.085881    1.355301    0.218650
    9         8         0     -2.578168   -0.875943   -0.515262
   10         6         0      0.769900   -2.906864    1.264290
   11         6         0      2.662156   -2.616850    0.062210
   12         6         0      0.208428    2.137199    0.249823
   13         8         0      1.964592    0.662816   -0.459206
   14         6         0     -1.155705    2.371103    0.477638
   15         8         0     -3.395953    1.639485    0.482157
   16         6         0     -3.917713   -0.573731   -0.336127
   17         6         0     -0.635894   -2.928312    1.779173
   18         7         0      1.759989   -3.422150    1.982016
   19         6         0      3.759135   -2.348555   -0.915523
   20         7         0      2.889767   -3.240706    1.240501
   21         8         0      1.077845    3.148483    0.549189
   22         6         0      2.822388    1.751377   -0.376565
   23         6         0     -1.592588    3.632783    0.982559
   24         6         0     -4.326490    0.663713    0.155719
   25         6         0     -4.856297   -1.546487   -0.655805
   26         6         0      4.164277   -3.723748    1.751179
   27         6         0      2.388671    2.976318    0.129077
   28         6         0      4.136226    1.594949   -0.798777
   29         7         0     -1.946868    4.661565    1.392721
   30         6         0     -5.673736    0.945607    0.335220
   31         6         0     -6.214784   -1.271600   -0.475149
   32         6         0      3.261657    4.051065    0.228502
   33         6         0      5.022557    2.671002   -0.695957
   34         6         0     -6.622252   -0.031070    0.018143
   35         6         0      4.588157    3.893636   -0.182484
   36         1         0     -1.320654   -3.353504    1.040114
   37         1         0     -0.992448   -1.917934    2.013047
   38         1         0     -0.678102   -3.524241    2.694166
   39         1         0      4.581097   -1.801395   -0.439458
   40         1         0      4.172011   -3.287706   -1.304187
   41         1         0      3.379174   -1.767782   -1.754550
   42         1         0     -4.510671   -2.500748   -1.039384
   43         1         0      4.597617   -4.462129    1.070285
   44         1         0      4.867789   -2.896063    1.881549
   45         1         0      3.967372   -4.189173    2.716046
   46         1         0      4.448675    0.638452   -1.203018
   47         1         0     -5.961068    1.918896    0.719597
   48         1         0     -6.949909   -2.030703   -0.722863
   49         1         0      2.893472    4.991379    0.625688
   50         1         0      6.050403    2.547841   -1.022109
   51         1         0     -7.676817    0.183895    0.158167
   52         1         0      5.274784    4.730329   -0.102784
--------------------------------------------------------------------
```

XYZ–coordinates of BDOSC in its first excited state.

```
--------------------------------------------------------------------
Center    Atomic    Atomic          Coordinates (Angstroms)
Number    Number    Type        X           Y           Z
```

```
----------------------------------------------------------------------
      1          6          0      -0.263360    -0.144440    -0.347623
      2         16          0       0.424440    -1.518299    -1.280181
      3          6          0      -1.669774     0.063566    -0.197351
      4          6          0       1.479602    -2.361125    -0.145443
      5          8          0      -0.678672    -2.432369    -1.633095
      6          8          0       1.267107    -0.984990    -2.374419
      7          6          0       0.529567     1.025688    -0.160198
      8          6          0      -2.215668     1.326344    -0.030283
      9          8          0      -2.479425    -1.048512    -0.129572
     10          6          0       1.064097    -3.053155     1.029018
     11          6          0       2.856137    -2.578016    -0.255513
     12          6          0      -0.018933     2.288816     0.008219
     13          8          0       1.893494     0.848539    -0.116573
     14          6          0      -1.423397     2.509989     0.012024
     15          8          0      -3.562472     1.515346     0.185479
     16          6          0      -3.818853    -0.871288     0.026717
     17          6          0      -0.301888    -3.172400     1.628591
     18          7          0       2.107253    -3.640272     1.604553
     19          6          0       3.881575    -2.155656    -1.257899
     20          7          0       3.177504    -3.345773     0.814215
     21          8          0       0.761617     3.396157     0.229335
     22          6          0       2.683842     1.950885     0.063497
     23          6          0      -1.985642     3.791330     0.108272
     24          6          0      -4.367941     0.416713     0.184326
     25          6          0      -4.645474    -1.994857     0.040543
     26          6          0       4.492132    -3.852336     1.175449
     27          6          0       2.119056     3.225610     0.237789
     28          6          0       4.067314     1.788651     0.082970
     29          7          0      -2.455409     4.861665     0.211336
     30          6          0      -5.740693     0.586060     0.355584
     31          6          0      -6.015385    -1.823267     0.207703
     32          6          0       2.931555     4.340240     0.429416
     33          6          0       4.880081     2.903638     0.272672
     34          6          0      -6.561679    -0.536992     0.364814
     35          6          0       4.314361     4.175663     0.445435
     36          1          0      -1.007836    -3.608342     0.915135
     37          1          0      -0.696973    -2.191389     1.915861
     38          1          0      -0.255511    -3.805072     2.518665
     39          1          0       4.743665    -1.688872    -0.766592
     40          1          0       4.256529    -3.018966    -1.822110
     41          1          0       3.444867    -1.450240    -1.962901
     42          1          0      -4.198265    -2.974690    -0.085780
     43          1          0       4.925625    -4.422534     0.348867
     44          1          0       5.168426    -3.033516     1.441231
     45          1          0       4.359067    -4.505499     2.037117
     46          1          0       4.481291     0.795679    -0.052844
     47          1          0      -6.135138     1.589119     0.476497
     48          1          0      -6.665912    -2.691577     0.214273
     49          1          0       2.466460     5.311270     0.561494
     50          1          0       5.958364     2.782648     0.285373
     51          1          0      -7.632087    -0.415690     0.493883
     52          1          0       4.953965     5.039761     0.592356
----------------------------------------------------------------------
```

XYZ–coordinates of heterodimer sub–unit (HDIMR) in its ground state.

```
----------------------------------------------------------------------
Center     Atomic     Atomic            Coordinates (Angstroms)
Number     Number     Type          X            Y            Z
----------------------------------------------------------------------
      1          6          0      -0.740850     3.979557    -0.675318
      2          6          0      -0.945025     4.761784    -2.018596
      3          6          0      -0.610319     4.888937     0.595145
      4          6          0       0.434980     4.849827    -2.743129
      5          6          0      -1.945955     3.124307    -0.307984
```

```
 6          6          0         0.535850      3.204087     -0.971120
 7          6          0        -1.995421      4.919866      1.314008
 8          6          0         0.276088      4.694792     -4.266277
 9          6          0         1.158865      6.181933     -2.441055
10          6          0         1.186507      3.686273     -2.109988
11          6          0        -2.638875      3.642782      0.789705
12          6          0        -2.394471      1.969851     -0.954589
13          6          0         1.077795      2.150781     -0.229944
14          6          0        -1.830944      4.917245      2.844325
15          6          0        -2.832847      6.150226      0.895807
16          6          0         2.394647      3.120269     -2.523606
17          6          0        -3.794683      3.012617      1.257036
18          6          0        -3.542366      1.346860     -0.484301
19          6          0         2.282231      1.595241     -0.641686
20          6          0         2.931031      2.076677     -1.781083
21          6          0        -4.236121      1.863848      0.613793
22          8          0        -3.973287      0.195334     -1.135069
23          8          0         2.821657      0.557913      0.109525
24          8          0         4.131868      1.523008     -2.202445
25          8          0        -5.383388      1.245991      1.100068
26          6          0        -5.110691     -0.385858     -0.656726
27          6          0         3.901212     -0.098189     -0.419487
28          6          0         4.543268      0.392934     -1.555031
29          6          0        -5.801020      0.128143      0.438709
30          6          0        -5.583153     -1.540514     -1.306145
31          6          0         4.372747     -1.260563      0.221743
32          6          0         5.664115     -0.272985     -2.072721
33          6          0        -6.968794     -0.508279      0.896049
34          6          0        -6.750438     -2.177378     -0.848225
35          6          0        -4.879768     -2.064443     -2.431846
36         16          0         3.438878     -1.876131      1.673412
37          6          0         5.512008     -1.917276     -0.284667
38          6          0         6.147909     -1.420250     -1.429583
39          6          0         6.316355      0.223984     -3.241091
40          6          0        -7.439776     -1.664032      0.247968
41          6          0        -7.675419      0.019286      2.017968
42          8          0        -7.169303     -3.294591     -1.511174
43          7          0        -4.308508     -2.490348     -3.350808
44          6          0         3.686469     -0.634754      2.890317
45          8          0         4.072089     -3.112910      2.147047
46          8          0         2.021900     -1.922025      1.278509
47          8          0         6.000193     -3.026203      0.347653
48          8          0         7.255238     -2.008477     -1.972636
49          7          0         6.846036      0.630713     -4.193047
50          8          0        -8.577182     -2.245933      0.728413
51          7          0        -8.250649      0.450294      2.932131
52          6          0        -8.327051     -3.898489     -1.035057
53          6          0         4.920097     -0.339508      3.542986
54          6          0         2.722195      0.184421      3.486223
55          6          0         7.076110     -3.676455     -0.233053
56          6          0         7.699091     -3.179137     -1.375456
57          6          0        -9.017552     -3.384238      0.063322
58          6          0        -8.785406     -5.037121     -1.683674
59          6          0         6.283063     -0.914873      3.312748
60          7          0         4.728645      0.599321      4.461199
61          6          0         1.249189      0.336045      3.289344
62          7          0         3.399061      0.898226      4.414797
63          6          0         7.529910     -4.847875      0.359776
64          6          0         8.780799     -3.841954     -1.938837
65          6          0       -10.171878     -4.004365      0.521740
66          6          0        -9.947070     -5.665230     -1.226064
67          6          0         2.860737      1.899787      5.323215
68          6          0         8.620298     -5.519846     -0.199886
69          6          0         9.243498     -5.019411     -1.344195
70          6          0       -10.637547     -5.150920     -0.127803
71          1          0        -1.387972      5.749425     -1.857475
72          1          0        -1.640749      4.197118     -2.649537
73          1          0        -0.252317      5.893352      0.349158
```

```
74          1          0        0.128746     4.441028      1.269532
75          1          0        1.246010     4.739204     -4.775575
76          1          0       -0.345911     5.502600     -4.669995
77          1          0       -0.197627     3.740292     -4.521124
78          1          0        2.153999     6.197003     -2.900689
79          1          0        0.588199     7.026919     -2.844775
80          1          0        1.287247     6.339601     -1.365050
81          1          0       -1.871391     1.540866     -1.803882
82          1          0        0.581366     1.748703      0.647232
83          1          0       -2.803145     4.923308      3.351161
84          1          0       -1.282701     5.808621      3.171824
85          1          0       -1.278057     4.033564      3.182681
86          1          0       -3.828414     6.117105      1.353477
87          1          0       -2.342121     7.075252      1.221618
88          1          0       -2.967721     6.199188     -0.189635
89          1          0        2.927742     3.462885     -3.405226
90          1          0       -4.358672     3.385400      2.106705
91          1          0       -8.228639    -5.415393     -2.534789
92          1          0        6.261714    -2.007683      3.351087
93          1          0        6.677667    -0.629006      2.330224
94          1          0        6.968839    -0.541127      4.077032
95          1          0        0.984076     1.386371      3.121271
96          1          0        0.700401    -0.003051      4.176745
97          1          0        0.922260    -0.257109      2.436661
98          1          0        7.024662    -5.214836      1.247121
99          1          0        9.244592    -3.430066     -2.829250
100         1          0      -10.688559    -3.583079      1.377919
101         1          0      -10.306545    -6.555541     -1.731938
102         1          0        2.050955     1.477348      5.924705
103         1          0        2.485443     2.765752      4.769236
104         1          0        3.675063     2.211497      5.975964
105         1          0        8.977288    -6.434634      0.262464
106         1          0       10.089791    -5.540580     -1.780226
107         1          0      -11.539685    -5.637004      0.229509
 -----------------------------------------------------------------------
```

XYZ–coordinates of HDIMR in its first excited state.

```
 -----------------------------------------------------------------------
Center     Atomic     Atomic            Coordinates (Angstroms)
Number     Number     Type         X           Y           Z
 -----------------------------------------------------------------------
    1          6          0       -0.761871     3.962164     -0.676024
    2          6          0       -0.974810     4.741785     -2.023380
    3          6          0       -0.640105     4.874634      0.591632
    4          6          0        0.403379     4.828897     -2.751353
    5          6          0       -1.963298     3.104013     -0.319145
    6          6          0        0.516180     3.189158     -0.973415
    7          6          0       -2.034166     4.918574      1.290280
    8          6          0        0.236979     4.666375     -4.273111
    9          6          0        1.124226     6.164479     -2.457955
   10          6          0        1.159784     3.670625     -2.116383
   11          6          0       -2.677001     3.639693      0.779821
   12          6          0       -2.390773     1.944618     -0.954373
   13          6          0        1.066109     2.143019     -0.227405
   14          6          0       -1.894903     4.940267      2.823537
   15          6          0       -2.869313     6.141325      0.838682
   16          6          0        2.369817     3.109722     -2.530656
   17          6          0       -3.827676     3.019208      1.248757
   18          6          0       -3.546437     1.320063     -0.488727
   19          6          0        2.272352     1.592547     -0.640422
   20          6          0        2.914225     2.072480     -1.785256
   21          6          0       -4.264104     1.857009      0.613756
   22          8          0       -3.968961     0.188410     -1.109027
   23          8          0        2.821747     0.565311      0.114711
   24          8          0        4.115654     1.525128     -2.207025
```

25	8	0	-5.387386	1.250189	1.074221
26	6	0	-5.121286	-0.409078	-0.641568
27	6	0	3.901235	-0.090414	-0.417219
28	6	0	4.535233	0.398206	-1.557566
29	6	0	-5.813997	0.109008	0.426052
30	6	0	-5.542322	-1.586675	-1.332468
31	6	0	4.379910	-1.248475	0.226416
32	6	0	5.655910	-0.264739	-2.079252
33	6	0	-7.009160	-0.488923	0.931991
34	6	0	-6.733234	-2.186084	-0.831737
35	6	0	-4.837000	-2.109125	-2.424849
36	16	0	3.456625	-1.861848	1.686358
37	6	0	5.518844	-1.902492	-0.283611
38	6	0	6.147235	-1.407500	-1.434295
39	6	0	6.300074	0.230959	-3.252651
40	6	0	-7.431328	-1.663805	0.246727
41	6	0	-7.712651	0.044984	2.019670
42	8	0	-7.158188	-3.317812	-1.480302
43	7	0	-4.245570	-2.544131	-3.340564
44	6	0	3.716483	-0.619169	2.899411
45	8	0	4.091901	-3.099093	2.155194
46	8	0	2.036659	-1.904731	1.302515
47	8	0	6.014736	-3.006382	0.350232
48	8	0	7.253597	-1.993575	-1.980148
49	7	0	6.823022	0.637267	-4.208455
50	8	0	-8.577548	-2.255795	0.713386
51	7	0	-8.299063	0.495586	2.931403
52	6	0	-8.304994	-3.917930	-1.020775
53	6	0	4.955782	-0.325017	3.541924
54	6	0	2.758267	0.202074	3.502191
55	6	0	7.089897	-3.655601	-0.233509
56	6	0	7.705068	-3.160557	-1.380975
57	6	0	-9.011155	-3.389588	0.070611
58	6	0	-8.756523	-5.067877	-1.661481
59	6	0	6.315925	-0.903178	3.302301
60	7	0	4.773013	0.615329	4.460324
61	6	0	1.284025	0.355908	3.316478
62	7	0	3.443569	0.916103	4.424352
63	6	0	7.550685	-4.823049	0.361598
64	6	0	8.786111	-3.821525	-1.947632
65	6	0	-10.171464	-4.009018	0.525156
66	6	0	-9.918966	-5.688604	-1.206164
67	6	0	2.914100	1.919284	5.336176
68	6	0	8.640505	-5.493219	-0.201278
69	6	0	9.255962	-4.995006	-1.350773
70	6	0	-10.623996	-5.161014	-0.116668
71	1	0	-1.416893	5.728892	-1.860104
72	1	0	-1.672444	4.175814	-2.650346
73	1	0	-0.272407	5.874903	0.345877
74	1	0	0.086232	4.423443	1.277179
75	1	0	1.204766	4.711535	-4.785986
76	1	0	-0.388791	5.470802	-4.677325
77	1	0	-0.234714	3.709328	-4.521610
78	1	0	2.116636	6.180338	-2.922958
79	1	0	0.548802	7.005647	-2.862538
80	1	0	1.258137	6.327142	-1.383340
81	1	0	-1.856868	1.507129	-1.791617
82	1	0	0.577979	1.742945	0.655337
83	1	0	-2.874580	4.961015	3.314304
84	1	0	-1.347509	5.835607	3.139604
85	1	0	-1.350435	4.061425	3.186209
86	1	0	-3.866935	6.118416	1.291126
87	1	0	-2.375401	7.068414	1.151702
88	1	0	-2.996333	6.171326	-0.247988
89	1	0	2.898421	3.451945	-3.414974
90	1	0	-4.399179	3.399686	2.088996
91	1	0	-8.190994	-5.455209	-2.502402
92	1	0	6.293480	-1.995792	3.345449

```
93        1           0      6.702561   -0.621992    2.315289
94        1           0      7.008632   -0.527252    4.059208
95        1           0      1.020896    1.405267    3.138799
96        1           0      0.741939    0.028714    4.212351
97        1           0      0.948213   -0.246090    2.473456
98        1           0      7.051291   -5.188453    1.252868
99        1           0      9.243723   -3.411541   -2.842096
100       1           0    -10.697587   -3.579376    1.371088
101       1           0    -10.274821   -6.585658   -1.702444
102       1           0      2.106013    1.499563    5.941796
103       1           0      2.539242    2.787151    4.784785
104       1           0      3.733126    2.227401    5.984731
105       1           0      9.003115   -6.404995    0.262605
106       1           0     10.101747   -5.514962   -1.789194
107       1           0    -11.528150   -5.647734    0.234406
-------------------------------------------------------------------
```

XYZ–coordinates of HDIMR in its second excited state.

```
-------------------------------------------------------------------
Center   Atomic      Atomic         Coordinates (Angstroms)
Number   Number      Type         X          Y           Z
-------------------------------------------------------------------
    1        6           0     -0.642767    4.101228   -0.514042
    2        6           0     -0.763558    5.003824   -1.788105
    3        6           0     -0.500193    4.892635    0.835018
    4        6           0      0.648352    5.106387   -2.445304
    5        6           0     -1.883046    3.261470   -0.242833
    6        6           0      0.604425    3.294301   -0.836088
    7        6           0     -1.897541    4.905409    1.531657
    8        6           0      0.555654    5.120953   -3.981717
    9        6           0      1.420326    6.359962   -1.968541
   10        6           0      1.326002    3.852792   -1.912944
   11        6           0     -2.571816    3.701184    0.888447
   12        6           0     -2.357546    2.183444   -0.994447
   13        6           0      1.045209    2.141279   -0.195155
   14        6           0     -1.754798    4.766829    3.058005
   15        6           0     -2.682982    6.197872    1.212544
   16        6           0      2.506987    3.267126   -2.357306
   17        6           0     -3.751500    3.064308    1.281365
   18        6           0     -3.529679    1.547745   -0.600497
   19        6           0      2.225319    1.560305   -0.642021
   20        6           0      2.943605    2.117695   -1.709560
   21        6           0     -4.226158    1.988175    0.537272
   22        8           0     -3.975763    0.487934   -1.355988
   23        8           0      2.678904    0.415376   -0.020114
   24        8           0      4.106663    1.517212   -2.141617
   25        8           0     -5.389510    1.380538    0.948238
   26        6           0     -5.065609   -0.207435   -0.840756
   27        6           0      3.808337   -0.173515   -0.453887
   28        6           0      4.526413    0.398353   -1.532263
   29        6           0     -5.744940    0.221445    0.263713
   30        6           0     -5.433902   -1.401906   -1.541750
   31        6           0      4.260102   -1.339433    0.186302
   32        6           0      5.707236   -0.196099   -1.997487
   33        6           0     -6.868041   -0.497001    0.788457
   34        6           0     -6.564883   -2.115049   -1.024736
   35        6           0     -4.724525   -1.845188   -2.663112
   36       16           0      3.220060   -2.076560    1.525188
   37        6           0      5.442641   -1.933065   -0.278632
   38        6           0      6.160744   -1.359476   -1.370283
   39        6           0      6.432677    0.376897   -3.084572
   40        6           0     -7.245720   -1.685124    0.081287
   41        6           0     -7.555388   -0.062822    1.927463
   42        8           0     -6.921502   -3.266385   -1.715437
   43        7           0     -4.123588   -2.212199   -3.604829
```

208

44	6	0	3.236817	-0.867248	2.785485
45	8	0	3.917217	-3.274072	2.000575
46	8	0	1.876532	-2.197537	0.947121
47	8	0	5.915675	-3.046222	0.304808
48	8	0	7.294822	-1.907948	-1.833082
49	7	0	7.024152	0.847120	-3.966853
50	8	0	-8.341009	-2.370139	0.591929
51	7	0	-8.130398	0.304047	2.884882
52	6	0	-8.010935	-3.951333	-1.221276
53	6	0	4.369346	-0.476071	3.561303
54	6	0	2.133382	-0.195089	3.329364
55	6	0	7.074295	-3.628335	-0.168614
56	6	0	7.768225	-3.063747	-1.237352
57	6	0	-8.707771	-3.511361	-0.088854
58	6	0	-8.413090	-5.108376	-1.880557
59	6	0	5.803117	-0.889029	3.436668
60	7	0	3.992182	0.386586	4.494354
61	6	0	0.671704	-0.212451	3.020103
62	7	0	2.645054	0.537443	4.342278
63	6	0	7.531620	-4.788571	0.444191
64	6	0	8.935032	-3.640078	-1.721091
65	6	0	-9.802878	-4.231058	0.377989
66	6	0	-9.513236	-5.832134	-1.411857
67	6	0	1.919383	1.414280	5.252686
68	6	0	8.701921	-5.373635	-0.035082
69	6	0	9.399014	-4.803593	-1.109870
70	6	0	-10.207357	-5.393925	-0.283823
71	1	0	-1.179296	5.988677	-1.557562
72	1	0	-1.448870	4.520759	-2.493061
73	1	0	-0.107382	5.902148	0.680489
74	1	0	0.212988	4.366120	1.480158
75	1	0	1.547740	5.186436	-4.443641
76	1	0	-0.020876	5.991565	-4.313868
77	1	0	0.059913	4.220556	-4.359970
78	1	0	2.431804	6.378644	-2.390150
79	1	0	0.899661	7.266245	-2.297726
80	1	0	1.511186	6.395869	-0.878276
81	1	0	-1.839617	1.815999	-1.875645
82	1	0	0.489704	1.679256	0.613057
83	1	0	-2.734342	4.760198	3.549590
84	1	0	-1.183943	5.607832	3.470090
85	1	0	-1.237555	3.838132	3.325821
86	1	0	-3.686555	6.158587	1.651178
87	1	0	-2.167891	7.074158	1.625034
88	1	0	-2.799245	6.344841	0.133684
89	1	0	3.086366	3.661294	-3.185533
90	1	0	-4.316482	3.377046	2.154551
91	1	0	-7.854705	-5.425375	-2.755930
92	1	0	5.900731	-1.978724	3.429919
93	1	0	6.254518	-0.507994	2.512116
94	1	0	6.370077	-0.486494	4.279253
95	1	0	0.263404	0.803966	2.999434
96	1	0	0.121195	-0.768968	3.788633
97	1	0	0.488192	-0.695520	2.061383
98	1	0	6.970134	-5.207756	1.271528
99	1	0	9.453167	-3.178782	-2.554401
100	1	0	-10.324589	-3.866637	1.257524
101	1	0	-9.821473	-6.734241	-1.931707
102	1	0	1.122958	0.863668	5.759762
103	1	0	1.487053	2.261496	4.712138
104	1	0	2.637131	1.778229	5.986390
105	1	0	9.072649	-6.280167	0.430798
106	1	0	10.308243	-5.269325	-1.474119
107	1	0	-11.063193	-5.950317	0.086329

C.2 TABLES OF GEOMETRICAL PARAMETERS

Table C.1: Geometrical parameters from crystal structures of dioxane and dioxin rings. Data were aggregated from references [152, 153, 173].
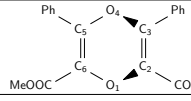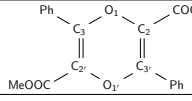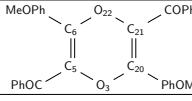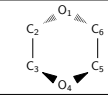
	2000Levin (DOI)			1994Nuretdinov (DOI)		1986Luger (DOI)	
1–2	1.394(2)	1–2	1.396(3)	22–21	1.3967	1–2	1.423(3)
1–6	1.403(2)	1–3	1.373(3)	22–6	1.3898	1–6	1.426(3)
4–3	1.394(2)	2–3'	1.341(3)	21–20	1.3272	2–3	1.478(3)
4–5	1.394(2)						
2–3	1.331(2)						
5–6	1.336(2)						
2–1–6	112.6(2)	2–1–3	116.4(2)	6–22–21	118.45	2–1–6	109.0(2)
3–4–5	115.6(1)	1–2–3'	122.4(2)	22–21–20	121.96	1–2–3	111.0(2)
1–2–3	119.6(1)	1–3–2'	121.2(2)	22–6–5	119.59	1–6–5	111.4(2)
4–3–2	118.8(1)						
4–5–6	118.6(1)						
1–6–5	119.3(1)						
6–1–2–3	-34.3(2)	1–2–3'–1'	-1.8(3)	Torsional		6–1–2–3	57.0(3)
2–1–6–5	35.1(2)	2–3'–1'–2'	1.7(3)	angles are	0.8	1–2–3–4	-58.3(3)
5–4–3–2	27.1(2)	3'–1'–2'–3	-1.7(3)	about		2–3–4–5	57.2(3)
3–4–5–6	-26.2(2)	1'–2'–3–1	1.8(3)				
1–2–3–4	3.8(2)	2'–3–1–2	-1.7(3)				
4–5–6–1	-5.3(2)	3–1–2–3'	1.7(3)				

Table C.2: Calculated Benzene–Benzene angles (in degrees) around the spiro center for various crystal structures and theoretical models. Choice of atom sequences shows the various types of angle that can be extracted using this method. Used crystal structures are from references [38, 179–182].

Structure	Atom sequence for considered planes $(A_1–B_1–C_1—A_2–B_2–C_2)$[a]				
	16–41–42—16–17–18	16–41–13—16–17–38	42–11–13—37–19–17[b]	42–41–13—18–17–38	12–11–43—37–36–19
SPIRO (S_0)	105.62	107.81	**74.53**	95.59	105.70
HDIMR (S_0)	105.25	107.53	**75.07**	95.14	104.93
HDIMR (S_1)	105.61	107.83	**74.81**	95.63	105.12
HDIMR (S_2)	107.08	107.91	**73.14**	96.28	106.93
1997Whitcomb[c]	85.78	87.29	**95.43**	84.88	84.71
2007Zhou[d]	109.98	114.83	**69.25**	70.14	110.92
2011McKeown[e]	85.28	85.26	**92.66**	85.21	87.31
2015Zhang[f]	110.31	108.63	**72.05**	110.43	71.43
2015Merkel[g]	102.56	109.48	**78.11**	102.16	101.66

[a] Angles are calculated between plane (P_1) containing atoms (A_1,B_1,C_1) and plane (P_2) containing atoms (A_2,B_2,C_2).
[b] This column is the primary indicator of the Benzene–Benzene angle around the spiro center.
[c] From *J. Chem. Crystallogr.* 1997, 27, 223–230. DOI: 10.1007/BF02575959
[d] From *Adv. Synth. Catal.* 2007, 349, 2477–2484. DOI: 10.1002/adsc.200700109
[e] From *J. Chem. Crystallogr.* 2011, 41, 98–104. DOI: 10.1007/s10870-010-9844-1
[f] From *Polymer* 2015, 57, 45–50. DOI: 10.1016/j.polymer.2014.12.010
[g] From *Polym. Chem.* 2015, 6, 5003–5008. DOI: 10.1039/C5PY00570A

Table C.3: Geometrical parameters of the models studied by DFT. Atoms numbering can be found in Figure 3.5.

No.	loc-ation label	Geometrical Parameters Length, Angle, Dihedral (Å,°) BDO/DC	BDOSC	SPIRO	isolated BDO S0	S1	T1	Exp[a]	isolated BDODC S0	S1	T1	isolated BDOSC S0	S1	T1	isolated SPIRO S0	BDODC within HDIMR framework S0	S1	S2	BDOSC within HDIMR framework S0	S1	S2	SPIRO within HDIMR framework S0	S1	S2
1	R1,R8	36–37	49–01	36–37	1.3905	1.3964	1.3968	1.3831	1.3882	1.3933	1.3915	1.3888	1.3930	1.3917	1.3926	1.3886	1.3944	1.3917	1.3891	1.3890	1.3895			
2		37–38	01–02	37–38	1.3974	1.3888	1.3906	1.3913	1.3976	1.3916	1.3930	1.3978	1.3927	1.3937	1.3983	1.3969	1.3888	1.3970	1.3977	1.3977	1.3934			
3		38–17	02–03	38–17	1.3952	1.4186	1.4080	1.3890	1.3955	1.4049	1.4018	1.3957	1.4028	1.4008	1.3957	1.3979	1.4156	1.3955	1.3958	1.3958	1.4021			
4		17–18	03–04	17–18	1.3974	1.3888	1.3906	1.3904	1.3976	1.3916	1.3930	1.3976	1.3926	1.3935	1.3992	1.3971	1.3894	1.3972	1.3978	1.3978	1.3937			
5		18–19	04–05	18–19	1.3905	1.3964	1.3968	1.3807	1.3882	1.3933	1.3915	1.3881	1.3925	1.3912	1.3908	1.3881	1.3937	1.3904	1.3881	1.3880	1.3883			
6		37–38–17	01–02–03	37–38–17	120.04	120.26	120.21	120.38	120.21	120.53	120.52	120.27	120.48	120.48	120.48	120.36	120.71	120.07	120.27	120.28	120.69			
7		38–17–18	02–03–04	38–17–18	120.04	120.26	120.21	120.28	120.21	120.53	120.52	120.15	120.40	120.43	120.44	120.71	121.03	120.76	120.19	120.20	120.66			
8		17–18–19	03–04–05	17–18–19	119.83	119.69	119.75	119.13	119.33	119.06	118.85	119.24	119.09	118.89	119.07	118.65	118.44	119.11	119.17	119.15	118.26			
9		18–19–36	04–05–49	18–19–36	120.11	120.03	120.03	120.71	120.44	120.40	120.62	120.69	120.57	120.72	120.66	120.69	120.57	120.27	120.72	120.73	121.16			
10		19–36–37	05–49–01	19–36–37	120.11	120.03	120.03	120.33	120.44	120.40	120.62	120.22	120.20	120.46	119.96	120.79	120.67	120.41	120.32	120.34	120.83			
11		36–37–38	49–01–02	36–37–38	119.83	119.69	119.75	119.15	119.33	119.06	118.85	119.38	119.22	118.97	119.36	118.76	118.54	119.34	119.29	119.28	118.38			
12		37–38–17–18	01–02–03–04	37–38–17–18	000.00	000.00	000.26	000.08	000.00	000.00	-000.00	-000.20	-000.00	-000.16	-000.19	-000.05	-000.18	-000.09	-000.01	-000.01	-000.02			
13		37–36–19–18	01–49–05–04	37–36–19–18	000.00	000.00	-000.08	000.08	-000.00	000.00	000.00	-000.53	000.10	-000.53	-000.09	000.11	000.11	000.01	-000.05	-000.05	-000.05			
14		38–37–18–19	02–01–04–05	38–37–18–19	180.00	-179.99	-179.95	-179.64	179.99	179.99	-179.99	-179.70	179.90	179.98	179.67	179.89	-179.87	179.81	-179.87	-179.87	179.99			
15	R2,R9	34–35	47–48		1.3803	1.3548	1.3641	1.3665	1.3647	1.3729	1.3577	1.3705	1.3760	1.3624		1.3643	1.3800	1.3922	1.3667	1.3661	1.3428			
16		35–36	48–49	35–36	1.3828	1.3709	1.3704	1.3972	1.3900	1.3662	1.3760	1.3883	1.3683	1.3772	1.3684	1.3908	1.3572	1.3753	1.3847	1.3849	1.3803			
17		19–36	05–49	19–36	1.3995	1.4209	1.4095	1.3901	1.3955	1.4087	1.3989	1.3943	1.4050	1.3972	1.4092	1.3979	1.4208	1.4048	1.3930	1.3929	1.3937			
18		19–20	05–06	19–20	1.3828	1.3709	1.3704	1.3915	1.3900	1.3662	1.3760	1.3872	1.3681	1.3763	1.3778	1.3911	1.3579	1.3758	1.3871	1.3873	1.3837			
19		20–21	06–07		1.3803	1.3548	1.3641	1.3665	1.3647	1.3729	1.3577	1.3668	1.3727	1.3591		1.3639	1.3796	1.3916	1.3664	1.3658	1.3420			
20		36–19–20	49–05–06	36–19–20	121.85	120.87	121.50	121.74	121.44	120.94	120.69	120.84	120.73	120.57	114.71	121.32	120.81	121.70	120.74	120.73	119.87			
21		19–20–21	05–06–07		119.20	120.18	118.39	115.55	116.40	117.65	118.07	116.28	117.68	118.01		116.55	117.77	115.81	116.84	116.86	118.81			
22		20–21–34	06–07–47		121.98	120.48	119.54	122.80	122.15	121.39	121.22	122.54	121.95	121.77		122.12	121.40	122.14	122.68	122.67	121.65			
23		21–34–35	07–47–48		121.98	120.48	119.54	122.49	122.15	121.39	121.22	122.51	120.34	120.34		122.12	121.39	122.14	120.25	120.23	119.22			
24		34–35–36	47–48–49		116.15	118.64	118.39	115.46	116.40	117.65	118.07	116.80	118.22	118.46		116.55	117.79	115.90	117.67	117.71	119.75			
25		35–36–19	48–49–05	35–36–19	121.85	120.87	121.50	121.86	121.44	120.94	120.69	121.21	120.99	120.82	119.96	121.31	120.81	121.52	121.58	121.56	120.66			
26		35–36–19–20	48–49–05–06	35–36–19–20	000.00	000.00	002.25	000.05	000.00	-000.00	000.00	-000.86	-000.11	-000.17	000.00	000.09	000.11	-000.10	-000.11	-000.12	000.00			
27		35–34–21–20	48–47–07–06		000.00	000.00	013.18	001.39	-000.00	-000.00	000.00	000.76	-000.36	001.30		000.09	000.11	-000.16	000.66	000.67	000.29			
28		36–35–20–21	49–48–06–07		180.00	180.00	-175.98	-177.67	-179.99	-179.99	-179.99	168.82	178.03	-179.19		-179.02	-179.18	172.51	176.33	176.29	179.39			
29	R3,R10	33–34	46–47		1.3914	1.3876	1.3878	1.3981	1.4062	1.4260	1.4294	1.4084	1.4258	1.4273		1.4063	1.4289	1.4327	1.4091	1.4089	1.4024			
30		21–34	07–47		1.3971	1.4532	1.4841	1.3851	1.3930	1.3832	1.3963	1.3937	1.3873	1.3988		1.3931	1.3740	1.3657	1.4008	1.4014	1.4270			
31		21–22	07–08		1.3914	1.3876	1.3878	1.3914	1.4063	1.4260	1.4294	1.4026	1.4217	1.4272		1.4064	1.4287	1.4331	1.4013	1.4011	1.3973			
32		22–23	08–09		1.3914	1.3876	1.3878	1.3974	1.4062	1.4260	1.4294	1.4014	1.4249	1.4273		1.4063	1.4241	1.4335	1.4027	1.4027	1.4014			
33		23–32	09–45		1.3971	1.4532	1.4841	1.3835	1.3930	1.3832	1.3963	1.4010	1.3858	1.4018		1.3929	1.3867	1.3680	1.3938	1.3932	1.4161			
34		32–33	45–46		1.3914	1.3876	1.3878	1.3971	1.4062	1.4260	1.4294	1.4089	1.4296	1.4317		1.4062	1.4241	1.4333	1.4087	1.4087	1.4047			
35		34–21–22	47–07–08		120.10	120.18	120.32	119.86	119.98	122.52	122.41	120.08	122.17	122.03		119.96	122.54	121.96	120.58	120.58	120.97			
36		21–22–23	07–08–09		119.78	119.63	119.33	120.47	120.02	114.95	115.16	119.64	114.83	114.99		120.01	115.04	116.16	119.67	119.63	118.52			
37		22–23–32	08–09–45		120.10	120.18	120.32	119.82	119.98	122.52	122.41	120.60	122.78	122.36		120.00	122.40	121.86	120.09	120.14	120.57			
38		23–32–33	09–45–46		120.10	120.18	120.32	119.68	119.98	122.52	122.41	119.70	122.19	121.85		119.98	122.38	121.88	120.48	120.50	121.27			
39		32–33–34	45–46–47		119.78	119.63	119.33	120.47	120.02	114.95	115.16	119.39	114.44	114.71		120.00	115.00	116.20	119.44	119.39	118.12			
40		33–34–21	46–47–07		120.10	120.18	120.32	119.65	119.98	122.52	122.41	120.55	122.90	122.43		120.01	122.61	121.91	119.69	119.71	120.51			
41		33–34–21–22	46–47–07–08		000.00	000.00	000.83	000.81	000.00	000.00	-000.00	-000.35	000.27	-001.70		000.08	000.09	-000.02	000.24	000.24	000.16			
42		33–32–23–22	46–45–09–08		000.00	000.00	000.83	-001.28	000.00	000.00	000.00	-000.28	-000.34	000.97		000.04	000.05	-000.03	000.29	000.27	000.56			
43		34–33–22–23	47–46–08–09		180.00	180.00	-179.57	179.43	180.00	-179.99	179.99	-179.13	-173.04	169.15		179.95	-179.99	-179.42	-178.93	-178.93	-179.92			
44	R4,R11	23–24	09–10		1.3803	1.3548	1.3641	1.3715	1.3647	1.3729	1.3577	1.3661	1.3770	1.3591		1.3649	1.3718	1.3891	1.3658	1.3666	1.3414			
45		24–25	10–11	10–11	1.3828	1.3709	1.3704	1.4009	1.3900	1.3662	1.3760	1.3873	1.3622	1.3764	1.3775	1.3898	1.3734	1.3784	1.3878	1.3859	1.3783			
46		25–30	11–43	11–43	1.3995	1.4209	1.4095	1.3879	1.3955	1.4087	1.3989	1.3929	1.4090	1.3979	1.4093	1.3955	1.4031	1.4005	1.3967	1.3974	1.4022			
47		30–31	43–44	43–44	1.3828	1.3709	1.3704	1.3942	1.3900	1.3662	1.3760	1.3848	1.3601	1.3721	1.3687	1.3899	1.3735	1.3785	1.3897	1.3882	1.3796			
48		31–32	44–45		1.3803	1.3548	1.3641	1.3705	1.3647	1.3729	1.3577	1.3665	1.3772	1.3582		1.3649	1.3718	1.3891	1.3695	1.3704	1.3455			
49		32–23–24	45–09–10		121.98	120.48	119.54	122.69	122.15	121.39	121.22	122.65	121.95	121.65		122.14	121.49	122.32	122.61	122.57	121.60			
50		23–24–25	09–10–11		116.15	118.64	118.39	115.05	116.40	117.65	118.07	116.84	117.87	118.25		116.41	117.44	115.87	116.55	116.56	119.01			
51		24–25–30	10–11–43	10–11–43	121.85	120.87	121.50	122.08	121.44	120.94	120.69	120.73	117.87	120.25	114.66	121.44	121.05	121.80	120.80	120.78	119.84			
52		25–30–31	11–43–44	11–43–44	121.85	120.87	121.50	121.86	121.44	120.94	120.69	121.56	121.04	120.76	119.97	121.43	121.05	121.80	121.19	121.19	120.30			
53		30–31–32	43–44–45		116.15	118.64	118.39	115.33	116.40	117.65	118.07	117.66	118.64	118.96		116.40	117.43	115.87	117.04	117.04	119.59			
54		31–32–23	44–45–09		121.98	120.48	119.54	122.86	122.15	121.39	121.22	122.05	119.88	119.89		122.15	121.50	122.31	120.59	120.55	119.62			
55		31–32–23–24	44–45–09–10		000.00	000.00	013.18	-001.69	-000.00	000.00	000.00	-000.74	-000.96	001.26		000.01	000.02	000.04	-000.84	-000.85	-000.23			
56		31–30–25–24	44–43–11–10	44–43–11–10	000.00	000.00	002.25	-001.75	-000.00	000.00	000.00	000.07	-000.11	000.01	-000.11	000.00	-000.00	-000.01	000.52	000.62	000.14			
57		32–31–24–25	45–44–10–11		180.00	179.99	-175.98	176.99	-179.99	-179.99	179.99	175.38	176.67	-176.02		-179.93	-179.99	-179.70	170.73	170.47	179.39			
58	R5,R12	25–26	11–12	11–12	1.3905	1.3964	1.3968	1.3776	1.3882	1.3933	1.3915	1.3880	1.3937	1.3916	1.3918	1.3885	1.3884	1.3910	1.3885	1.3884	1.3897			
59		26–27	12–13	12–13	1.3974	1.3888	1.3906	1.3841	1.3976	1.3916	1.3930	1.3979	1.3911	1.3928	1.3992	1.3976	1.3942	1.3977	1.3968	1.3965	1.3911			
60		27–28	13–41	13–41	1.3952	1.4186	1.4080	1.3884	1.3955	1.4049	1.4018	1.3958	1.4062	1.4025	1.3958	1.3955	1.4008	1.3951	1.3974	1.3972	1.4114			
61		28–29	41–42	41–42	1.3974	1.3888	1.3906	1.3924	1.3976	1.3916	1.3930	1.3977	1.3907	1.3924	1.3985	1.3976	1.3942	1.3978	1.3973	1.3976	1.3908			
62		29–30	42–43	42–43	1.3905	1.3964	1.3968	1.3793	1.3882	1.3933	1.3915	1.3890	1.3949	1.3925	1.3919	1.3882	1.3916	1.3911	1.3888	1.3887	1.3892			
63		30–25–26	43–11–12	43–11–12	120.11	120.03	120.03	120.41	120.44	120.40	120.62	120.72	120.57	120.79	120.70	120.43	120.39	120.04	121.05	121.08	121.51			
64		25–26–27	11–12–13	11–12–13	119.83	119.69	119.75	119.45	119.33	119.06	118.85	119.16	119.14	118.71	119.14	119.34	119.21	119.95	118.70	118.71	117.77			
65		26–27–28	12–13–41	12–13–41	120.04	120.26	120.21	120.39	120.21	120.53	120.52	120.20	120.55	120.55	120.21	120.21	120.39	120.00	120.27	120.22	120.73			
66		27–28–29	13–41–42	13–41–42	120.04	120.26	120.21	120.39	120.21	120.53	120.52	120.27	120.59	120.56	120.71	120.21	120.38	120.01	120.78	120.88	121.16			
67		28–29–30	41–42–43	41–42–43	119.83	119.69	119.75	119.10	119.33	119.06	118.85	119.29	119.04	118.79	119.30	119.34	119.21	119.95	118.72	118.66	117.88			
68		29–30–25	42–43–11	42–43–11	120.11	120.03	120.03	120.60	120.44	120.40	120.62	120.33	120.28	120.57	119.91	120.44	120.40	120.03	120.45	120.42	120.91			
69		29–30–25–26	42–43–11–12	42–43–11–12	000.00	000.00	-000.08	-001.04	000.00	000.00	-000.00	000.03	-000.00	000.08	000.01	-000.00	-000.01	000.00	000.26	000.33	000.09			
70		29–28–27–26	42–41–13–12	42–41–13–12	-000.00	000.00	000.26	-000.58	000.00	000.00	000.00	-000.00	000.00	000.01	-000.19	-000.00	-000.00	-000.00	-000.10	-000.04	-000.44			
71		30–29–26–27	43–42–12–13	43–42–12–13	180.00	180.00	-179.95	179.69	179.99	179.99	-179.99	-179.84	179.81	-179.90	179.71	179.99	179.99	179.98	-179.70	-179.72	-179.97			
72	R3,R10 Subst-ituent	22–54	54–55	50–51				1.4398	1.4270	1.4012	1.4004	1.4274	1.4025	1.4021		1.4270	1.4013	1.3989	1.4274	1.4274	1.4270			
73		54–55	50–51					1.1456	1.1628	1.1736	1.1737	1.1728	1.1834	1.1722		1.1628	1.1730	1.1758	1.1628	1.1628	1.1616			
74		33–56	46–60					1.4346	1.4270	1.4012	1.4004	1.8334	1.7972	1.7788		1.4270	1.4010	1.3993	1.8325	1.8330	1.8486			
75		56–57	60–61					1.1486	1.1628	1.1737	1.1728	1.4717	1.4804	1.4769		1.1629	1.1739	1.1755	1.4679	1.4677	1.4649			
76			60–62									1.4679	1.4754	1.4757					1.4716	1.4715	1.4676			
77			60–63									1.7555	1.7639	1.7679					1.7559	1.7559	1.7467			
78		21–22–54	07–08–50					119.44	119.98	122.52	122.41	120.16	122.56	122.44		120.00	122.40	121.72	120.19	120.22	120.74			
79		22–54–55	08–50–51					179.26	179.99	179.89	179.41	179.58	179.89	179.11		179.96	179.86	179.64	179.87	179.94	179.76			
80		34–33–56	47–46–60					120.12	119.98	122.52	122.41	117.85	118.46	120.28		119.96	122.36	122.83	122.69	122.67	123.07			
81		33–26–57	46–60–63					177.85	179.99	179.99	179.99	103.83	105.09	106.03		179.93	179.78	179.84	103.86	103.81	103.95			
82			61–60–62									118.38	118.15	118.10					118.39	118.45	119.74			
83		34–21–22–54	47–07–08–50					178.96	179.99	-179.99	-179.99	-179.38	-176.42	175.44		179.73	179.70	-179.21	-179.81	-179.85	179.69			
84		21–34–33–56	47–47–46–60					176.74	179.99	-179.99	-179.99	177.86	151.80	-155.06		-179.98	-179.89	179.40	177.53	177.57	176.18			
85			47–46–60–63									067.58	079.72	049.55					114.21	113.81	118.86			
86			47–46–60–62									-048.81	-035.70	-066.25					-000.69	-001.11	003.46			
87			47–46–60–62									-177.48	-165.37	164.54					-129.41	-129.85	-124.94			
88			46–60–63–64									-115.79	-119.58	-114.13					116.73	116.75	120.02			
89	R6			13–14											1.5238							1.5230	1.5221	1.5212
90				14–15											1.5607							1.5611	1.5610	1.5607
91				15–16											1.5678							1.5677	1.5711	1.5660
92				16–41											1.5237							1.5227	1.5229	1.5199
93				41–13–14											111.87							111.87	111.99	111.42
94				13–14–15											101.46							101.54	101.63	101.62
95				14–15–16											108.15							108.09	107.93	108.09
96				15–16–41											101.24							101.35	101.42	101.35
97				16–41–13											111.96							111.89	111.80	111.78
98				16–41–13–14											000.02							-000.25	-000.26	000.01
99				41–13–14–15											-013.84							-013.55	-013.54	-014.34
100	R7			38–39											1.5242							1.5231	1.5196	1.5226
101				39–40											1.5609							1.5608	1.5599	1.5614
102				40–16											1.5676							1.5678	1.5666	1.5705
103				16–17											1.5230							1.5227	1.5189	1.5221
104				17–38–39											111.69							111.83	111.46	111.90
105				38–39–40											101.54							101.52	101.76	101.61
106				39–40–16											108.14							108.10	108.01	107.82
107				40–16–17											101.16							101.31	101.56	101.47
108				16–17–38											112.14							111.92	111.55	111.88
109				16–17–38–39											-000.17							-000.01	-000.15	000.43
110				17–38–39–40											-013.71							-013.82	-014.13	-014.19
111	Param-eters around the SPIRO bridge			33–46																		11.386	11.436	11.176
112				22–08																		11.344	11.300	11.215
113				42–16–18											085.32							085.44	085.22	084.01
114				33–22–08																		120.18	120.41	119.56
115				46–08–22																		056.65	057.00	054.76
116				42–41–17–18											-071.28							-071.71	-071.34	-070.17
117				42–41–16–17											-045.73							-045.86	-046.82	-043.13
118				42–41–16––16–17–18[b]											105.62							105.25	105.61	107.08
119				13–41–16––16–17–38[b]											107.81							107.53	107.83	107.91
120				42–11–13––37–19–17[b]											074.53							075.07	074.81	073.14

[a] From *J. Am. Chem. Soc.* 2018, 140, 40, 12715–12719. DOI: 10.1021/jacs.8b08374
[b] These angles are calculated between plane (P1) containing atoms (A1,B1,C1) and plane (P2) containing atoms (A2,B2,C2). see text for details.

211

APPENDIX D

MISCELLANEOUS SUPPORTING INFORMATION

D.1 LOGARITHMIC–NORMAL DISTRIBUTION (LOGN) FUNCTION: PROPERTIES AND DERIVATION

The logarithmic–normal distribution (Logn) function is a phenomenological function introduced by Siano and Metzler in 1969. [97] This function represents an alternative to the symmetrical Gaussian function to simulate the entire asymmetrical electronic ultraviolet–visible absorption (UV–VIS) spectra of organic chromophores in solutions. Metzler argued that the asymmetry of the Logn function is a good representation of electronic band asymmetry originating from vibronic progression. Burstein and Emelyanenko introduced the mirror–symmetric version of this function in 1996. [98] In their work, they argued that the mirror–symmetric Logn function is good descriptor to the smooth, asymmetric photoluminescence (PL) spectra of organic molecules in solution.

Several studies utilized both versions of this function to analyze the complex UV–VIS and PL of organic chromophores in solution. [211–221] Maroncelli and Fleming simulated the UV–VIS spectra of coumarin 153. [211] Baumann and co–workers decomposed the complex UV–VIS spectra of 3-arylazopropenoic acid esters using Logn function. [212]. Similarly, Millié and co–workers decomposed UV–VIS spectra of DNA bases using Logn function. [214] Several other studies utilized this Logn function for simulation and decomposition of complex UV–VIS and PL spectra. [213,

215–220] Vauthey and co–workers highlighted the importance and success of this function in simulating the asymmetric electronic transition profiles in time–dependent spectroscopy. [221] A visualization of both UV–VIS and PL variations of Logn function are depicted in Figure D.1.
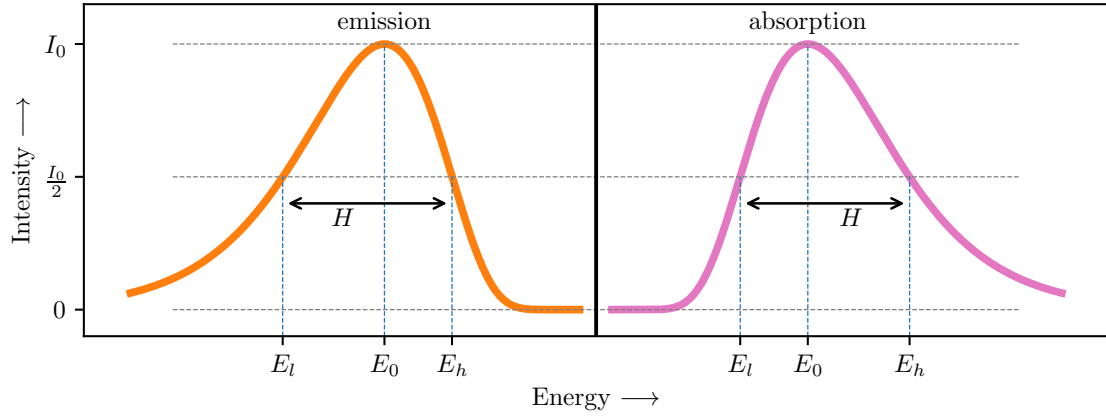
Figure D.1: A graphical representation of both UV–VIS and PL variations of the Logn function. The main function parameters were posted on each plot; I_0, E_0, E_h, E_l, and H.

Herein, a derivation to rewrite Metzler's Logn original form, Equation D.1, similar to that of Burstein's mirror–symmetric form, Equation D.2,

$$\varepsilon(E; \varepsilon_0, a, b, c) = \begin{cases} \dfrac{\varepsilon_0\, b}{E - a} exp\left(-c^2\right) \left\{ -\dfrac{1}{2c^2} \left[\ln \dfrac{E - a}{b} \right]^2 \right\} & \text{for} \quad E > a \\ 0 & \text{for} \quad E \leq a \end{cases} \tag{D.1}$$

where:

$$c = \frac{\ln \rho}{(2 \ln 2)^{1/2}} \qquad b = H \left[\frac{\rho}{\rho^2 - 1} \right] exp\left(c^2\right) \qquad a = E_0 - H \left[\frac{\rho}{\rho^2 - 1} \right]$$

and

$$H = E_h - E_l \qquad \rho = \frac{E_h - E_0}{E_0 - E_l}$$

ε_0 is the extinction coefficient at the band's central transition energy E_0, while E_l and E_h are the energies at the band's half maximum on the lower and higher energy sides, respectively.

$$I(E; I_0, E_0, H, \rho) = \begin{cases} I_0 \; exp\left\{-\dfrac{\ln 2}{(\ln \rho)^2}\left[\ln\dfrac{a-E}{a-E_0}\right]^2\right\} & \text{for} \quad E < a \\ \\ 0 & \text{for} \quad E \geq a \end{cases} \tag{D.2}$$

where:

$$a = E_0 + H\left[\dfrac{\rho}{\rho^2-1}\right] \qquad H = E_h - E_l \qquad \rho = \dfrac{E_0 - E_l}{E_h - E_0}$$

Derivation:

using the expression of "a" and substituting in "b"

$$H\dfrac{\rho}{\rho^2-1} = E_0 - a \; \Rightarrow \; b = (E_0 - a)\; e^{c^2}$$

substituting and rearranging the second exponent in Metzler expression

$$-\dfrac{1}{2c^2}\left[\ln\dfrac{E-a}{b}\right]^2 = -\dfrac{1}{2c^2}\left[\ln\dfrac{E-a}{(E_0-a)\; e^{c^2}}\right]^2 = -\dfrac{1}{2c^2}\left[\ln\left(\dfrac{E-a}{E_0-a}\right) - c^2\right]^2$$

let $\ln\dfrac{E-a}{E_0-a} = x$

$$\Rightarrow \; -\dfrac{1}{2c^2}\left(x - c^2\right)^2 = -\dfrac{1}{2c^2}\left(x^2 - 2c^2 x + c^4\right) = \dfrac{-x^2}{2c^2} + \dfrac{2c^2 x}{2c^2} - \dfrac{c^4}{2c^2}$$

$$= \dfrac{-x^2}{2c^2} + x - \dfrac{c^2}{2} \quad |||(1)$$

taking Metzler pre–exponential term, and substituting "b"

$$\dfrac{\varepsilon_0\; b}{E-a} = \dfrac{\varepsilon_0\; (E_0-a)\; e^{c^2}}{E-a} = \varepsilon_0\left(\dfrac{E_0-a}{E-a}\right) e^{c^2} \quad |||(2)$$

substituting (1) and (2) in Metzler form

$$\varepsilon(E) = \varepsilon_0 \left(\frac{E_0 - a}{E - a}\right) \; \cancel{exp\left(c^2\right)} \; \cancel{exp\left(-c^2\right)} \; exp\left\{\frac{-x^2}{2c^2} + x - \frac{c^2}{2}\right\}$$

$$\varepsilon(E) = \varepsilon_0 \left(\frac{E_0 - a}{E - a}\right) \; exp\left\{\frac{-x^2}{2c^2}\right\} \; exp\left\{x\right\} \; exp\left\{-\frac{c^2}{2}\right\}$$

but $x = \ln \dfrac{E - a}{E_0 - a}$ then

$$\varepsilon(E) = \varepsilon_0 \; exp\left\{-\frac{c^2}{2}\right\} \cancel{\left(\frac{E_0 - a}{E - a}\right)} \cancel{exp\left\{\ln\frac{E - a}{E_0 - a}\right\}}^{\frac{E-a}{E_0-a}} exp\left\{\frac{-\left(\ln\frac{E-a}{E_0-a}\right)^2}{2c^2}\right\}$$

from "c" expression $\Rightarrow c^2 = \dfrac{(\ln \rho)^2}{2\ln 2}$

$$\varepsilon(E) = \varepsilon_0 \; exp\left\{-\frac{\frac{(\ln \rho)^2}{2\ln 2}}{2}\right\} exp\left\{\frac{-\left(\ln\frac{E-a}{E_0-a}\right)^2}{2\frac{(\ln \rho)^2}{2\ln 2}}\right\}$$

let $I_0 = \varepsilon_0 \; exp\left\{-\dfrac{(\ln \rho)^2}{4\ln 2}\right\}$ then

$$I(E) = I_0 \; exp\left\{-\frac{\ln 2}{(\ln \rho)^2}\left(\ln\frac{E - a}{E_0 - a}\right)^2\right\} \quad \text{for } E > a$$

D.2 EXPONENTIALLY MODIFIED GAUSSIAN FUNCTION: PROPERTIES AND DERIVATION

ExpGaus function is the analytical solution of convoluting a Gaussian function with an Exponential function. It takes the form:

$$EG(t; I_o, \mu, \sigma, \tau) = I_o e^{-\frac{1}{\tau}\left(t - \mu - \frac{\sigma^2}{2\tau}\right)} \left[1 + \text{erf}\left(\frac{t - \mu - \frac{\sigma^2}{\tau}}{\sqrt{2}\sigma}\right)\right] \tag{D.3}$$

Where I_o is the intensity, μ is the instrument response function (IRF) center, σ is the IRF width, and τ is the decay lifetime. The error function, erf, is defined as:

$$\text{erf}(x) = \frac{1}{\sqrt{\pi}} \int_{-x}^{x} e^{-t^2} dt \tag{D.4}$$
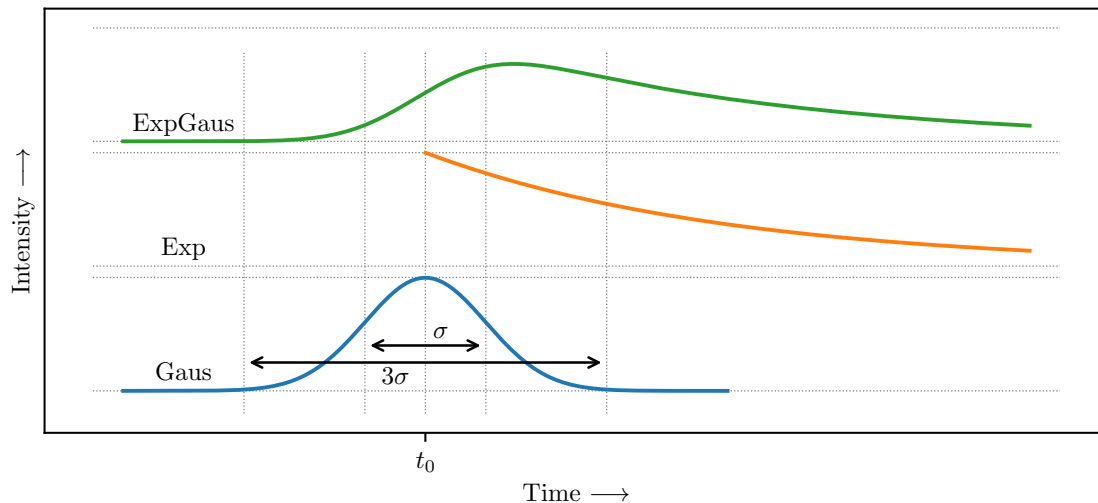
Figure D.2: Graphical representation of the exponentially modified gaussian (ExpGaus) function. The Gaussian width, σ, is shown on the figure in relation with the exponential decay and resulting ExpGaus function curves.

This form was taken from a derivation performed By Dr. David Forest and Dr. Carl Wheldon from University of Birmingham. The derivation details and function properties can be found in Dr. Forest and Dr. Wheldon's white paper [222]. The form used in this work replaces the rate constant (λ) with the time constant (τ). In Figure D.2 a visualization of the ExpGaus function compared with the individual Gaussian and exponential decay functions is presented.

D.3 PARAMETER CORRELATION TABLES FROM LINE FITTING OF STEADY–STATE AND TIME–RESOLVED SPECTRAL DATA

Table D.1: Parameter correlation of UV–VIS decomposition of BDODC.

	$I_{o,BDODC}$	$E_{o,BDODC}$	H_{BDODC}	ρ_{BDODC}
$I_{o,BDODC}$	+1.00	-0.12	-0.61	-0.01
$E_{o,BDODC}$	-0.12	+1.00	+0.19	-0.80
H_{BDODC}	-0.61	+0.19	+1.00	+0.02
ρ_{BDODC}	-0.01	-0.80	+0.02	+1.00

Table D.2: Parameter correlation of UV–VIS decomposition of HTRMR.

	$I_{o,BDODC}$	$E_{o,BDODC}$	H_{BDODC}	ρ_{BDODC}	$I_{o,BDOSC}$	$E_{o,BDOSC}$	H_{BDOSC}	ρ_{BDOSC}
$I_{o,BDODC}$	+1.00	+0.87	+0.66	+0.43	-0.69	+0.80	+0.45	+0.31
$E_{o,BDODC}$	+0.87	+1.00	+0.92	+0.75	-0.94	+0.98	+0.79	+0.01
H_{BDODC}	+0.66	+0.92	+1.00	+0.94	-1.00	+0.96	+0.95	-0.17
ρ_{BDODC}	+0.43	+0.75	+0.94	+1.00	-0.93	+0.84	+0.97	-0.25
$I_{o,BDOSC}$	-0.69	-0.94	-1.00	-0.93	+1.00	-0.97	-0.94	+0.14
$E_{o,BDOSC}$	+0.80	+0.98	+0.96	+0.84	-0.97	+1.00	+0.86	-0.13
H_{BDOSC}	+0.45	+0.79	+0.95	+0.97	-0.94	+0.86	+1.00	-0.26
ρ_{BDOSC}	+0.31	+0.01	-0.17	-0.25	+0.14	-0.13	-0.26	+1.00

Table D.3: Parameter correlation of UV–VIS decomposition of OLGMR.

	$I_{o,BDODC}$	$E_{o,BDODC}$	H_{BDODC}	ρ_{BDODC}	$I_{o,BDOSC}$	$E_{o,BDOSC}$	H_{BDOSC}	ρ_{BDOSC}
$I_{o,BDODC}$	+1.00	+0.87	+0.64	+0.38	-0.68	+0.80	+0.50	+0.31
$E_{o,BDODC}$	+0.87	+1.00	+0.92	+0.72	-0.93	+0.98	+0.82	+0.07
H_{BDODC}	+0.64	+0.92	+1.00	+0.93	-1.00	+0.96	+0.97	-0.06
ρ_{BDODC}	+0.38	+0.72	+0.93	+1.00	-0.92	+0.81	+0.96	-0.11
$I_{o,BDOSC}$	-0.68	-0.93	-1.00	-0.92	+1.00	-0.97	-0.97	+0.02
$E_{o,BDOSC}$	+0.80	+0.98	+0.96	+0.81	-0.97	+1.00	+0.88	-0.05
H_{BDOSC}	+0.50	+0.82	+0.97	+0.96	-0.97	+0.88	+1.00	-0.04
ρ_{BDOSC}	+0.31	+0.07	-0.06	-0.11	+0.02	-0.05	-0.04	+1.00

Table D.4: Parameter correlation of UV–VIS decomposition of PLYMR.

	$I_{o,BDODC}$	$E_{o,BDODC}$	H_{BDODC}	ρ_{BDODC}	$I_{o,BDOSC}$	$E_{o,BDOSC}$	H_{BDOSC}	ρ_{BDOSC}
$I_{o,BDODC}$	+1.00	+0.86	+0.64	+0.40	-0.67	+0.77	+0.39	+0.17
$E_{o,BDODC}$	+0.86	+1.00	+0.92	+0.74	-0.93	+0.97	+0.76	-0.19
H_{BDODC}	+0.64	+0.92	+1.00	+0.94	-1.00	+0.97	+0.94	-0.40
ρ_{BDODC}	+0.40	+0.74	+0.94	+1.00	-0.94	+0.85	+0.97	-0.48
$I_{o,BDOSC}$	-0.67	-0.93	-1.00	-0.94	+1.00	-0.98	-0.93	+0.37
$E_{o,BDOSC}$	+0.77	+0.97	+0.97	+0.85	-0.98	+1.00	+0.86	-0.36
H_{BDOSC}	+0.39	+0.76	+0.94	+0.97	-0.93	+0.86	+1.00	-0.50
ρ_{BDOSC}	+0.17	-0.19	-0.40	-0.48	+0.37	-0.36	-0.50	+1.00

Table D.5: Parameter correlation of excitation PL decomposition of BDODC.

	$I_{o,BDODC}$	$E_{o,BDODC}$	H_{BDODC}	ρ_{BDODC}
$I_{o,BDODC}$	+1.00	-0.14	-0.60	+0.04
$E_{o,BDODC}$	-0.14	+1.00	+0.25	-0.79
H_{BDODC}	-0.60	+0.25	+1.00	-0.08
ρ_{BDODC}	+0.04	-0.79	-0.08	+1.00

Table D.6: Parameter correlation of excitation PL decomposition of HTRMR.

	$I_{o,BDODC}$	$E_{o,BDODC}$	H_{BDODC}	ρ_{BDODC}	$I_{o,BDOSC}$	$E_{o,BDOSC}$	H_{BDOSC}	ρ_{BDOSC}
$I_{o,BDODC}$	+1.00	+0.92	+0.75	+0.53	-0.76	+0.82	+0.31	-0.38
$E_{o,BDODC}$	+0.92	+1.00	+0.94	+0.79	-0.94	+0.97	+0.63	-0.68
H_{BDODC}	+0.75	+0.94	+1.00	+0.95	-1.00	+0.99	+0.85	-0.86
ρ_{BDODC}	+0.53	+0.79	+0.95	+1.00	-0.95	+0.91	+0.95	-0.92
$I_{o,BDOSC}$	-0.76	-0.94	-1.00	-0.95	+1.00	-0.99	-0.84	+0.86
$E_{o,BDOSC}$	+0.82	+0.97	+0.99	+0.91	-0.99	+1.00	+0.78	-0.82
H_{BDOSC}	+0.31	+0.63	+0.85	+0.95	-0.84	+0.78	+1.00	-0.93
ρ_{BDOSC}	-0.38	-0.68	-0.86	-0.92	+0.86	-0.82	-0.93	+1.00

Table D.7: Parameter correlation of excitation PL decomposition of OLGMR.

	$I_{o,BDODC}$	$E_{o,BDODC}$	H_{BDODC}	ρ_{BDODC}	$I_{o,BDOSC}$	$E_{o,BDOSC}$	H_{BDOSC}	ρ_{BDOSC}
$I_{o,BDODC}$	+1.00	+0.87	+0.59	+0.29	-0.61	+0.69	+0.10	-0.22
$E_{o,BDODC}$	+0.87	+1.00	+0.90	+0.66	-0.90	+0.95	+0.54	-0.63
H_{BDODC}	+0.59	+0.90	+1.00	+0.92	-1.00	+0.99	+0.84	-0.87
ρ_{BDODC}	+0.29	+0.66	+0.92	+1.00	-0.92	+0.86	+0.95	-0.92
$I_{o,BDOSC}$	-0.61	-0.90	-1.00	-0.92	+1.00	-0.99	-0.84	+0.87
$E_{o,BDOSC}$	+0.69	+0.95	+0.99	+0.86	-0.99	+1.00	+0.77	-0.83
H_{BDOSC}	+0.10	+0.54	+0.84	+0.95	-0.84	+0.77	+1.00	-0.92
ρ_{BDOSC}	-0.22	-0.63	-0.87	-0.92	+0.87	-0.83	-0.92	+1.00

Table D.8: Parameter correlation of excitation PL decomposition of PLYMR.

	$I_{o,BDODC}$	$E_{o,BDODC}$	H_{BDODC}	ρ_{BDODC}	$I_{o,BDOSC}$	$E_{o,BDOSC}$	H_{BDOSC}	ρ_{BDOSC}
$I_{o,BDODC}$	+1.00	+0.80	+0.48	+0.19	-0.50	+0.60	+0.07	-0.06
$E_{o,BDODC}$	+0.80	+1.00	+0.88	+0.64	-0.88	+0.93	+0.58	-0.56
H_{BDODC}	+0.48	+0.88	+1.00	+0.92	-1.00	+0.98	+0.88	-0.82
ρ_{BDODC}	+0.19	+0.64	+0.92	+1.00	-0.92	+0.86	+0.96	-0.87
$I_{o,BDOSC}$	-0.50	-0.88	-1.00	-0.92	+1.00	-0.98	-0.88	+0.81
$E_{o,BDOSC}$	+0.60	+0.93	+0.98	+0.86	-0.98	+1.00	+0.81	-0.79
H_{BDOSC}	+0.07	+0.58	+0.88	+0.96	-0.88	+0.81	+1.00	-0.89
ρ_{BDOSC}	-0.06	-0.56	-0.82	-0.87	+0.81	-0.79	-0.89	+1.00

Table D.9: Parameter correlation of emission PL decomposition of BDODC.

	I_{o,S_1}	E_{o,S_1}	H_{S_1}	ρ_{S_1}
I_{o,S_1}	+1.00	+0.12	-0.59	+0.04
E_{o,S_1}	+0.12	+1.00	-0.21	+0.78
H_{S_1}	-0.59	-0.21	+1.00	-0.09
ρ_{S_1}	+0.04	+0.78	-0.09	+1.00

Table D.10: Parameter correlation of emission PL decomposition of HTRMR.

	I_{o,S_1}	E_{o,S_1}	H_{S_1}	ρ_{S_1}	I_{o,S_2}	E_{o,S_2}	H_{S_2}	ρ_{S_2}
I_{o,S_1}	+1.00	-0.63	+0.01	-0.55	-0.62	-0.00	-0.55	+0.35
E_{o,S_1}	-0.63	+1.00	-0.53	+0.81	+0.81	+0.04	+0.66	-0.11
H_{S_1}	+0.01	-0.53	+1.00	-0.18	-0.52	-0.08	-0.55	-0.39
ρ_{S_1}	-0.55	+0.81	-0.18	+1.00	+0.58	-0.01	+0.34	-0.35
I_{o,S_2}	-0.62	+0.81	-0.52	+0.58	+1.00	+0.08	+0.44	-0.04
E_{o,S_2}	-0.00	+0.04	-0.08	-0.01	+0.08	+1.00	-0.03	+0.66
H_{S_2}	-0.55	+0.66	-0.55	+0.34	+0.44	-0.03	+1.00	+0.02
ρ_{S_2}	+0.35	-0.11	-0.39	-0.35	-0.04	+0.66	+0.02	+1.00

Table D.11: Parameter correlation of emission PL decomposition of OLGMR.

	I_{o,S_1}	E_{o,S_1}	H_{S_1}	ρ_{S_1}	I_{o,S_2}	E_{o,S_2}	H_{S_2}	ρ_{S_2}
I_{o,S_1}	+1.00	-0.62	+0.05	-0.52	-0.61	+0.00	-0.45	+0.31
E_{o,S_1}	-0.62	+1.00	-0.57	+0.72	+0.84	+0.01	+0.63	-0.06
H_{S_1}	+0.05	-0.57	+1.00	-0.05	-0.59	-0.05	-0.67	-0.47
ρ_{S_1}	-0.52	+0.72	-0.05	+1.00	+0.50	-0.05	+0.14	-0.43
I_{o,S_2}	-0.61	+0.84	-0.59	+0.50	+1.00	+0.07	+0.48	+0.04
E_{o,S_2}	+0.00	+0.01	-0.05	-0.05	+0.07	+1.00	-0.07	+0.62
H_{S_2}	-0.45	+0.63	-0.67	+0.14	+0.48	-0.07	+1.00	+0.19
ρ_{S_2}	+0.31	-0.06	-0.47	-0.43	+0.04	+0.62	+0.19	+1.00

Table D.12: Parameter correlation of emission PL decomposition of PLYMR.

	I_{o,S_1}	E_{o,S_1}	H_{S_1}	ρ_{S_1}	I_{o,S_2}	E_{o,S_2}	H_{S_2}	ρ_{S_2}
I_{o,S_1}	+1.00	-0.56	+0.02	-0.45	-0.52	-0.01	-0.35	+0.34
E_{o,S_1}	-0.56	+1.00	-0.58	+0.63	+0.82	+0.02	+0.58	-0.07
H_{S_1}	+0.02	-0.58	+1.00	+0.10	-0.66	-0.04	-0.73	-0.48
ρ_{S_1}	-0.45	+0.63	+0.10	+1.00	+0.33	-0.03	-0.05	-0.52
I_{o,S_2}	-0.52	+0.82	-0.66	+0.33	+1.00	+0.08	+0.49	+0.10
E_{o,S_2}	-0.01	+0.02	-0.04	-0.03	+0.08	+1.00	-0.07	+0.59
H_{S_2}	-0.35	+0.58	-0.73	-0.05	+0.49	-0.07	+1.00	+0.26
ρ_{S_2}	+0.34	-0.07	-0.48	-0.52	+0.10	+0.59	+0.26	+1.00

Table D.13: Parameter correlation of IRF fit from TRPL.

	I_o	μ	σ
I_o	+1.00	-0.00	+0.58
μ	-0.00	+1.00	-0.00
σ	+0.58	-0.00	+1.00

Table D.14: Parameter correlation of TRPL decay fit of BDODC.

	I_o	μ	τ
I_o	+1.00	+0.21	-0.74
μ	+0.21	+1.00	-0.29
τ	-0.74	-0.29	+1.00

Table D.15: Parameter correlation of TRPL decay fit of HTRMR.

	I_o	μ	τ
I_o	+1.00	+0.23	-0.75
μ	+0.23	+1.00	-0.31
τ	-0.75	-0.31	+1.00

Table D.16: Parameter correlation of TRPL decay fit of OLGMR.

	I_o	μ	τ
I_o	+1.00	+0.25	-0.75
μ	+0.25	+1.00	-0.33
τ	-0.75	-0.33	+1.00

Table D.17: Parameter correlation of TRPL decay fit of PLYMR.

	I_o	μ	τ
I_o	+1.00	+0.23	-0.75
μ	+0.23	+1.00	-0.31
τ	-0.75	-0.31	+1.00

Table D.18: Parameter correlation of PIA$_1$ decay fit of BDODC.

	I_{IRF}	$t_{0,IRF}$	I_{d_1}	τ_{d_1}	I_{d_3}
I_{IRF}	+1.00	+0.62	-0.35	+0.25	-0.05
$t_{0,IRF}$	+0.62	+1.00	-0.24	+0.16	-0.03
I_{d_1}	-0.35	-0.24	+1.00	-0.19	-0.52
τ_{d_1}	+0.25	+0.16	-0.19	+1.00	-0.49
I_{d_3}	-0.05	-0.03	-0.52	-0.49	+1.00

Table D.19: Parameter correlation of PIA$_1$ decay fit of HTRMR.

	I_{IRF}	$t_{0,IRF}$	I_{d_1}	τ_{d_1}	I_{d_2}	τ_{d_2}	I_{d_3}
I_{IRF}	+1.00	+0.87	-0.58	+0.44	-0.12	+0.09	-0.03
$t_{0,IRF}$	+0.87	+1.00	-0.46	+0.31	-0.08	+0.06	-0.02
I_{d_1}	-0.58	-0.46	+1.00	-0.33	-0.21	+0.26	-0.11
τ_{d_1}	+0.44	+0.31	-0.33	+1.00	-0.48	+0.42	-0.16
I_{d_2}	-0.12	-0.08	-0.21	-0.48	+1.00	-0.10	-0.52
τ_{d_2}	+0.09	+0.06	+0.26	+0.42	-0.10	+1.00	-0.68
I_{d_3}	-0.03	-0.02	-0.11	-0.16	-0.52	-0.68	+1.00

Table D.20: Parameter correlation of PIA$_1$ decay fit of OLGMR.

	I_{IRF}	$t_{0,IRF}$	I_{d_1}	τ_{d_1}	I_{d_2}	τ_{d_2}	I_{d_3}
I_{IRF}	+1.00	+0.77	-0.17	+0.36	-0.17	+0.12	-0.04
$t_{0,IRF}$	+0.77	+1.00	-0.13	+0.24	-0.11	+0.08	-0.02
I_{d_1}	-0.17	-0.13	+1.00	+0.45	-0.77	+0.72	-0.27
τ_{d_1}	+0.36	+0.24	+0.45	+1.00	-0.78	+0.59	-0.20
I_{d_2}	-0.17	-0.11	-0.77	-0.78	+1.00	-0.64	-0.06
τ_{d_2}	+0.12	+0.08	+0.72	+0.59	-0.64	+1.00	-0.59
I_{d_3}	-0.04	-0.02	-0.27	-0.20	-0.06	-0.59	+1.00

Table D.21: Parameter correlation of PIA$_1$ decay fit of PLYMR.

	I_{IRF}	$t_{0,IRF}$	I_{d_1}	τ_{d_1}	I_{d_2}	τ_{d_2}	I_{d_3}
I_{IRF}	+1.00	+0.68	-0.37	+0.41	-0.17	+0.11	-0.04
$t_{0,IRF}$	+0.68	+1.00	-0.27	+0.27	-0.11	+0.07	-0.02
I_{d_1}	-0.37	-0.27	+1.00	+0.11	-0.54	+0.54	-0.21
τ_{d_1}	+0.41	+0.27	+0.11	+1.00	-0.68	+0.52	-0.17
I_{d_2}	-0.17	-0.11	-0.54	-0.68	+1.00	-0.47	-0.23
τ_{d_2}	+0.11	+0.07	+0.54	+0.52	-0.47	+1.00	-0.61
I_{d_3}	-0.04	-0.02	-0.21	-0.17	-0.23	-0.61	+1.00

Table D.22: Parameter correlation of PIA$_2$ decay fit of BDODC.

	I_{IRF}	$t_{0,IRF}$	I_g	τ_g	I_{d_1}	τ_{d_1}	I_{d_3}
I_{IRF}	+1.00	+0.85	+0.08	+0.06	+0.02	-0.02	+0.00
$t_{0,IRF}$	+0.85	+1.00	+0.20	+0.26	+0.11	-0.08	+0.02
I_g	+0.08	+0.20	+1.00	-0.24	-0.66	+0.62	-0.22
τ_g	+0.06	+0.26	-0.24	+1.00	+0.74	-0.56	+0.17
I_{d_1}	+0.02	+0.11	-0.66	+0.74	+1.00	-0.59	-0.13
τ_{d_1}	-0.02	-0.08	+0.62	-0.56	-0.59	+1.00	-0.57
I_{d_3}	+0.00	+0.02	-0.22	+0.17	-0.13	-0.57	+1.00

Table D.23: Parameter correlation of PIA$_2$ decay fit of HTRMR.

	I_{IRF}	$t_{0,IRF}$	I_g	τ_g	I_{d_1}	τ_{d_1}	I_{d_2}	τ_{d_2}	I_{d_3}
I_{IRF}	+1.00	+0.77	+0.19	+0.04	-0.00	-0.00	+0.00	-0.00	+0.00
$t_{0,IRF}$	+0.77	+1.00	+0.65	+0.43	-0.04	-0.07	+0.01	-0.04	+0.03
I_g	+0.19	+0.65	+1.00	+0.70	+0.01	+0.00	+0.00	+0.01	-0.01
τ_g	+0.04	+0.43	+0.70	+1.00	-0.18	-0.33	+0.03	-0.18	+0.16
I_{d_1}	-0.00	-0.04	+0.01	-0.18	+1.00	+0.93	+0.32	+0.95	-0.89
τ_{d_1}	-0.00	-0.07	+0.00	-0.33	+0.93	+1.00	+0.13	+0.85	-0.77
I_{d_2}	+0.00	+0.01	+0.00	+0.03	+0.32	+0.13	+1.00	+0.57	-0.70
τ_{d_2}	-0.00	-0.04	+0.01	-0.18	+0.95	+0.85	+0.57	+1.00	-0.98
I_{d_3}	+0.00	+0.03	-0.01	+0.16	-0.89	-0.77	-0.70	-0.98	+1.00

Table D.24: Parameter correlation of PIA$_2$ decay fit of OLGMR.

	I_{IRF}	$t_{0,IRF}$	I_g	τ_g	I_{d_1}	τ_{d_1}	I_{d_2}	τ_{d_2}	I_{d_3}
I_{IRF}	+1.00	+0.74	-0.48	-0.45	+0.06	+0.10	-0.03	+0.06	-0.05
$t_{0,IRF}$	+0.74	+1.00	-0.32	-0.30	+0.04	+0.06	-0.02	+0.04	-0.03
I_g	-0.48	-0.32	+1.00	+0.18	+0.25	+0.33	-0.11	+0.23	-0.20
τ_g	-0.45	-0.30	+0.18	+1.00	-0.27	-0.40	+0.14	-0.26	+0.23
I_{d_1}	+0.06	+0.04	+0.25	-0.27	+1.00	+0.96	+0.09	+0.97	-0.93
τ_{d_1}	+0.10	+0.06	+0.33	-0.40	+0.96	+1.00	-0.08	+0.90	-0.84
I_{d_2}	-0.03	-0.02	-0.11	+0.14	+0.09	-0.08	+1.00	+0.31	-0.44
τ_{d_2}	+0.06	+0.04	+0.23	-0.26	+0.97	+0.90	+0.31	+1.00	-0.99
I_{d_3}	-0.05	-0.03	-0.20	+0.23	-0.93	-0.84	-0.44	-0.99	+1.00

Table D.25: Parameter correlation of PIA$_1$ decay fit of PLYMR.

	I_{IRF}	$t_{0,IRF}$	I_g	τ_g	I_{d_1}	τ_{d_1}	I_{d_2}	τ_{d_2}	I_{d_3}
I_{IRF}	+1.00	+0.89	-0.69	-0.57	+0.01	+0.13	-0.01	+0.05	-0.04
$t_{0,IRF}$	+0.89	+1.00	-0.51	-0.41	+0.01	+0.09	-0.01	+0.04	-0.03
I_g	-0.69	-0.51	+1.00	+0.59	+0.06	+0.09	-0.01	+0.05	-0.04
τ_g	-0.57	-0.41	+0.59	+1.00	-0.06	-0.41	+0.04	-0.18	+0.14
I_{d_1}	+0.01	+0.01	+0.06	-0.06	+1.00	+0.77	+0.22	+0.89	-0.79
τ_{d_1}	+0.13	+0.09	+0.09	-0.41	+0.77	+1.00	+0.02	+0.74	-0.62
I_{d_2}	-0.01	-0.01	-0.01	+0.04	+0.22	+0.02	+1.00	+0.57	-0.75
τ_{d_2}	+0.05	+0.04	+0.05	-0.18	+0.89	+0.74	+0.57	+1.00	-0.97
I_{d_3}	-0.04	-0.03	-0.04	+0.14	-0.79	-0.62	-0.75	-0.97	+1.00

Table D.26: Parameter correlation of SE decay fit of BDODC.

	I_{IRF}	$t_{0,IRF}$	I_g	τ_g	I_{d_1}	τ_{d_1}	I_{d_3}
I_{IRF}	+1.00	-0.50	-0.09	+0.16	-0.07	-0.05	-0.01
$t_{0,IRF}$	-0.50	+1.00	-0.45	+0.33	-0.12	-0.09	-0.02
I_g	-0.09	-0.45	+1.00	-0.23	-0.33	-0.33	-0.12
τ_g	+0.16	+0.33	-0.23	+1.00	-0.67	-0.49	-0.14
I_{d_1}	-0.07	-0.12	-0.33	-0.67	+1.00	+0.51	-0.22
τ_{d_1}	-0.05	-0.09	-0.33	-0.49	+0.51	+1.00	+0.56
I_{d_3}	-0.01	-0.02	-0.12	-0.14	-0.22	+0.56	+1.00

Table D.27: Parameter correlation of SE decay fit of HTRMR.

	I_{IRF}	$t_{0,IRF}$	I_g	τ_g	I_{d_1}	τ_{d_1}	I_{d_2}	τ_{d_2}	I_{d_3}
I_{IRF}	+1.00	-0.81	+0.36	-0.13	+0.00	+0.02	+0.01	+0.01	+0.00
$t_{0,IRF}$	-0.81	+1.00	-0.78	+0.52	-0.05	-0.13	-0.06	-0.04	-0.03
I_g	+0.36	-0.78	+1.00	-0.77	+0.07	+0.09	+0.04	+0.03	+0.01
τ_g	-0.13	+0.52	-0.77	+1.00	-0.14	-0.44	-0.22	-0.16	-0.09
I_{d_1}	+0.00	-0.05	+0.07	-0.14	+1.00	-0.52	-0.64	-0.78	-0.53
τ_{d_1}	+0.02	-0.13	+0.09	-0.44	-0.52	+1.00	+0.73	+0.65	+0.40
I_{d_2}	+0.01	-0.06	+0.04	-0.22	-0.64	+0.73	+1.00	+0.40	-0.07
τ_{d_2}	+0.01	-0.04	+0.03	-0.16	-0.78	+0.65	+0.40	+1.00	+0.84
I_{d_3}	+0.00	-0.03	+0.01	-0.09	-0.53	+0.40	-0.07	+0.84	+1.00

Table D.28: Parameter correlation of SE decay fit of OLGMR.

	I_{IRF}	$t_{0,IRF}$	I_g	τ_g	I_{d_1}	τ_{d_1}	I_{d_2}	τ_{d_2}	I_{d_3}
I_{IRF}	+1.00	+0.45	-0.81	+0.75	-0.03	-0.19	-0.10	-0.07	-0.03
$t_{0,IRF}$	+0.45	+1.00	-0.80	+0.60	-0.02	-0.13	-0.07	-0.05	-0.02
I_g	-0.81	-0.80	+1.00	-0.87	+0.04	+0.16	+0.08	+0.06	+0.03
τ_g	+0.75	+0.60	-0.87	+1.00	-0.04	-0.39	-0.22	-0.15	-0.07
I_{d_1}	-0.03	-0.02	+0.04	-0.04	+1.00	-0.65	-0.82	-0.83	-0.50
τ_{d_1}	-0.19	-0.13	+0.16	-0.39	-0.65	+1.00	+0.83	+0.67	+0.36
I_{d_2}	-0.10	-0.07	+0.08	-0.22	-0.82	+0.83	+1.00	+0.63	+0.10
τ_{d_2}	-0.07	-0.05	+0.06	-0.15	-0.83	+0.67	+0.63	+1.00	+0.78
I_{d_3}	-0.03	-0.02	+0.03	-0.07	-0.50	+0.36	+0.10	+0.78	+1.00

Table D.29: Parameter correlation of SE decay fit of PLYMR.

	I_{IRF}	$t_{0,IRF}$	I_g	τ_g	I_{d_1}	τ_{d_1}	I_{d_2}	τ_{d_2}	I_{d_3}
I_{IRF}	+1.00	+0.15	-0.61	+0.62	-0.12	-0.19	-0.08	-0.06	-0.03
$t_{0,IRF}$	+0.15	+1.00	-0.80	+0.59	-0.08	-0.15	-0.06	-0.05	-0.02
I_g	-0.61	-0.80	+1.00	-0.84	+0.12	+0.16	+0.07	+0.05	+0.02
τ_g	+0.62	+0.59	-0.84	+1.00	-0.24	-0.44	-0.20	-0.15	-0.08
I_{d_1}	-0.12	-0.08	+0.12	-0.24	+1.00	-0.35	-0.59	-0.69	-0.42
τ_{d_1}	-0.19	-0.15	+0.16	-0.44	-0.35	+1.00	+0.71	+0.61	+0.33
I_{d_2}	-0.08	-0.06	+0.07	-0.20	-0.59	+0.71	+1.00	+0.40	-0.13
τ_{d_2}	-0.06	-0.05	+0.05	-0.15	-0.69	+0.61	+0.40	+1.00	+0.80
I_{d_3}	-0.03	-0.02	+0.02	-0.08	-0.42	+0.33	-0.13	+0.80	+1.00

D.4 SPECTROSCOPY DATA FROM THE PERVOSKITE NANOSTRUCTURE PROJECT

femtosecond transient absorption pump–probe (fsTAPP) spectroscopy was employed to study Methylammonium lead bromide pervoskite nanostructures. This project was a follow–up to our previously reported study on similar nanostructures. [223] The two studied samples were nanocubes and nanoplateletes. The nanocubes had an edge length of $\sim 12\,\mathrm{nm}$. The nanoplatelets had dimensions of $\sim 55\,\mathrm{nm} \times 8\,\mathrm{nm} \times 2\,\mathrm{nm}$.

Raw data are shown in Figure D.4 to Figure D.7. Analysis of the fluence dependent measurements are depicted in Figure D.3. Analysis of the spectroscopy data showed these nanostructures behave similarly to those previously reported. The reader is referred to our previous report [223] for further details on the analysis and the mathematical models used.
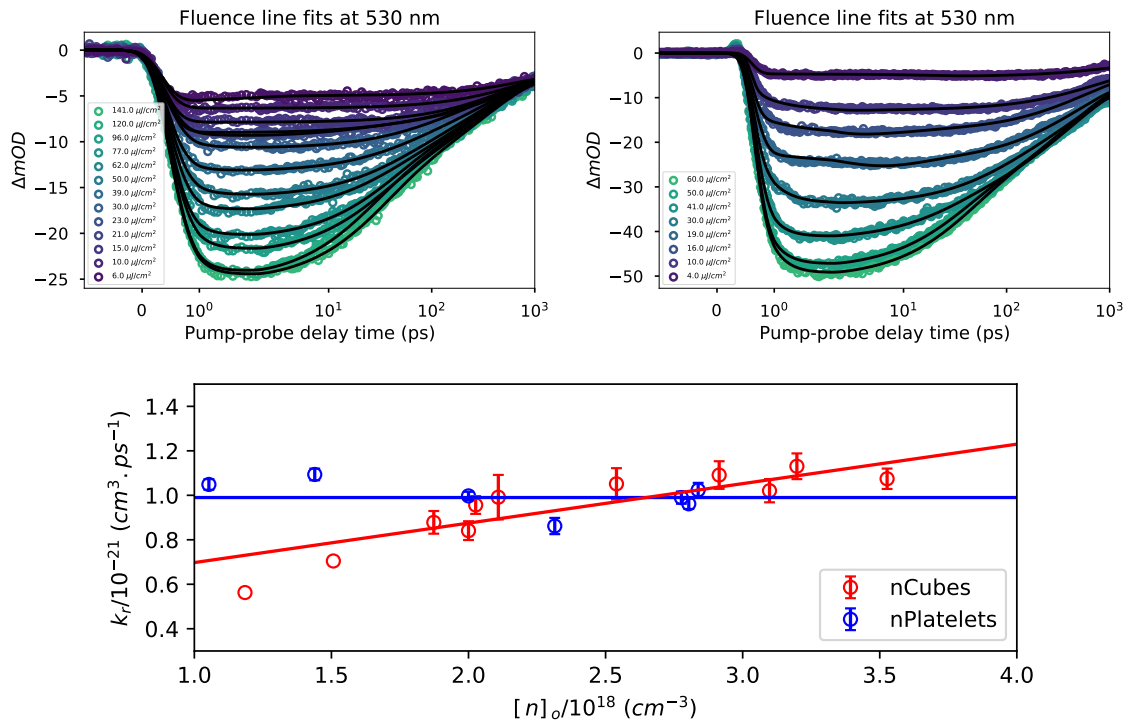
Figure D.3: Analysis of fluence–dependent fsTAPP spectra, excitation at 388 nm, of MaPbBr3 nanocubes (left) and nanoplatelets (right). (bottom) Effective charge carrier recombination rate constants (k_r) of the studied nanostructures.
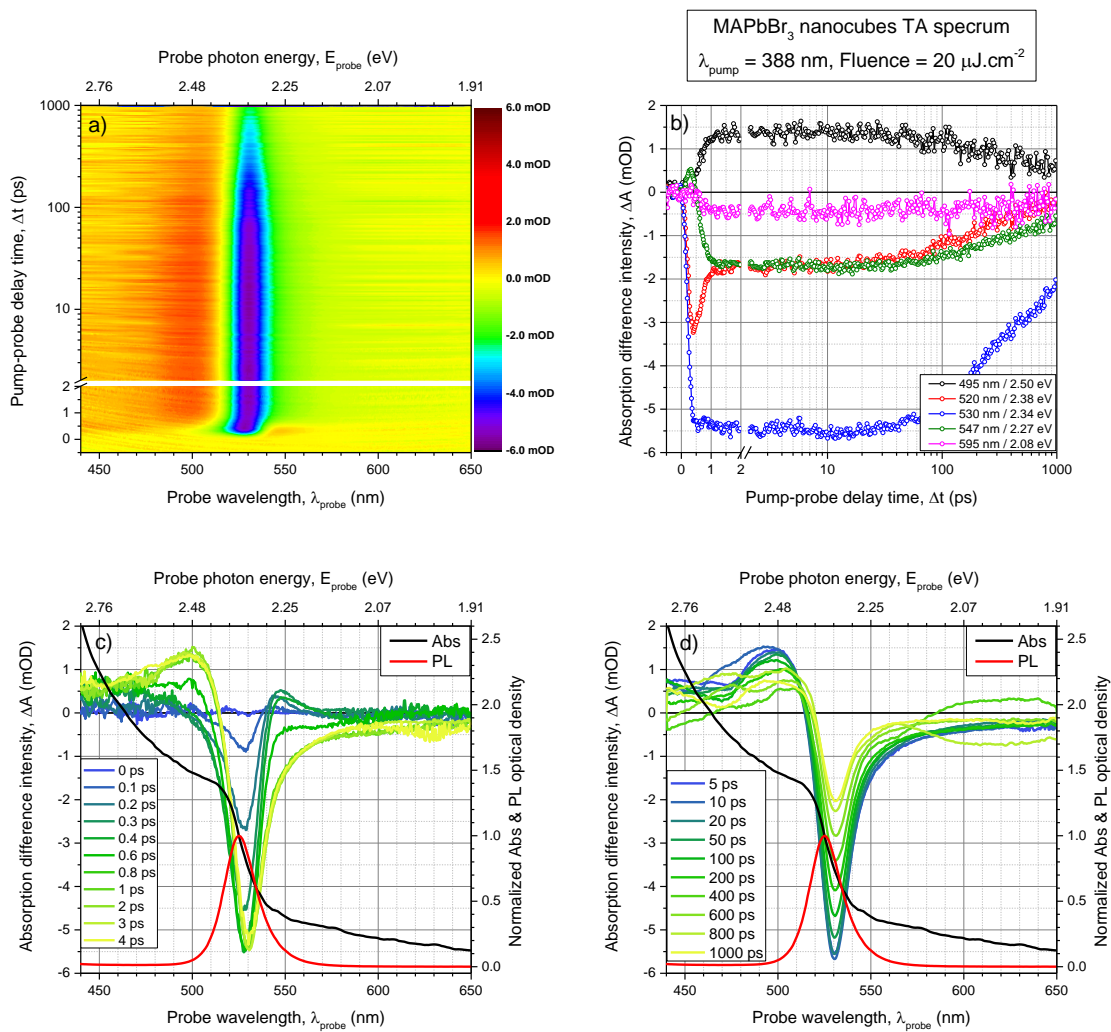
Figure D.4: fsTAPP of Methylammonium lead bromide nanocubes. Excitation at 388 nm, solvent is Toluene.
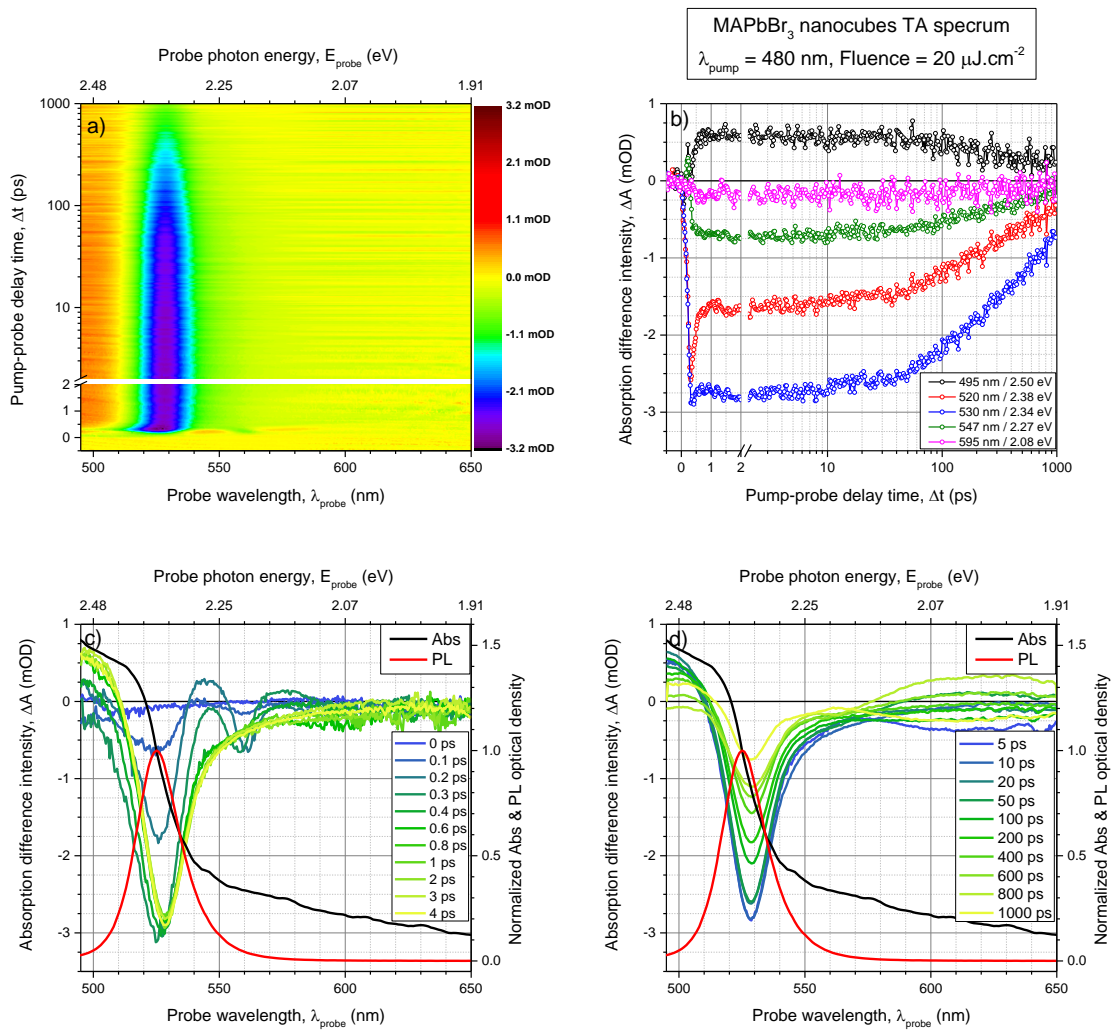
Figure D.5: fsTAPP of Methylammonium lead bromide nanocubes. Excitation at 480 nm, solvent is Toluene.
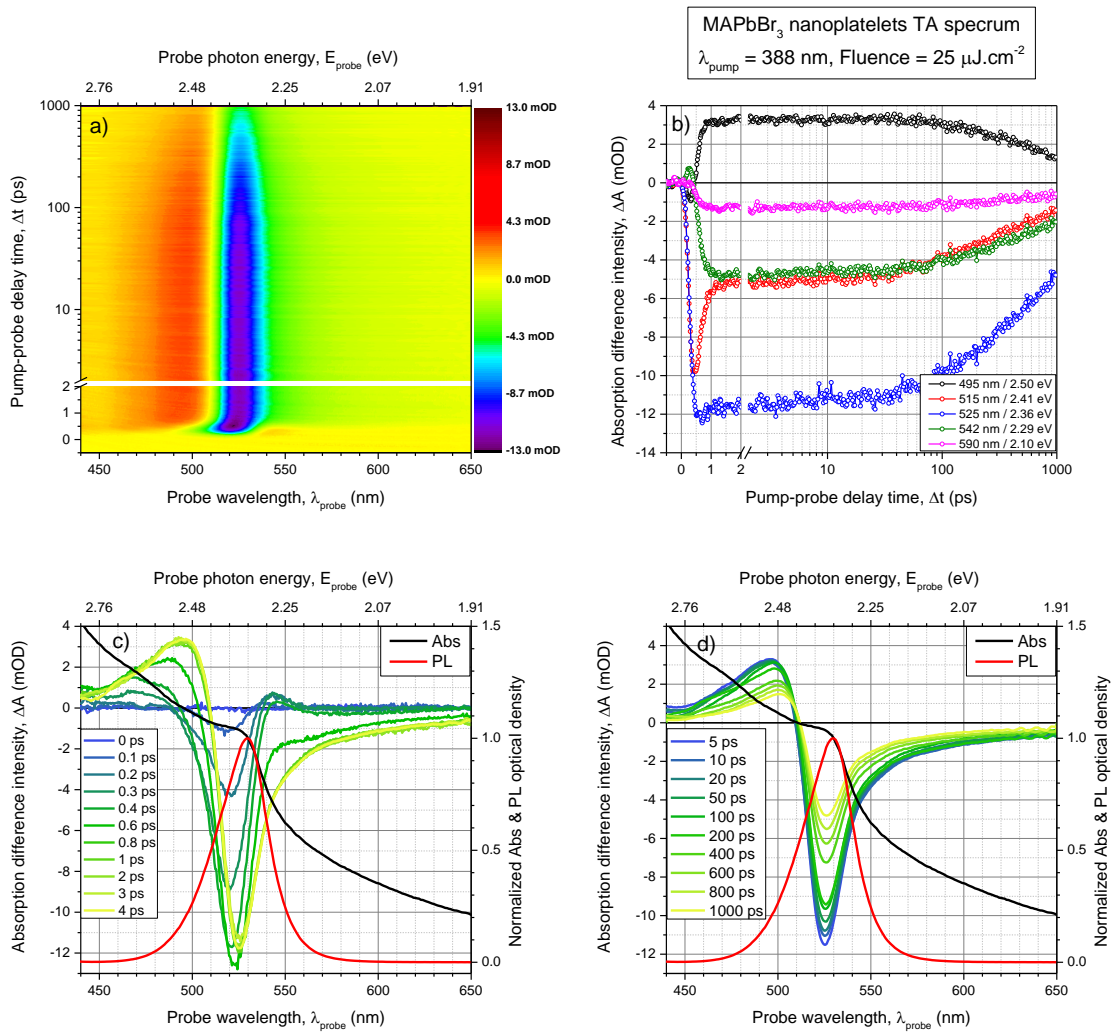
Figure D.6: fsTAPP of Methylammonium lead bromide nanocubes. Excitation at 388 nm, solvent is Toluene.
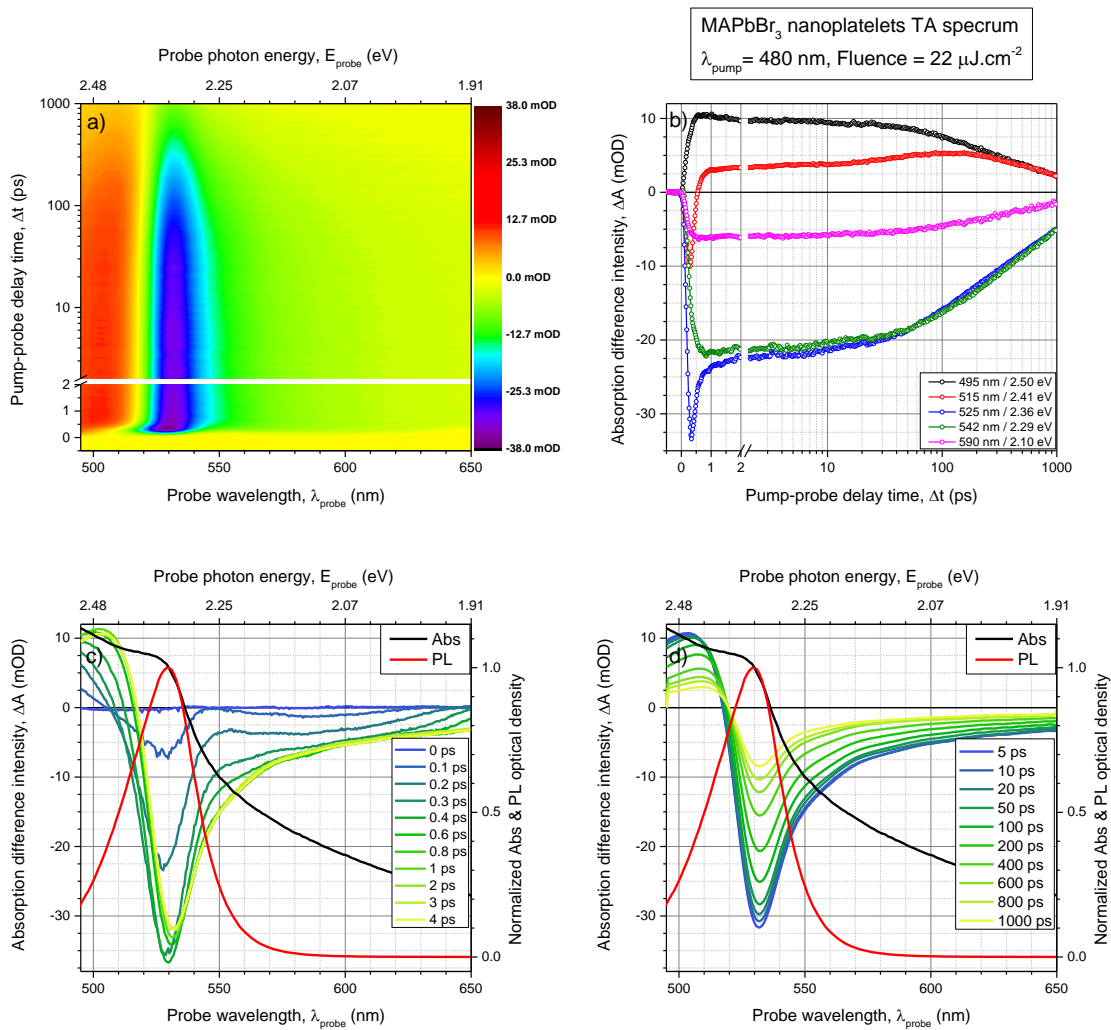
Figure D.7: fsTAPP of Methylammonium lead bromide nanocubes. Excitation at 480 nm, solvent is Toluene.

APPENDIX E

OPERATIONAL PROCEDURES OF THE TAPPS APPARATUS

E.1 OPERATION OF THE FEMTOSECOND CHIRPED PULSE REGENERATIVE AMPLIFIER

The daily operational procedures of the femtosecond chirped pulse regenerative amplifier (CPA) are listed below. Please refer to the CPA user manual for more directions and controller screenshots [104].

E.1.1 POWER ON

1. Ensure the water levels in the ORC water tank (below the Controller, DT-506), and the "Lyton" chiller are with the expected tolerance. If the levels are not satisfactory, refill as needed with deionized water.

2. If you are not logged–in, tab on "Power Login" under the "Master" tab on the DT-506 laser controller and enter "1 2 3 4" to access the advanced controls.

3. Switch the Lyton chiller on pressing the power button ⏻ on the front panel. Wait for few minutes until the temperature stabilizes to the set temperature. The set temperature is currently fixed to 17 °C.

4. Switch the laser on by taping the "System Start" under "System Controls" in the "Master" tab. "System Status" indicator in the "Master" tab should read "Start up". And all the other system indicator should be green. The system will take

$\sim$30 min to warm up.

5. Once warmed up, go to the "Pump Laser" tab and tap the numbered button to the left of "Pump power". In the pop–up dialog box enter the desired pump power, currently set at 6.25 W. Tap "OK" the power should start climbing. Additionally, the "Lamp Current" should change accordingly. Please note, the lamp current should always be under 30 A.

6. Finally, tap "Open Output" in the "Shutter Controls" section to allow the laser beam to exit the CPA.

E.1.2   POWER OFF

1. Tap "Pump Power" in "Pump Laser" tab and adjust the value to 5 W and hit "OK". Wait for the "Lamp Current" to stabilize. The stabilization value will depend on the age of the flashlamp installed.

2. Go to "Master" tab and tap "Stop System".

3. Wait for the button to turn blue, then turn off the Lyton chiller by pressing the power button ⏻ on the front panel.

E.1.3   FINE–TUNING

Occasionally, the CPA requires fine–tuning to improve its performance. This fine–tuning consists of improving the amplification efficiency, as well as improving the compression efficiency. The optical components in this procedure refer to Figure 2.5 on page 28. Please note that the components mentioned here are accessible through designated doors in the top cover of the CPA housing. The following steps may be taken to fine–tune the CPA.

1. Place the power meter sensor between m_{24} and m_{25}.

2. Adjust m_6 horizontally and vertically while observing the powermeter reading, and the pulse train on the oscilloscope.

3. Adjust m_7 horizontally and vertically while observing the powermeter reading, and the pulse train on the oscilloscope.

4. Repeat steps 2 and 3 until the maximum power output is achieved.

5. Place the powermeter sensor after m_{36}. The next steps should be performed while observing the powermeter reading of the 387.5 nm beam.

6. Optimize the Pockel cell timing by adjusting the first digit from the right in "Delay 1" and "Delay 2". Delay 1 and 2 can be found under the "Timing Unit" tab on the DT-506 controller.

7. Optimize the positioning of the compressor's back mirrors (m_{19} and m_{20}) by adjusting the "Pulse Width". The Pulse Width can be found under the "Amplifier" tab. When tapped, a pop–up dialog box is initiated. Use the small increment adjuster (the left one). Simply set the increment to 5 and hit the up and arrow keys for adjustments. Then set the increment to 1 and repeat.

8. Repeat steps 6 and 7 until the highest power is achieved.

Finally, The DT-506 controller may occasionally require a hard restart to keep the controlling software and the OS under the hood lag and hang–free. For a hard restart, toggle the power switch located on the lower–left corner of the back of the controller, off then on. This will reboot the controller, as well as restart the seed laser oscillator. When this is needed, one needs to wait 12–24 h for the seed laser to stabilize, and achieve optimal operation.

E.2 NON–COLLINEAR OPTICAL PARAMETRIC AMPLIFIER OPERATION AND WAVELENGTH TUNING

Both non–collinear optical parametric amplifiers (NOPAs) operations, and wavelength tuning is fairly similar. Therefore, NOPA–Vis will be discussed in this section, in conjunction with brief comments on NOPA–IR operations when needed. All optic notations in this section refer to NOPA–Vis box presented in Figure 2.5 on page 28. We start by placing the fiber end of a portable spectrometer (USB2000, Ocean optics) between m_{61} and p_4 and observe the spectra. A diffusing element, like lens tissue or glass diffuser (DG10-600, Thorlabs), is placed between the fiber and m_{59} to allow for even intensity distribution. When both amplification stages are near optimal operation, a business card may be placed between m_{61} and the diffusing element to avoid the spectrometer saturation. The spectrometer aids in maintaining a signal and observing the signal strength during the fine–tuning and wavelength tuning processes. In NOPA–IR, since the signal wavelength is outside the spectrometer detection range, the fiber end is placed higher than m_{43} or m_{45} and behind it, to detect the idler's wavelength. The signal wavelength can be calculated using the relation $\frac{1}{\lambda_{pump}} = \frac{1}{\lambda_{signal}} + \frac{1}{\lambda_{idler}}$, where λ_{pump} is 387.5 nm, λ_{idler} is the wavelength detected on the spectrometer, and λ_{signal} is the wavelength of NOPA–IR output.

E.2.1 FINE–TUNING

In no particular order, these adjustments may improve upon the power and wavelength of the final output of NOPA–Vis. For the first amplification stage, block the second stage pump by placing a beam blocker between bs_{11} and m_{54}.

- Adjust the angle of the β–Barium borate $(BBO)_d$, to fine–tune the efficiency of the second harmonic generation (SHG).

- Adjust the lever to vary the opening of i_2. This will improve the intensity and

233

stability of the output. However, this may cause the wavelength center on the spectrometer to shift.

- Adjust the position of the manual translation stage on which bs_{11} is mounted. This operation adjusts the temporal overlap between the supercontinuum (seed) and the SHG (pump). This adjustment is very sensitive. The typical temporal pulse width is $\sim$150 fs, making the range of operations $<$300 fs, which translates to $<$90 µm, You may lose the signal entirely, and may cause the wavelength center on the spectrometer to shift. Just carry the adjustment with care, and track back what you did when something goes wrong.

- Adjust the horizontal and vertical knobs of bs_{11} and m_{53}.

- Adjust the manual translation stage on which BBO_m is mounted, as well as the crystal angle.

For the second amplification stage, remove the beam blocker between bs_{11} and m_{54}, and place a business card in front of the diffusing element to prevent spectrometer saturation.

- Adjust the position of the manual translation stage on which m_{56} is mounted. This is also sensitive, carry it out with care.

- Adjust the horizontal and vertical knobs of m_{56} and m_{57}.

- Adjust the manual translation stage on which BBO_m is mounted, and its angle.

E.2.2   WAVELENGTH TUNING

Wavelength tuning procedures of the NOPAs largely uses the same optical components used in fine–tuning it. However, it is more methodological, and relies heavily on the pump mirrors preceding the mixing crystals. The list below highlights the major steps required to tune NOPA–VIS. Tuning of NOPA–IR largely follows

the same steps, however the beam needs to be observed using an IR viewer, or an IR special card. Also, please note that this process is not straight forward, it requires patience, and sometimes repeating the listed steps multiple times to achieve the desired output.

1. Block the second stage pump by placing a beam blocker between bs_{11} and m_{54}.

2. Place the spectrometer's fiber end between m_{59} and m_{60}. Adjust the fiber positions, the diffusing element, and the spectrometer integration time so that there is no detector saturation.

3. Place a ruler $\sim100\,mm$ in front of the first stage mixing crystal and measure the beam separation. Then place a ruler $\sim100\,mm$ behind the first stage mixing crystal and do the same.

4. Refer to Table 2.2 on page 33 and assess the current separation from the ideal value listed in the table. Please note that a more expansive table is listed in Clark–MXR's NOPA manual [106].

5. Walk the pump beam vertically to match that of the number listed in the table associated with the desired wavelength. Please keep your eye on the signal on the spectrometer to avoid losing it while walking the beam. This acts as a fail–safe to aid you in maintaining a working NOPA while attempting the tuning procedure. During the beam walking procedure, you may need to perform some fine–tuning on the pump and the first stage components when needed to maintain a sufficient signal. Walking the beam can be achieved by following the steps listed below:

   (a) place the ruler at $\sim100\,mm$ in front of the crystal and use the vertical knob of bs_{11} so that the separation between beam spots on the ruler matches the number listed in the table.

(b) place the ruler at ~100 mm behind the crystal and use the vertical knob of m_{53} so that the separation between beam spots on the ruler matches the number listed in the table.

(c) Repeat the first two steps until the beam spots separation at the front and back positions match, and match the value listed in the table.

6. Fine–tune the pump and the first stage to achieve the highest intensity possible at the desired wavelength.

7. Remove the beam blocker between bs_{11} and m_{54}.

8. Place the spectrometer's fiber end between m_{61} and p_4. Adjust the fiber positions, the diffusing element, and the spectrometer integration time to eliminate detector saturation. You may see two peaks on the spectrometer; one from the newly tuned first stage, and one from the second stage. Additionally, at this point you probably will not need a business card to shield the spectrometer just yet.

9. Place a ruler ~100 mm in front of the second stage mixing crystal and measure the beam separation. Then place a ruler ~100 mm behind the second stage mixing crystal and do the same.

10. Walk the pump beam vertically to match that of the number listed in the table associated with the desired wavelength. Remember to fine–tune the second stage as you walk the beam. Additionally, detector saturation may occur while walking the beam. At this point you will need a business card placed in front of the diffusing element to prevent detector saturation. Walking the beam can be achieved by following the steps listed below:

(a) place the ruler at ~100 mm in front of the crystal and use the vertical knob of m_{56} so that the separation between beam spots on the ruler matches the number listed in the table.

(b) place the ruler at $\sim$100 mm behind the crystal and use the vertical knob of m_{57} so that the separation between beam spots on the ruler matches the number listed in the table.

(c) Repeat the first two steps until the beam spots separation at the front and back positions match, and match the value listed in the table.

11. Fine–tune the pump and the first and second stages to achieve the highest intensity possible at the desired wavelength.

12. Place a powermeter sensor between m_{67} and m_{68} and fine–tune the pump's crystal, the compressor prism p_4, to achieve the highest output possible.

In cases where the SHG of NOPA–Vis is required, the doubling crystal "BBO$_d$" needs to be placed into its mount and the crystal angle needs to be adjusted. Additionally, p_6 angle and m_{72} will need to be aligned to allow for the SHG to exit the box in the place of the visible beam of NOPA–Vis.

E.3 PREPARATION PROCEDURE OF THE FEMTOSECOND TRANSIENT ABSORPTION PUMP–PROBE EXPERIMENT

The complex and sensitive nature of the femtosecond transient absorption pump–probe (fsTAPP) experimental conditions call for the carrying out of an equally elaborate procedure. Devised and refined during the years spent carrying out various fsTAPP experiments using this system, this procedure primarily ensures data reliability and reproducibility. The influence of potential artifacts on the data quality is also minimized. As such, the latest version is segmented and presented below for future reference, and to allow for easier experiment reproduction. Segmentation will focus on the pump alignment, the probe optimization, and the special and temporal pump–probe overlap. Please note that this procedure focuses on the broadband detection,

rather than the single–wavelength detection. Also, all optical components mentioned in the procedures below refer to Figure 2.6a on page 35 unless indicated otherwise.

E.3.1   PUMP ALIGNMENT

To avoid any spacial shift of the pump during the scanning process, the beam needs to be perfectly parallel with the linear actuator range of motion. Irises i_1 and i_2 provide anchor points to align the pump beam in such a way. Alignment is generally carried out using two mirrors in conjunction with these two irises. Mirrors m_{35} and m_{36} are used for the 387.5 nm pump alignment and mirrors m_{72} and m_{74} are used for NOPA–Vis and its SHG. Refer to Figure 2.5 on page 28 for mirror locations of NOPA–Vis in the setup.

1. Move the linear actuator to the middle of the scanning range (typical 800 000 fs) via the "Target Time Delay (fs)" in the "Scan Data" tab in the "Spectra Based Scan.vi"

2. Check the alignment on i_1 and re–align using mirror m_{35}/m_{72} if necessary.

3. Check the alignment on i_2 and re–align using mirror m_{36}/m_{74} if necessary.

4. Repeat steps 2 and 3 until the beam is perfectly centered on both irises.

E.3.2   BROADBAND PROBE OPTIMIZATION

The quality of the supercontinuum intensity and stability is essential to increase the signal–to–noise ratio during the broadband probe detection. Additionally, affirming the wavelength calibration on the spectrograph improves the data quality in a way that helps avoid misleading signal locations and labeling. Please note that these steps are not needed when performing a single–wavelength scan. The following steps can be taken to improve the quality and calibration of the broadband supercontinuum probe.

1. Place a cuvette filled with solvent in the sample holder. Ensure that the supercontinuum beam is passing through cuvette without any obstruction. If necessary, move the x– and y–axes of the sample holder so that the beam is passing through the cuvette unobstructed.

2. Navigate to the supercontinuum acquisition parameters and set the value of "Pairs of Laser Shots" to 50. The parameters can be found in "Spectra Based Scan.vi" under "Detector Controls" in the "Basic Parameters" tab.

3. Navigate to the supercontinuum spectral graphs in the LabView acquisition software, and click "START". The graphs can be found in "Spectra Based Scan.vi" under "Detector Controls" in the "White Light Noise" tab.

4. In no particular order, and while observing the noise and spectra live graphs, fine–tune the following optical components:

   (a) The variable neutral density filter fw_1.

   (b) The entrance, beam shrinking iris i_3.

   (c) The variable neutral density filter fw_2.

   (d) The filtering irises i_5 and i_6.

   (e) Vertical and horizontal knobs of mirrors m_{16} and m_{17}.

5. If the supercontinuum quality is not satisfactory, adjust the positioning of the stage on which lens l_1 is mounted.

6. To accommodate for the focal point change resulting from the previous step, adjust the stage on which mirror m_{16} is mounted.

7. Repeat steps 4, 5 and 6 until the intensity and noise are within the proper levels. Namely, maximum intensity <65000 counts, noise <0.04 for the regions of interest.

8. Mount the 533 nm notch filter on the inside of the spectrograph box, after i_6.

9. Use the horizontal knob on m_{17} to shift the spectrum horizontally so that the dip matches 533 nm on the scale.

10. Remove the notch filter and the solvent cuvette from the sample mount and click "STOP" in the "White Light Noise" window to terminate the acquisition sequence.

Please note that adjustments of iris i_3 and lens l_1 stage may allow the user to increase the intensity toward the lower wavelength range when needed. Additionally, due to the nature of supercontinuum generation and detection, the noise levels in regions below 450 nm and 700–825 nm are higher than the rest of the spectrum. Therefore, even with a well–optimized supercontinuum, their levels may never drop below 0.04.

E.3.3 SPACIAL PUMP–PROBE OVERLAP AND ALIGNMENT QUALITY CONFIRMATION

In preparation for the fsTAPP experiment, the user must ensure that pump and probe beams are intersecting in the sample; whether the sample is a thin film, or a solution in a cuvette. Additionally, during this procedure, it is possible to estimate the pump and probe beam sizes within the range of intersection. The known sizes are required to calculate the pump's fluence and fluence rate.

The previous pump alignment through irises i_1 and i_2 is generally an adequate starting point, however, because the alignment depends on the visual inspection of the user, it is usually not accurate enough to eliminate artificial decay in the temporal axis of fsTAPP data. Also, a small special shift in the pump–probe overlap can easily induce such decays. Therefore, a confirmation procedure was introduced and integrated into the spacial overlap procedure to assess the linear actuator alignment

quality and perform any required corrections to the pump alignment through the actuator. To construct a robust, and reliable pump–probe spacial overlap, and collect the data necessary to confirm the pump alignment quality, the following steps should be followed.

1. Mount the overlap photodiode detector PD_{ol} right after the sample holder, as depicted in Figure 2.6 on page 35. Adjust the detector positioning so that it detects the maximum probe intensity while still detecting a pump intensity. This configuration can be confirmed by alternatively blocking the pump and probe beams and assessing the intensity of the other beam.

2. Adjust the pump intensity to match that of the probe. Use the neutral density filter wheel fw_1 depicted in Figure 2.5 on page 28.

3. Block the probe beam anywhere after the "Al_2O_3" crystal. Move the linear actuator at the start then end of the scanning range (typical 0 and 1 600 000 fs, respectively) via the "Target Time Delay (fs)" in the "Scan Data" tab in the "Spectra Based Scan.vi"

4. Read and record the pump intensity. These readings will constitute the $I_{start,0}$ and $I_{end,0}$ values, respectively.

5. Move the linear actuator to the middle of the scanning range (typical 800 000 fs).

6. Read and record the pump and probe intensities. Carry out the reading by alternatively blocking the pump and probe, and reading the passing beam. These readings will constitute $I_{0,pump}$ and $I_{0,probe}$ values, respectively.

7. Mount a precision pinhole onto the sample holder. The pinhole that was used in the experiments presented in this work had a 100 µm diameter (P100D, Thorlabs). The pinhole was mounted in a lens mount (LMR1, Thorlabs) that emulates the approximate location of where the sample would be placed.

8. Block the pump beam anywhere before the sample holder with a business card or a beam blocker.

9. Position the sample holder using the x– and y–axes directions until maximum probe transmission is achieved.

10. Move the sample holder in the z–axis while optimizing the x– and y–axes until maximum probe transmission is achieved. Once optimized, record the probe intensity through the pinhole. This reading will constitute the I_{probe} value.

11. Block the probe beam anywhere after the "Al_2O_3" window. Then unblock the pump beam.

12. Use mirror m_5 to align the pump beam onto the pinhole. And fine–tune the alignment so that maximum transmission is achieved. Once optimized, record the pump intensity through the pinhole. This reading will constitute the I_{pump} value.

13. Similar to Step 3, Block the probe beam anywhere after the "Al_2O_3" crystal. Move the linear actuator at the start then end of the scanning range.

14. Read and record the pump intensity. These readings will constitute the I_{start} and I_{end} values, respectively.

15. Remove the pinhole from the sample mount.

16. Confirm the intensity reading of the full pump and probe after the pinhole removal. Namely, $I_{0,pump}$, $I_{0,probe}$, $I_{0,pump}$, and $I_{0,probe}$. Update the previously recorded values if necessary.

17. Read and record the micrometer knobs for the x–, y–, and z–axes on the sample holder for reference.

Please note that it is possible to construct an inaccurate overlap quickly if the need arises. Simply use a visual assessment of the beam transmission through the pinhole on a business card. Similar to the robust overlap procedure, use the sample holder to align the probe beam through the pinhole, and m_5 to align the pump beam through the pinhole. It is also worth noting that the calculations related to this procedure were carried out using a home–built spreadsheet designed for this purpose. A depiction of this spreadsheet can be found in Figure Figure E.1, and an interactive version of it can be loaded through this link.

E.3.4   TEMPORAL PUMP–PROBE OVERLAP

The final step in the fsTAPP experimental perpetration is locating and optimizing the temporal pump–probe overlap. This is generally done through trial–and–error using a reference sample, like a dye solution. Typically, a dichloromethane solution of Coumarin 120 (7-Amino-4-methyl-2H-chromen-2-one) is used for the 387.5 nm pump, and an ethanol solution of DCM dye (4-(Dicyanomethylene)-2-methyl-6-(4-dimethylaminostyryl)-4H-pyran) is used for the NOPA pump. Follow the steps listed below to locate and optimize the temporal overlap:

1. Place a cuvette filled with the appropriate reference dye solution in the sample holder. Ensure that both probe and pump beams pass through the cuvette without obstruction.

2. Increase the pump intensity to the maximum by rotating fw_1 shown in Figure 2.5 on page 28

3. Start the chopper by pressing on the dial knob located on chopper controller. Wait for the frequency to stabilize.

4. On the LabView software "Spectra Based Scan.vi", go to "Stage controls" and read the "Lower Limit Time Delay (fs)" and "Upper Limit Time Delay (fs)".

Overlap parameters

Quantity	Symbol	Pump		Probe	
Pinhole trasmission ratio	I (mV)	0.58	ratio	3.8	ratio
	I_o (mV)	6.16	0.094156	6.68	0.568862
pinhole Diameter	D	100	µm	100	µm
spot radius	ω	0.022486	cm	0.007709	cm
spot area	Area	0.001588	cm²	0.000187	cm²

Stage & sample quality

	I_o	I
I_{end} (mV)	6.2	0.424
I_{start} (mV)	6.36	0.524
%change	17.00%	

	x	y	z
	11.02	18.07	10.83
actual-z	11.44		

Pump parameters

Pump wavelength	λ_{pump}	388	nm
Average power	P_{ave}		µW
Photodiode voltage	$PD_{Voltage}$	3.58	V
Photodiode Power	PD_{P_ave}	456.2551	µW
Peak energy	E_p	0.456255	µJ
‹Pump Fluence›	$\langle F_o \rangle_{pump}$	511.9351	µJ.cm⁻²
‹Photon Fluence rate›	$\langle E_{p,o} \rangle_{pump}$	1.50E+36	s⁻¹.m⁻²

DET10A measurments Optics

30:70 Beam splitter	UP	
Optics before the Photodiode		
Diffuser1	120G	
Diffuser2	Sel Grid	
ND-Filter1	Sel Type	Sel OD
ND-Filter2	Sel Type	Sel OD
Optics before the sample		
ND-Filter	Sel Type	Sel OD

Scan time calculation

P.o.L.S.	50
G.t.A	10
Scan Pts	681
Passes	5
Time	1:00:15

spot radius reference http://en.wikipedia.org/wiki/Gaussian_beam#Power_through_an_aperture

Effective overlap relative area according to the calculated radii
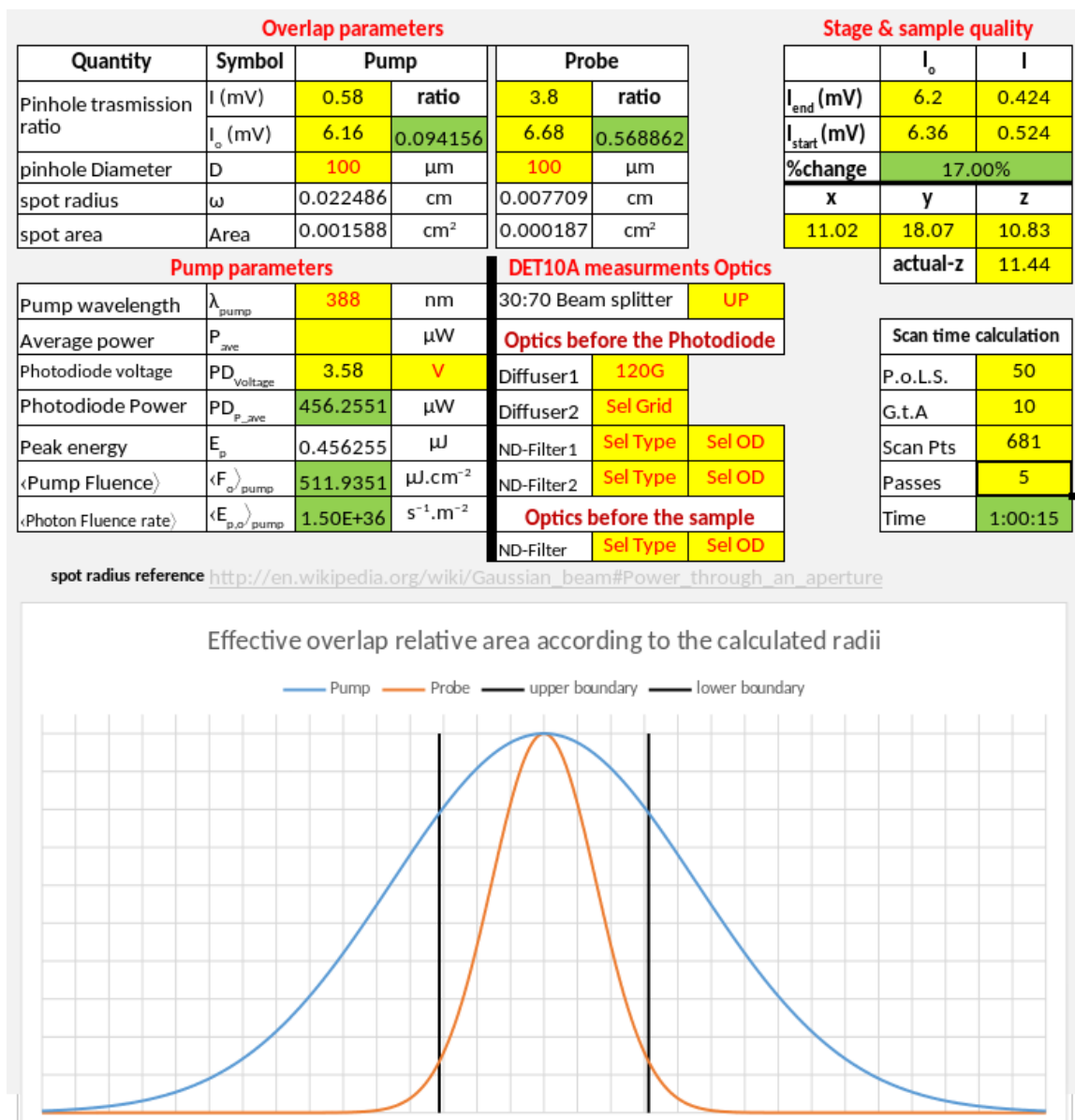
— Pump — Probe — upper boundary — lower boundary

Figure E.1: Screenshot of the Overlap Calculator spreadsheet.

These values indicate the possible range of the scan on the current actuator configuration. Round–down the values to the closest 1000 fs.

5. Under "Scan Range Settings" go to "Single region Linear Scan" and set up the scan parameters. Initially, the lower and upper limits are the values deduced from the previous step, with the number of points set to 100, and step size is set to 0.

6. Set the acquisition averaging by settings "Pairs of Laser Shots" and "Grabs to Average" to 50 and 10, respectively. These parameters can be found under "Basic Parameters" in "Detector Controls"

7. Go to "Scan Data" tab, then click "Scan Data".

8. Once the scan starts, you should see spectra presented in the plot changing as the actuator moves forward. Switch to the temporal data by click on "Time Series Data" tab. The appearance of a temporal signal indicates the optimal pump-probe temporal overlap.

9. When the scan is done, approximate where the signal starts on the time axis, dubbed as "Time Zero". This is generally considered the first value in the rise curve of the signal. Pay more attention to the curve of the shortest wavelength chosen in the time series tab (typically 450 nm).

10. Go to "Scan Range Setting" and set another linear scan with shorter range specified around the signal appearance, then re–scan. For example, if the approximate "Time Zeros" was ∼7500 fs, the scan parameters would be 5000–9000 fs. The previous two steps may have to be repeated multiple times, until an accurate "Time Zero" is located for the signal starting point.

11. Move the actuator to the determined "Time Zero" + 200 fs. This can be done by inputting the value+200 fs into "Target Time Delay (fs)" then clicking "Move". Finally, click the "Set" button besides "Set Current Position to Time Zero". This will update the "Time Zero" value in the software to the one that was located during this procedure.

12. Move the stage to 3000 fs.

13. Go to "Free Running Delta OD" located under "Detector Controls", and click

"OK" under "Start Free Running". Please note that this acquisition sequence do not work unless the chopper is already running.

14. Adjust the z–axis micrometer knob on the sample holder until the maximum signal intensity is achieved. This step allows fine–tuning the sample location with respect to the pump–probe optimal crossing. Typically, $0.5\,\mathrm{mm}$ of adjustment or less is required.

15. Once satisfied with the signal intensity, click "Stop" under "Stop Free Running" and remove the reference sample from the sample.

Once this last procedure is carried out, the system is now ready to acquire data from samples of interest. Please note that some beam optimization can still be done after the overlap configuration has been achieved using only the variable neutral density filter fw_1 depicted in Figure 2.6 on page 35, in addition to any optical component proceeding the sample holder. It is generally advisable to use the same overlap setup to scan samples that will be compared later. Using the same overlap allows for more robust comparison, since the overlap–to–overlap variations and artifacts are not a factor anymore.

CURRICULUM VITAE

Abdelqader M. Jamhawi

Physical chemistry | Ultrafast laser spectroscopy

Phone: (502) 298–4447 | email: a.jamhawi@zoho.com | Linkedin: /in/ajamhawi

Education

PhD/MSc	Department of Chemistry, University of Louisville, KY, USA
	Expected graduation August 2021
	Dissertation: "photophysics of substituted [1,4]benzodioxino[3,2-b]oxanthrene (bdo) chromophores and their macromolecules: A spectroscopy and density functional theory study"
MSc	Department of Chemistry, Yarmouk University, Irbid, Jordan
	August 2010
	Thesis: "The use of fluorescence spectroscopy to identify and classify Jordan's olive oil according to origin"
BSc	Department of Chemistry, Yarmouk University, Irbid, Jordan
	June 2006
	Research project: "Synthesis and characterization of selected silyl enol ethers"

Publications and presentations

- Justin D. Smith*, Abdelqader M. Jamhawi*, Jacek B. Jasinski, Fabrice Gallou, Jin Ge, Rigoberto Advincula, Jinjun Liu, and Sachin Handa; "Organopolymer with Dual Chromophores and Fast Charge–Transfer Properties for Sustainable Photocatalysis" Nature Communications 10, 1837 (2019).
  DOI: 10.1038/s41467-019-09316-5

- Hamzeh Telfah, Abdelqader Jamhawi, Meghan B. Teunis, Rajesh Sardar, and Jinjun Liu; "Ultrafast Exciton Dynamics in Shape–Controlled Methylammonium Lead Bromide Perovskite Nanostructures: Effect of Quantum Confinement on Charge Carrier Recombination"; The Journal of Physical Chemistry C 2017 121 (51), 28556–28565.
  DOI: 10.1021/acs.jpcc.7b10377

- Abdelqader Jamhawi, Anam C. Paul, Justin D. Smith, Sachin Handa, and Jinjun Liu ; "Ultrafast transient absorption spectroscopy of polymer–based organophotoredox catalysts mimicking transition–metal complexes"; Presentation at 72nd International Symposium on Molecular Spectroscopy, Champaign–Urbana, IL. July 2017
  DOI: 10.15278/isms.2017.TG03

- Abdelqader Jamhawi, Hamzeh Telfah, Meghan B. Teunis, Rajesh Sardar, and Jinjun Liu; "Ultrafast transient absorption spectroscopy investigation of excited–state dynamics of methyl ammonium lead bromide perovskite nanostructures"; Presentation at 72nd International Symposium on Molecular Spectroscopy, Champaign–Urbana, IL. July 2017
  DOI: 10.15278/isms.2017.WB06

- Abdelqader Jamhawi, Hamzeh Telfah, Mahendra Sunkara, and Jinjun Liu; "Spectroscopic investigation of charge carrier dynamics in novel solar cell materials"; Poster presented at 3rd biennial renewable energy & energy efficiency workshop (RE[3]), Louisville, KY. March 2015.

---

*Equal contribution

Research

Research interests

My research interests remain in the field of femtosecond laser spectroscopy, with special emphasis on:

- The employment of ubiquitous and cutting–edge spectral techniques in unraveling the fundamental physical properties of chemical systems in impactful applications such as renewable energy, catalysis, biochemistry, and medicine.
- Supplementing spectroscopic investigations with theoretical and quantum chemical studies using first principle, DFT, and molecular dynamics.
- Development and innovation in spectral methods and spectral tools, with emphasis on accuracy, efficiency, and affordability.
- The advancement of time–resolved multi–beam, and microscopy experimental apparatus in the spectral regions of X–Ray, UV–Vis, IR, and THz, and the temporal regions between attosecond and millisecond.

Current research

My current research focuses on two main areas:

1. Spectroscopic and microscopic investigation of self–assembled chromophores. These chromophores include Naphthalenediimide amphiphiles, Guanidinium–substituted Naphthalenediimides, and Porphyrins. The self–assembled nanostructures carry potential applications in photovolatics, and optoelectronics.

2. The employment of steady–state, time–resolved, and femtosecond transient absorption pump–probe (fsTAPP) spectroscopy techniques in studying charge carrier relaxation and transfer dynamics in catalytic polymers and photovoltaic material. Some of which are:

   - 6,13–substituted [1,4]benzodioxino[2,3–b]oxanthrene ladder–type polymers.
   - transition metal complexes of substituted perylenediimide.
   - Methylammonium lead bromide perovskite nanostructures of various shapes and sizes.
   - Hot carries in high–absorption, low–bandgap iron(II) sulfide nanowires with titania interface.
   - Alkylammonium lead halide perovskite with titania interface.

   Additionally, I explored the dynamics of substituted azobenzene molecular switches, as well as oxidized and reduced graphene quantum dots. Femtosecond experiments were supplemented with various time–resolved and steady–state spectroscopic techniques, such as UV–Vis, PL, FTIR, TRPL, and TCSPC. Occasionally DFT calculations were also carried out using Gaussian package.

Past research

During my masters degree research, I explored the utilization of fluorescence spectroscopy; excitation, emission, synchronous, excitation–emission matrix, and TCPSC, combined with chemometrics such as; principle component analysis, partial least–square analysis, and parallel factor analysis, in characterizing and classifying food matrices, such as: honey, jam, and vegetable oils, especially olive oil.
A one semester project during my undergraduate involved the synthesis, isolation, and characterization of selected silyl enol ethers.

Work Experience

- Sep 2019–present: Research assistant, Dep. of Chemistry, Uni. of Akron, Akron, OH.
- May 2019–Sep 2019: Research assistant, Dep. of Chemistry, Uni. of Louisville, Louisville, KY.
- Aug 2013–May 2019: Teaching assistant, Dep. of Chemistry, Uni. of Louisville, Louisville, KY.
- Sep 2011–Jun 2013: Lecturer, Basic sciences, KSAU–HS, Riyadh, Saudi Arabia.
- Sep 2007–Aug 2011: Research associate, Chemistry Department, Yarmouk Uni., Jordan.
- Sep 2006–Aug 2011: Middle School/High school teacher, Ministry of Education, Jordan.

During my current and past graduate school career I have trained and mentored five graduate students.

Key Skills

Laser and experimental systems

Operating, realigning, and routinely maintaining following laser systems and experimental setups:

- Ti:Sapphire chirped pulse regenerative amplifier (Shapeshifter, CPA Clark–MXR). This CPA is based on flash–pumped Intracavity frequency doubled Nd:YAG laser, and a 1550 nm Femtosecond fiber oscillator.
- Two noncollinear optical parametric amplifier, one of which tuned to the visible region (450–700 nm), and the other is tuned to the Near–IR region (0.8–1.6 μm).
- Dual probe transient absorption pump–probe experimental setup, with a NIR single wavelength probe, and a Sapphire–based supercontinuum broadband probe. Detection utilized lock–in amplifier for the single wavelenegth, and a liner CMOS camera for the broadband probe, incorporated in a customizable spectrograph.

Additionally, the following were built and added to the existing experimental setup.

- Time–resolved photoluminescence apparatus, utilizing femtosecond pulses for pump, with photodiode and oscilloscope acquisition scheme.
- Dual–output second and third harmonic generator from the CPA femtosecond fundamental beam.
- Motorized CaF_2 supercontinuum generator to replace the sapphire generator in the probe arm.
- In–line photodiode detector on the pump arm for continuous fluence monitoring and pump reference correction.
- A secondary motorized linear actuator to expand the temporal scan range.

Commercial instrumentation

In the course of my research history, the following commercial instruments were routinely used:

- Spectrophotometer, Cary Bio 50, Agilent Technologies.
- Spectrophotometer, UV–1800, Shimadzu.
- Spectrophotometer, UV–1601, Shimadzu.
- Spectrofluorometer, fluorolog-2, Horiba.
- Spectrofluorometer, LS 55, PerkinElmer.
- Spectrofluorometer, FS900SDT, Edinburgh Instruments.
- FT–IR spectrometer, Spectrum 100, PerkinElmer,
- Photometers and fluorometers using on ocean optics miniature spectrographs and light–sources.
- Diode–laser TCSPC instrument, Edinburgh Instruments.
- Aerograph, Model 3400, Varian.

Wet chemistry

Basic wet chemistry skills were also utilized during my current and past research ventures, such as:

- Accurate solutions preparation, and concentration assessment.
- Assembling synthetic apparatus under ambient and inert gas conditions, including reflux and drop–wise reactant addition.
- Various work–up techniques such as liquid–liquid extraction, centrifugation, filtration, and column chromatography.

Electronics

I have also acquired various skills in understanding and operating electronic equipments during my current and past research ventures. Some of which include:

- Understanding of the inner working of computer hardware.
- Utilization of microcontrollers and single–board computers.
- Operations of Lock-in amplifiers, and oscilloscopes.
- Utilization of DAQ, vision, and control cards.
- Utilization of CCD/CMOS detector arrays, as well as photodiodes and photomultiplier tubes.
- Utilization of delay and function generators.
- Utilization of various mechanical chopping and shutter techniques.
- Utilization of various continuous and discreet UV–Vis light sources.

Computers OS, software, Programming and scripting

The following is a list of software environments and tools I have experience using:

- Microsoft DOS, and windows 3.11–10, all iteration of Microsoft Office suit, and EndNote.
- Various Linux distributions such as Fedora, CentOS, OpenSUSE, and Ubuntu.
- Open source office suits like LibreOffice, OpenOffice, and WPS.
- Data analysis and visualization tools like OriginLab, SigmaPlot, SciDAVis, and GNUPlot.
- Gaussian, GaussView, and Gabedit for quantum chemical calculations.
- Hardware and tool design like SolidWorks and OpenSCAD.

I Also have experience with programming and scripting in the following environments:

- Python 3.x employing packages such as NumPy, SciPy, matplotlib, lmfit.
- Latex and bibtex.
- Linux Bash/shell, used mainly for task automation.
- LabView for data acquisition and instrument automation.
- To some extent, MatLab and Julia language.

Personal skills

- Motivated
- Self–learning
- Leadership

- Independent
- Collaborative
- Analytical

- Problem solving
- Teaching
- Communication